The HERMES Experiment:
From the Design to the First Results

by

Michael Düren

The HERMES Experiment:
From the Design to the First Results

Den Naturwissenschaftlichen Fakultäten

der Friedrich-Alexander-Universität Erlangen-Nürnberg

zur

Erlangung des Dr. rer. nat. habil.

vorgelegt von

Dr. Michael Düren

aus

Birkesdorf, jetzt Düren

Abstract

HERMES is a new experiment at HERA (DESY) designed to study the spin structure of the nucleon by deep inelastic scattering of polarised electrons or positrons at 27 GeV, off polarised protons and neutrons. The aims, the design, the preparation of the analysis and the first results are presented.

HERMES makes use of two novel techniques: a longitudinally polarised electron (positron) beam in a storage ring and an internal polarised gas target. In May 1994 for the first time longitudinal electron polarisation was produced in a high energy storage ring. The polarisation is naturally in the transverse direction due to the Sokolov-Ternov effect. Spin rotators are used to rotate the spin into the longitudinal direction. A fast Compton polarimeter monitors the polarisation and allows for its interactive optimisation of the polarisation. Values of up to 70% have been reached.

HERMES uses the 'storage cell' technique to obtain optimal luminosity. A storage cell increases the density of the target gas by two orders of magnitude compared to a free gas jet.

Data taking will begin in 1995 with measurements of polarised spin structure functions and also of semi-inclusive polarised hadron production. The inclusive physics program is in competition with experiments at CERN and SLAC. The semi-inclusive physics program of HERMES promises to solve basic questions of the spin structure of matter by decomposing the spin contributions from gluons, from angular momentum and from the different quark flavours.

Contents

Chapter 1

Introduction

The quest for higher and higher energies is one route that elementary particle physics follows in order to understand the substructure of matter. A second route which is not so straight forward but at the end also gives new insights into the substructure of matter and into the properties of the underlying forces makes use of polarised beams and targets.

Spin physics is not a new subject, however, two recent technological developments have opened a new and exciting future for this field. The first development concerns the know-how for producing *high longitudinal spin polarisation in an electron storage ring*. This was successfully demonstrated at HERA for the first time [1, 2]. Secondly, the development of the *storage cell* technique has lead to polarised gas targets with high polarisation at densities which are about two orders of magnitude larger than what could be achieved with polarised gas jets. This technique was successfully demonstrated in the Heidelberg test storage ring in 1992 [3]. The HERMES experiment [4] at HERA will combine those two techniques and will be able to take precision data on polarised spin and flavour distributions of the quarks in the nucleon.

This paper starts with the physics motivation for the HERMES experiment. The formalism of polarised deep inelastic scattering is described and the current knowledge of the spin structure of the nucleon is summarised. The physics program of HERMES is described in the context of the recent results from the competing spin experiments at CERN and SLAC.

The next chapter describes the design criteria for spin experiments in general and applies these concepts to the design of the HERMES experiment. The aim of HERMES is to measure the spin structure of nucleons as completely and as precisely as possible.

The following chapter covers to the generation, optimisation and measurement of polarisation in storage rings. HERA is first high energy storage ring which achieved longitudinal polarisation by the use of spin rotators. A fast and reliable Compton polarimeter is used as feedback monitor during the interactive optimisation of the beam parameters. Polarisation values of up to 70% have been achieved. This is well above optimistic expectations and the HERMES experiment will profit from it. The polarised internal gas target and the spectrometer are described in the following

chapters. The use of a storage cell in a high energy electron ring is a novel technique. Special care was taken in the design of the target and of the spectrometer to keep possible background from synchrotron radiation and beam losses under control.

One chapter will focus in the preparation of the physics analysis. This has three aspects: the preparation of the reconstruction and analysis software, the understanding of the performance of the detectors and the extraction and correction of the physics results from the measured count rates. HERMES has developed its own software packages which allow for an efficient and transparent processing of the data. A Monte Carlo program has been developed which allows for a detailed simulation of the detector performance and of the expected physics results. The reconstruction and analysis software has been successfully tested with Monte Carlo and real data. The anticipated precision of the experiment has been estimated by means of Monte Carlo methods. The understanding of the performance of the detectors is currently in progress.

This paper ends up with presenting first measurements of deep inelastic scattering processes. HERMES has the potential to be a first-rate experiment in many aspects of polarised and unpolarised deep inelastic scattering physics during the next decade.

Chapter 2

The Physics Motivation

From Atoms to Quarks

Since the beginning of atomic physics, scattering experiments have been a key method to probe the substructure of matter. A prominent example is the discovery of the atomic nucleus by Geiger, Marsden and Rutherford in 1909 who scattered α-particles off a gold foil [5]. Later the nucleons and finally the substructure of the proton and neutron have been resolved by increasing the energies of the projectiles.

By the end of the 60's, deep inelastic scattering experiments had shown that the structure functions of the nucleon are to a large extent independent of the momentum transfer Q^2. This 'scaling behaviour' of the structure functions implies that nucleons consist of sub-particles, called 'partons' [6]. In the years prior to that, the investigation of symmetry properties of meson and baryon multiplets had lead to a mathematical model which assumed that hadrons are composed of hypothetical particles with fractional charge, called 'quarks' [7, 8]. The quark model allowed sum rules for the structure functions to be predicted which were verified by the scattering experiments. The charged partons could in this way be identified as being quarks.

However, one of the experimental results showed that only about 50% of the nucleon's momentum is carried by quarks [9, 10]. The missing momentum could be explained in the framework of quantum chromodynamics (QCD) which describes the force between quarks by the exchange of vector bosons, called 'gluons'. The missing momentum is carried by gluons which do not show up in the electro-weak scattering processes as they carry no electro-weak charge. QCD also explains the experimentally observed 'scaling violation' of the structure functions at high momentum transfer [11, 12].

The investigation of the hadronic final state in deep inelastic scattering allows a deeper insight into the sub-nuclear processes than the inclusive measurement alone. One of the key properties of QCD, the colour confinement, shows up experimentally by the fact that quarks are never observed as free particles. When a quark inside a nucleon obtains a high momentum during a scattering process, it fragments into a bundle of hadrons, called a jet, when it tries to leave the colour 'bag' of the nucleon. Experimentally, the momentum, the charge and the flavour of a struck quark can be measured indirectly by analysing the composition of the hadron jet. The first direct evidence for the existence of gluons was the observation of multi-jet events [13].

The momentum distributions of the various quark flavours in the proton and neutron are experimentally known with good precision nowadays. Besides the 'valence' quarks, which define the quantum numbers of the nucleon, there is a sea of virtual quark anti-quark pairs. An experimental surprise was that the light quark sea is not flavour symmetric, a fact which contradicted naive expectations. It was discovered as a violation of the Gottfried sum rule [14]. A second experimental surprise was the discovery of the (nuclear) EMC effect where the quark distributions in a nucleus are not identical to the quark distribution in free nucleons [15]. The EMC effect may play a key role in the attempt to explain nuclear forces in the framework of fundamental processes in QCD.

The Spin Structure of the Nucleon

The spin and the magnetic moment of elementary particles can be understood in the framework of the Dirac theory which was developed in the late 20's [16]. The properties of electrons and other fundamental fermions are perfectly described when higher order QED corrections are taken into account.

The magnetic moments of the nucleons seemed to disagree with the Dirac predictions. One of the convincing features of the quark model was that it was able to explain the magnetic moments of the nucleons and also of the hyperons as a vector sum of the magnetic moments of the valence quarks. The experimental results are in surprisingly good agreement with the calculations from the quark model as shown in figure 2.1 [17]. The quarks themselves are spin-1/2 Dirac particles. The
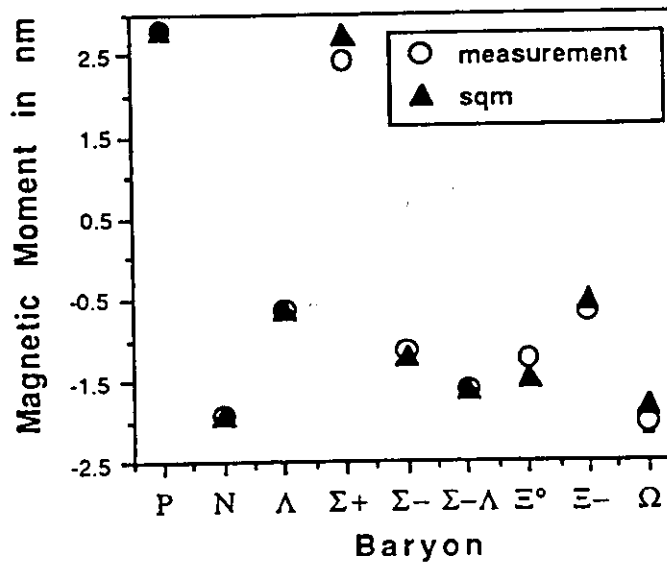
Figure 2.1: Comparison of the measured magnetic moments (circles) to the expectations from the simple quark model (triangles). The largest deviation from the naive model is only 20%.

value 1/2 for the spin of the quarks can be experimentally derived from the angular

distribution of jets in e^+e^--collisions and also from the approximate validity of the Callan-Gross relation of the structure functions in deep-inelastic scattering.

The magnetic moment of the nucleon reflects a static property of the nucleon. The internal dynamic spin structure of the nucleon can be probed by scattering polarised beams off polarised targets. As it is non-trivial to produce polarised nuclear targets and high energy polarised beams, the spin distributions of quarks inside the nucleon remained inaccessible over many years.

In 1966, prior to the development of QCD, Bjørken found a fundamental relationship between the spin-dependent structure functions and the weak coupling constant [18]. The Bjørken sum rule is derived from current algebra assumptions and obtains some QCD-corrections at finite energies. Unfortunately it could not be verified experimentally at this time. A second sum rule was derived by Ellis and Jaffe which is less fundamental as it assumes some SU(3) symmetry arguments, however it was easier to measure [19]. First experiments at SLAC in 1976 and 1983 were in agreement with the predictions, however the experimental uncertainties were large.

The Spin Crisis

The EMC collaboration repeated these measurements with higher precision and published in 1987 a result for the spin structure function of the proton which disagreed with the predictions of the Ellis-Jaffe sum rule [20]. The measured value for the Ellis-Jaffe sum was used in combination with SU(3) symmetry considerations to calculate the fraction of the nucleon's spin which was carried by the up, down and sea quarks. The surprising result was that the majority of the spin of the nucleon was not carried by the spin of the quarks. This experimental result caused much excitement [21]. It was especially surprising as the calculations of the static magnetic moments which use similar symmetry arguments, worked so well in the quark model. F.E. Close mentioned in this context that if the violation would have been discovered in the 60's, may be the quark model would have been discarded.

Obviously, more and better experiments were needed. The confirmation of the EMC result was one aim. The most important check would be a measurement of the Bjørken sum rule. R. Feynman wrote about the Bjørken sum rule: "Its verification, or failure, would have a most decisive effect on the direction of future high-energy theoretical physics" [22]. Bjørken stated "If my sum rule is wrong then QCD is wrong as well".

The investigation of the sum rule is the first step. However, the main aim in the long term has to be to get the full experimental information about the spin composition of the nucleon. Generally, the nucleon's spin s_z^N is composed of the spin contribution of the valence quarks Δu_v and Δd_v, the sea quarks Δq_s, the contributions from the gluons ΔG and possibly by angular momentum L_z:

$$s_z^N = \frac{1}{2} = \frac{1}{2}\left(\Delta u_v + \Delta d_v + \Delta q_s\right) + \Delta G + L_z \ . \tag{2.1}$$

The goal of the spin experiments is to measure these spin contributions as function of the kinematic quantities x and Q^2. The results will become a crucial test for

every model that tries to describe the wave function of the nucleon. Some of the results will test QCD itself. The Q^2 dependence of the Bjørken sum can be used to determine the strong coupling constant α_s.

2.1 The Basic Formalism of Deep Inelastic Scattering

Deep inelastic scattering is the study of lepton-hadron scattering in the limit of high momentum transfer. In the following sections we will concentrate on the electromagnetic lepton-nucleon scattering. In lowest order QED the scattering process is described by the exchange of a virtual photon. Figure 2.2 shows the basic Feynman diagram. In inclusive scattering experiments, only the scattered lepton is analysed whereas semi-inclusive scattering experiments observe the hadronic final state in coincidence with the scattered lepton.
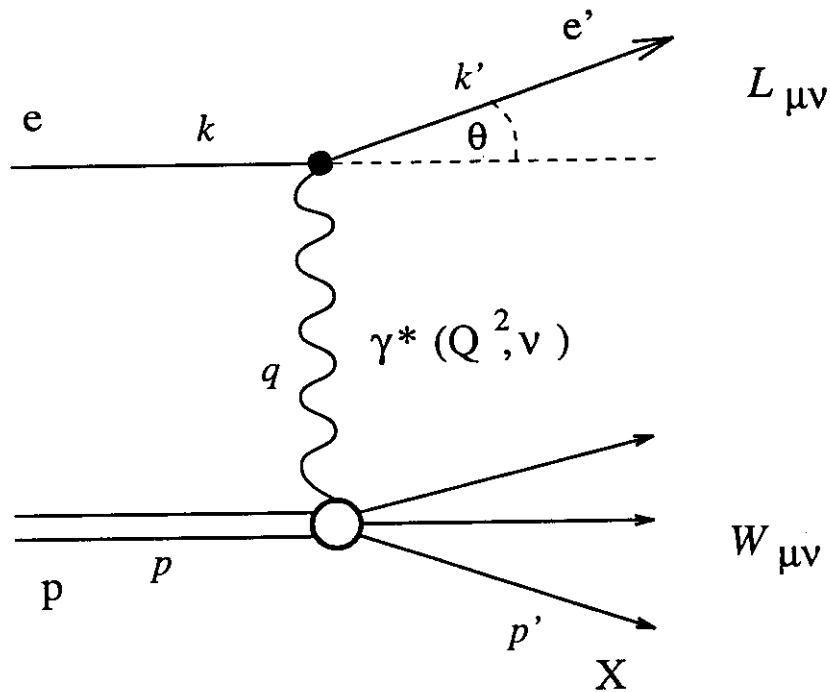
Figure 2.2: Deep inelastic electron proton scattering in lowest order QED.

2.1.1 The Kinematics

The relevant kinematic variables of the scattering process are the four-momenta of the incoming lepton (k), of the scattered lepton (k'), of the nucleon (p), of the final state (p') and the four-momentum of the exchanged virtual photon $q = k - k'$. The following Lorentz invariants are defined in the standard way as [23]:

$$s = (k + p)^2 \qquad (2.2)$$

$$Q^2 = -q^2 = -(k - k')^2 > 0 \tag{2.3}$$

$$\nu = \frac{p \cdot q}{M} \tag{2.4}$$

$$W^2 = p'^2 = M^2 + 2M\nu - Q^2. \tag{2.5}$$

M is the mass of the proton. The mass m of the lepton can be neglected in most situations. In the laboratory frame of a fixed target experiment with E and E' being the energies of the lepton before and after the scattering process and θ being the scattering angle, the Lorentz invariants can be calculated as

$$Q^2 \stackrel{lab}{=} 4EE' \sin^2 \frac{\theta}{2} \tag{2.6}$$

$$\nu \stackrel{lab}{=} E - E' \tag{2.7}$$

where ν is the energy transfer of the virtual photon to the nucleon and Q^2 is the invariant mass of the exchanged photon which defines the resolution of the scattering process. The dimensionless scaling variables x and y are defined as

$$x = \frac{Q^2}{2p \cdot q} = \frac{Q^2}{2M\nu} \tag{2.8}$$

$$\text{and} \quad y = \frac{p \cdot q}{p \cdot k} \stackrel{lab}{=} \frac{\nu}{E}. \tag{2.9}$$

In the case of elastic nucleon scattering ($W^2 = M^2$) from equation (2.5) it follows that

$$Q^2 = 2M\nu \tag{2.10}$$

and x has the value 1. In general the kinematically allowed ranges of the variables are

$$0 < x \leq 1 \tag{2.11}$$

$$0 < y < \frac{1}{1 + xM/2E} < 1. \tag{2.12}$$

For a fixed beam energy E, the kinematics of deep inelastic scattering is determined completely by two variables. The experimentally measured pair of variables (E', θ) is usually converted into the pair (x, Q^2) or (ν, Q^2) which can be interpreted in the parton frame. Figure 2.3 shows the allowed range of deep inelastic scattering for the case of the HERMES experiment with a beam energy E of 28 GeV.

In case of transversely polarised targets, a third degree of freedom plays a role, namely the angle ϕ between target polarisation direction and the scattering plane of the lepton as illustrated in figure 2.4. α is the polar angle of the target polarisation in respect to the beam direction.

In case of semi-inclusive measurements, a Lorentz invariant scaling variable z is introduced which relates (in the lab frame) the energy E_h of the hadron to the maximal available energy ν:

$$z = \frac{p \cdot p_h}{p \cdot q} \stackrel{lab}{=} \frac{E_h}{\nu} \tag{2.13}$$

$$0 < z < 1. \tag{2.14}$$
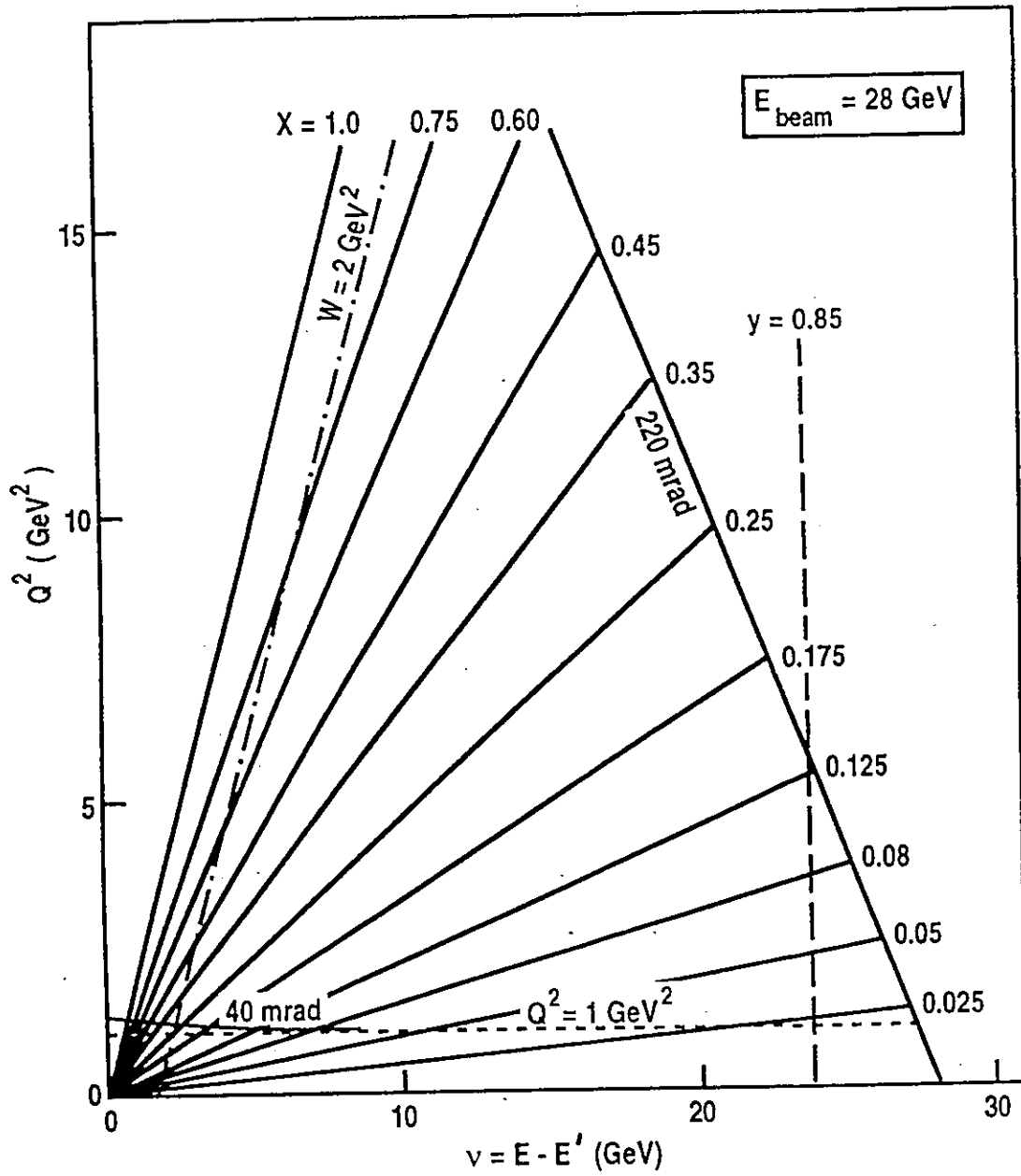
Figure 2.3: The kinematic plane of deep inelastic scattering at 28 GeV is shown. For a given beam energy and Q^2 and ν value, all other kinematic variables are defined. Lines of constant x, θ, Q^2, W and y are shown.

polarisation plane

scattering plane
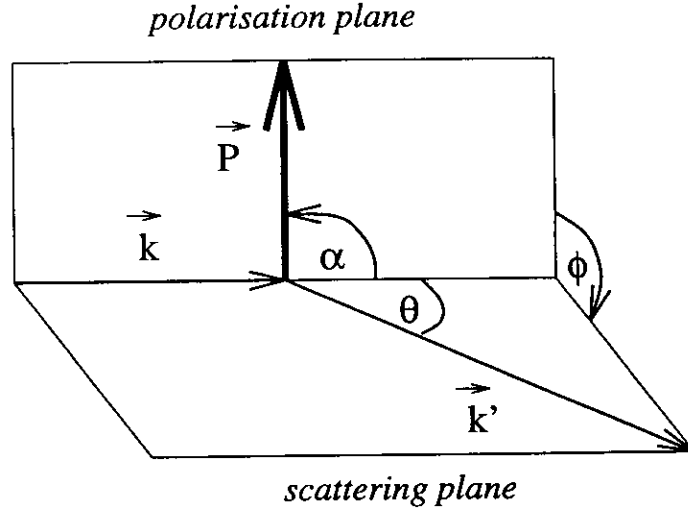
Figure 2.4: Definition of the angles between the incoming beam $\vec{k}$, the scattered electron $\vec{k'}$ and the direction $\vec{P}$ of the target polarisation.

2.1.2 The Unpolarised Cross-Section

The cross section in deep inelastic scattering can be expressed in terms of a leptonic tensor $L^{\mu\nu}$ and a hadronic tensor $W_{\mu\nu}$:

$$\frac{d^2\sigma}{d\Omega\,dE'} = \frac{\alpha^2 E'}{Q^4 E} L^{\mu\nu} W_{\mu\nu} \tag{2.15}$$

with $\alpha_s = 1/137.04$ being the fine-structure constant. The leptonic tensor is calculated from the spinors u according to the Feynman rules:

$$L^{\mu\nu} = \sum_{s_l'} (\bar{u}(k',s_l')\gamma^\mu u(k,s_l)) \cdot (\bar{u}(k,s_l)\gamma^\nu u(k',s_l')). \tag{2.16}$$

The spin states s_l' are summed as the spin of the final state is not observed. In case of unpolarised beams and targets, the initial spins s_l are averaged, and the leptonic tensor becomes

$$L^{\mu\nu} = 2\left[k'^\mu k^\nu + k^\mu k'^\nu + (m_e^2 - k\cdot k')g^{\mu\nu}\right]. \tag{2.17}$$

The electron mass m_e can be neglected. $g^{\mu\nu}$ is the metric tensor. The hadronic tensor reflects the structure of the nucleon and cannot be calculated from first principles. Symmetry arguments and the conservation laws of QED reduce the tensor to two real functions W_1 and W_2:

$$\begin{aligned}
W_{\mu\nu} &= W_1(Q^2,\nu)\left(-g_{\mu\nu} + \frac{q_\mu q_\nu}{q^2}\right) \\
&+ \frac{W_2(Q^2,\nu)}{M^2}\left(p_\mu - \frac{p\cdot q}{q^2}q_\mu\right)\left(p_\nu - \frac{p\cdot q}{q^2}q_\nu\right).
\end{aligned} \tag{2.18}$$

By introducing the dimensionless structure functions

$$F_1(x, Q^2) = MW_1(Q^2, \nu) \tag{2.19}$$

$$F_2(x, Q^2) = \nu W_2(Q^2, \nu), \tag{2.20}$$

the unpolarised cross section becomes

$$\frac{d^2\sigma}{dx dQ^2} = \frac{4\pi\alpha^2}{Q^4} \cdot \left[F_1(x, Q^2) \cdot y^2 + \frac{F_2(x, Q^2)}{x} \cdot \left(1 - y - \frac{Mxy}{2E} \right) \right]. \tag{2.21}$$

Photon Absorption Cross Section

The cross section can alternatively be described in terms of absorption cross sections for longitudinally (σ_L) and transversely (σ_T) polarised photons:

$$\frac{d^2\sigma}{dx dQ^2} = \Gamma(\sigma_T + \epsilon\sigma_L). \tag{2.22}$$

Γ describes the flux of virtual photons and ϵ is the degree of transverse polarisation of the virtual photon:

$$\epsilon = \frac{1 - y}{1 - y + y^2/2}. \tag{2.23}$$

The ratio $R = \sigma_L/\sigma_T$ of the longitudinal and transverse cross sections is related to the structure functions by the following equation:

$$R(x, Q^2) = \frac{(1 + 4M^2x^2/Q^2)F_2(x, Q^2) - 2xF_1(x, Q^2)}{2xF_1(x, Q^2)}. \tag{2.24}$$

2.1.3 The Polarised Cross-Sections and Asymmetries

In case of polarised beam and target, the cross section contains additional terms [23, 24, 25, 26]. The differential cross section has to take into account the azimuthal angle ϕ of the scattered lepton in respect to the target polarisation in case the polarisation is not longitudinal:

$$\frac{d^3\sigma}{d\cos\theta d\phi\, dE'} = \frac{\alpha^2 E'}{Q^4 E} L^{\mu\nu} W_{\mu\nu} \tag{2.25}$$

The leptonic tensor $L^{\mu\nu}$ in equation (2.16) becomes:

$$L^{\mu\nu} = 2\left[k'^\mu k^\nu + k^\mu k'^\nu - k \cdot k' g^{\mu\nu} - i\epsilon^{\mu\nu\alpha\beta}q_\alpha s_{l\beta} \right] \tag{2.26}$$

where $s_{l\beta}$ is the spin four-vector of the incoming lepton defined as

$$s_l^\mu = \frac{1}{2}\bar{u}(k, s_l)\gamma^\mu\gamma_5 u(k, s_l). \tag{2.27}$$

$\epsilon^{\mu\nu\alpha\beta}$ is the totally anti-symmetric Levi-Civita tensor. The general form of the hadronic tensor is

$$
\begin{aligned}
W_{\mu\nu} &= W_1(Q^2,\nu)\left(-g_{\mu\nu} + \frac{q_\mu q_\nu}{q^2}\right) \\
&+ \frac{W_2(Q^2,\nu)}{M^2}\left(p_\mu - \frac{p\cdot q}{q^2}q_\mu\right)\left(p_\nu - \frac{p\cdot q}{q^2}q_\nu\right) \\
&+ G_1(Q^2,\nu)M\, i\epsilon_{\mu\nu\lambda\sigma}q^\lambda s_h^\sigma \\
&+ \frac{G_2(Q^2,\nu)}{M}i\epsilon_{\mu\nu\lambda\sigma}q^\lambda(p\cdot q s_h^\sigma - s_h\cdot q p^\sigma)\,.
\end{aligned}
\tag{2.28}
$$

Here s_h is the (axial) polarisation vector of a spin-1/2 target. The spin independent part of the leptonic tensor is symmetric in $\mu\nu$ and probes the symmetric part of $W_{\mu\nu}$, whereas the spin dependent part is anti-symmetric in $\mu\nu$, so that the polarisation asymmetry of the cross section is completely determined by the anti-symmetric part of $W_{\mu\nu}$.

In analogy to the unpolarised case the dimensionless spin-structure functions g_1 an g_2 are introduced:

$$
g_1(x,Q^2) = M^2\nu G_1(Q^2,\nu) \tag{2.29}
$$

$$
g_2(x,Q^2) = M\nu^2 G_2(Q^2,\nu)\,. \tag{2.30}
$$

The spin-dependent part of the polarised deep inelastic cross section is then given by the following formula:

$$
\begin{aligned}
\frac{d^3(\sigma(\alpha) - \sigma(\pi + \alpha))}{dx\,dy\,d\phi} &= \frac{e^4}{4\pi^2 Q^2}\left[\cos\alpha\left(\left[1 - \frac{y}{2} - \frac{y^2}{4}\gamma^2\right]g_1(x,Q^2) - \frac{y}{2}\gamma^2\,g_2(x,Q^2)\right)\right. \\
&\left. - \sin\alpha\cos\phi\sqrt{\gamma^2\left[1 - y - \frac{y^2}{4}\gamma^2\right]}\left(\frac{y}{2}g_1(x,Q^2) + g_2(x,Q^2)\right)\right].
\end{aligned}
\tag{2.31}
$$

γ is defined as $\gamma = \sqrt{Q^2}/\nu$ and α is the polar angle of the target polarisation with respect to the beam direction. The difference $\sigma(\alpha) - \sigma(\pi + \alpha)$ describes the cross section difference which is achieved by reversing the target polarisation.

Spin Asymmetries

Experimentally, the spin structure functions $g_1(x)$ and $g_2(x)$ can be determined by a combined asymmetry measurement off a longitudinally ($\alpha = 0°, 180°$) and a transversely ($\alpha = 90°, 270°$) polarised target. Because of the mixing of g_1 and g_2 a precise determination of g_1 from a longitudinally polarised target alone is not possible. The experimentally measured cross section asymmetries $A_\parallel$ and $A_\perp$:

$$
A_\parallel = \frac{\sigma^{\uparrow\downarrow} - \sigma^{\uparrow\uparrow}}{\sigma^{\uparrow\downarrow} + \sigma^{\uparrow\uparrow}}\,; \qquad A_\perp = \frac{\sigma^{\uparrow\rightarrow} - \sigma^{\uparrow\leftarrow}}{\sigma^{\uparrow\rightarrow} + \sigma^{\uparrow\leftarrow}} \tag{2.32}
$$

obtained by spin flip of a longitudinally and transversely polarised target can be related to the asymmetries A_1 and A_2 of the exchanged virtual photon by the relations

$$A_\parallel = D \cdot (A_1 + \eta \cdot A_2) \quad \text{and} \tag{2.33}$$

$$A_\perp = d \cdot (A_2 - \xi \cdot A_1). \tag{2.34}$$

The kinematic factors D, d and η, ξ are defined by

$$D = \frac{y(2-y)}{y^2 + 2(1-y)(1+R)} \tag{2.35}$$

$$\eta = \frac{2\gamma(1-y)}{(2-y)} \tag{2.36}$$

$$d = D\sqrt{\frac{2\epsilon}{1+\epsilon}} \tag{2.37}$$

$$\xi = \eta\frac{1+\epsilon}{2\epsilon} \tag{2.38}$$

with ϵ being the degree of transverse polarisation of the virtual photon (see eq.(2.23)). D and d can be regarded as depolarisation factors of the virtual photon. $R(x, Q^2)$ is the ratio of cross-sections for longitudinally and transversely polarised virtual photons (see eq.(2.24)).

Photon Absorption Cross Section

From the measured asymmetries $A_\parallel$ and $A_\perp$, the virtual photon asymmetries A_1 and A_2 can be calculated which are independent of the kinematics of the lepton and are directly related to the photon absorption cross section of the nucleon for a given x and Q^2:

$$A_1 = \frac{\sigma_{1/2} - \sigma_{3/2}}{\sigma_{1/2} + \sigma_{3/2}} = \frac{g_1 - \gamma^2 g_2}{F_1} \tag{2.39}$$

$$A_2 = \frac{\sigma_{TL}}{\sigma_T} = \frac{\gamma(g_1 + g_2)}{F_1}. \tag{2.40}$$

Here $\sigma_{(1/2)}$ and $\sigma_{(3/2)}$ are the virtual photo-absorption cross section when the projection of the total angular momentum of the photon-nucleon system along the incident photon direction is 1/2 or 3/2 respectively. $\sigma_T = 1/2(\sigma_{(1/2)} + \sigma_{(3/2)})$ is the total transverse photo-absorption cross section and σ_{TL} is a term arising from the interference between transverse and longitudinal amplitudes. It follows that $\sigma_{TL} \leq \sqrt{\sigma_L \sigma_T}$ and therefore there is a positivity limit on the value of A_2:

$$A_2 = \frac{\sigma_{TL}}{\sigma_T} \leq \sqrt{\frac{\sigma_L \sigma_T}{\sigma_T^2}} = \sqrt{R(x, Q^2)} \tag{2.41}$$

The structure function $F_1(x)$ in eqs. (2.39) and (2.40) is calculated according to equation (2.24) from the experimentally known functions $F_2(x)$ and $R(x)$.

2.1.4 The Interpretation of Structure Functions in the Quark-Parton Model

Structure functions describe the internal composition of the target nucleon. The structure functions of the nucleons show 'scaling behaviour', i.e. they are approximately independent of the variable Q^2. As Q^2 defines the resolution of the scattering process, the independence of Q^2 has to be interpreted in the way that the internal structure of the components is point-like or at least much smaller than the resolution of the process. The quark-parton model accounts for this and describes the nucleon as being composed by point-like on-shell particles. In the framework of QCD, this behaviour of the quarks is maintained in the limit of high momentum transfer, where quarks behave approximately like free particles due to the asymptotic freedom of QCD. The deep-inelastic scattering process is actually the incoherent superposition of elastic scattering off partons.

Elastic Quark Scattering

From the kinematics of elastic scattering the following conditions can be derived in analogy to equation (2.10):

$$Q^2 = 2m\nu \qquad (2.42)$$

$$x = \frac{Q^2}{2M\nu} = \frac{m}{M} \qquad (2.43)$$

where m is an apparent mass of the parton in the scattering process. The picture of the infinite momentum frame is used to illustrate the meaning of the Bjørken variable x in an intuitive way. The parton carries the fraction $p_q = xp$ of the momentum p of the nucleon. Momentum distributions $q_f(x)$ are assigned in the quark model which describe the probability to find a quark of flavour f with a momentum fraction x inside the nucleon.

The cross section for the scattering off quarks can be directly calculated from the probability distribution $q_f(x)$. The hadronic tensor $W_{\mu\nu}$ becomes similar to the leptonic tensor in formula (2.26) where k and k' are replaced by xp and p' and the 'charge density' $e_f^2 q_f(x)$ and a phase space factor is added to the formula:

$$W_{\mu\nu} = \frac{e_f^2 q_f(x)}{2M xp \cdot q} \left[xp_\mu p'_\nu + xp_\nu p'_\mu - g_{\mu\nu} xp \cdot p' + ih\epsilon_{\mu\nu\alpha\beta} q^\alpha xp^\beta \right]. \qquad (2.44)$$

Here, h is the helicity of the quark. With the relation $p' = xp + q$ and after omitting the p^μ and p^ν terms (they disappear in the contraction with $W_{\mu\nu}$ due to current conservation) the equation becomes:

$$W_{\mu\nu} = \frac{e_f^2 q_f(x)}{2M xp \cdot q} \left[2xp_\mu xp_\nu - g_{\mu\nu} xp \cdot q + ih\epsilon_{\mu\nu\alpha\beta} q^\alpha xp^\beta \right]. \qquad (2.45)$$

This formula has to be compared with the parametrisation of $W_{\mu\nu}$ in terms of structure functions. The following formula is deduced from equation (2.28) by omitting

q_μ, q_ν terms (they disappear when $W_{\mu\nu}$ is contracted with $L^{\mu\nu}$). The expression for $W_{\mu\nu}$ becomes:

$$
\begin{aligned}
W_{\mu\nu} = {} & -\frac{F_1(Q^2,\nu)}{M}g_{\mu\nu} \\
& + \frac{F_2(Q^2,\nu)}{Mp\cdot q}p_\mu p_\nu \\
& + \frac{ig_1(Q^2,\nu)}{M\nu}\epsilon_{\mu\nu\lambda\sigma}q^\lambda s_h^\sigma \\
& + \frac{ig_2(Q^2,\nu)}{M^2\nu^2}\epsilon_{\mu\nu\lambda\sigma}q^\lambda(p\cdot qs_h^\sigma - s_h\cdot qp^\sigma).
\end{aligned}
\tag{2.46}
$$

The individual structure functions can now be related to the quark distributions. With the notation that $q_f^{+(-)}$ is the probability to find a quark of momentum fraction x with the helicity parallel (anti-parallel) to the nucleon spin, the structure functions are identified as:

$$
F_1(x,Q^2) = \sum_f \frac{e_f^2}{2}\left(q_f^+(x) + q_f^-(x)\right)
\tag{2.47}
$$

$$
F_2(x,Q^2) = \sum_f e_f^2 x\left(q_f^+(x) + q_f^-(x)\right)
\tag{2.48}
$$

$$
g_1(x,Q^2) = \sum_f \frac{e_f^2}{2}\left(q_f^+(x) - q_f^-(x)\right)
\tag{2.49}
$$

$$
g_2(x,Q^2) = 0
\tag{2.50}
$$

The sum is over all quark and anti-quark flavours which contribute to the structure of the nucleon at a given momentum transfer.

The Unpolarised Quark Distributions

In the simple parton model, all structure functions are independent of Q^2. The structure functions $F_1(x)$ and $F_2(x)$ are determined by the unpolarised quark distributions

$$
q_f(x) = q_f^+(x) + q_f^-(x).
\tag{2.51}
$$

From formula (2.47) and (2.48) it follows that $F_1(x)$ and $F_2(x)$ are directly correlated by the equation

$$
F_1(x) = 2xF_2(x),
\tag{2.52}
$$

which is known as the Callan-Gross relation [27]. From equation (2.24) it follows that in the scaling limit the Callan-Gross relation is equivalent to the fact that $R(x,Q^2)$ and the longitudinal photon absorption cross section σ_L are (approximately) zero. The reason is the helicity conservation in the scattering process off the quarks which have half-integer spin.

Explicitly, the structure function $F_2^p(x)$ for the proton is

$$
F_2^p(x) = x\left(\frac{4}{9}u(x) + \frac{1}{9}d(x) + \frac{1}{9}s(x) + \frac{4}{9}\bar{u}(x) + \frac{1}{9}\bar{d}(x) + \frac{1}{9}\bar{s}(x)\right).
\tag{2.53}
$$

The contribution by charm and heavier quarks is neglected at moderate momentum transfer. Assuming SU(2) isospin symmetry, the structure function of the neutron is

$$F_2^n(x) = x \left(\frac{1}{9} u(x) + \frac{4}{9} d(x) + \frac{1}{9} s(x) + \frac{1}{9} \bar{u}(x) + \frac{4}{9} \bar{d}(x) + \frac{1}{9} \bar{s}(x) \right). \tag{2.54}$$

Note that u(x) is the momentum distribution of the 'up' quark in the proton and of the 'down' quark in the neutron:

$$u(x) = u^p(x) = d^n(x) \tag{2.55}$$

$$d(x) = d^p(x) = u^n(x). \tag{2.56}$$

A different parametrisation distinguishes between valence distributions $q_v(x)$ which account for the quantum numbers of the nucleon and sea distributions $q_s(x) = \bar{q}_s(x)$ which arise from the production of quark-antiquark pairs due to quantum fluctuations:

$$\begin{aligned} F_2^p(x) &= x \left(\frac{4}{9} \left[u_v(x) + u_s(x) + \bar{u}_s(x) \right] \right. \\ &\left. + \frac{1}{9} \left[d_v(x) + d_s(x) + \bar{d}_s(x) + s_s(x) + \bar{s}_s(x) \right] \right). \end{aligned} \tag{2.57}$$

It should be mentioned that according to recent measurements [14], the light quark sea is not flavour symmetric:

$$u_s(x) \neq d_s(x). \tag{2.58}$$

The Polarised Quark Distributions

It has been shown that the structure function $F_2(x)$ reflects the momentum distributions of the quarks. In a similar way the function $g_1(x)$ is determined by the spin distributions $\delta q_f(x)$ of the quarks:

$$\delta q_f(x) = q_f^+(x) - q_f^-(x). \tag{2.59}$$

Explicitly, the spin structure function $g_1^p(x)$ for the proton is given as

$$g_1^p(x) = \frac{1}{2} \left(\frac{4}{9} \delta u(x) + \frac{1}{9} \delta d(x) + \frac{1}{9} \delta s(x) + \frac{4}{9} \delta \bar{u}(x) + \frac{1}{9} \delta \bar{d}(x) + \frac{1}{9} \delta \bar{s}(x) \right). \tag{2.60}$$

The spin structure function $g_2(x)$ is zero in this simple model which neglects masses and intrinsic momenta of the quarks inside the nucleon.

2.1.5 QCD and Sum Rules

The 'spin-statistics problem' of the naive quark model, which is related to the symmetry properties of quark wave functions, leads to the introduction of a quantum number – the 'colour' of quarks. 'Colour' is based on a SU(3) symmetry group. Quantum Chromo Dynamic (QCD) is the corresponding non-Abelian gauge theory which uses the colour quantum number of the quarks as sources of colour force fields.

The field bosons of QCD are called gluons and carry colour charges themselves. QCD very successfully explained the confinement of quarks, the basic features of fragmentation and the asymptotic freedom of quarks at high momentum transfer.

QCD in principle should be able to predict the quark wave functions of the nucleons, however theory is still far away from this goal as pertubative methods are not applicable and lattice calculations are very difficult and not yet far enough advanced. Nevertheless, techniques have been developed to approach the calculation of structure functions in QCD. The Altarelli-Parisi equations describe the Q^2 evolution of the structure functions [11]. They can be illustrated by the following intuitive picture: with increasing Q^2 the resolution of the scattering process increases and more and more of the substructure is resolved. Therefore the structure functions become softer at higher momentum transfer. The experimental results are in excellent agreement with the QCD predictions. The variation of the structure functions with Q^2 is used to extract the (running) coupling constant (α_s) of the strong interaction [28, 29].

A powerful technique to derive sum rules of the structure functions is the operator product expansion (OPE) [30]. In OPE the virtual photon-proton scattering amplitude is divided into a part which represents the long-distance physics and another which describes the light-cone physics. The latter can be handled by techniques of pertubative QCD. The importance of these sum rules comes from the fact that they are derived directly from QCD and allow for a model independent test of QCD.

2.2 Inclusive Spin Physics at CERN, SLAC and DESY

The first polarised deep inelastic scattering experiments were the SLAC-Yale experiments E-80 [31] in 1976 and later E-130 [32] and the EMC experiment NA2' [20] which generated the 'spin crisis' in 1987. Since then there were new experiments proposed at SLAC (E-142/143) [33, 34], CERN (SMC) [35] and DESY (HERMES) [4].

The experiment E-142 uses a polarised ^3He gas target in an external polarised electron beam of $E = 19.4$, 22.7 and 25.5 GeV. The data cover a kinematic range of $0.03 < x < 0.6$ at discrete scattering angles of 4.5° and 7° and an average Q^2 of 2 GeV^2.

The experiment E-143 uses polarised ammonia and deuterated ammonia targets and beam energies of $E = 9.7$, 16.2 and 29.1 GeV. The kinematic range for the published data at $E = 29.1$ GeV is $0.029 < x < 0.8$ and 1.3 (1.0) GeV$^2 < Q^2 <$ 10 GeV^2 for the proton (deuteron) data.

Two more experiments (E-154 and E-155) are planned at SLAC using a 50 GeV electron beam starting in late 1995.

The SMC experiment scatters polarised muons off a polarised butanol and deuterated butanol target. The beam energy is 190 GeV (100 GeV) and the kinematic range of the data is $0.003(0.006) < x < 0.7(0.6)$ and 1 GeV$^2 < Q^2 < 60(30)$ GeV^2

for the proton (deuteron) measurements.

In the following sections the first experimental results will be presented together with the proposed measurements of the HERMES experiment. The statistical accuracy of the anticipated HERMES results refer to a 'standard run' which corresponds to a certain beam and target polarisation and integrated luminosity for each of the targets. The actual running time which is needed for one standard run is approximately 9 weeks and depends on the performance of HERMES and HERA. The anticipated precision of HERMES will be discussed in detail in chapter 7.

2.2.1 The Spin Structure Function $g_1(x)$ of Proton and Neutron

The spin structure function $g_1(x)$ is extracted from the longitudinal spin asymmetry $A_{\parallel}(x)$ according to eqs. (2.33) and (2.39) by neglecting the contribution from $g_2(x)$:

$$g_1(x) = \frac{A_1(x)F_2(x,Q^2)}{2x(1+R(x,Q^2))} \ . \qquad (2.61)$$

$F_2(x,Q^2)$ and $R(x,Q^2)$ are taken from unpolarised deep inelastic scattering experiments [36, 37].

The Proton Data

The figures 2.5 and 2.6 show the world data on the asymmetry $A_1^p(x)$ and on the spin structure function $g_1^p(x)$ of the proton. The plots contain data from the original measurements at E-80 [31], E-130 [32] and EMC [20], and recent data from SMC [42] and E-143 [34]. The bands below the points show the systematic errors of the measurements. All data sets are compatible within their errors. E-143 has the most precise measurement. The SMC data extend to very low x, however with large statistical errors. $g_1^p(x)$ is positive for all x. The SMC data show some indication that $g_1^p(x)$ increases towards very low x, however this behaviour is statistically not significant.

The anticipated precision of the HERMES data from one 'standard run' is shown in the top part of figure 2.6. The size of the error bars has to be scaled down when HERMES decides to take more data on hydrogen then just 9 weeks. The predicted precision of E-143 and one HERMES standard run are comparable. The experimental techniques of the two experiments are very different and each of the experiments will be a cross check of the other one.

Extraction of $g_1^n(x)$

The neutron structure function is experimentally extracted by two methods. It is firstly derived from the comparison of deuterium and hydrogen targets and secondly from ^3He. The deuteron is a spin-1 target and therefore has in principle three possible orientations $m_I = 1, 0, -1$ of the spin vector relative to the quantisation axis.
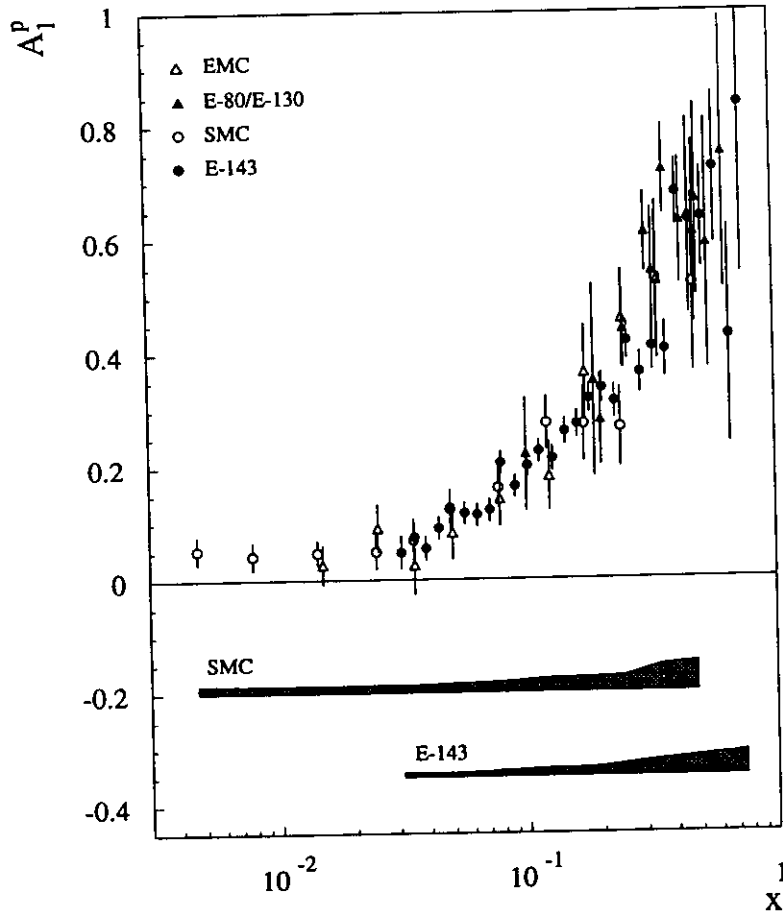
Figure 2.5: The world data on the spin asymmetry $A_1^p(x) = g_1(x)/F_1(x)$ of the proton. The plot shows the original EMC data, the old and new SLAC and the new SMC data. The bars below the figures indicate the systematic errors. The new data confirm the EMC measurement that lead to the spin-crisis. The new SLAC data are very precise at medium x. The main interest in the SMC data are the low x points which might indicate an unexpected large contribution in the Ellis-Jaffe integral coming from the low x extrapolation.
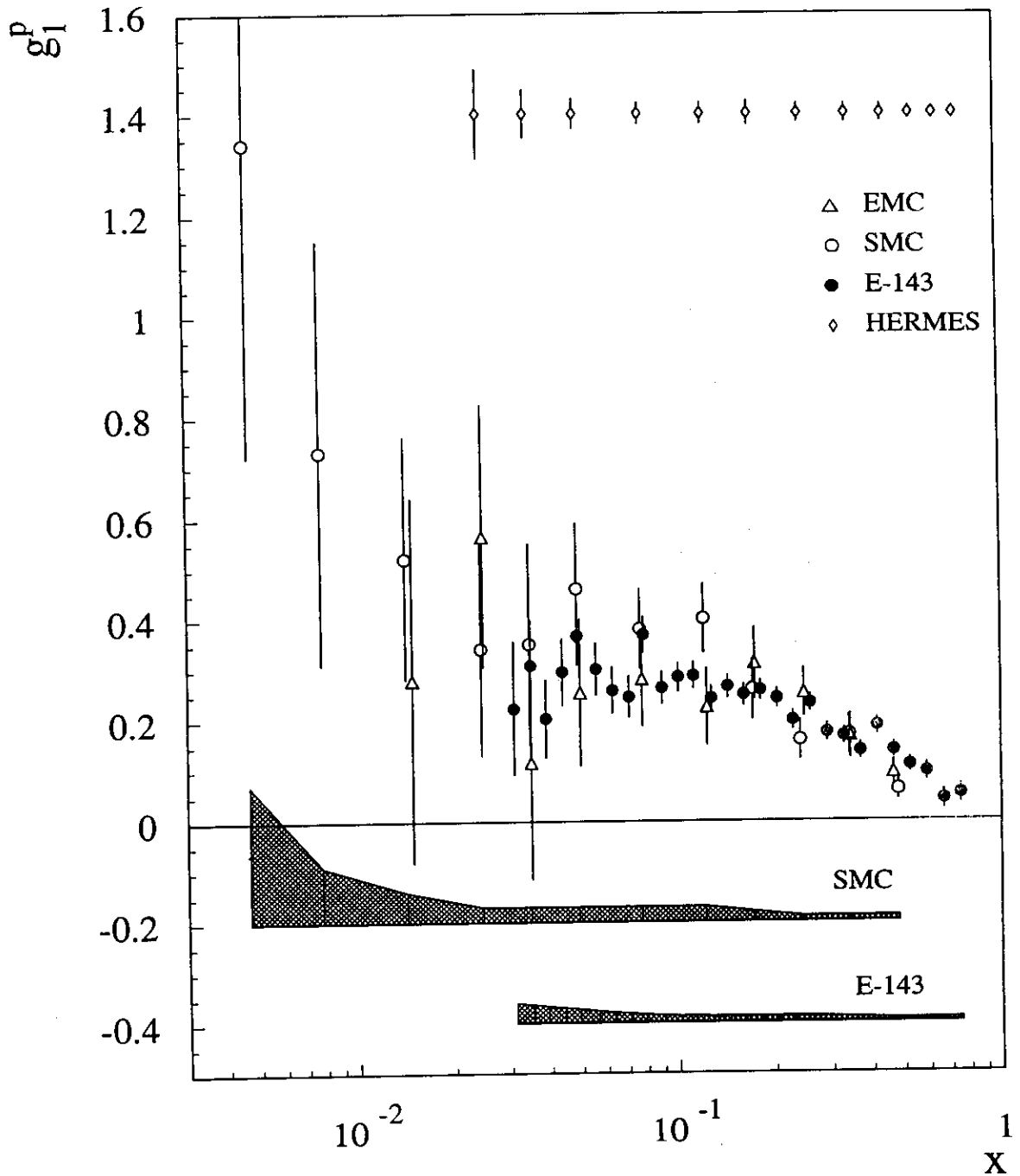
Figure 2.6: The world data on the spin structure function $g_1^p(x)$ of the proton. Besides the original measurement of EMC and the recent measurements of SMC and E-143, the anticipated precision of the HERMES experiment is indicated in the error bars at the top part of the figure. The errors correspond to a standard run of 9 weeks and can be reduced by longer running.

The $m_I = 0$ component of the cross-section ($\sigma^{\uparrow 0}$) dilutes the measured asymmetries:

$$A_\parallel^d = \frac{3}{2}\frac{\sigma^{\uparrow\uparrow} - \sigma^{\uparrow\downarrow}}{\sigma^{\uparrow\uparrow} + \sigma^{\uparrow 0} + \sigma^{\uparrow\downarrow}} \; ; \qquad A_\perp^d = \frac{3}{2}\frac{\sigma^{\uparrow\rightarrow} - \sigma^{\uparrow\leftarrow}}{\sigma^{\uparrow\rightarrow} + \sigma^{\uparrow 0} + \sigma^{\uparrow\leftarrow}} \tag{2.62}$$

If one assumes that the deuteron is simply composed of a proton and a neutron in S-state then the $m_I = 0$ component is

$$\sigma^{\uparrow 0} = \frac{1}{2}(\sigma^{\uparrow\uparrow} + \sigma^{\uparrow\downarrow}) \tag{2.63}$$

and the asymmetries are equal to the asymmetries of a spin-1/2 particle as defined in equation (2.32). As the SLAC and CERN experiments cannot measure the $m_I = 0$ component, nuclear effects in deuterium are accounted for by a global depolarisation factor according to the following equation:

$$A_1^n = \frac{A_1^D}{1 - 1.5 w_D}\frac{\sigma^D}{\sigma^D - \sigma^H} - A_1^H\frac{\sigma^H}{\sigma^D - \sigma^H} \; , \tag{2.64}$$

where $w_D \approx 0.05$ denotes the D-state probability of the deuteron. In the HERMES experiment the $m_I = 0$ component can be measured directly as the polarisation of the gas target can be arranged in all substates separately. This way an unambiguous determination of $A_\parallel^d$ will be possible.

In ^3He the spins of the two protons are mostly anti-parallel so that ^3He can be regarded as an approximate neutron target. The asymmetries are however diluted by the protons and additionally small nuclear corrections have to be applied to correct for the S'- and D-wave components of the nuclear wave function.

The Deuteron Data

The spin structure function $g_1^d(x)$ of the deuteron has been measured by SMC [35] and E-143 [38]. The data for $A_1^d(x)$ and $g_1^d(x)$ are shown in figure 2.7 and 2.8. Both data sets are compatible. Similar to the proton data, the SLAC results have the better statistical precision and the CERN results reach lower x, however with low accuracy. The structure function $g_1^d(x)$ is small for all x and is slightly negative at low x. The anticipated precision of the HERMES experiment is indicated in figure 2.8. The precision of one standard run is comparable or better than the E-143 measurement.

The ^3He Data

The E-142 [33] experiment has measured $g_1^n(x)$ using a ^3He target. The results for $A_1^n(x)$ and $g_1^n(x)$ are shown in figure 2.9 and 2.10. Overlaid are the results for $g_1^n(x)$ derived from the E-143 $D - H$ data. All data sets are compatible within their errors, also the results from the SMC $D - H$ data which are not shown in the figure. $g_1^n(x)$ is small and negative over the full range of x. The precision of $g_1^n(x)$ is still very poor. The anticipated precision for the ^3He and $D - H$ measurements of HERMES are indicated in the top of the figure. Compared to the SLAC data the precision for one standard run will be better especially at large x.
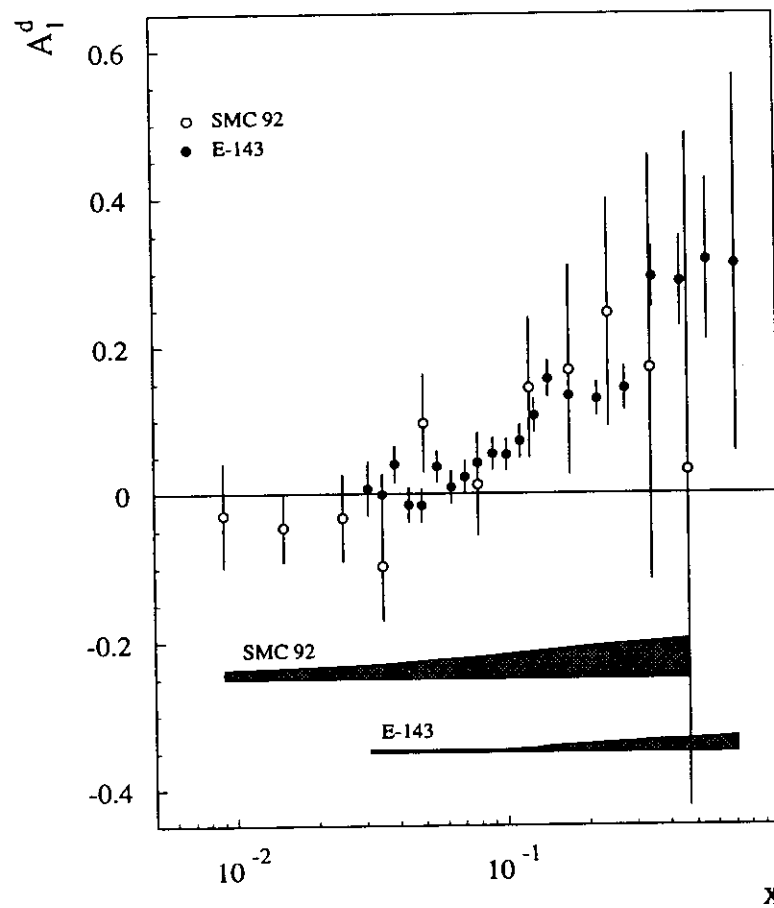
Figure 2.7: The world data on the spin asymmetry $A_1^d(x)$ of deuterium.
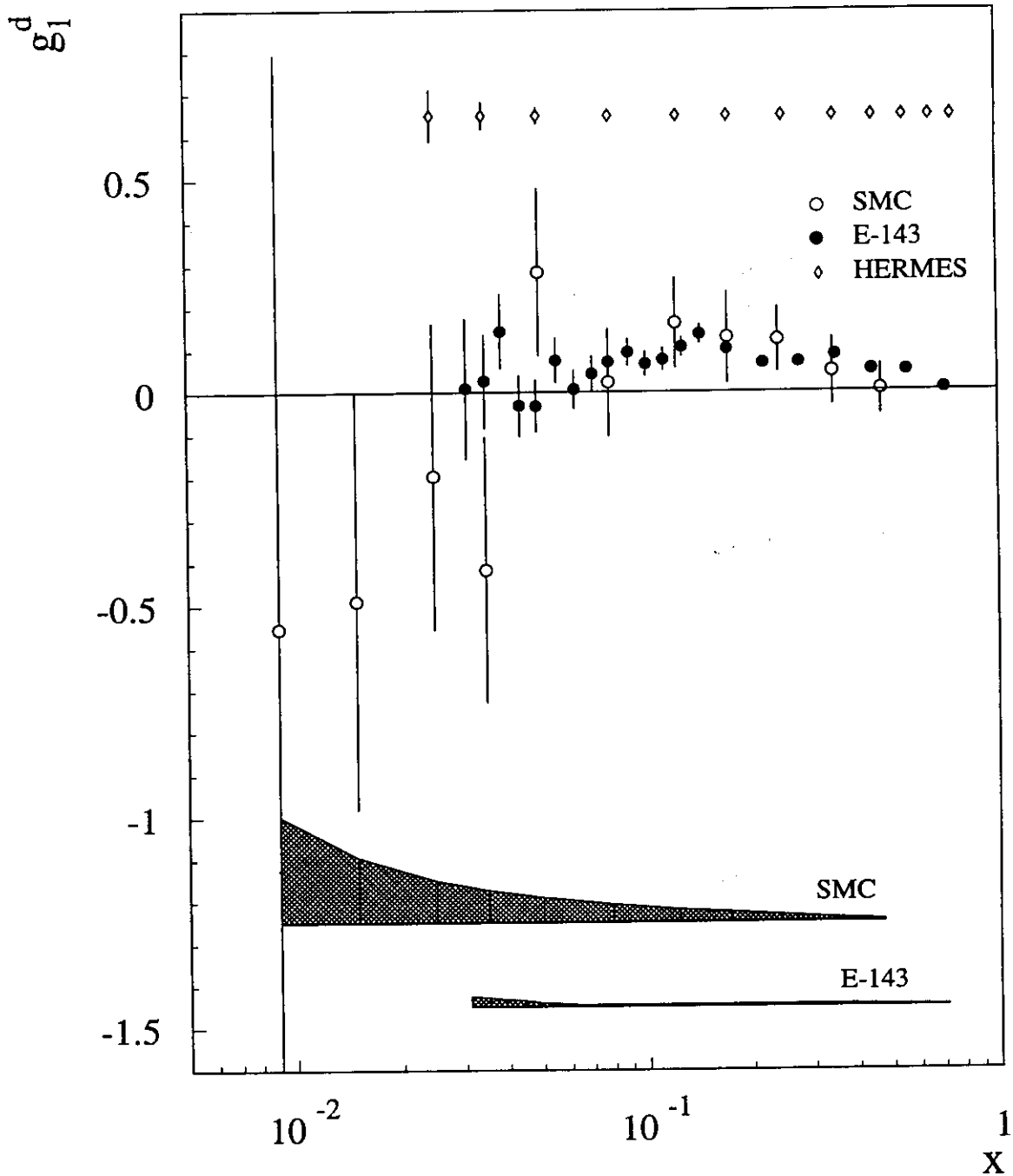
Figure 2.8: The world data on the spin structure function $g_1^d(x)$ of deuterium are plotted. The error bars at the top of the figure indicate the statistical precision of one HERMES standard run of 9 weeks.
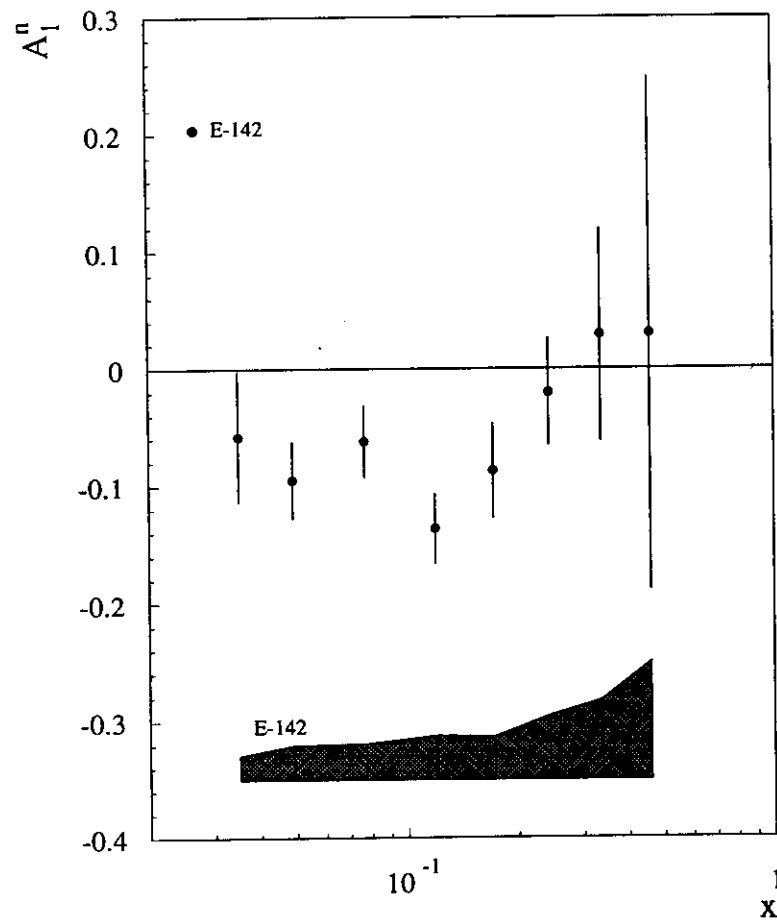
Figure 2.9: World data on the ^3He spin asymmetry $A_1^{n(^3He)}(x)$.
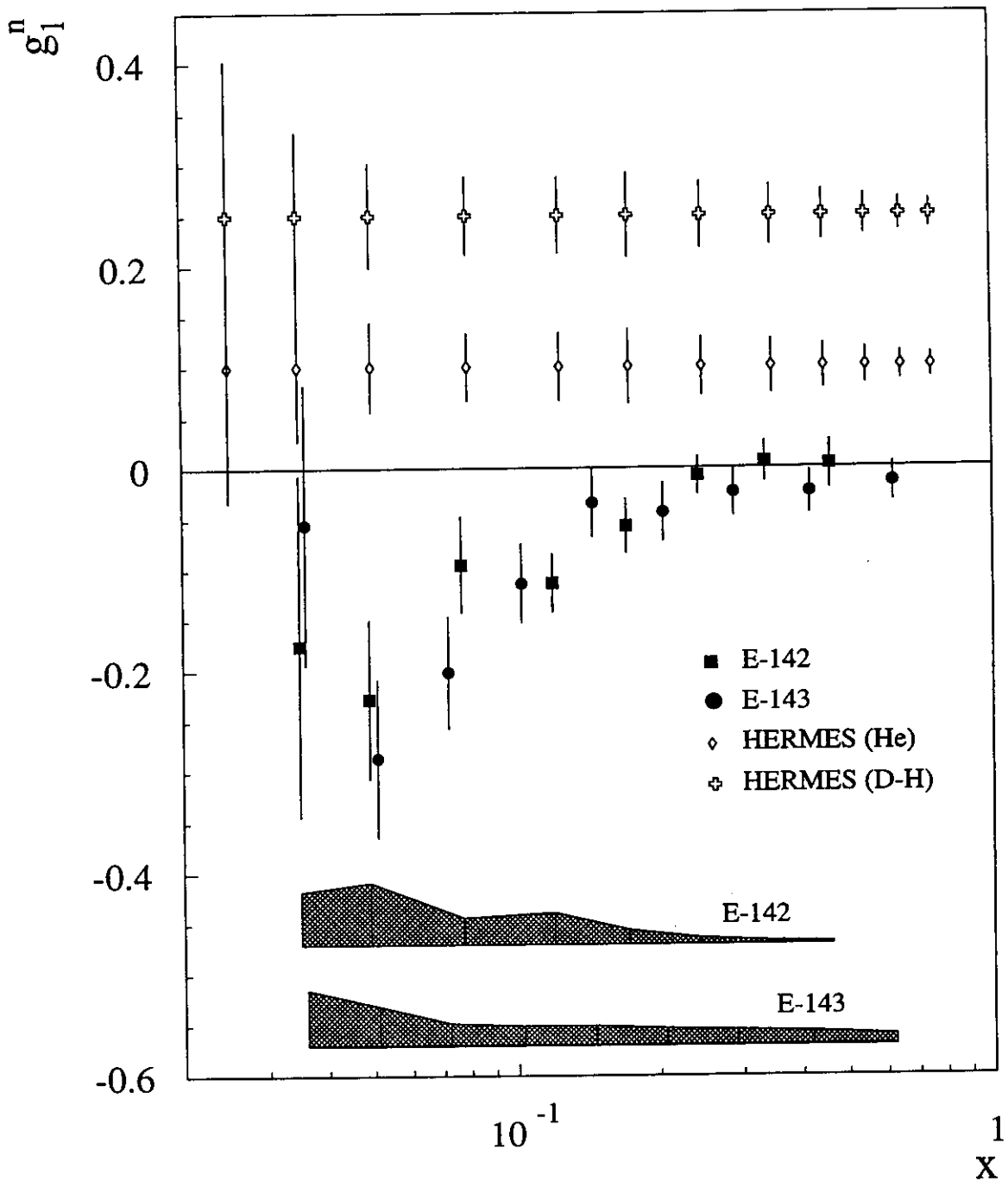
Figure 2.10: The the neutron spin structure function $g_1^n(x)$ obtained from ^3He and from hydrogen and deuterium data at SLAC. The upper part of the figure shows the anticipated precision of the HERMES experiment using ^3He or $D - H$ for one standard run of each target.

2.2.2 The Sum Rules and the Determination of α_s

The shape of the various structure functions is of importance for testing different models of the nucleon. Their integrals are of special interest as they allow important tests of basic assumptions about the spin structure of the nucleon.

Ellis-Jaffe Sum Rule

Using $SU(3)_f$ symmetry arguments, the spin fraction which is carried by the u, d and s quarks in the nucleon can be related to the axial coupling known from baryon-octet decays. With the definition $\int_0^1 \delta q_f(x)\, dx = \Delta q_f(x)$, the first moment of $g_1(x)$ can be expressed as follows [19, 39]:

$$\Gamma_1^{p(n)} = \int_0^1 g_1^{p(n)}(x)\, dx \;\; = \;\; \frac{1}{12}\left(\pm a_3 + \frac{a_8}{3}\right) + \frac{1}{9}a_0 + \text{QCD corrections} \quad (2.65)$$

with

$$a_3 = \;\; g_a/g_v = F + D \;\; = \Delta u - \Delta d \quad (2.66)$$

$$a_8 = \;\;\;\;\;\; 3F - D \;\;\;\; = \Delta u + \Delta d - 2\Delta s \quad (2.67)$$

$$a_0 = \;\;\;\;\;\;\;\; \Delta\Sigma \;\;\;\;\;\; = \Delta u + \Delta d + \Delta s \quad (2.68)$$

a_3 and a_8 are known from neutron and from hyperon decay. The numerical values are [40, 39]:

$$F + D \;\; = 1.2573 \pm 0.0028 \quad F/D \;\; = 0.575 \pm 0.016 \quad (2.69)$$

$$\text{or} \;\;\; F \;\;\;\; = 0.459 \pm 0.008 \quad D \;\;\;\;\; = 0.798 \pm 0.008 \; . \quad (2.70)$$

$\Delta\Sigma$ denotes the total spin carried by quarks. The Ellis-Jaffe sum rule [19] is derived from the (reasonable but probably false) assumption, that the total spin contribution of the strange quarks is negligible:

$$\Delta s \stackrel{!}{=} 0 \; . \quad (2.71)$$

The Ellis-Jaffe sum rules for proton and neutron follow (without QCD corrections) from equation (2.65) to (2.68) directly as:

$$\Gamma_1^p = \int_0^1 g_1^p(x)\, dx \;\; = \;\; \frac{1}{18}\left(9F - D\right) = 0.185 \quad (2.72)$$

$$\Gamma_1^n = \int_0^1 g_1^n(x)\, dx \;\; = \;\; \frac{1}{18}\left(6F - 4D\right) = -0.024 \; . \quad (2.73)$$

In 1987, the Ellis-Jaffe integral was measured by the EMC [20] and compared to the theoretical value with first order QCD corrections:

$$\int_0^1 g_1^p(x)\, dx = (0.189)_{theor} = (0.126 \pm 0.010 \pm 0.015)_{EMC/SLAC} \; . \quad (2.74)$$

The violation of the sum rule caused the so-called *'spin crisis'*. Hundreds of theoretical papers were written that tried to explain the failure by different models and

theoretical assumptions. The situation of the theoretical approaches is reviewed in [21]. The need for more experimental data became obvious. At this time the HERMES experiment was proposed [4].

The new data from SLAC [33, 34, 38, 41] and SMC [35, 42] confirm the violation of the Ellis-Jaffe sum rule at the 3-σ level. Table 2.1 gives a summary of the experimental results for the proton, deuteron and neutron. The measured values are compared to the theoretical predictions. Recently, QCD corrections of higher order have been calculated [43, 44]. Taking into account three flavours ($n_f = 3$), the sum rules can be written as:

$$
\begin{aligned}
\int_0^1 g_1^{p(n)}(x, Q^2)\, dx \;=\; & \frac{1}{12}\left(\pm a_3 + \frac{a_8}{3}\right) \times \left[1 - \left(\frac{\alpha_s(Q^2)}{\pi}\right) - 3.5833\left(\frac{\alpha_s(Q^2)}{\pi}\right)^2 \right.\\
& \left. -20.2153\left(\frac{\alpha_s(Q^2)}{\pi}\right)^3 - \mathcal{O}(130)\left(\frac{\alpha_s(Q^2)}{\pi}\right)^4 + \ldots \right]\\
& +\frac{1}{9}\Delta\Sigma(Q^2) \times \left[1 - \left(\frac{\alpha_s(Q^2)}{\pi}\right) - 1.0959\left(\frac{\alpha_s(Q^2)}{\pi}\right)^2 \right.\\
& \left. -\mathcal{O}(6)\left(\frac{\alpha_s(Q^2)}{\pi}\right)^3 + \ldots \right].
\end{aligned}
\tag{2.75}
$$

The QCD corrections introduce a Q^2 dependence as well in the integrals as in $\Delta\Sigma(Q^2)$, the total spin carried by the quarks. One of the sources of the Q^2 dependence is the anomalous dimension of the singlet axial current due to the Adler-Bell-Jackiw anomaly [45, 46].

The anticipated precision of the HERMES data is included in table 2.1. Quoted is the statistical error for one standard run and the systematic error which is taken from the proposal by adjusting it to the new absolute values of the integrals. An updated version of the systematic errors will be given when first data are available. The calculation of the errors is described in chapter 7.

Bjørken Sum Rule

The Bjørken sum rule [47]:

$$
\int_0^1 [g_1^p(x) - g_1^n(x)]\, dx = \frac{1}{6}\left|\frac{g_A}{g_V}\right| + \text{QCD corrections}
\tag{2.76}
$$

relates the spin structure functions $g_1^{p,n}$ to the axial charges g_A and g_V measured in Gamow-Teller nuclear β-decay. The derivation of the Bjørken sum rule needs no assumptions about the strange sea as the influence of the strange quarks compensates when the difference of proton and neutron is taken. It is derived from pure current algebra assumptions plus some QCD corrections. A violation of the Bjørken sum rule would cast doubt on the validity of the quark-parton model or pertubative QCD. First results from SLAC and SMC confirm the Bjørken sum rule at the one sigma level with a precision of about 10% as shown in table 2.1.

Table 2.1: Summary of the results of the Ellis-Jaffe and the Bjørken sum rules. The estimated statistical errors for HERMES are taken for one standard run and can be improved by a longer running. The quoted systematic errors are compiled from the official numbers in the HERMES proposal and will be updated when real data are available.

Ellis-Jaffe (proton):

experiment (target)	result	theory	$\langle Q^2 \rangle$ [GeV^2]
EMC (NH_3)	$0.126 \pm .010 \pm .015$	$0.189 \pm .005$	10
SMC (C_4H_9OH)	$0.136 \pm .011 \pm .011$	$0.176 \pm .006$	10
E143 (NH_3)	$0.127 \pm .004 \pm .010$	$0.160 \pm .006$	3
HERMES (H_1)	$\pm .004 \pm .007$		~ 2.5

Ellis-Jaffe (deuterium):

experiment (target)	result	theory	$\langle Q^2 \rangle$
SMC (C_4D_9OD)	$0.023 \pm .020 \pm .015$	$0.085 \pm .005$	4.6
E143 (ND_3)	$0.042 \pm .003 \pm .004$	$0.069 \pm .004$	3
HERMES (D_1)	$\pm .003$		~ 2.5

Ellis-Jaffe (neutron):

experiment (target)	result	theory	$\langle Q^2 \rangle$
SMC(C_4D_9OD) & EMC(NH_3)	$-0.08 \pm .04 \pm .04$	$0.002 \pm .005$	4.6
E142 (^3He)	$-0.022 \pm .007 \pm .009$	$-0.021 \pm .018$	2
E143 (ND_3&NH_3)	$-0.037 \pm .008 \pm .011$	$-0.021 \pm .018$	2
HERMES (H_1&D_1)	$\pm .007 \pm .004$		~ 2.5
HERMES (^3He)	$\pm .006 \pm .003$		~ 2.5

Bjørken:

experiment (targets)	result	theory	$\langle Q^2 \rangle$
SMC(C_4D_9OD) & EMC(NH_3)	$0.20 \pm .05 \pm .04$	$0.191 \pm .002$	4.6
SMC(C_4H_9OH & C_4D_9OD) & E142 (^3He)	$0.163 \pm .017$	$0.185 \pm .004$	5
E142 (^3He) & EMC (NH_3)	$0.146 \pm .021$	$0.183 \pm .007$	2
E143 (NH_3) & E142 (^3He)	$0.149 \pm .014$	$0.171 \pm .008$	3
E143 (ND_3) & E143 (NH_3)	$0.163 \pm .010 \pm .016$	$0.171 \pm .008$	3
HERMES (H_1&D_1)	$\pm .010 \pm .011$		~ 2.5
HERMES (H_1&^3He)	$\pm .008 \pm .007$		~ 2.5

HERMES will measure the Ellis-Jaffe integral of hydrogen, deuterium and ^3He and will thus have two independent ways to determine the Bjørken integral. Note that the deuteron integral has to be corrected for the D-state contribution and contains an additional factor of 2 from normalisation conventions: $\Gamma_1^d = (1-1.5w_D)(\Gamma_1^p + \Gamma_1^n)/2$. The anticipated precision of the measurements of the Bjørken sum rule by HERMES is included in table 2.1. The quoted systematic errors are compiled from the official numbers in the HERMES proposal and will be updated when real data are available. Especially the large error on the $H\&D$ determination of the Bjørken sum will decrease as new F_2 input functions from NMC will reduce one of the main error sources.

The Quark Spin Content of the Nucleus

Using the results for the Ellis-Jaffe integrals for proton and neutron, the spin fraction which is carried by the u, d and s quarks in the nucleon can be determined separately [39] according to equation (2.66) to (2.68). With QCD corrections to third order (eq. (2.75)) the following results were obtained from the SMC and SLAC data quoted at a renormalisation scale $Q^2 = 10$ GeV^2 [44]:

$$\Delta u = 0.85 \pm 0.03 \tag{2.77}$$

$$\Delta d = -0.41 \pm 0.03 \tag{2.78}$$

$$\Delta s = -0.08 \pm 0.03 \tag{2.79}$$

$$\Delta \Sigma = 0.37 \pm 0.07. \tag{2.80}$$

Basically all data sets are compatible. It should be noted however, that the data only agree when higher order QCD corrections are applied. Figure 2.11 [44] shows the total spin carried by quarks $(\Delta\Sigma)$ versus the order of the QCD perturbation theory. The coefficients of the higher order corrections in equation (2.75) are large. Doubts could be raised if the next order QCD correction is really small and under control.

The surprising result of the spin-EMC effect remains: the fraction of the spin carried by quarks $\Delta\Sigma$ is smaller than naively expected and the strange sea Δs is significantly polarised and negative.

Determination of α_s

If one takes the attitude that the Bjørken sum rule is so fundamental that it is beyond any doubts, then the dependence of the Bjørken integral on QCD corrections can be used to extract the value of the strong coupling constant $\alpha_s(Q^2)$ [43, 44]. From equation (2.75) follows:

$$\int_0^1 [g_1^p(x) - g_1^n(x)]\, dx = \frac{1}{6}\left|\frac{g_A}{g_V}\right|\left[1 - \left(\frac{\alpha_s(Q^2)}{\pi}\right) - 3.5833\left(\frac{\alpha_s(Q^2)}{\pi}\right)^2 \right.$$
$$\left. -20.2153\left(\frac{\alpha_s(Q^2)}{\pi}\right)^3 - \mathcal{O}(130)\left(\frac{\alpha_s(Q^2)}{\pi}\right)^4 + \ldots\right] \tag{2.81}$$

× *E142,* + *E143,* ◇ *SMC-d,* □ *SMC-p,* ⋈ *EMC*

all ΔΣ values evolved to $Q^2=10$ GeV²
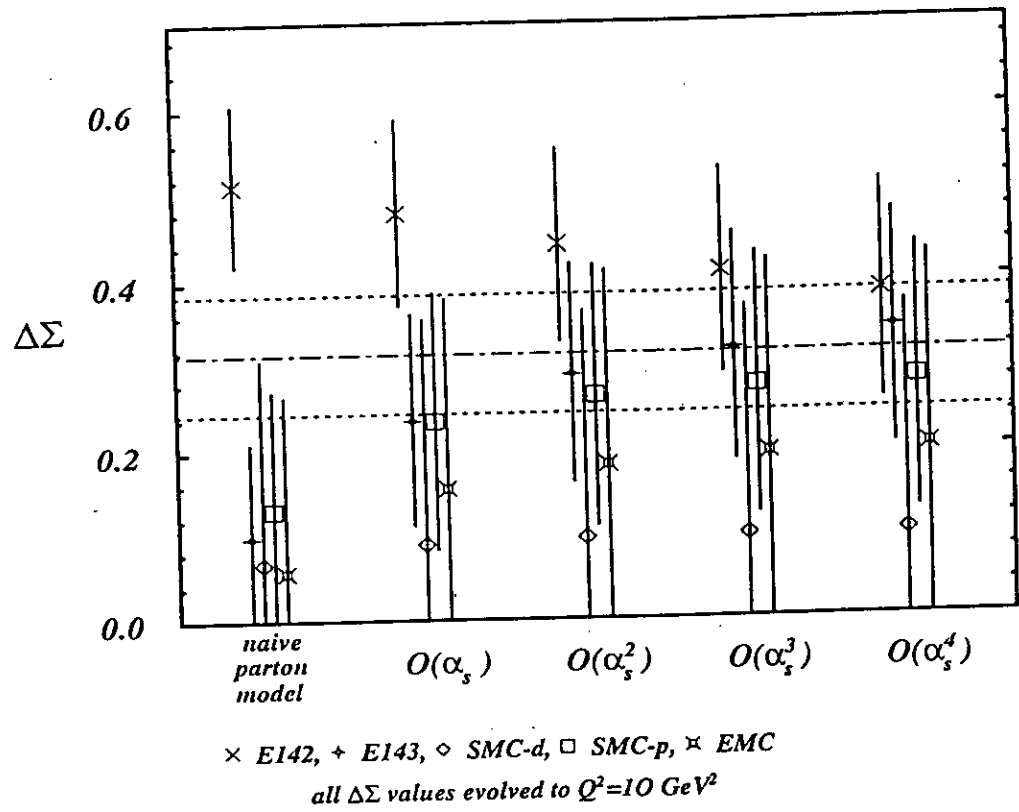
Figure 2.11: Plotted is the proton spin fraction carried by quarks versus the order of QCD perturbation theory. If one restricts the analysis of the data to low orders of QCD correction, there is only a poor agreement between the different data sets. Including higher order QCD corrections, the agreement improves. The total spin carried by the quarks is about one third of the nucleon spin.

$\alpha_s(Q^2)$ as extracted from spin structure functions can be compared with the value extracted from high energy jet physics. An agreement of those values would be (another) convincing proof of the universal validity of QCD as a theory of hadronic interactions. A first analysis of the SLAC data with QCD corrections to 4th order gave a value of [44]:

$$\alpha_s(2.5 \ GeV^2)|_{\overline{MS},N_f=3} = 0.375^{+0.062}_{-0.081} \qquad (2.82)$$

which corresponds at the Z_0 energy domain to a value of:

$$\alpha_s(M_z^2)|_{\overline{MS},N_f=5} = 0.122^{+0.005}_{-0.009} \ . \qquad (2.83)$$

This is in good agreement with the results measured at LEP: $\alpha_s(M_z^2) = 0.117\pm.005$. The advantage of results obtained from the Bjørken sum rule is that they can be taken in a low energy domain where they can be used to confirm the running coupling behaviour, i.e. the Q^2-dependence, of α_s. Figure 2.12 [44] visualises the agreement of the result with the world data on α_s. The nonlinear propagation of the error on α_s with Q^2 leads to the effect that values taken at SLAC or HERMES energies with certain relative errors obtain smaller relative errors when they are extrapolated to the Z_0 mass. This way the α_s values measured by spin experiments can become competitive to the precision measurements of α_s at the Z_0 mass.

The measurements are however not free of uncertainties. It has to be ensured that higher order QCD corrections are small and higher-twist effects are understood.

Extrapolation at $x \to 0$

One of the dominant systematic uncertainties in the measurement of the sum rules is the extrapolation of the structure function from the measured region towards $x \to 0$. The SMC data show some hint that $g_1^p(x)$ might be rising for $x < 0.01$. If this trend would be confirmed, the naive Regge pole extrapolation is inadequate and g_1 should not longer be extrapolated like $g_1(x \to 0) \sim x^\alpha$ with $-0.5 \le \alpha \le 0$. Instead it was discussed that from the exchange of two non-pertubative gluons the small-x behaviour becomes $g_1^p(x \to 0) \sim -(1 + 2\ln x)$ [48]. Figure 2.13 [49] shows some extreme models for the extrapolation of the SMC and EMC data towards low x. Models can be found which bring the data in agreement with the Ellis-Jaffe sum rule. It is clear that precise data at very low x would be important. The ideal experiment would certainly be to polarise the proton beam at HERA and to measure spin structure functions at HERA in collider mode at high Q^2 and very low x.

The alternative, and for the next years more realistic way to approach the problem is not to try to extract the valence and sea polarisation from the sum rules but instead to measure the valence, sea and gluon polarisation directly. The HERMES experiment will be able to do that by studying semi-inclusive spin asymmetries as described in chapter 2.3.

2.2.3 The Q^2-Dependence of $g_1(x)$

The Q^2-dependence of the spin structure functions is interesting for several reasons: first of all the sum rule integrals require data over a range of x at fixed Q^2. As
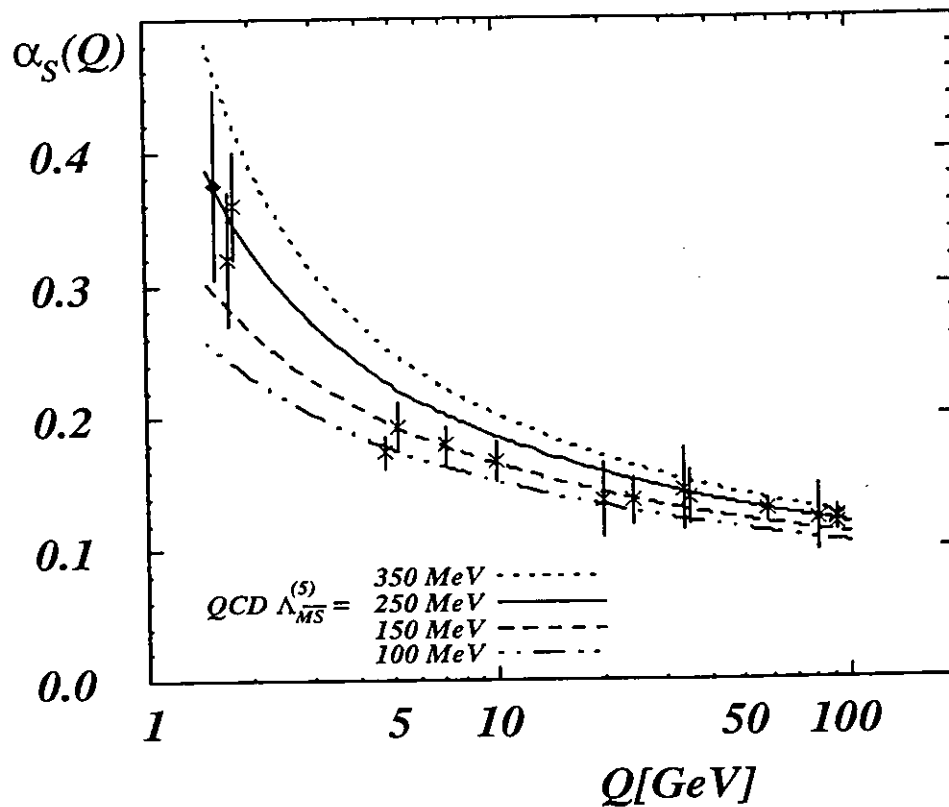
◆ **Bjorken sum rule**

✕ **compilation of world $\alpha_S(Q)$ data by S. Bethke (1994)**

Figure 2.12: World data of the strong coupling constant α_s are plotted as a function of Q. The data support the running coupling behaviour as predicted by QCD (lines). The extracted value of α_s from the analysis of the QCD corrections of the Bjørken sum rule (diamond point) agrees with the data of the other experiments. HERMES will be able to improve the precision of this result.
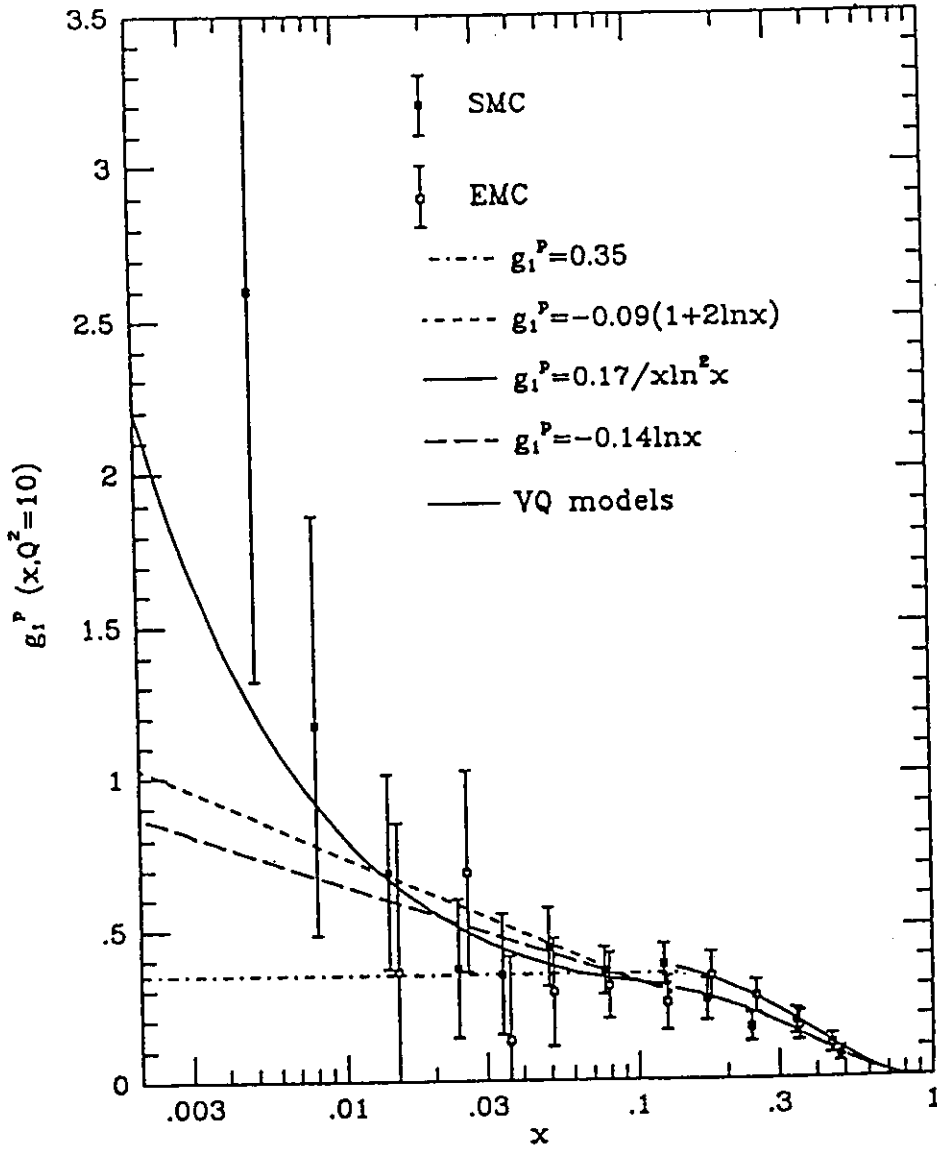
Figure 2.13: The data of $g_1^p(x)$ at low x are compared to various models. The SMC data show a trend to rise towards low x. If $g_1^p(x)$ rises logarithmically the contribution to the Ellis-Jaffe sum from $x \rightarrow 0$ becomes so large that the data are consistent with the original prediction of the Ellis-Jaffe sum rule.

however the data from all existing experiments have different mean Q^2 values at different x, the data have to be corrected. This is only possible when the Q^2-dependence is known. Secondly, the Q^2 evolution of the spin structure functions can be calculated by QCD. A verification would be an important test of QCD.

The evolution equation for the quark spin distributions δq is given by [11, 50]:

$$\frac{d}{dQ^2}\delta q = \frac{\alpha_s(Q^2)}{2\pi}\frac{1}{Q^2}\left[\int_x^1\frac{dz}{z}\delta q(z)\Delta P_{qq}(\frac{x}{z}) + 2\int_x^1\frac{dz}{z}\delta G(z)\Delta P_{qg}(\frac{x}{z})\right] \quad (2.84)$$

with

$$\Delta P_{qq}(z) = \frac{4}{3}\left(\frac{1+z^2}{1-z}\right)_+ \quad \text{and} \quad \Delta P_{qg}(z) = \frac{z^2 - (1-z)^2}{2} \quad (2.85)$$

and $\delta G(x) = G^+(x) - G^-(x)$ being the gluon spin distribution. This equation shows that a prediction of the Q^2 dependence of the spin structure functions requires a knowledge of the gluon spin distribution. Figure 2.14 [50] shows the calculated Q^2
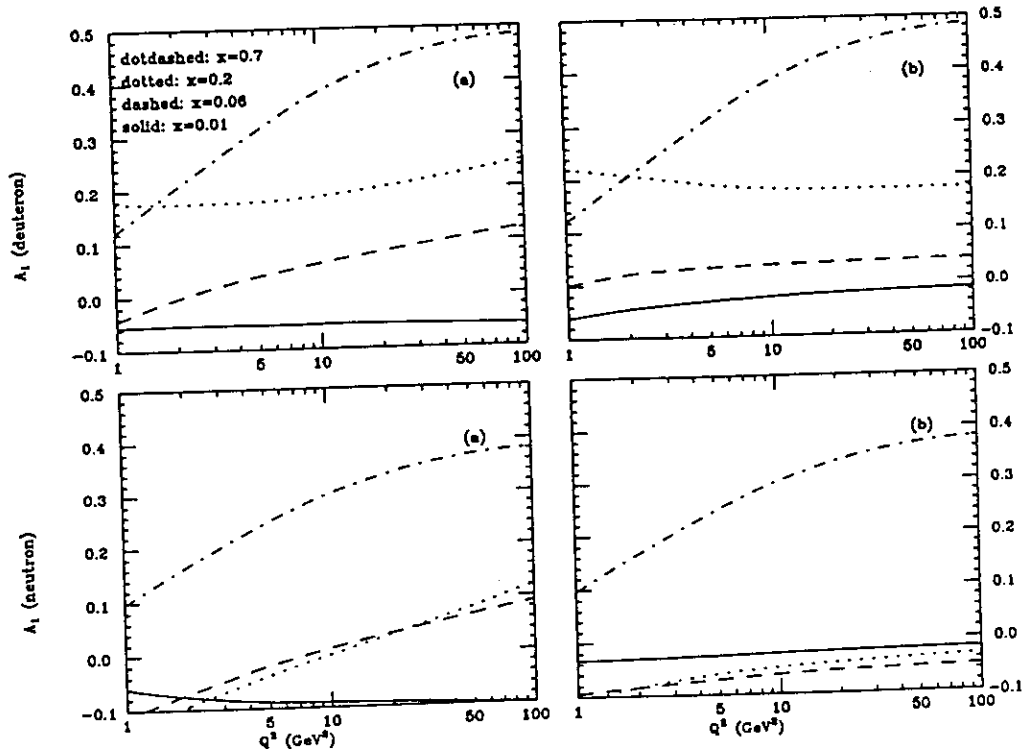
Figure 2.14: Computed Q^2 dependence of the deuteron and neutron asymmetry with (a) and without (b) the gluon contribution

evolution of the asymmetries A_1 of deuteron and neutron for various x bins. The calculations were done for two different assumptions for δG: in the left figures (a) the contribution of the gluons is zero and in the right figures (b) δG has an integral value of 5 for $Q^2_{EMC} = 10.7$ GeV as suggested by the original EMC data but rescaled

to the value of the measurement:

$$\int_0^1 \delta G(x, Q^2) = 5 \frac{\alpha_s(Q_{EMC}^2)}{\alpha_s(Q^2)} \ . \tag{2.86}$$

The figures show that the effect of the gluons is, as expected, only significant for small x.

Figure 2.15 shows summary of the world data on the Q^2 dependence of A_1^p and A_1^d [51]. Within the statistical and systematic errors of the current measurements, there is no evidence for a Q^2 dependence, however the precision of the data is not good enough to detect the predicted Q^2 evolution. HERMES will study the Q^2 dependence of the spin structure functions over the whole kinematic plane which is accessible (see figure 2.3) including the Q^2 dependence of resonance production. It is clear that a longer running period than 9 weeks is required for a precision measurement of the Q^2 dependence.

2.2.4 The Spin Structure Function $g_2(x)$

Because of the mixing of $g_1(x)$ and $g_2(x)$ in the cross section formula (2.31), it is not possible to determine $g_1(x)$ precisely without the knowledge of $g_2(x)$. Only the combined measurement of the longitudinal $A_\parallel$ and transverse $A_\perp$ asymmetries allows the extraction of $g_1(x)$ without ambiguities. $g_1(x)$ and $g_2(x)$ are calculated according to the formula (2.33) to (2.40).

The determination of $g_2(x)$ has however also a physical interest in its own. $g_2(x)$ is needed to construct and distinguish between different models of the nucleon. Additionally, $g_2(x)$ is sensitive to quark gluon correlations. It offers the unique possibility to measure a QCD twist-3 operator in leading order [26]. For a free particle $g_2(x)$ vanishes (see eqn. (2.50)):

$$g_2^{free}(x) = 0 \ . \tag{2.87}$$

Only interactions between quarks and gluons contribute to $g_2(x)$. The operator product expansion (OPE) of the virtual photon forward Compton amplitude can be used to relate higher moments of the spin structure functions to twist-2 (a_i) and twist-3 (d_i) matrix elements [26, 52, 53, 54, 55, 56]:

$$\int_0^1 x^n g_1(x, Q^2) \, dx \ = \ \frac{a_n}{4} \qquad\qquad n = 0, 2, 4, ... \tag{2.88}$$

$$\int_0^1 x^n g_2(x, Q^2) \, dx \ = \ \frac{1}{4} \frac{n}{n+1} (d_n - a_n) \qquad n = 2, 4, ... \tag{2.89}$$

In the Wandzura-Wilczek approach twist-3 contribution are neglected [52], and thus all moments of g_2 are determined by the moments of g_1 and the structure functions are related by:

$$g_2^{WW}(x, Q^2) = -g_1(x, Q^2) + \int_x^1 g_1(x', Q^2) \frac{dx'}{x'} \ . \tag{2.90}$$
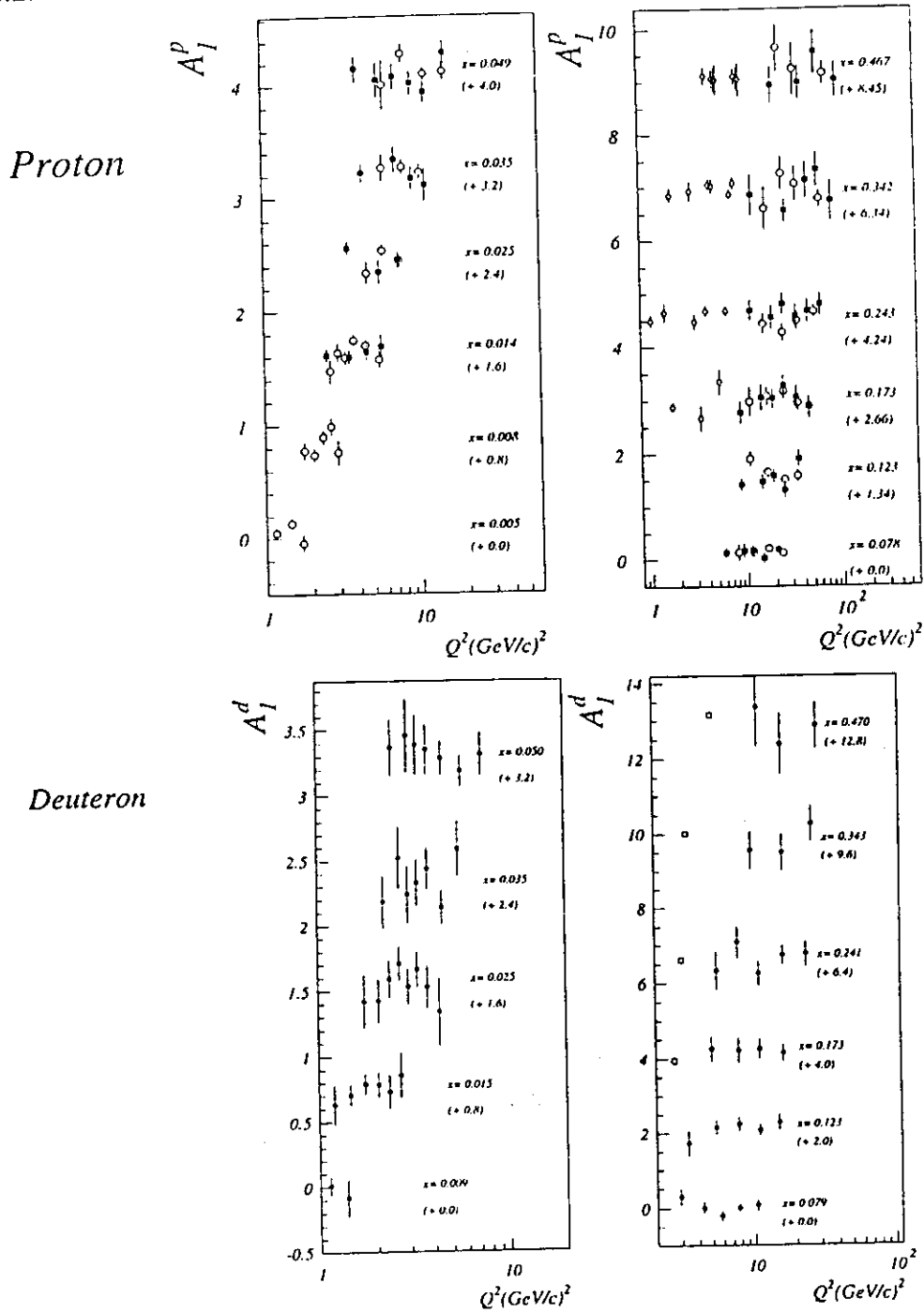
Figure 2.15: The figures show the Q^2 dependence of the spin asymmetries $A_1(x)$ for proton and deuteron. Plotted are points from EMC (filled squares), SMC (circles) and SLAC (diamonds and open squares). The scale has a different offset for each x bin as noted below the points. There is no significant Q^2 dependence observed but there is also none expected in this large scale.

There is however no strong reason to assume that twist-3 contributions cancel. Instead, g_2 is an ideal function to measure the twist-3 contributions $\tilde{g}_2(x)$ using the equation:

$$g_2(x, Q^2) = g_2^{WW}(x, Q^2) + \tilde{g}_2(x, Q^2) \tag{2.91}$$

Bag model calculations show that $\tilde{g}_2(x, Q^2)$ may be non-zero [57].

The experimental situation of g_2 is still very open. First data from E-142 [33] indicate that $A_2^n(x)$ is limited by $|A_2^n(x)| < 0.25$ and SMC data [58] indicate that A_2^p is small compared to the positivity limit $\sqrt{R}$ (see eqn. (2.41)). The results for $g_2^p(x)$ are shown in figure 2.16. $g_2^p(x)$ is known with only marginal precision. HERMES will be able to determine it much more precisely as shown in the top part of the figure. More recent data from SLAC are currently discussed at conferences. They indicate that $g_2(x)$ is small.
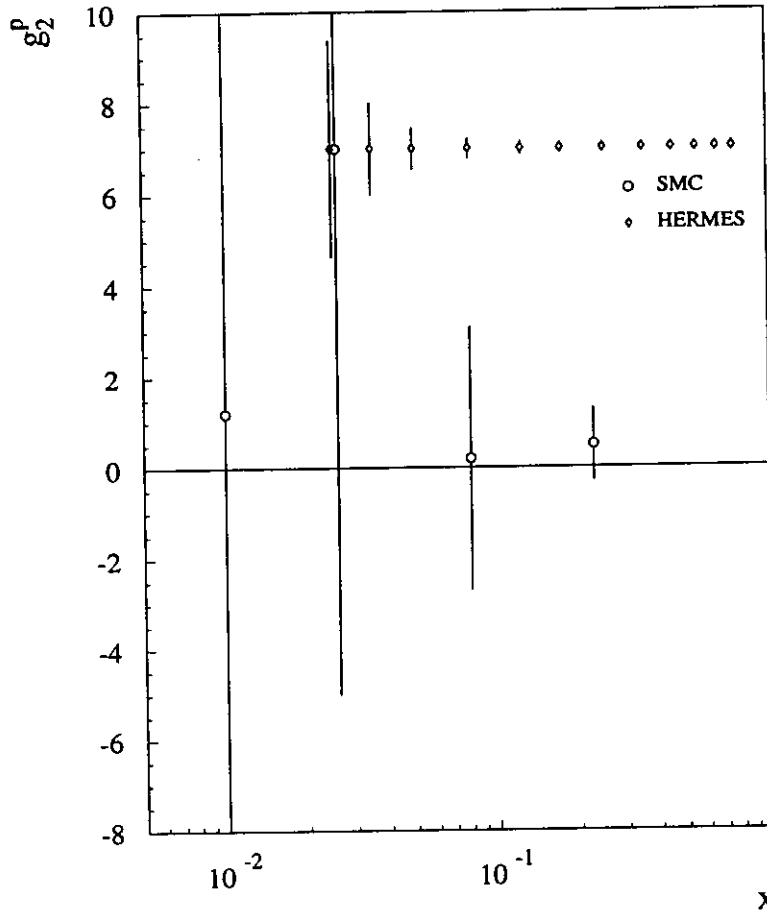
Figure 2.16: First data on the second spin structure function $g_2^p(x)$ as taken by SMC. The measurement of $g_2(x)$ requires a high statistic experiment as it is derived form the difference of the longitudinal and the transverse asymmetries, both two numbers which are large compared to the signal. The precision for HERMES standard runs is indicated at the top part of the figure.

Burkhardt-Cottingham Sum Rule and d_2

The Burkhardt-Cottingham sum rule [59]

$$\int_0^1 g_2(x)\,dx = 0 \qquad (2.92)$$

is less fundamental than the Bjørken sum rule, but its violation would rule out certain classes of spin models of the nucleon [26]. The sum rule is also suggested by equation (2.89) by assuming that the equation holds for $n \to 0$ and the coefficients a_0 and d_0 are finite.

Higher moments

$$\int_0^1 x^n g_2(x, Q^2)\,dx \qquad (2.93)$$

are interesting because they test results from QCD operator product expansion which are model independent [53].

Of special interest is the moment $n = 2$ which allows to extract d_2:

$$d_2 = 4 \int_0^1 x^2 g_1(x, Q^2)\,dx + 6 \int_0^1 x^2 g_2(x, Q^2)\,dx \ . \qquad (2.94)$$

d_2 is a fundamental quantity which can be interpreted as the QCD analogon to the average magnetic field in the nucleon [60].

Experimentally the determination of higher moments requires precision data for g_1 and g_2 especially at medium and large x. The HERMES kinematic is optimal for this measurement. The statistical error on d_2 for a standard run on longitudinal and transverse target spin is approximately

$$\delta d_2 = 0.008. \qquad (2.95)$$

2.2.5 Tensor Spin Observables

As the deuteron is a spin-1 target there exist two higher multipole structure functions called $b_1^d(x)$ and $\Delta^d(x)$. The functions can be measured by scattering an *unpolarised* beam off a longitudinally tensor-polarised and a transversely polarised target respectively. Both functions are expected to be small.

In the quark-parton frame $b_1^d(x)$ accounts for the difference of quark distributions in a helicity zero target compared to a helicity one target:

$$b_1^d(x) = \sum_f e_f^2 \left(\frac{q_f^+(x) + q_f^-(x)}{2} - q_f^0(x) \right) \ . \qquad (2.96)$$

q_f^0 is the probability distribution of quarks (with arbitrary helicity) in a helicity zero target. $q_f^{+(-)}$ denotes as usual the quark helicity distributions for a vector polarised target with the spin parallel (antiparallel) to the quark spin. Experimentally $b_1^d(x)$ can be extracted from the asymmetry

$$A_{\uparrow 0}^d = \frac{\sigma^{\uparrow\uparrow} + \sigma^{\uparrow\downarrow} - 2\sigma^{\uparrow 0}}{\sigma^{\uparrow\uparrow} + \sigma^{\uparrow 0} + \sigma^{\uparrow\downarrow}} \qquad (2.97)$$

by switching the target polarisation between vector and tensor polarisation. As indicated in formula (2.62) the knowledge of the structure function $b_1^d(x)$ is required for a precise derivation of $g_1^n(x)$ and $g_2^n(x)$ from deuterium. A non-zero $b_1^d(x)$ would indicate that the quark distributions of the nucleons change due to nuclear binding effects.

$\Delta^d(x)$ has a similar interpretation. It probes gluon components which are not assigned to individual nucleons within the nucleus [26]. It can be determined by measuring the azimuthal asymmetry of the scattered electron in respect to the direction of the transversely polarised target. The contribution to the cross section is:

$$\frac{d^3\sigma}{dxdyd\phi} = \frac{2\alpha^2}{Q^4}ME \cdot \left[F_1(x,Q^2) \cdot xy^2 + F_2(x,Q^2) \cdot (1-y) \right. \quad (2.98)$$
$$\left. -\Delta^d(x) \cdot \frac{x(1-y)}{2}\cos 2\phi \right]$$

2.3   Semi-Inclusive Spin Physics Program of HER-MES

Inclusive asymmetries allow the extraction of information about the spin contributions of the different quark flavours in a very indirect manner only. Semi-inclusive hadron measurements are a method to directly separate the spin content of the different quark flavours. The basic idea is as follows. The scattered lepton is measured in coincidence with the leading hadrons. The kinematics of the scattered quark is completely determined by the kinematic variables x and Q^2 which are extracted from the scattered lepton kinematics θ and E'. At the same time the flavour of the struck quark is determined by identifying the type of the leading hadron in the current jet. This kind of flavour tagging works only statistically and requires the knowledge of the fragmentation functions. However results from EMC [61] have shown that it works well when the right cuts are applied. The main cut is on the fractional energy z

$$z \overset{lab}{=} E_h/\nu \qquad (2.99)$$

with E_h being the energy of the hadron. Table 2.2 shows the number of hadrons expected in about 2 standard runs of the HERMES experiment as function of different values for the z-cut. The calculations have been done with the Monte Carlo program PEPSI [62] which has been developed to simulate the hadron production in polarised deep inelastic scattering. It is based on the string fragmentation programs LEPTO and JETSET of the Lund group [63].

In semi-inclusive measurements, HERMES is superior to the other spin experiments. The SLAC experiments E-142 and E-143 have no possibilities for semi-inclusive measurements and SMC has only a very limited statistics and a large dilution of the asymmetries. There is however a new proposal for an upgrade of the SMC experiment for polarised hadron physics [64]. Figure 2.17 shows some first results from semi-inclusive spin asymmetries measured by SMC [65]. Plotted are the

Table 2.2: Expected statistics of hadrons for different cuts on the hadronic energy z. The table was calculated for about two standard HERMES runs at 35 GeV.

z-cut	>0.0	>0.1	>0.6	>0.8
γ	1125,000	466,000	154,000	–
π^+	582,000	468,000	48,000	13,500
π^-	430,000	313,000	27,000	6,300
K^+	66,000	63,000	18,000	7,500
K^-	44,000	38,000	4,100	1,200

quark spin distributions extracted from the virtual photon asymmetry for a proton and deuterium target:

$$A^{+(-)} = \frac{\sigma_{1/2}^{+(-)} - \sigma_{3/2}^{+(-)}}{\sigma_{1/2}^{+(-)} + \sigma_{3/2}^{+(-)}} \tag{2.100}$$

where $\sigma_{1/2[3/2]}^{+(-)}$ is the yield of positive (negative) hadrons and the indices 1/2 and 3/2 refers to the total spin projection in the direction of the virtual photon. The figures show the valence distribution $\delta u_v(x)$ (a) and $\delta d_v(x)$ (b) and the non-strange sea distribution $\delta \bar{q}(x)$ (c). The fluctuations of the points are large and comparable with the range of the positivity limit and one can certainly agree with the conclusion of the author that a continuation of this kind of study is highly desirable [65].

2.3.1 Fragmentation Functions

Due to the confinement of QCD, a quark which is kicked out of a nucleon produces a jet of hadrons. The fragmentation into hadrons can be described by the phenomenological fragmentation functions $D_f^h(z)$ which denote the probability that a hadron h with the energy fraction z is produced from a quark with flavour f [66, 67]. The differential cross section $d\sigma^h$ for producing a hadron of type h is given as

$$\frac{d\sigma^h(z, x, Q^2)}{dz} = \frac{\sum_f e_f^2 q_f(x, Q^2) D_f^h(z)}{\sum_f e_f^2 q_f(x, Q^2)} \sigma^T(x, Q^2), \tag{2.101}$$

where $\sigma^T(x, Q^2)$ is the total (inclusive) cross section. The formula assumes that the quark scattering process and the fragmentation process factorise and that the fragmentation functions scale and only depend on the fractional energy z. Both assumptions are experimentally confirmed [68, 69]. The fragmentation functions are normalised to the total multiplicity n_h

$$\sum_f \int_0^1 D_f^h(z)\, dz = n_h \tag{2.102}$$

and constrained by momentum conservation:

$$\sum_h \int_0^1 z D_f^h(z)\, dz = 1. \tag{2.103}$$
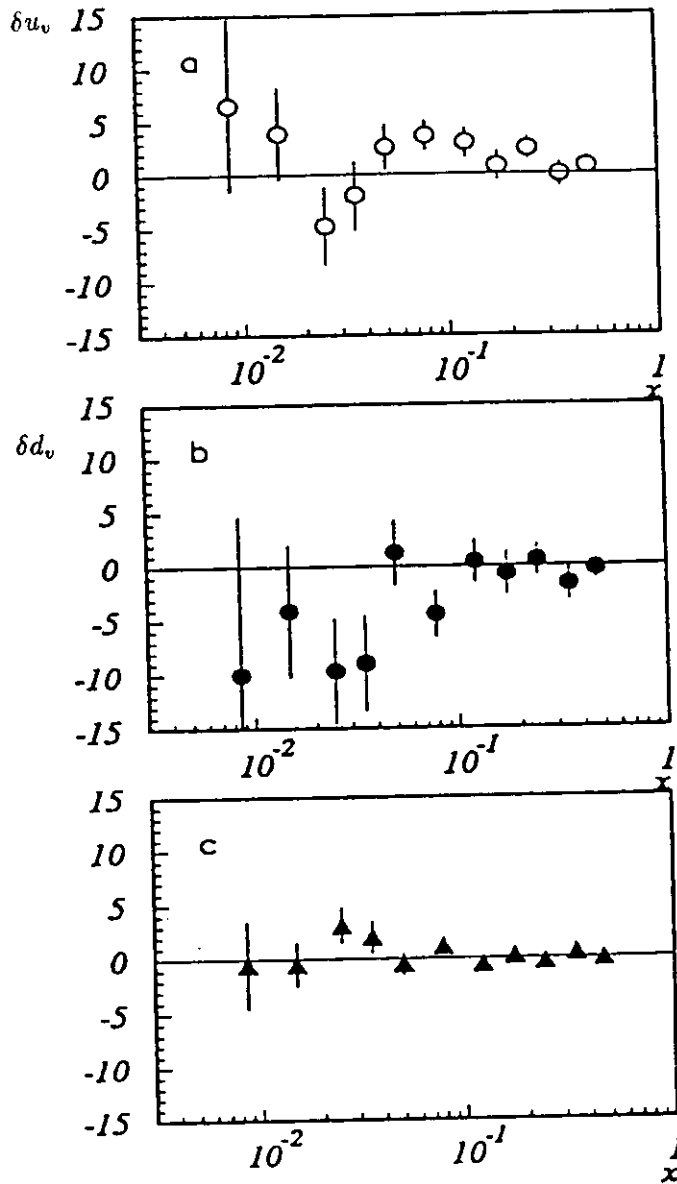
Figure 2.17: Quark spin distribution functions $\delta u_v(x)$ (a), $\delta d_v(x)$ (b) and $\delta \bar{q}(x)$ (c) as extracted from semi-inclusive SMC data.

Figure 2.18 shows the fragmentation functions of pions for the u and d quarks as measured by EMC [70]. The number of different fragmentation functions which describe the production of charged pions can be reduced to three by applying charge and isospin symmetries:

$$\begin{aligned}
D_1(z) &= D_u^{\pi^+}(z) = D_d^{\pi^-}(z) = D_{\bar{d}}^{\pi^+}(z) = D_{\bar{u}}^{\pi^-}(z) \\
D_2(z) &= D_d^{\pi^+}(z) = D_u^{\pi^-}(z) = D_{\bar{u}}^{\pi^+}(z) = D_{\bar{d}}^{\pi^-}(z) \\
D_s(z) &= D_s^{\pi^+}(z) = D_s^{\pi^-}(z) = D_{\bar{s}}^{\pi^+}(z) = D_{\bar{s}}^{\pi^-}(z)
\end{aligned} \tag{2.104}$$

As seen in figure 2.18, the hadron that contains the struck quark is favoured com-
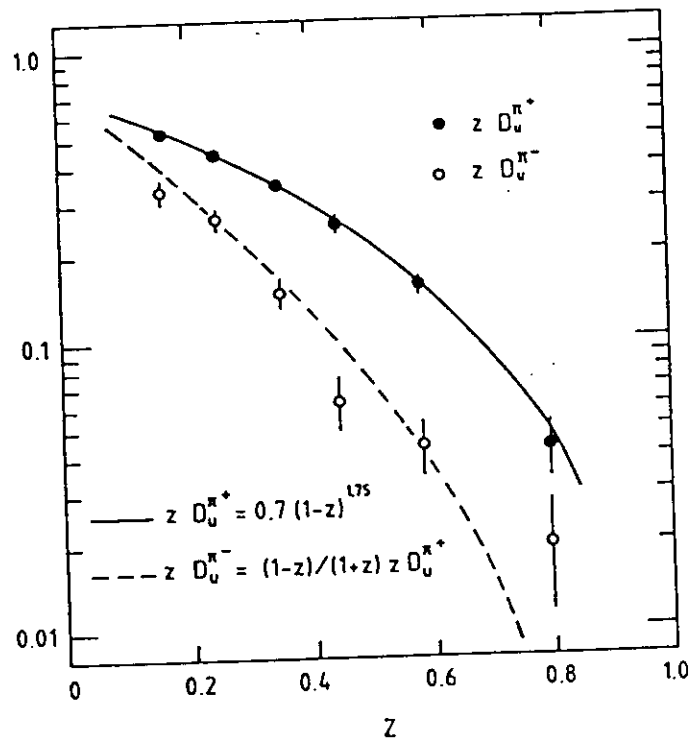
Figure 2.18: The fragmentation functions $D_u^{\pi^+}$ and $D_u^{\pi^-}$ as measured by EMC.

pared to the hadron which does not contain the struck quark. $D_1(z)$ $(D_2(z))$ is called the favoured (unfavoured) fragmentation function. The suppression factor $1/\eta$ is defined and parametrised as

$$D_2(z) = \frac{1}{\eta} D_1(z) = \frac{1-z}{1+z} D_1(z). \tag{2.105}$$

2.3.2 Flavour Decomposition of Spin Valence Distributions

The most important and direct method of quark flavour decomposition makes use of the spin asymmetries of the pion charge differences. It requires a longitudinally

polarised beam and a longitudinally polarised target and tags on identified positive and negative pions at high z:

$$\vec{e}\vec{p} \rightarrow e'\,\pi^{\pm}\,X \tag{2.106}$$

Only the charge difference $N^{\pi^+-\pi^-} = N^{\pi^+} - N^{\pi^-}$ is used in the analysis which ensures that effects from the (charge symmetric) sea and from resonance and vector meson decays cancel to a large extend.

Under the assumption that the fragmentation process and the quark scattering process factorise and that the fragmentation process is approximately independent of the helicity of the quark, formula (2.101) can be applied to the production rate of charged pions for both spin states separately:

$$N_{\uparrow\uparrow}^{\pi^{\pm}} \sim \sum_f e_f^2 q_f^+(x, Q^2) D_f^{\pi^{\pm}}(z) \tag{2.107}$$

$$N_{\uparrow\downarrow}^{\pi^{\pm}} \sim \sum_f e_f^2 q_f^-(x, Q^2) D_f^{\pi^{\pm}}(z) \tag{2.108}$$

In terms of the favoured and unfavoured structure functions, the spin differences are given explicitly as

$$\begin{aligned}
N_{\uparrow\uparrow}^{\pi^+} - N_{\uparrow\downarrow}^{\pi^+} \sim\ & \frac{4}{9}\delta u(x) D_1(z) + \frac{1}{9}\delta d(x) D_2(z) + \frac{1}{9}\delta s(x) D_s(z) \\
& + \frac{4}{9}\delta\bar{u}(x) D_2(z) + \frac{1}{9}\delta\bar{d}(x) D_1(z) + \frac{1}{9}\delta\bar{s}(x) D_s(z) \tag{2.109}
\end{aligned}$$

$$\begin{aligned}
N_{\uparrow\uparrow}^{\pi^-} - N_{\uparrow\downarrow}^{\pi^-} \sim\ & \frac{4}{9}\delta u(x) D_2(z) + \frac{1}{9}\delta d(x) D_1(z) + \frac{1}{9}\delta s(x) D_s(z) \\
& + \frac{4}{9}\delta\bar{u}(x) D_1(z) + \frac{1}{9}\delta\bar{d}(x) D_2(z) + \frac{1}{9}\delta\bar{s}(x) D_s(z). \tag{2.110}
\end{aligned}$$

It can be easily seen that in the difference between positive and negative pions only the valence quarks $q_v = q - \bar{q}$ contribute:

$$N_{\uparrow\uparrow}^{\pi^+-\pi^-} - N_{\uparrow\downarrow}^{\pi^+-\pi^-} \sim \left(\frac{4}{9}\delta u_v(x) - \frac{1}{9}\delta d_v(x)\right)(D_1(z) - D_2(z)) \tag{2.111}$$

and that in the pion asymmetry ratio A_π

$$A_\pi(x) = \frac{N_{\uparrow\downarrow}^{\pi^+-\pi^-} - N_{\uparrow\uparrow}^{\pi^+-\pi^-}}{N_{\uparrow\downarrow}^{\pi^+-\pi^-} + N_{\uparrow\uparrow}^{\pi^+-\pi^-}} \tag{2.112}$$

all fragmentation effects cancel:

$$A_\pi^p(x) = \frac{4\delta u_v(x) - \delta d_v(x)}{4u_v(x) - d_v(x)}. \tag{2.113}$$

This equation has been derived for a proton target. Similar relations hold for deuteron and ^3He targets:

$$A_\pi^D(x) = \frac{\delta u_v(x) + \delta d_v(x)}{u_v(x) + d_v(x)} \tag{2.114}$$

$$A_\pi^{^3He}(x) = \frac{\delta u_v(x) - 4\delta d_v(x)}{7u_v(x) - 2d_v(x)}. \tag{2.115}$$

As the unpolarised flavour distributions u_v and d_v are known, the above equations (2.113)-(2.115) allow the extraction of the spin distributions δu_u and δd_v separately and as a function of x. Two different targets are needed. Figure 2.19 shows the projected precision of the HERMES experiment for δu_v and δd_v using the hydrogen and deuterium targets and two different models [39, 53] of polarised quark distributions as input for the PEPSI program [71].
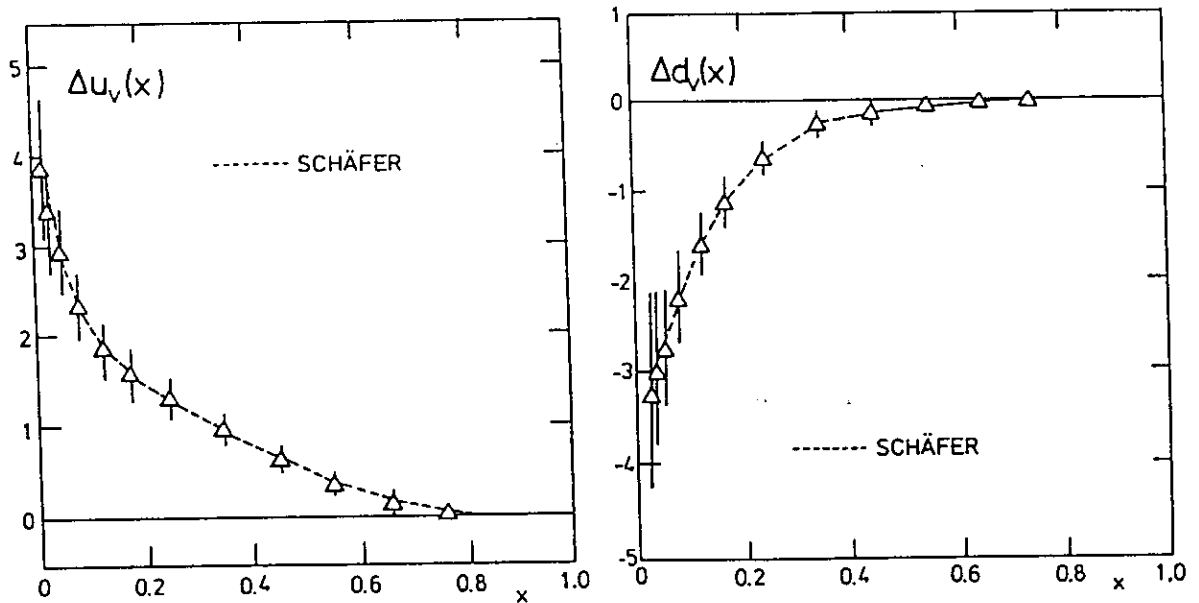
Figure 2.19: Projected precision of the HERMES experiment for δu_v and δd_v. The results were obtained with the PEPSI Monte Carlo using input spin distribution model from Schäfer for two standard HERMES runs with polarised hydrogen and deuterium.

Sea Contribution to Nucleon Spin

Using one spin structure function (e.g. of deuterium) in addition to the semi-inclusive results and assuming some average charge of the sea $\langle e_s^2 \rangle$, in principle the sea contributions $\delta q_s(x)$ can also be extracted using the following formula:

$$g_1^d(x) = \frac{5}{18}\delta u_v(x) + \frac{5}{18}\delta d_v(x) + \langle e_s^2 \rangle \delta q_s(x). \tag{2.116}$$

As $\langle e_s^2 \rangle$ is constrained by the quark charges, the above equation defines limits for the contribution of the sea quarks once the valence contributions are known.

Table 2.3: Expected uncertainties in the extraction of the valence spin distributions for a HERMES standard run on hydrogen and deuterium.

	statistical	extrapolation
Δu_v	0.06	0.10
Δd_v	0.09	0.06

Integral Valence Contributions

The integral valence contributions can be calculated from the semi-inclusive results

$$\Delta u_v = \int_0^1 \delta u_v(x)\, dx \tag{2.117}$$

$$\Delta d_v = \int_0^1 \delta d_v(x)\, dx \tag{2.118}$$

$$\Delta q_s = \int_0^1 \delta q_s(x)\, dx \tag{2.119}$$

and can be compared to the results obtained from the Ellis-Jaffe integrals (eqs. (2.65) – (2.68)) and also applied to the helicity conservation formula

$$\frac{1}{2}\left[\Delta u_v + \Delta d_v + \Delta q_s\right] + \Delta G + L_z = \frac{1}{2}. \tag{2.120}$$

The projected precision for two standard HERMES runs of hydrogen and deuterium are shown in table 2.3. The error has three components, the statistical error, the theoretical uncertainty in the extrapolation of the integral in the unmeasured region and the systematic uncertainty coming from the limited knowledge of the unpolarised valence distributions. The latter will be small as HERMES has the capability to measure the unpolarised distributions $u_v(x)$ and $d_v(x)$ with high precision as described in chapter 2.4.2.

2.3.3 A Direct Measurement of the Non-Strange Sea Polarisation

The *non-strange* sea contribution $\delta\bar{q}(x)$ can be measured by tagging leading π^- mesons at high z and low x:

$$\vec{e}\,\vec{p} \rightarrow e'\,\pi^-\,X\ . \tag{2.121}$$

The pion spin asymmetry is defined as

$$A_{\pi^-}(x) = \frac{N^{\pi^-}_{\uparrow\downarrow} - N^{\pi^-}_{\uparrow\uparrow}}{N^{\pi^-}_{\uparrow\downarrow} + N^{\pi^-}_{\uparrow\uparrow}} \tag{2.122}$$

with $N^{\pi^-}_{\uparrow\uparrow}$ ($N^{\pi^-}_{\uparrow\downarrow}$) being the number of π^- produced in the scattering of longitudinally polarised electrons off a longitudinally polarised proton target with the spin

parallel (anti-parallel) to the electron spin. From equation (2.110) follows with the assumption that $D_s \approx D_2$:

$$A^p_{\pi^-}(x) = \frac{4\delta u_v + \eta \delta d_v + 5(1+\eta)\delta \bar{q} + 2\delta s}{4u_v + \eta d_v + 5(1+\eta)\bar{q} + 2s} \qquad (2.123)$$

Figure 2.20 illustrates the sensitivity of the pion asymmetry $A^p_{\pi^-}(x)$ [72]. The three curves are calculated by Monte Carlo assuming an unpolarised sea (circles), a maximum strange sea polarisation (squares) and a maximum total sea polarisation (triangles). Maximum polarisation is achieved when $\delta q = q$. The pion asymmetry is not sensitive to the strange sea but it is sensitive to the non-strange sea contribution at low x. At high x the sensitivity is diluted by valence quark contributions. Figure 2.21 shows the asymmetry plotted versus the scaling variable z at small x

Figure 2.20: Monte Carlo simulation of $A^p_{\pi^-}(x)$ as a function of x for three different assumptions: unpolarised sea (circles), maximum strange sea (squares) and maximum sea polarisation (triangles). At low x the measurement is sensitive to the total sea polarisation.

[72]. The sensitivity is good over the whole z range. The error bars correspond to two HERMES standard runs.

2.3.4 Strange Sea Contribution to the Nucleon Spin

K^- Asymmetries

The *strange* sea contribution $\delta s(x)$ can be directly measured by tagging leading K^- mesons at high z and low x:

$$\vec{e}\vec{p} \rightarrow e' K^- X . \qquad (2.124)$$

Figure 2.21: Monte Carlo simulation of $A^p_{\pi^-}(x)$ as a function of z for three different assumptions: unpolarised sea (circles) , maximum strange sea (squares) and maximum sea polarisation (triangles). At low x the measurement is sensitive to the total sea polarisation over a wide z range.

As the K^- meson consists of $(s\bar{u})$ quarks, leading K^- mesons originate to a large extend in fragmentation from s-quarks from the sea. There is however a large dilution by unfavoured fragmentation functions. $K^+ = (u\bar{s})$ mesons are not useful for this kind of analysis as they are dominated by fragmentation of valence-u quarks.

In terms of fragmentation functions, the situation is as follows. The unfavoured kaon fragmentation function is suppressed by $1/\eta$ in a similar way as the pion functions:

$$D_u^{K^-}(z) = \frac{1}{\eta(z)} D_{\bar{u}}^{K^-}(z) \tag{2.125}$$

Additionally, the generation of an s quark during fragmentation is suppressed by a factor $\lambda \approx 0.3$ compared to the production of an u or d quark:

$$D_{\bar{u}}^{K^-}(z) = \lambda D_s^{K^-}(z). \tag{2.126}$$

For the production rate of K^- it follows that:

$$N^{K^-} \sim \left[\frac{4}{9}u(x) + \frac{1}{9}d(x) + \frac{1}{9}s(x)\frac{\eta}{\lambda} + \frac{4}{9}\bar{u}(x)\eta + \frac{1}{9}\bar{d}(x) + \frac{1}{9}\bar{s}(x)\frac{\eta}{\lambda} \right] D_u^{K^-}(z) \tag{2.127}$$

The kaon spin asymmetry A_{K^-} is defined as:

$$A_{K^-}(x) = \frac{N_{\uparrow\downarrow}^{K^-} - N_{\uparrow\uparrow}^{K^-}}{N_{\uparrow\downarrow}^{K^-} + N_{\uparrow\uparrow}^{K^-}} \tag{2.128}$$

with $N_{\uparrow\uparrow}^{K^-}$ ($N_{\uparrow\downarrow}^{K^-}$) being the number of K^- produced in the scattering of longitudinally polarised electrons off a longitudinally polarised proton target with the spin parallel (anti-parallel) to the electron spin. From equation (2.127) it follows:

$$A_{K^-}^p(x) = \frac{4\delta u_v + \delta d_v + (6 + 4\eta)\delta\bar{q} + (\frac{\eta}{\lambda} + 1)\delta s}{4u_v + d_v + (6 + 4\eta)\bar{q} + (\frac{\eta}{\lambda} + 1)s} \tag{2.129}$$

Here, $\bar{q}$ denotes the non-strange quark sea with the assumption that $\delta\bar{q} = \delta u_s = \delta d_s = \delta\bar{u} = \delta\bar{d}$.

Figure 2.22 shows the predictions of the K^- asymmetries $A_{K^-}^p$ generated by the HERMES Monte Carlo program [72]. The low x region has been selected where the valence contribution is small. The three different symbols denote as in the previous figure the three cases that the sea unpolarised, maximum polarised or that the strange sea is maximum polarised. The sensitivity increases as expected with z, however also at high z the effect of strange sea polarisation is small.

Experimentally, the threshold Čerenkov counter will separate kaons and pions only for energies above ~ 8 GeV, which corresponds to a z cut of about $z > 0.4$. This z cut reduces the statistics, however it selects the leading z region which is most sensitive to the flavour of the struck quark. The separation of anti-protons and K^- is achieved experimentally either by a RICH counter or by running the threshold Čerenkov counter with two different thresholds in the upper and lower part of the detector and correcting for the $\bar{p}$ contamination statistically. The correction is not so critical as the production of leading $\bar{p}$ is suppressed twice in the fragmentation process: firstly, the $\bar{p}$ is an unfavoured hadron for the valence quark fragmentation and secondly the $\bar{p}$ requires a diquark – anti-diquark generation which is suppressed because of its mass.
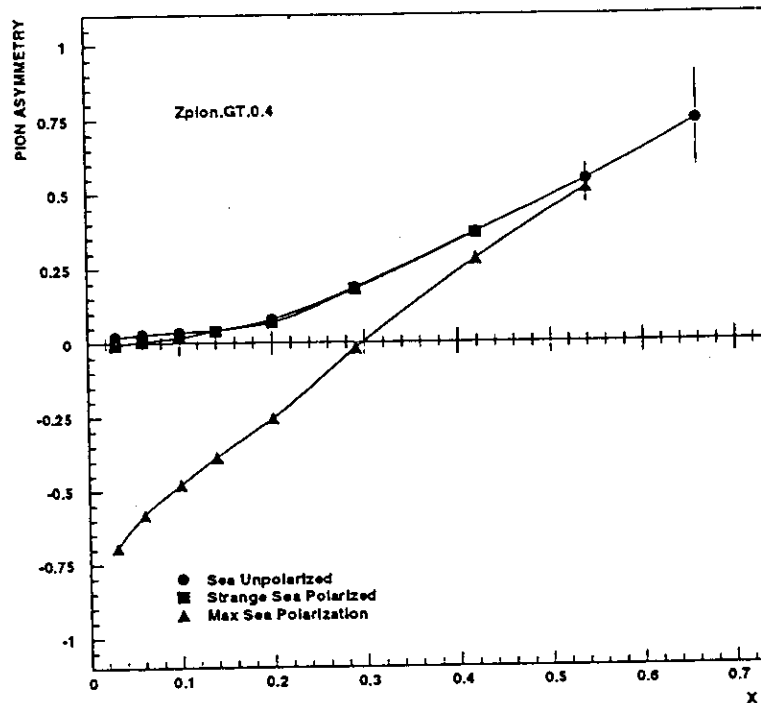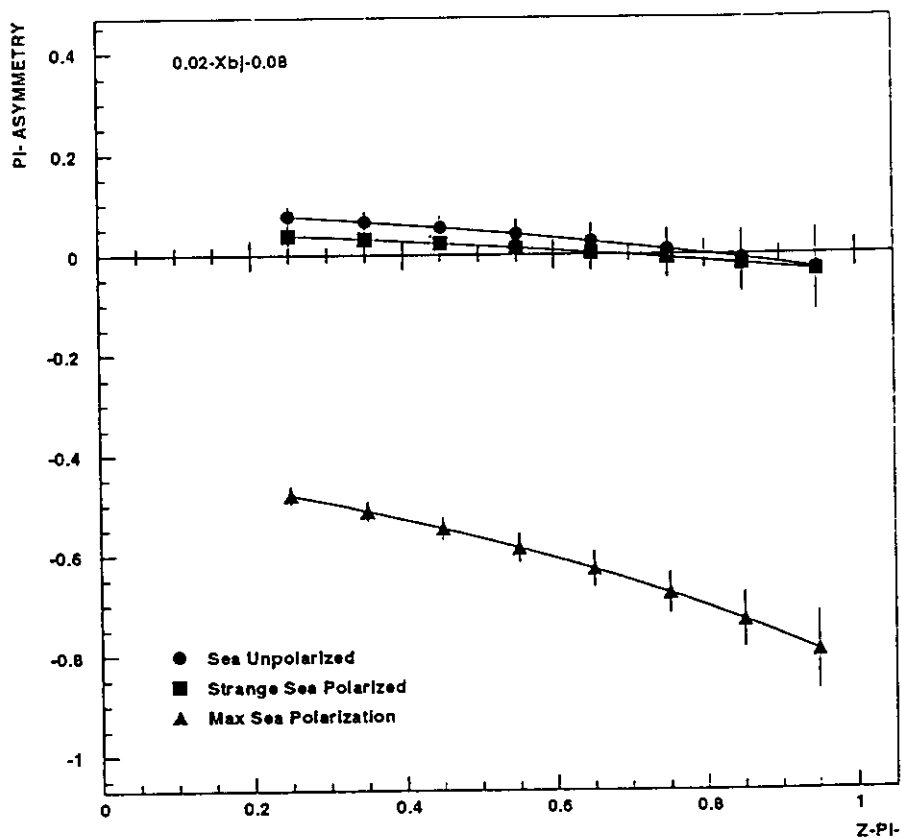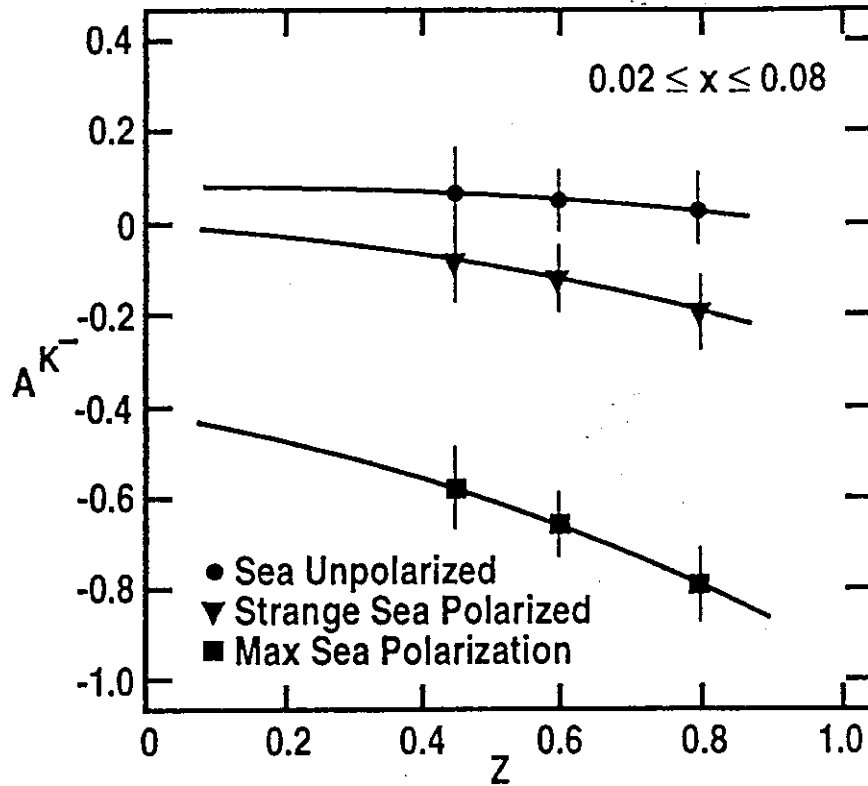
Figure 2.22: Monte Carlo simulation of $A^p_{K^-}(x)$ as a function of z for three different assumptions: unpolarised sea (circles) , maximum strange sea (triangles) and maximum sea polarisation (squares). The measurement shows a small sensitivity to the strange sea polarisation.

$\bar{\Lambda}$ Asymmetries

A second, independent method of studying the (strange) sea asymmetries is the investigation of polarised $\bar{\Lambda}$ production:

$$\vec{e}\vec{p} \rightarrow e' \bar{\Lambda} X \rightarrow e' \bar{p}\pi^+ X \tag{2.130}$$

The $\bar{\Lambda}$ is experimentally detected by measuring the $\bar{p}\pi^+$ decay products coming from a secondary vertex. As $\bar{\Lambda}$ contains $(\bar{u}\bar{d}\bar{s})$ quarks, it is also an 'all sea' product. Measured is the spin asymmetry $A^{\bar{\Lambda}}_{\parallel}$ which denotes the asymmetry in the production rate of $\bar{\Lambda}$ for two opposite spin states of the target. As shown in a study by [73] the expected asymmetry for a target polarisation of 0.8 and a beam polarisation of 0.5 is of the order of $A^{\bar{\Lambda}}_{\parallel} \approx -1.4\%$ in the sea region ($x < 0.1$) and $A^{\bar{\Lambda}}_{\parallel} \approx 3.4\%$ in the valence region ($x > 0.2$).

Λ and $\bar{\Lambda}$ Polarisation

Besides the asymmetry in the production rate, also the polarisation of Λ and $\bar{\Lambda}$ can be measured. As Λ-hyperons decay by weak interaction, the momenta of the decay products are correlated with the spin of the hyperon. Experimentally the transverse as well as the longitudinal component of the Λ polarisation can be measured. Leading Λ and $\bar{\Lambda}$ at low x should contain information about the polarisation of the struck strange quark. Λ's in the target region should contain information of the fragmentation process and possibly about the polarisation of the strange sea and the gluons in the nucleon [64]. Further studies are needed to explore the possibilities of Λ production.

2.3.5 Tensor Charge of the Nucleon

Recently it has been discovered that there is a leading twist, chiral-odd structure function $h_1(x)$ that can in principle be measured in deep inelastic scattering [74]. As the function is leading twist, it is a fundamental quantity which does not disappear at high energies. The function is connected to a helicity flip amplitude of the transverse spin components of the quarks (transversity). Therefore a transverse polarised target is required. It can not be directly measured in inclusive processes. However, h_1 is connected to pion asymmetries $A(x,z)$ in the current fragmentation region by the formula

$$A(x,z) = A_k(Q^2)\frac{\Sigma_a e_a^2[h_1^a(x)\hat{e}^a(x) + \hat{f}_1^a(z)xg_T^a(x)]}{\Sigma_a e_a^2 f_1^a(x)\hat{f}_1^a(z)}. \tag{2.131}$$

$\hat{f}_1^a(z)$ is the quark fragmentation function for flavour a obtained from unpolarised semi-inclusive scattering, $\hat{e}_1^a(z)$ is a new chiral-odd fragmentation function, $g_T = g_1 + g_2$ and $A_k(Q^2)$ is a kinematic factor. It has to be studied how well $h_1(x)$ can be experimentally disentangled from the fragmentation effects.

2.3.6 Angular Momentum Contribution to the Nucleon Spin

There is a method to directly identify angular momentum of quarks in the nucleon [75]: using an unpolarised beam on a transversely polarised target, rotating constituents produce an azimuthal asymmetry of the hadrons. The asymmetry is periodic with $\phi = \pi$, i.e. the azimuthal distribution has two maxima and two minima and can this way be distinguished from other spin effects which have a period of $\phi = 2\pi$. It is however not completely clear how to derive quantitatively the total angular momentum of the constituents out of the measured asymmetries.

2.3.7 Gluon Contributions

A direct way to extract gluonic contributions in deep inelastic scattering is the observation of spin asymmetries of high-p_t jets or J/Ψ production in the gluon fusion process [76]. Due to the relatively low energies at HERMES, those processes are suppressed. Nevertheless, inelastic J/Ψ production can be observed at HERMES by detecting the decay electron and positron:

$$
\begin{aligned}
\vec{e}\vec{p} &\rightarrow e' \; J/\Psi \; X \\
J/\Psi &\rightarrow e^+ e^-
\end{aligned}
\tag{2.132}
$$

The energy of the J/Ψ is restricted by the acceptance of the experiment to be approximately $E_{J/\Psi} \approx 23$ GeV. The kinematics of the J/Ψ can be determined without detecting the scattered electron. The number of J/Ψ for a standard HERMES run is of the order of $N_{J/\Psi} \approx 400$ and should be sufficient to give a first result on the size of the gluon spin contribution $\delta G(x)$ for $x \approx 0.2...0.4$.

An alternative method to observe the possibly large anomalous gluon contribution [77] in polarised nucleon scattering uses semi-inclusive asymmetries of charged, leading ($z > z_m = 0.2$) pions scattered off a longitudinally polarised proton target [78]:

$$
A^p_{\pi^+ + \pi^-} = \frac{N^{\pi^+ + \pi^-}_{\uparrow\downarrow} - N^{\pi^+ + \pi^-}_{\uparrow\uparrow}}{N^{\pi^+ + \pi^-}_{\uparrow\downarrow} + N^{\pi^+ + \pi^-}_{\uparrow\uparrow}}
\tag{2.133}
$$

The semi-inclusive asymmetry $A^p_{\pi^+ + \pi^-}(x, z_m)$ can be compared to the inclusive asymmetry $A^p_1(x)$. The difference depends on the strange spin content $\delta s(x)$ and on the anomalous gluon contribution $\Delta\Gamma$:

$$
\begin{aligned}
A^p_{\pi^+ + \pi^-}(x, z_m) - A^p_1(x) &= s(x)\frac{a(z_m)}{18F_1(x)}\frac{g_1(x)}{F_1(x)} \\
&- \delta s(x)\frac{a(z_m)}{18F_1(x)} \\
&+ \Delta\Gamma\frac{(\alpha_s/2\pi)}{18F_1(x)}[6(1-\lambda) + \lambda a(z_m)]
\end{aligned}
\tag{2.134}
$$

with

$$
a(z_m) = \frac{\int_{z_m}^1 [z/(z+1)]D(z)\,dz}{\int_{z_m}^1 [1/(z+1)]D(z)\,dz}
\tag{2.135}
$$

and $D(z)$ being a fragmentation function. The analysis requires certain symmetries of the fragmentation process: spin independence and charge and isospin invariance. λ is an unknown parameter which has to be determined experimentally. It accounts for the unknown fragmentation behaviour of events generated by the gluon anomaly. Details can be found in reference [78].

2.4   Unpolarised Physics Program of HERMES

It should be mentioned that the HERMES storage cell target can be filled with any *unpolarised* gas at any density, limited only by beam lifetime considerations. Asymmetries between different gas types can be measured by a rapid change of the gas. Here is a list of some of possible physics topics which make use of this feature:

- determination of the flavour asymmetry $\bar{d}(x)/\bar{u}(x)$ of the quark sea,

- precision measurement of the valence flavour distribution $d_v(x)/u_v(x)$,

- study of colour transparency and colour coherence phenomena in the production of ρ- and other vector mesons in different nuclei,

- study of the pion cloud of constituent quarks by the observation of pions at $z \to 1$,

- study of structure functions of different nuclei where the recoil nucleus is tagged by a recoil detector which can be added to the HERMES spectrometer,

- study of the nuclear EMC effect at ^3He or any other gas types,

- ...

This list of interesting unpolarised measurements at HERMES can certainly be extended. Currently the collaboration works out details of a possible future program of HERMES. In the following, the first two items will be described in more detail.

2.4.1   The Flavour Asymmetry of the Quark-Sea

The Gottfried sum rule has been measured by the NMC recently and was found to be violated [14]:

$$I_G = \int_0^1 \frac{F_2^p(x) - F_2^n(x)}{x}\, dx = 0.235 \pm 0.026 \neq \frac{1}{3}. \tag{2.136}$$

In terms of the quark parton model, the violation of the Gottfried sum rule can be interpreted as evidence that the light-quark sea is not flavour symmetric ($\bar{u}(x) \neq \bar{d}(x)$):

$$I_G = \frac{1}{3}\underbrace{\int_0^1 (u_v(x) - d_v(x))\, dx}_{1} + \frac{2}{3}\int_0^1 \left(\bar{u}(x) - \bar{d}(x)\right)\, dx \tag{2.137}$$

With the definitions [79]:

$$\tau(x) = u(x) - d(x) \qquad \bar{\tau}(x) = \bar{d}(x) - \bar{u}(x) \tag{2.138}$$

it follows that

$$\int_0^1 \tau(x)\,dx = 0.85 \pm 0.02 \quad \text{and} \quad \int_0^1 \bar{\tau}(x)\,dx = 0.15 \pm 0.02. \tag{2.139}$$

HERMES has a rather direct way to measure the quantities τ and $\bar{\tau}$ by studying the isospin distributions in semi-inclusive pion production. The quantity which is measured is the ratio $r(x,z)$ defined as:

$$r(x,z) = \frac{N^{p\pi^-}(x,z) - N^{n\pi^-}(x,z)}{N^{p\pi^+}(x,z) - N^{n\pi^+}(x,z)}. \tag{2.140}$$

From this, the quantity $R(x,z) = (1 + r(x,z))/(1 - r(x,z))$ is formed:

$$R(x,z) = \frac{N^{p\pi^-}(x,z) - N^{n\pi^-}(x,z) + N^{p\pi^+}(x,z) - N^{n\pi^+}(x,z)}{N^{p\pi^+}(x,z) - N^{n\pi^+}(x,z) - N^{p\pi^-}(x,z) + N^{n\pi^-}(x,z)}. \tag{2.141}$$

By making use of charge conjugation invariance of the fragmentation process and using the equations (2.101) and (2.104), the ratio $R(x,z)$ becomes

$$R(x,z) = \frac{3}{5} \cdot \frac{\tau(x) - \bar{\tau}(x)}{\tau(x) + \bar{\tau}(x)} \cdot \frac{D_1(z) + D_2(z)}{D_1(z) - D_2(z)}. \tag{2.142}$$

Using the experimental parametrisation for $\eta = D_1(z)/D_2(z)$ from equation (2.105), the result can be further simplified:

$$R(x,z) = \frac{3}{5} \cdot \frac{\tau(x) - \bar{\tau}(x)}{\tau(x) + \bar{\tau}(x)} \cdot \frac{1}{z}. \tag{2.143}$$

Figure 2.23 shows Monte Carlo predictions for the ratio $r(x,z)$ under the assumption that the sea is either flavour symmetric ($\bar{\tau} = 0$) or that it has a finite value $(\tau(x) - \bar{\tau}(x))/(\tau(x) + \bar{\tau}(x)) = 0.5$. The number expected from the observed flavour asymmetry in the Gottfried integral is $(\tau(x) - \bar{\tau}(x))/(\tau(x) + \bar{\tau}(x)) = 0.72$. The errors indicate a statistical precision of about 4 standard runs. By increasing the target density of the unpolarised gas, the same statistics can be obtained in a much shorter time.

2.4.2   The Valence Quark Distributions

In regions where the sea contribution can be neglected, the valence quark distributions $u_v(x)$ and $d_v(x)$ can be extracted from the inclusive structure functions $F_2(x)$ from proton and neutron. In the low x region where the sea dominates, neutrino results are required to disentangle the valence and the sea contributions.
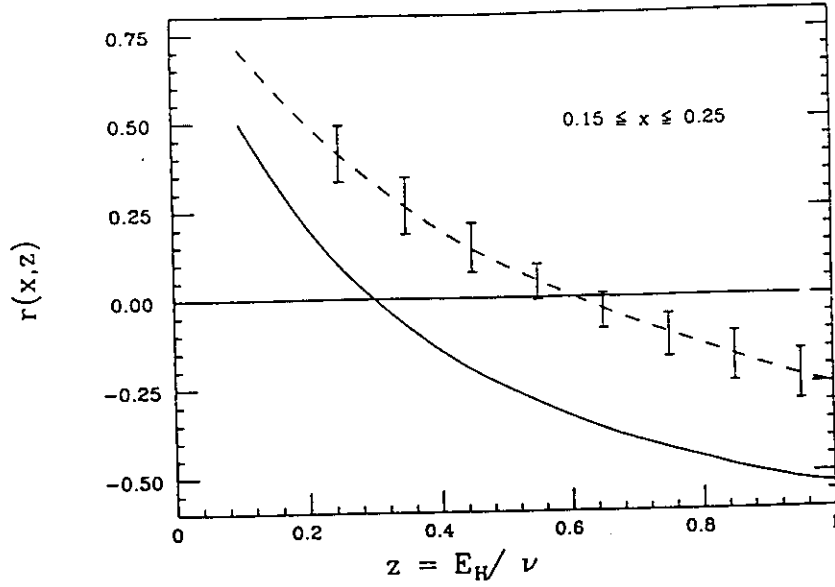
Figure 2.23: The ratio $r(x,z)$ plotted as function of z. The dashed curve describes a flavour symmetric sea whereas the solid curve assumes $(\tau(x) - \bar{\tau}(x))/(\tau(x) + \bar{\tau}(x)) = 0.5$.

A completely different approach to extract the valence distributions makes use of the fact that the leading hadrons in fragmentation reflect the flavour of the struck quark. The experimentally measured quantity is the pion ratio $R_\pi(x)$:

$$R_\pi(x) = \frac{N^{d\pi^+}(x) - N^{d\pi^-}(x)}{N^{p\pi^+}(x) - N^{p\pi^-}(x)} \cdot \frac{N^p(x)}{N^d(x)} \cdot (1 + \frac{F_2^n(x)}{F_2^p(x)}) - 1. \qquad (2.144)$$

Here, $N^{p/d,\pi^{+(-)}}(x)$ is the total yield of π^+ (π^-) at a given x integrated over all z and $N^{p/d}(x)$ is the total inclusive rate for a given target (proton or deuteron). In case of equal luminosities (per atom) and acceptances for the hydrogen and deuterium target, the equation simplifies as follows:

$$R_\pi(x) = \frac{N^{d\pi^+}(x) - N^{d\pi^-}(x)}{N^{p\pi^+}(x) - N^{p\pi^-}(x)} - 1. \qquad (2.145)$$

By assuming charge conjugation invariance of the fragmentation process and using the equations (2.101) and (2.104), the ratio $R_\pi(x)$ becomes:

$$R_\pi(x) = \frac{\frac{3}{9}u_v(x) + \frac{3}{9}d_v(x)}{\frac{4}{9}u_v(x) - \frac{1}{9}d_v(x)} \cdot \frac{D_1(z) - D_2(z)}{D_1(z) - D_2(z)} - 1. \qquad (2.146)$$

It should be mentioned that in the charge difference ratio $R_\pi(x)$ as well the z dependence of the fragmentation process as also the isospin asymmetry of the sea cancels. The ratio of the valence quark distributions can be directly calculated from the measured ratio $R_\pi(x)$:

$$\frac{d_v(x)}{u_v(x)} = \frac{4R_\pi(x) + 1}{R_\pi(x) + 4}. \qquad (2.147)$$

Figure 2.24 shows the precision with which HERMES can measure the valence dis-
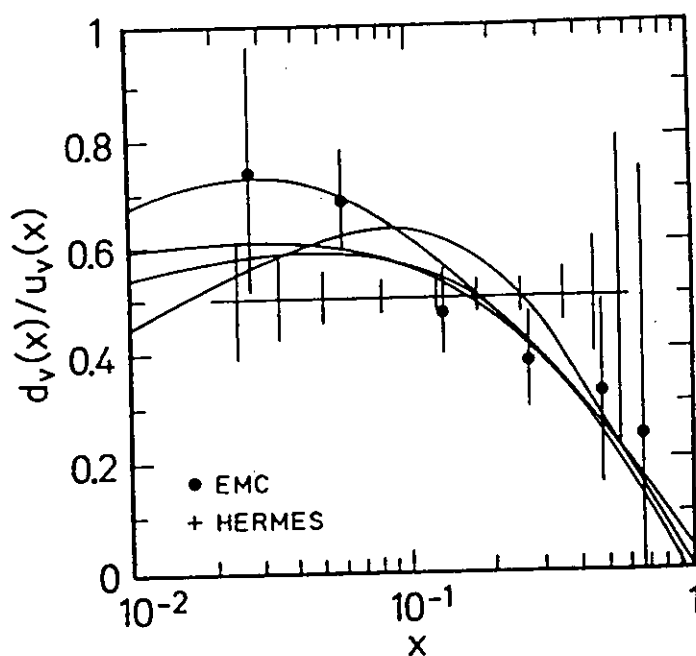
Figure 2.24: The anticipated precision of the HERMES measurement for the ratio d_v/u_v (vertical bars). The circles denote measurements by EMC. The lines are different fits of structure function data.

tribution ratio. By using a high density target, the measuring time for the quoted statistical errors is about 160 h.

Chapter 3

The Conceptual Design of HERMES

3.1 Design Criteria of Spin Experiments

After the discovery of the violation of the Ellis-Jaffe sum rule for the proton in the EMC experiment in 1987, several ideas were discussed to repeat the measurement with higher precision and reliability and especially also to measure the sum rules for the neutron. Besides the proposal of the HERMES experiment in 1990, other experiments were proposed at CERN (SMC and HELP) and at SLAC (E-142, E-143,...) as shown in the previous chapter. How well the experiments can fulfill the goal of understanding of the spin structure of proton and neutron depends on the following criteria:

- the completeness of experimental information,

- the statistical precision

- and the systematic precision.

Completeness

The experimental investigation of the spin structure of the nucleon in deep inelastic scattering requires polarised beams and polarised targets. The direction of the beam polarisation has to be longitudinal (i.e. right- or left-handed) in order to be able to probe the basic asymmetries between the right- and the left-handed quarks in the nucleon. The full set of spin structure functions requires asymmetry measurements with all target orientations: longitudinal and transverse spin directions in the case of spin-1/2 targets and additionally tensor polarisation in the case of spin-1 targets.

The spin structure of the proton can be measured directly using a hydrogen target. The spin structure of the neutron can be extracted from the difference of the deuterium and the hydrogen asymmetries. The nuclear effects in deuterium are small. An alternative neutron target is the ^3He nucleus as the two proton spins in ^3He are anti-parallel and spin asymmetries of ^3He are dominated by the neutron

in ^3He. Nuclear corrections for ^3He are larger than for deuterium, but they are understood with sufficient precision. Since the discovery of the (nuclear) EMC-effect, not only the spin structure of the nucleon but also the investigation of the quark spin distributions in heavier nuclei should be of interest. Currently there are no such experiments planned.

The verification or falsification of spin sum rules is a first, important check of basic assumptions and can be done in low statistics experiments already. The investigation of spin sum rules requires that the inclusive cross section is measured at a fixed Q^2 over a large range of x. Due to possible divergences at small x, the measurement and the extrapolation of the structure functions in this range are of special importance.

A much more complete picture of the spin structure is given when not only the sum rules are determined but when a precise measurement of the shape of the spin structure functions for all accessible values of x and Q^2 is done. The shape of the x distribution can be compared with detailed models of the quark structure of the nucleon. The evolution of the structure functions in Q^2 can be compared with QCD predictions. The transition region between the resonance production and the scaling limit is of special interest as this is the region where there are the strongest variations of the structure functions.

A comparison of the spin sum rules of proton and neutron give some hints about the flavour composition of the spin distributions. The only direct method to disentangle spin and flavour distributions is to study the complete hadronic final state. This requires that the experiment is able to register and reconstruct complete events and to identify pions and kaons. Certain quark flavours are tagged by selecting different types of leading hadrons. A measurement of the gluon spin distribution is possible by detecting asymmetries in J/Ψ production or in open charm production. Another direct method to study gluon asymmetries is to study events with two forward jets. Events with two forward jets at low x are predominantly gluon-fusion events. However, the beam energy has to be sufficiently high to allow for the experimental identification of jets.

Radiative corrections have to be applied to all measured cross sections before physics can be extracted. If the experiment allows for the detection of photons in the final state, a cross check of the QED corrections is possible and gives confidence in the result.

Statistical Precision

Precision measurements require high statistical accuracy. The statistical precision of a spin experiment can be expressed approximately by the following figure of merit F:

$$F = n\, I\, t\, (P_B\, P_T\, f)^2 \qquad (3.1)$$

with n being the target thickness (in nucleons/area), I the average beam current, t the total running time, P_B the average beam polarisation, P_T the average target polarisation and f the dilution factor. The dilution factor f, which is the number of polarisable nucleons compared to the number of all nucleons in the target, makes

the crucial difference between experiments which use gas targets and those which use solid targets. Polarised gas targets can have dilution factors close to one ($f^2 = 1$ for hydrogen) whereas polarised solid targets have typically small dilution factors ($f^2 = 0.018$ in the case of butanol).

Systematic Precision

The statistical precision of an experiment can always be improved by repeating it and by having longer running periods. The final limitation of the experiment is defined by its inherent systematic precision.

The most important rule in a spin experiment is to flip the spin rapidly and to measure asymmetries between the two polarisation states averaged over many flip cycles. The polarisation reversal should be faster than possible performance changes in the beam, the target and the detector. As long as the changes in the apparatus and the flip of the polarisation are uncorrelated, all inefficiencies cancel in the asymmetry to first order.

The larger a measured asymmetry is, the higher is the systematic precision of the result. This implies that in a spin experiment, the polarisation of the beam and the target should be as large as possible and the dilution by unpolarised target nucleons as small as possible. The following example illustrates how much a physics asymmetry can be hidden behind a large number of unpolarised scattering processes. The measured spin asymmetry in the original EMC experiment had values of typically $A_{meas} = 0.001 - 0.01$ whereas the physics asymmetry has values of $A_1 = 0.1 - 0.5$ for $x = 0.02 - 0.4$. A part of the discrepancy is due to the depolarisation of the virtual photon, but the largest effect comes from the large dilution factor of the ammonia target.

Another important item in spin experiments is a good beam and target polarimetry. Systematic uncertainties in the determination of beam and target polarisation enter directly into the physics results. If the target contains unpolarised material, the amount of unpolarised material has to be known precisely, as it dilutes the asymmetry.

Thin targets with low radiation length have the advantage that external radiative corrections are small. The amount of material which the scattered particles have to pass on their way through the detectors should be minimised in order to reduce secondary interactions and multiple scattering.

The systematic precision of a measurement depends critically on the acceptance and resolution of the detector and on the background conditions of the experiment. An important tool to study the performance of the detector is to divide the data sample into different subsamples with different instrumental quality and to compare the results from those subsamples. At this point, high statistics helps in the understanding of the systematic uncertainties.

Finally, it has to be mentioned that the history of deep inelastic scattering showed that it is not sufficient to have one experiment only. The analysis of scattering processes is so complex that a complete and reliable picture can be only obtained by having different experiments which use different methods and different beam types

and beam energies.

3.2   Overview of the HERMES Concepts

The aim of the HERMES design is to cover as many of the above design criteria as possible. The basic novelty of HERMES compared to previous experiments is that it makes use of a polarised gas target in a stored polarised beam.

3.2.1   The Choice of the Target Technology

From the experience of the EMC experiment it was clear that the major source of systematic errors originated from the fact that due to the high dilution factor the measured asymmetries were tiny and that the polarisation reversal could only be done occasionally because the switching time was as large as 8 hours. There is no technology available which allows for polarising solid material without dilution by a large number of unpolarised nuclei. Therefore HERMES decided to use gas targets as they can be polarised to a high degree without or with only small dilution by unpolarised nuclei. They also allow for rapid polarisation reversal and are therefore an ideal choice to minimise systematic errors which originate in time dependent instrumental effects.

High luminosity is another requirement for a precision experiment. Using a gas target, the only choices to increase the target density are either to increase the pressure of the gas or to use the novel technique of a storage cell. A high pressure gas target requires strong windows which unavoidably produce external Bremsstrahlung in an electron beam. Secondly they can obviously not be used in a storage ring. Therefore HERMES uses the storage cell technique where polarised gas is fed into a T-shaped elliptical cell. The stored beam passes through the openings of the cell without interfering with the cell walls. The gas atoms undergo several hundred wall bounces before they leave the cell. In this way the density of the gas target is increased by a factor of about 100 compared to a free gas jet. By additionally cooling the storage cell to low temperatures, the target density can be increased further. At HERMES a target thickness of about 10^{14} - 10^{15} polarised atoms/cm^2 is achieved in the storage cell.

Polarised gas sources for hydrogen, deuteron and ^{3}He have been developed by HERMES in order to be able to measure the proton and the neutron spin structure.

3.2.2   The Choice of the Accelerator

The measurement of spin structure functions requires a polarised high energy beam. The higher the polarisation, the higher is the measured asymmetry and the smaller are the statistical and systematic errors. To obtain high luminosity using a gas target, a high beam current is required. The obvious choice to get high current is to use the beam in a storage ring.

HERMES had in principle the choice to use the HERA or the LEP electron beam. Due to the higher current and the higher chance of getting longitudinal polarisation

(from the point of view of 1989), HERA was chosen. Another advantage of HERA is that the polarisation build-up time at HERA is significantly shorter (35 min) than at LEP (5 h). The optimal choice would of course be not to use a fixed target at HERA but to use the collider mode of HERA with a polarised proton and deuteron beam. However, the polarisation of the HERA proton beam is hardly feasible in near future.

Originally it was suspected that high polarisation of the electron beam at HERA cannot be maintained during the running of the collider experiments H1 and ZEUS due to possible depolarisation effects of the proton-electron collisions and of the large solenoid fields of the detectors. It has been experimentally proven in the meantime that this is not the case. All three experiments HERMES, H1 and ZEUS can run in parallel and take data during the full time of beam operation.

HERA can store as well electrons as positrons. The physics of charge current interactions in the collider experiments are different for e^-p and e^+p interactions. For HERMES it does not make a difference if HERA runs e^- or e^+ beams as the electromagnetic cross sections are identical (except for higher order radiative corrections). Therefore I will not distinguish between electron and positron beams in the following. Currently HERA runs positrons due to the longer beam lifetime. The electron beam has a reduced lifetime because of ionised dust particles which are captured by the electron beam due to their positive charge.

The HERA East Hall where the HERMES experiment is installed was originally foreseen for a possible third collider experiment. For HERMES the electron and proton beam have been separated by 72 cm and run in different beam pipes. This ensures that the proton operation and especially the proton vacuum conditions are not effected by the operation of the internal gas target. The separate proton pipe of course has consequences in the detector design. Figure 3.1 shows a simplified sketch of the arrangement in the HERA East Hall.

Beam Lifetime

The prominent interaction between the target and the stored beam is the lifetime reduction of the stored beam due to the target gas. Big differential pumping stations are installed that pump away the gas leaking out of the storage cell and such prevent that the vacuum in the rest of the storage ring is effected. The remaining lifetime reduction from the gas inside the storage cell is dominated by the process of atomic Bremsstrahlung. If the energy loss of an electron exceeds $dE/E \sim 1\%$ of its energy, it leaves the RF capture bucket and is lost somewhere in the arcs. The lifetime τ of the beam as a function of the charge Z of the gas atom is given by the formula [80]:

$$\tau \approx T_0 \left[Z(Z+1) \ln \frac{183}{Z^{1/3}} \cdot \frac{n}{8.1 \cdot 10^{25} \text{atoms/cm}^2} \right]^{-1}, \qquad (3.2)$$

where n is the target thickness (in atoms/cm^2) and $T_0 = 21$ μs is the revolution time of HERA. For efficient data taking the life time of HERA has to be large compared to the filling time and compared to the polarisation build-up time. In order to minimise the impact of HERMES on the integrated luminosity of the two
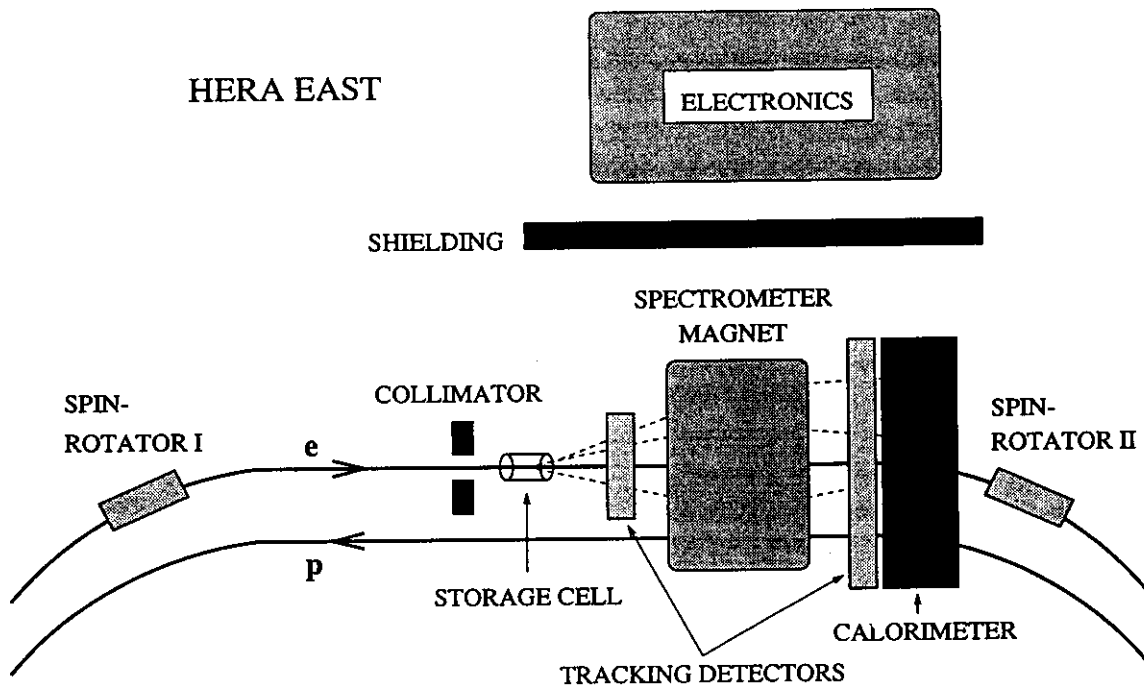
Figure 3.1: Sketch of the HERMES experiment. The electron (positron) beam and the proton beam of HERA stay separated in the East Hall. Spin rotators turn the transverse polarisation of the electron beam into longitudinal direction in the straight section where the experiment is and back to transverse direction in the arc. The electron beam interacts with gas atoms in the storage cell. A collimator system protects the storage cell. The detector consists mainly of tracking chambers, a spectrometer magnet and a calorimeter. Additionally, detectors for particle identification are installed. The readout electronics is separated by a shielding wall and is accessible during data taking. The figure is not to scale.

collider experiment, the beam lifetime due to the HERMES target should not fall below a value of about $\tau_{target} \sim 45$ h. This gives an upper limit of the allowed target thickness of the order of $n_{max} = 1 \cdot 10^{15}$ atoms/cm^2 for hydrogen and deuterium or $n_{max} = 3.5 \cdot 10^{14}$ atoms/cm^2 for ^{3}He.

Beam-Target Interactions

Besides the reduction of the beam lifetime there are other serious constraints in the interplay between the target system and the machine operation. Synchrotron radiation with a power of several kW is produced in every meter of the bending magnets of the HERA electron ring and has the potential to destroy the storage cell. The HERA beam lattice has been changed in order to reduce the amount of synchrotron radiation in the beam section around HERMES and a double collimator system has been developed that efficiently protects the storage cell against synchrotron radiation and also against the scraping of the electron beam tails at the wall of the storage cell.

The collimators and the storage cell are small apertures in the HERA ring. Small apertures can affect the stability of the beam operation especially during injection times. Wake fields and RF-excitations can be produced in the vacuum chambers which may destroy the storage cell material. The bunch fields of the electron beam can influence the polarisation of the target atoms. Very homogeneous magnetic holding fields are necessary to reduce depolarising effects in the gas. All these effects have carefully been taken into account in the design of the target area. As storage cell targets are a novel technology, not much experience has been made so far with those kind of targets in electron machines. Many Monte Carlo calculations and a test experiment were done as preparation for a reliable target system for HERMES.

3.2.3 The Concepts of the Detector

Physics Requirements

The detector has to be able to measure the scattered electron and the total hadronic final state in a wide kinematic range and with a good angular and momentum resolution. To maximise acceptance, an open spectrometer is the appropriate type of detector. A dipole spectrometer magnet with a large gap in combination with tracking chambers before and behind the magnet allow for good momentum resolution.

A clear identification of electrons is required to be able to separate scattered electrons of deep inelastic scattering from the large pion background of photoproduction processes. An electromagnetic calorimeter in combination with a transition radiation detector fulfils this requirement. The electro-magnetic calorimeter needs some spatial resolution and good energy resolution to identify photons in order to allow for checks of the radiative corrections and also for the reconstruction of π^0's in the hadronic final state.

The magnetic field of the spectrometer can be inverted and the spectrometer is build right-left symmetric (the magnetic field is vertical). This way the ratio of positrons versus electrons can be determined with high systematic precision and

can be used to separate the scattering process from pair production by photon conversion.

Identification of charged pions and kaons allows for flavour separation of the semi-inclusive results. HERMES included a threshold Čerenkov counter for this purpose which may be upgraded to a ring-image Čerenkov in future.

A precise luminosity monitor, based on the coincident observation of symmetric Møller (or Bhabha) scattering is needed, because as well the target density as the beam intensity are not constant.

The trigger rates are of the order of 10 Hz for good deep inelastic events in the acceptance of the detector. The total trigger rate which the data acquisition has to accept due to background was estimated to be of the order of 50 Hz.

Storage Ring Requirements

As HERMES makes use of a stored beam, two additional requirements have to be considered: the detector may not influence the stored beam and the detector has to fit into the environment of the ring. As the detector makes use of an open spectrometer magnet the stored electron beam has to be shielded against the magnetic field in order not to disturb the beam optics and especially not to disturb the polarisation of the beam. The HERA proton beam also passes the area of the experiment. By moving the proton beam pipe to a distance of 72 cm parallel to the electron pipe and in the same horizontal plane, it was possible to shield both beams from the magnetic field by implementing a horizontal iron plate (septum plate) into the centre of the dipole magnet with two holes for the beam pipes. This way the magnetic field in the magnet gap remains symmetric and the whole detector is made out of two mirror-symmetric parts, an upper and a lower half. The length of the detector is restricted by the size of the experimental hall and the requirement that the target is at the focal point of the beam optics which is about in the centre of the hall. In principle the focal point of the machine could be moved longitudinally by introducing asymmetric optics, however for having optimal conditions for polarisation optimisation, an asymmetric layout of the beta functions was discarded.

The septum plate introduces a lower limit of the angular acceptance of the detector of $\theta_{min} = 40$ mrad in the vertical projection. The septum plate is an unfortune limitation of the experiment as it reduces the angular acceptance especially for tracks which are not in the vertical plane. A reduction of the angle cut below 40 mrad is not possible for the following reasons:

- At lower angles the background from Møller or Bhabha scattering and photoproduction is so large that the operation of the chambers would be questioned.

- The thickness of the septum plate could not be reduced without increasing the remaining magnetic field in the electron and proton pipes which go through the plate. The magnet could also not be moved further away because the experimental hall leaves only a space of about 8.5 m behind the interaction point for the total detector.

- the cut also matches the acceptance of the detectors just behind the target window. Due to the necessary size of the beam pipe and the frame of the front detectors, an angular acceptance of smaller than 40 mrad would be very difficult to achieve. Ideas to place tracking detectors inside the vacuum were discarded due to the difficult environment of the bunched HERA beam which produces strong wake fields.

Concepts of Background Suppression

The most dangerous background for HERMES is synchrotron radiation which could however be drastically reduced by introducing the double-collimator system. The same collimator system also shields against showers that accompany the beam. The system is designed such that most of the showers produced by scraping the beam particles at the first, narrow collimator are absorbed by the second one.

To prevent that particles which leave the target gas produce showers in the region close to the target, the storage cell and all elements in the target region downstream the interaction point are made from thin and light material as far as possible. As the septum plate unavoidably produces showers, it is wedge shaped pointing to the target and the surface is 'coated' with several mm of heavy material (copper). The field clamps of the spectrometer magnet and the area between the detectors and the beam pipe are covered with lead to absorb electromagnetic showers and synchrotron radiation.

In order to reduce the potential radiation damage which the proton beam can cause, the two halves of the lead glass calorimeter are installed in movable frames and are moved vertically away from the proton beam during dumping and injection of the beams.

Cost & Time Requirements

Additional considerations for the design of the detector were to have an optimal price-performance ratio and to be able to build it without much R&D work within two years after the approval of the experiment. The latter requirement implied that as far as possible standard techniques were used for the spectrometer in order not to risk a delay of the experiment.

Chapter 4

The Polarised Beam at HERA

HERA is the world's first high energy electron storage ring which achieved longitudinal polarisation [1, 2]. Although polarisation has always been an integral part of the design of HERA, there were many doubts in the past concerning the strength of the depolarising mechanisms, the degree of polarisation and the functionality of the spin rotators. Only the systematic study of the response of the electron polarisation to variations of numerous machine parameters lead to the present situation where polarisation at HERA is high, stable, reproducible and understood. The reliable and fast HERA polarimeter [82, 81] was an essential experimental precondition and the SITROS spin tracking program [83] was the theoretical counterpart.

4.1 Self-Polarisation of Electrons

Electrons in storage rings become naturally transversely polarised due to the Sokolov-Ternov effect [84]: the synchrotron radiation process contains a small asymmetric spin-flip amplitude that enhances the polarisation state anti-parallel to the magnetic fields of the bending magnets. The probability for spin-flip synchrotron emission in a homogeneous magnetic field is given by the formula [84, 85]:

$$w^{\uparrow\downarrow} = \frac{1}{2\tau_P}\left(1 + \frac{8\sqrt{3}}{15}\right) = \frac{0.962}{\tau_P} \tag{4.1}$$

$$w^{\downarrow\uparrow} = \frac{1}{2\tau_P}\left(1 - \frac{8\sqrt{3}}{15}\right) = \frac{0.038}{\tau_P} \tag{4.2}$$

$$\text{with} \quad \tau_P = \frac{8m_e}{5\sqrt{3}r_e\hbar c^2}\frac{\rho^3}{\gamma^5} = \frac{\rho^3}{\gamma^5}\cdot 2.83\ 10^{18}\frac{\text{s}}{\text{m}^3} \tag{4.3}$$

with $r_e = e^2/4\pi\epsilon_0 m_e c^2$ being the classical electron radius and ρ being the bending radius in the magnetic field.

For HERA at an energy of $E = 27.5$ GeV and $\gamma = E/m_e = 53\ 800$ and an average bending radius of about $\rho = 707$ m, the probability for an electron to flip the spin is

$$w^{\uparrow\downarrow} = \frac{1}{38.5\ \text{min}} \quad \text{and} \quad w^{\downarrow\uparrow} = \frac{1}{16.2\ \text{h}}. \tag{4.4}$$

This numerical example illustrates how rare the process is that causes the self-polarisation. The rate is suppressed by 10 orders of magnitude compared to the emission of ordinary (non spin-flip) synchrotron radiation. The suppression factor is proportional to the ratio $(E/E_c)^2$ with $E_c = 3\hbar c\gamma^3/2\rho$ being the characteristic energy of synchrotron radiation.

The polarisation P of the electron beam is defined as

$$P = \frac{N^\downarrow - N^\uparrow}{N^\downarrow + N^\uparrow} \tag{4.5}$$

with $N^\uparrow$ ($N^\downarrow$) being the number of electrons in the storage ring with the spin parallel (anti-parallel) to the magnetic field of the bending magnets. From the differential equations:

$$\frac{dN^\uparrow}{dt} = N^\downarrow w^{\downarrow\uparrow} - N^\uparrow w^{\uparrow\downarrow} \tag{4.6}$$

$$\frac{dN^\downarrow}{dt} = N^\uparrow w^{\uparrow\downarrow} - N^\downarrow w^{\downarrow\uparrow} \tag{4.7}$$

follows with (4.1) and (4.2) directly the exponential law of the polarisation rise:

$$P(t) = P_{ST} \cdot (1 - e^{-t/\tau_P}) \tag{4.8}$$

with $P_{ST} = \frac{8}{5\sqrt{3}} = 92.38\%$ being the asymptotic degree of polarisation. The high degree of polarisation is caused by the large asymmetry of the spin-flip rates in (4.1) and (4.2). Figure 4.1 (a) illustrates the exponential rise of polarisation.

A stored positron beam is polarised according to the same formulae as an electron beam, however the polarisation direction is opposite, i.e. parallel to the magnetic field. For both beams, the polarisation direction corresponds to the direction of minimal magnetic energy. It has been shown by Jackson [86] that this is rather a coincidence than a cause.

A Generalised Rise-Time Curve

In a realistic storage ring, the polarisation build up is disturbed by depolarising effects. Before the general three-dimensional equations of motions will be described, the situation is discussed here for the case of a 'flat' machine, i.e. a storage ring where the magnetic field is always vertical. The depolarising effects can be treated phenomenologically by an effective depolarisation time τ_D which describes the additional spin transitions:

$$w_D^{\uparrow\downarrow} = w_D^{\downarrow\uparrow} = \frac{1}{2\tau_D}. \tag{4.9}$$

This approach is correct for all depolarising processes which do not depend on the sign or value of the polarisation. The numerical value of τ_D depends on details of the electron orbit. The transition equations (4.1) and (4.2) become

$$w^{\downarrow\uparrow} = \frac{1}{2\tau_P}(1 + P_{ST}) + \frac{1}{2\tau_D} \tag{4.10}$$

$$\text{and} \quad w^{\uparrow\downarrow} = \frac{1}{2\tau_P}(1 - P_{ST}) + \frac{1}{2\tau_D} \tag{4.11}$$
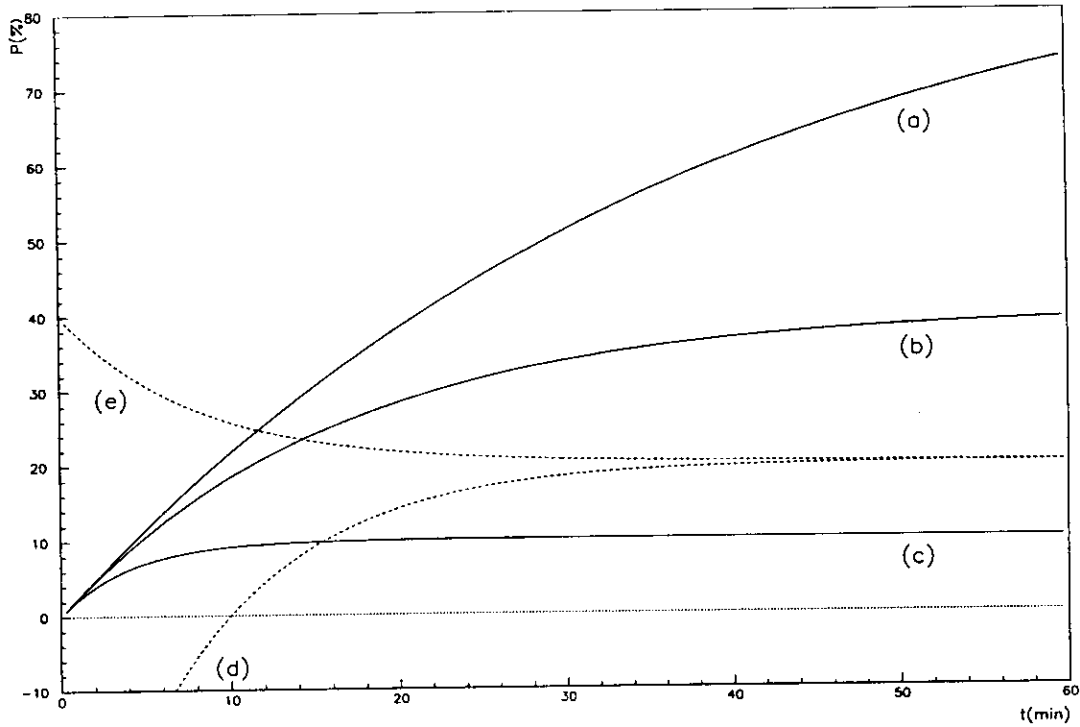
Figure 4.1: Examples of rise time curves. Depending on the initial polarisation and the strength of the depolarising resonances, the curves have different starting points and asymptotic polarisation values. The curve (a) shows the Sokolov-Ternov rise without depolarising effects. It approaches the maximal possible value of 92.38%. The curves (b) and (c) approach lower values of 40% and 10%. Curve (d) shows an example where the initial polarisation is negative and approaches a value of 20%. In all cases, the slope at the zero crossing $P = 0$ is independent of the depolarisation effects. For completeness, curve (e) shows the behaviour of polarisation when the initial polarisation is higher than the equilibrium polarisation. In this case the polarisation falls exponentially. The time constant is defined by the asymptotic value.

and the differential equation for the polarisation follows as:

$$\frac{dP}{dt}(t) = \frac{P_{ST}}{\tau_P} - P(t)\left(\frac{1}{\tau_P} + \frac{1}{\tau_D}\right).$$ (4.12)

It has the general solution

$$P(t) = P_\infty \cdot \left(1 \pm e^{-(t-t_0)/\tau}\right)$$ (4.13)

with

$$\frac{1}{\tau} = \frac{1}{\tau_P} + \frac{1}{\tau_D} \quad \text{and} \quad P_\infty = P_{ST} \cdot \frac{\tau}{\tau_P}.$$ (4.14)

The '+'-sign stands for the polarisation rise, whereas the '−'-sign denotes a polarisation fall which happens if the initial polarisation is larger than the asymptotic polarisation, e.g. after a change of τ_D. From the equations (4.14) follows that depolarising effects reduce the time constant τ of the polarisation rise but they also reduce the asymptotic value P_∞ of polarisation. $P_{ST} = \frac{8}{5\sqrt{3}} = 92.38\%$ is the maximal achievable polarisation. A high value of asymptotic polarisation can only be maintained if the depolarising time τ_D is large compared to the polarising time τ_P. t_0 is the time where the polarisation rise starts or where it crosses $P = 0$ in case the initial value of polarisation was negative (e.g. after a spin flip). The slope of the polarisation rise at this time has the characteristic value:

$$\frac{dP}{dt}\Big|_{P=0} = \frac{P_\infty}{\tau} = \frac{P_{ST}}{\tau_P}$$ (4.15)

which is independent of the depolarisation mechanisms and can be used to cross-check or calibrate the absolute scale of the polarisation measurement. At HERA with $E = 27.5$ GeV the numerical value is $dP/dt|_{P=0} = 2.5$ %/min.

Figure 4.1 shows some examples of polarisation rise curves for different equilibrium polarisations. It illustrates that the time constant of the rise or fall of polarisation is determined by the value of the equilibrium polarisation.

4.2 Spin Dynamics in Storage Rings

The dynamics of spins in the strong and inhomogeneous magnetic fields of storage rings is far from trivial. In the following the basic ideas will be presented, a more complete description is found in [87, 88, 89, 83, 85]. The relativistic equation of motion of a spin vector $\vec{S}$ in a magnetic field is described by the Thomas-Bargmann-Michel-Telegdi (T-BMT) equation [91, 92] which is given here in the ultra-relativistic ($\gamma \gg 1$) approximation:

$$\frac{d\vec{S}}{dt} = \vec{\Omega}_{BMT} \times \vec{S}$$

$$\text{with} \quad \vec{\Omega}_{BMT} = -\frac{e}{m_e\gamma}\left[(1 + a\gamma)\vec{B}_\perp + (1 + a)\vec{B}_\parallel\right].$$ (4.16)

$a = (g - 2)/2 = 1.16 \cdot 10^{-3}$ is the gyro-magnetic anomaly and $\vec{B}_\parallel$ ($\vec{B}_\perp$) is the component of the magnetic field parallel (perpendicular) to the motion of the particle. The revolution frequency of the particle is

$$\Omega_c = \frac{eB_\perp}{m_e c\gamma},\tag{4.17}$$

from which follows that the spin precesses $(1 + a\gamma)$ times for every revolution in the storage ring. The product $a\gamma$ is called the spin tune ν_s. For a HERA energy of $E = 27.5 \ GeV$, the spin tune is:

$$\nu_s = a\gamma = 62.5\tag{4.18}$$

which means that the spins of the electrons in HERA precess 62.5 times in every revolution. The equation (4.18) is strictly true only for flat machines and obtains corrections when the orbit is twisted e.g. by spin rotators.

The Sokolov-Ternov Effect on the Closed Orbit

In a non-flat machine, the spin vectors are in general not vertical and the magnetic fields are not homogeneous. The polarisation of the beam is described by a polarisation vector $\vec{P}$:

$$\vec{P} = \frac{1}{N} \sum_{i=1}^{N} \vec{S}_i,\tag{4.19}$$

where N is the number of particles in an ensemble of electrons. The Sokolov-Ternov formula has been generalised by Baier-Katkov-Strakhovenko (BKS) [93]. The equation of motion (4.16) obtains an additional term:

$$\frac{d\vec{P}}{dt}|_{ST} = \Omega_{BMT} \times \vec{P} - \frac{1}{\tau_{ST}} \left(\vec{P} - \frac{2}{9}(\vec{P}\vec{\beta})\vec{\beta} + P_{ST}\frac{\vec{\beta} \times \dot{\vec{\beta}}}{|\vec{\beta} \times \dot{\vec{\beta}}|} \right).\tag{4.20}$$

Here, $\vec{\beta} = \vec{v}/c$ is the velocity vector and $\tau_{ST} = 5\sqrt{3}r_e\hbar c^2\gamma^5/8m_e\rho^3$ is the rise time for a flat machine. This equation can be solved on the closed orbit. – The closed orbit is the periodic solution of the particle motion in a storage ring. – It can be shown that a periodic solution $\vec{n}_0(s)$ for the spin motion exists and that the polarisation of a particle ensemble along the closed orbit asymptotically aligns parallel to $\vec{n}_0(s)$ with a polarisation of

$$P_\infty = P_{ST}\frac{\oint |\rho|^{-3}(\vec{b}\vec{n}_0) \ ds}{\oint |\rho|^{-3}\left[1 - \frac{2}{9}(\vec{\beta}\vec{n}_0)^2\right] \ ds}.\tag{4.21}$$

$\vec{b}$ is a unit vector in the direction of the magnetic field and s is the longitudinal coordinate. The build-up time is given as

$$\frac{1}{\tau_P} = \frac{5\sqrt{3}r_e\hbar c^2}{8m_e}\frac{\gamma^5}{L} \oint |\rho|^{-3}\left[1 - \frac{2}{9}(\vec{\beta}\vec{n}_0)^2\right] \ ds.\tag{4.22}$$

with L being the total length of the orbit.

4.2.1 Depolarising Effects in Storage Rings

There are several different mechanisms which lead to depolarisation in a storage ring. The first one concerns the tilt of the $\vec{n}_0(s)$-axis. From equation (4.21) follows that the maximum polarisation of particles along the closed orbit is achieved when the $\vec{n}_0$-vector is everywhere parallel to the magnetic field. In a realistic storage ring, quadrupoles have alignment errors and the closed orbit passes the quadrupoles off axis. Horizontal dipole components in the quadrupoles tilt the $\vec{n}_0$-axis out of the vertical direction and thus reduce the strength of the Sokolov-Ternov effect.

The second effect is spin diffusion: electrons in a storage ring emit synchrotron radiation photons, a process which leads to a stochastic excitation of longitudinal synchrotron oscillations and due to the dispersion also to strong horizontal betatron oscillations. Additionally vertical betatron oscillations are excited due to a non-zero vertical emittance of the beam. Particles on dispersion and vertical betatron orbits experience horizontal fields in the quadrupoles where their spin is tilted. As every electron has an individual orbit and energy, the spin tilt and the spin precession is incoherent and will lead to a diffusion of the spin orientations and to a decrease of the value of polarisation.

The third effect are the depolarising resonances [94]: the strength of a depolarising effect increases immensely if the excitation is in resonance with the spin tune ν_s. The resonance condition is given by the formula:

$$\nu_s = n + n_x \cdot Q_x + n_y \cdot Q_y + n_s \cdot Q_s \tag{4.23}$$

where $Q_{x,(y)}$ denote the fractional parts of the horizontal (vertical) betatron tune, Q_s is the synchrotron tune and n, n_x, n_y and n_s are integers.

It is very difficult to calculate the strength of the depolarising effects in detail. All three effects are closely related: a tilt of the $\vec{n}_0$-axis enhances spin diffusion and spin diffusion determines the strength and width of the depolarising resonances. A semi-classical quantum mechanical approach to all the effects has been derived by Derbenev and Kondratenko [95] and Mane [96]. The concept of the $\vec{n}_0$-axis of the closed orbit is generalised to a quantisation axis $\vec{n}$ for each particle in the beam phase space. The total beam polarisation is given by averaging over all particles in the phase space:

$$P_\infty = P_{ST} \frac{\langle \oint |\rho|^{-3} \vec{b} \left[\vec{n} - \gamma \frac{\partial \vec{n}}{\partial \gamma} \right] \, ds \rangle}{\langle \oint |\rho|^{-3} \left[1 - \frac{2}{9}(\vec{\beta}\vec{n}_0)^2 + \frac{11}{18}|\gamma \frac{\partial \vec{n}}{\partial \gamma}|^2 \right] \, ds \rangle}. \tag{4.24}$$

The energy derivative of the quantisation axis $\gamma \frac{\partial \vec{n}}{\partial \gamma}$ is called the spin-orbit coupling vector and describes the diffusion and the resonance processes which are driven by the synchrotron radiation.

A pragmatic and straight forward approach to the calculation of depolarising effects is the use of the Monte Carlo method. The SITROS program [97, 83] has been developed which tracks an ensemble of classical spin vectors through the magnet lattice of the storage ring by applying the equation of spin motion in every magnet. It also simulates damping effects and synchrotron emission. The spin diffusion and

the depolarisation time is measured by tracking the ensemble of spin vectors many thousand turns through the lattice and by observing the decay of the polarisation vector.

4.2.2 Optimisation of Transverse Polarisation

As seen from the equations of motions (4.16) and (4.17), the spin precession angle in a magnetic field is $(1 + a\gamma)$ times larger than the deflection of the particle in the same field. This means that for example a small kink which the orbit obtains by a misaligned quadrupole is magnified by a factor $(1+a\gamma)$ in the spin motion. From this follows that the complications by depolarising effects increase with energy. Special care has therefore been taken at HERA. All quadrupoles have been mechanically re-aligned for local bumps to a precision of better than 1 mm over the whole 6.3 km long ring. Additionally special optimisation programs smooth the closed orbit. They reduce the mean deviation of the closed orbit from the centre of the quadrupoles to better than $\Delta x_{RMS} \approx 0.8$ mm and $\Delta y_{RMS} \approx 0.9$ mm by the use of correction dipoles.

Several measures have been taken to reduce the influence of resonances on the polarisation. First, the beam energy is chosen to be close to a half-integer spin tune $(\nu_s = 62.5)$. Close to integer spin tune, the polarisation is small due to resonances that are connected to machine imperfections and due to strong synchrotron resonances. Second, the fractional parts of the betatron tunes Q_x and Q_y were chosen to be small, such that only higher order side band resonances occur at half integer spin tune: $Q_x = 0.11$ to 0.12, $Q_z = 0.19$ to 0.20. Synchrotron tunes of $Q_s = 0.063$ to 0.082 were obtained by using a circumference voltage of $U \approx 140$ MV. The condition $Q_x + Q_s \approx Q_z$ puts the two families of synchrotron satellites on top of each other. Third, for a given energy and given betatron tunes, a scan of the synchrotron tune is made to avoid synchrotron side band resonances empirically. The separation of the side bands is $\Delta E = E Q_s/a\gamma \approx 30$ MeV.

The most efficient method at HERA to obtain high polarisation is the empirical optimisation of harmonic correction bumps [98]. It works as follows:

In an electron storage ring there is an unavoidable horizontal excitation of the orbital motion due to synchrotron radiation. On the other hand, spin motion is not very sensitive to horizontal motion and only vertical deflections precess the spin vector away from the vertical direction and thus lead to depolarisation. In a realistic storage ring there is however a spin coupling between the horizontal and vertical motion. The harmonic correction scheme allows to reduce this coupling by adding vertical distortions that compensate the effect of the original distortions. At HERA a combination of 8 vertical closed bumps at 'strategic' positions is used. The coupling can not be completely eliminated. It is sufficient however to reduce those harmonic components which are close to the spin tune (61 to 64) in case of $\nu_s = 62.5$.

The harmonic correction bumps are introduced empirically at HERA by varying bump amplitudes and optimising the measured polarisation values. Results of several scans of the 60th and 61st bumps are plotted in figure 4.2. The scans were taken at a slightly lower beam energy of 26.6 GeV with $\nu_s = 60.5$.

In future the harmonic bump optimisation will be preceded by the following opti-
misation procedure as described by Böge [99]: first, the method of beam-based align-
ment will be used to determine the precise location of the beam position monitors
relative to the quadrupoles. With this knowledge the orbit-kicks in the quadrupoles
can be minimised such that the mean tilt of the $\vec{n}_0$-axis is minimised with the result
that spin diffusion decreases. According to Monte Carlo calculations, a polarisation
of 60% can be achieved by this method alone. Followed by empirical harmonic bump
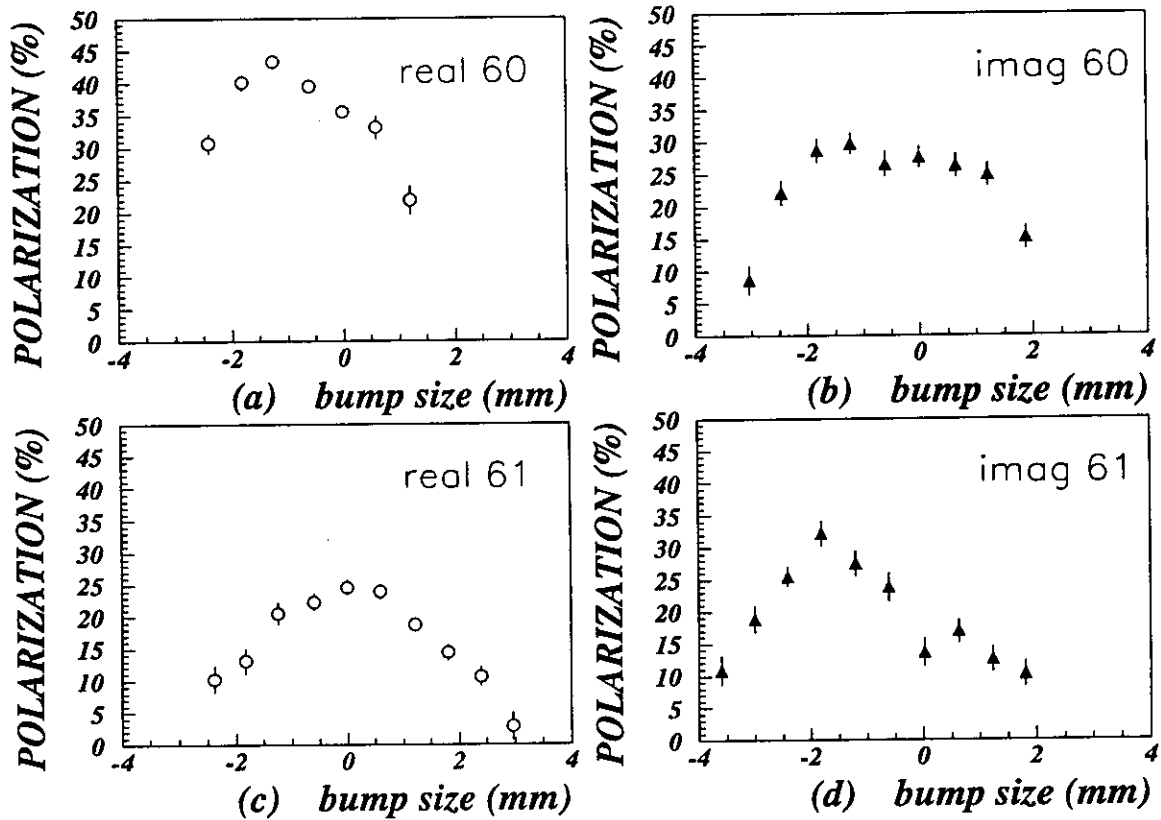optimisation, 80% polarisation should be possible.

Figure 4.2: Scan of four harmonic corrections bumps. The polarisation is plotted versus
the maximal orbit deviations due to the bumps. The plots are not corrected for rise
time effects. The figure shows that polarisation strongly depends on the amplitude of the
bumps. Polarisation is optimised by finding the maximum of the curve for each harmonic.

4.2.3   Spin Tracking Monte Carlo Program

A combined theoretical and experimental approach was important for understanding
the depolarising mechanisms and for the development of tools that allow optimisa-
tion of the machine. Details of the theoretical approaches can be found in [83] and
[90].

The SITROS spin tracking Monte Carlo allows one to simulate details of the
HERA machine. The best performance check of this program is shown in figure 4.3.

The beam energy has been scanned between 26.55 and 26.75 GeV and shows a broad plateau of high polarisation with some dips due to resonances. The centre of the plateau is expected to be at half integer spin tune (E=26.66 GeV). The measurement shows, that the calibration of the HERA energy was off by about 50 MeV. (This measurement has been done before the beam energy was calibrated by rf-depolarisation [100].) The SITROS calculation is overlaid on the plot taking the shift of energy into account. It reproduces the main features of this measurement.
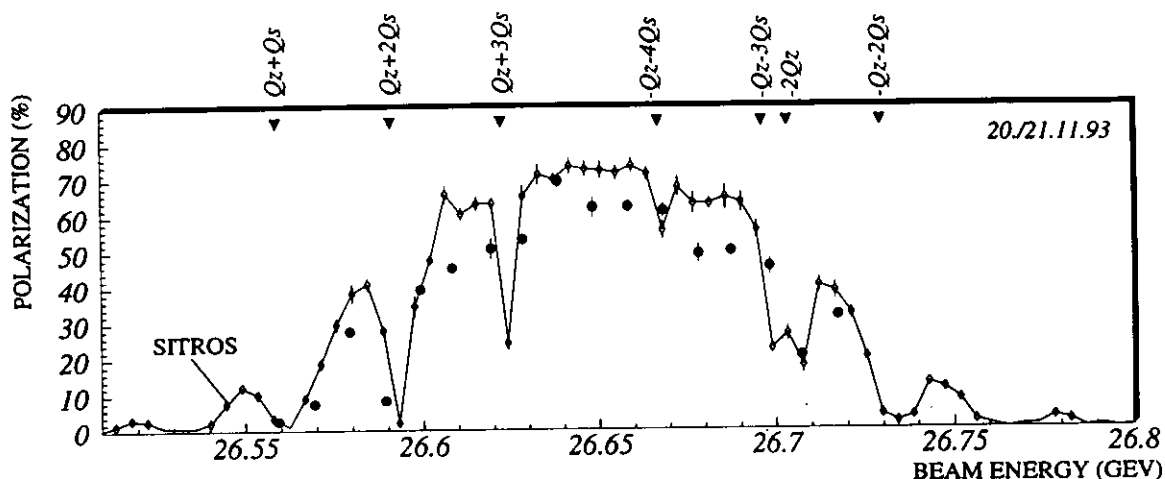

Figure 4.3: Comparison of the measured (dark dots) versus the calculated polarisation at HERA as a function of beam energy. Two side-band resonances could be measured (at 26.59 GeV and 26.71 GeV). The bell-shaped behaviour of polarisation versus energy is reproduced. The absolute value of polarisation depends on the quality of the harmonic bump optimisation.

4.3 The HERA Spin Rotators

The Sokolov-Ternov effect produces vertical polarisation in the arcs of an electron storage ring. As the experiments require longitudinal polarisation, two spin rotators are required at each interaction region that rotate the spin into the longitudinal direction and back to the vertical direction behind the IP as shown in figure 4.4. A pair of 'Mini-Rotators' was installed in winter 93/94 in HERA around the HERMES interaction region. The 'Mini-Rotators', designed by Buon and Steffen [101], consist of interleaved horizontal and vertical dipole magnets as shown in figure 4.5. They have a length of only 56 m and produce a vertical closed bump of about 20 cm. The actual size of the bend depends on the beam energy. The horizontal bending of the rotators is an integral part of the arc. The purpose of the additional two weak dipoles H3b and H3c in figure 4.5 is to reduce background in the HERMES experiment. The spin precession of those magnets is taken into account by a reduced strength of the last rotator magnet H3a.
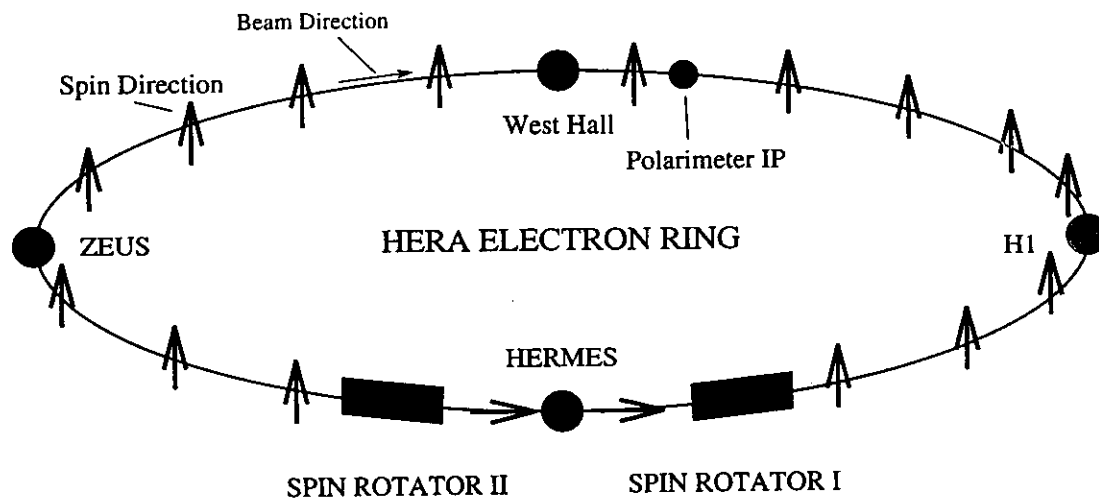
Figure 4.4: A sketch of the HERA electron ring showing the positions of the spin rotators. Polarisation is longitudinal in the straight section at the HERMES IP. Transverse polarisation is measured with the Compton polarimeter in the West area.
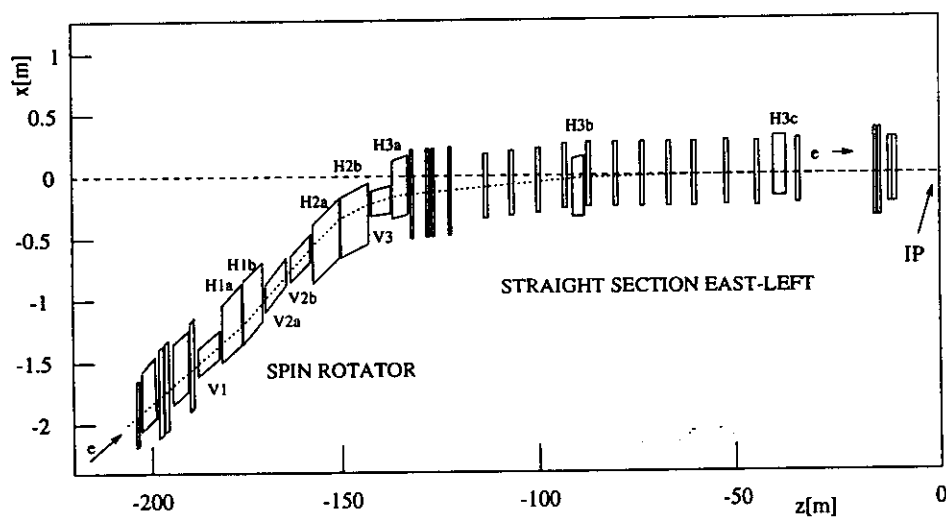

Figure 4.5: Horizontal projection of the layout of one 90° spin rotator. H1-3 (V1-3) indicate the horizontal (vertical) bending dipoles of the Mini-Rotator. The thin boxes indicate quadrupoles.
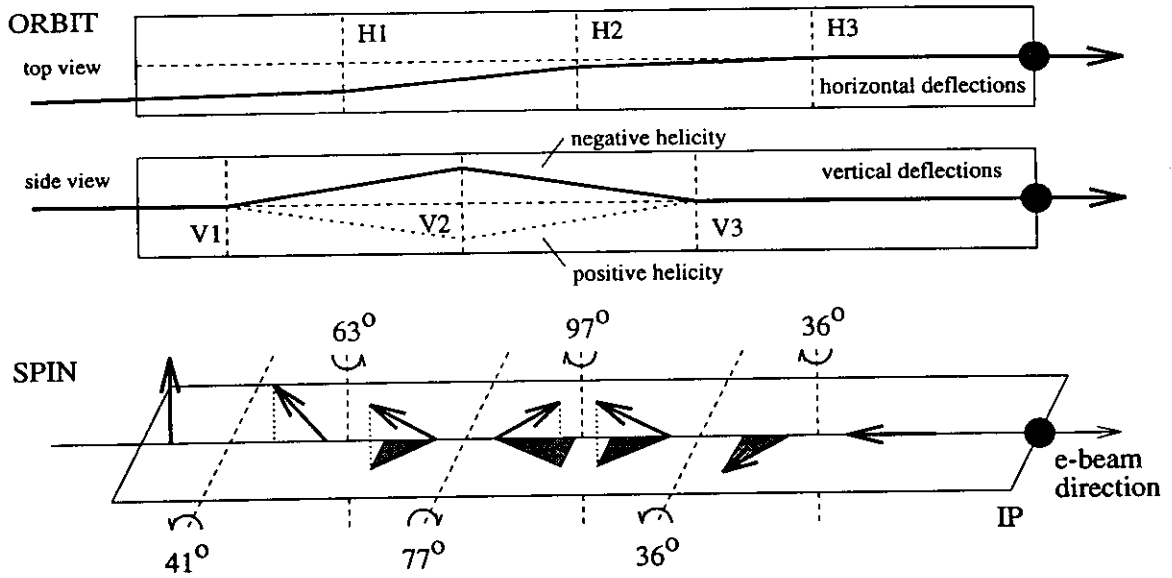
Figure 4.6: A functional diagram of the Mini-Rotator showing the horizontal and vertical deflections of the orbit and the corresponding spin precession angles. The size of the vertical bump is about 22 cm. The spin precession is a factor of 63 larger compared to the orbital kicks. Due to the non-Abelian behaviour of rotations, it is possible to rotate the spin by 90° and at the same time move the orbit back to its nominal position and slope.

Figure 4.6 illustrates how the rotators work: Small angular orbital deflections in the dipoles are magnified by the factor 63.5 according to eq. (4.16). As the spin rotations do not commute, horizontal and vertical bending magnets can be combined in such a way that the spin direction is turned by effectively 90° and at the same time the beam position and slope at the IP is not changed.

To invert the helicity of the electrons at the IP, the direction of the vertical bumps has to be reversed. To facilitate that the spin rotator magnets are mounted on remotely controlled jacks that move the chain of magnets without breaking the vacuum in the chambers. The rotators function over an energy range of 27 to 35 GeV. However, an energy change of greater than ±200 MeV requires manual horizontal adjustment of the rotator magnets.

4.4 Longitudinal Electron Polarisation

Spin rotators are potential sources of depolarisation for several reasons: a small deviation from a 90° rotation would tilt the equilibrium spin direction and thus depolarise the beam. Therefore the magnets have to be calibrated very precisely. Secondly, as the spin is not vertical in the straight section, the large horizontal size of the beam and the horizontal betatron motion can easily lead to spin diffusion due to the vertical magnetic field in the quadrupoles. Quadrupoles inside the spin rotator could be avoided at HERA due to the short length of the 'Mini'-Rotators.

A special spin matching procedure was used to reduce the spin diffusion [102]:
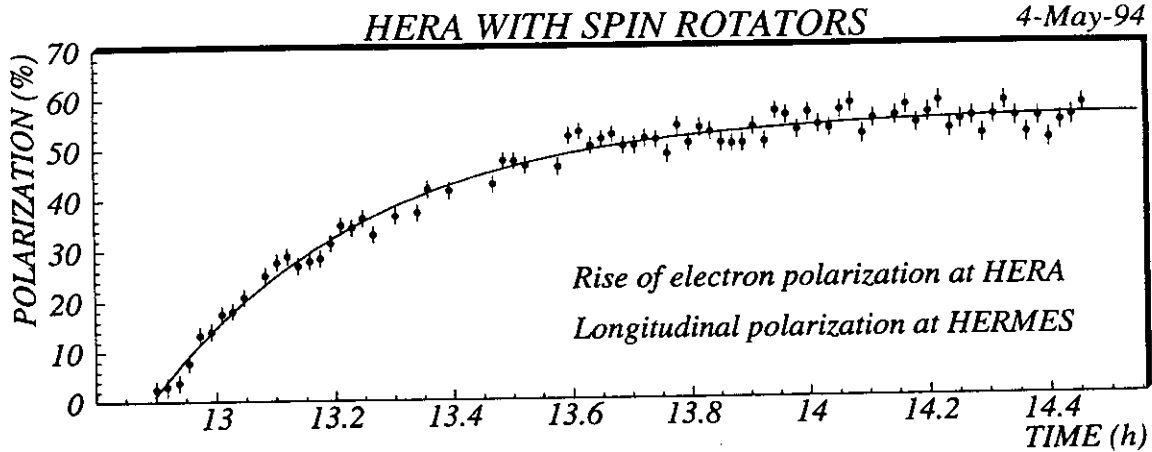
Figure 4.7: First observation of longitudinal polarisation at HERA. Overlaid is the result of a fit of the expected exponential build-up curve with the parameters $P_\infty = 56.6 \pm 0.5\%$ and $\tau = 20.8 \pm 0.7$ min.

the lattice in the straight section between the rotators was made horizontally 'spin transparent' and the remaining arc is vertically 'spin transparent'. A piece of lattice is described as 'spin transparent' when certain elements in the spin-orbit transport matrices vanish. Then the spin precession of the individual electrons is independent of their betatron motion. Thus this piece does not contribute to spin diffusion.

On May 4th, 1994 the spin rotators were brought into operation for the first time. Due to the non-Abelian behaviour of rotations, the spin rotators cause a change of spin tune ($\nu_s \neq \gamma a$) which was compensated by changing the beam energy by 20 MeV. Without any fine-tuning the polarisation went up to a value of about 57% at the first try as shown in figure 4.7. After a small change of the beam energy longitudinal polarisation went up close to 70% and reached values which were equal to the maximal achieved polarisation without spin rotators (see figure 4.8).

Polarisation is measured with the transverse polarimeter in the HERA West area. The degree of polarisation is the same all over the ring but the direction is manipulated by the rotators. There is confidence that the spin direction is longitudinal in the HERMES region within a few degrees due to the precise calibration of the rotator magnets and due to the fact that if the spin direction were tilted from the nominal direction, large polarisation would not be possible due to strong depolarising effects in the rest of the ring. HERMES plans to build a second, longitudinal polarimeter between the rotators to reduce the systematic error of the polarisation measurement.

4.5 Polarisation during Luminosity Conditions

HERA switched from e^-p to e^+p operation in July '94 to solve a lifetime problem that is caused by positively ionised dust particles which are captured by the negatively charged electron beam. At the same time the spin rotators had a vacuum problem which has been solved by replacing some vacuum chambers in Nov. '94.
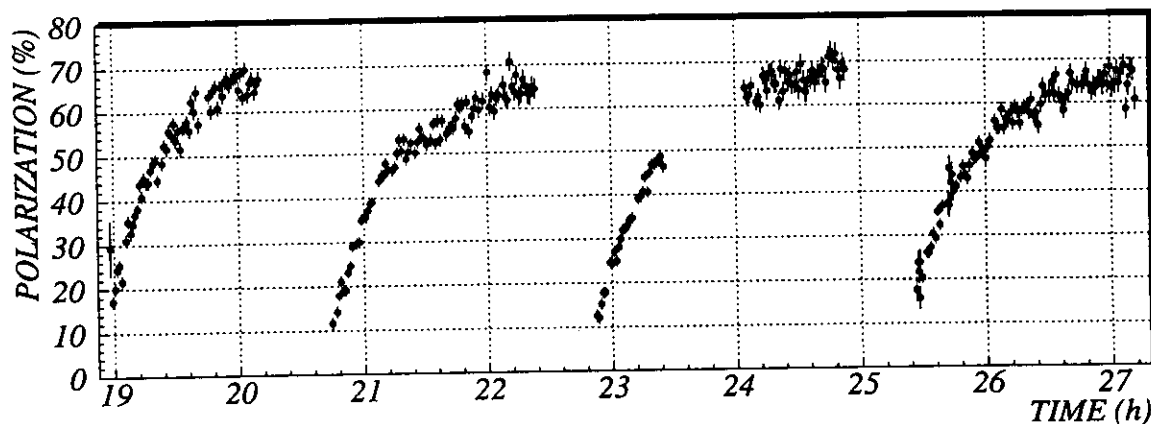
Figure 4.8: Recording of longitudinal polarisation during HERA bake-out runs. After each injection and ramping of a new beam, the polarisation rises exponentially and reproduces high values close to $P = 70\%$.
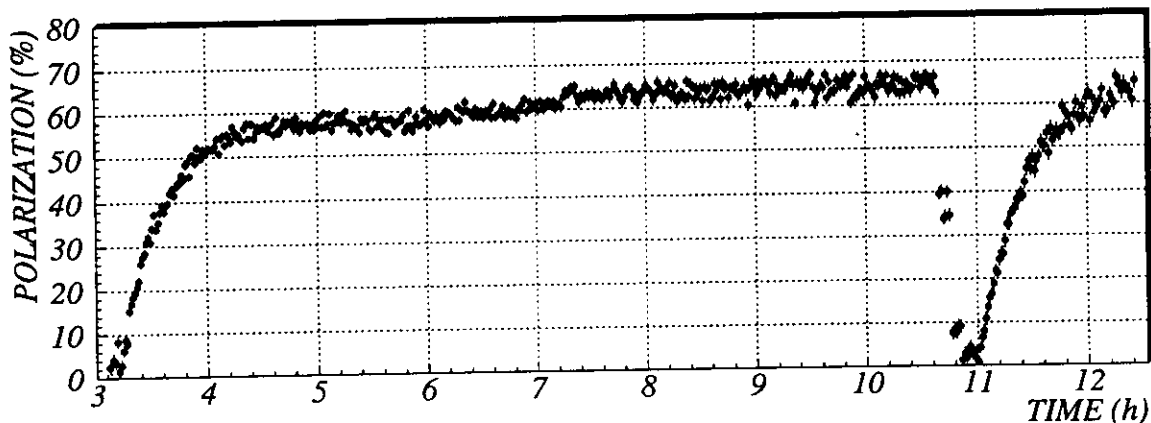
Figure 4.9: Polarisation during a long luminosity run. The polarisation rose after ramping the beam to 27.5 GeV. At 6:00 it is likely that beam conditions changed slightly which led to an increase of polarisation. At 10:30 the beam was depolarised by rf-resonance to perform an energy calibration and to cross check the polarimeter calibration. At 12:30 the beam was dumped.

Therefore HERA operated in 1994 mostly with positrons and without spin rotation. High, stable (transverse) positron polarisation of 60 – 70% is achieved routinely at HERA during luminosity conditions. The large solenoid fields of the H1 and ZEUS detectors are compensated locally by anti-solenoids. There is no evidence for beam-beam depolarisation by the proton beam at the current conditions. Figure 4.9 shows polarisation during a full luminosity fill of over 9 hours. SITROS calculations have predicted a decrease of polarisation by about 10% at maximal currents (close to the beam-beam limit) [103].

It should be mentioned that the achieved polarisation is already now well above the design goal for the HERMES experiment of 50%. Spin rotators for the collider experiments H1 and ZEUS are ordered and will be installed at the earliest in 1996.

4.6   RF-Depolarisation and Energy Calibration of HERA

The method of resonant spin depolarisation has been successfully tested at HERA and was used to calibrate precisely the HERA beam energy [100]. A variable sweeping frequency of about half the revolution frequency was applied to a vertical dipole magnet with a strength of $B \cdot l \approx 2 \cdot 10^{-4}$ Tm. Resonant depolarisation occurs when the precession of the polarisation vector is in resonance with the excitation frequency. Besides the main resonance also synchrotron side bands are present and have been observed. In order to distinguish side bands and mirror frequencies from the main resonance, depolarisation has been studied at slightly different beam energies and synchrotron tunes. Figure 4.10 shows several frequency scans and its effect on polarisation. Spin flip has not been observed as the depolarisation magnet was not strong enough to rotate the spin vector before spin diffusion occurs [104].

The beam energy in an ideal storage ring is determined from the depolarisation frequency f_{dep} and the revolution frequency f_{rev} according to the formula [105]

$$E_{beam} = \left(n \pm \frac{f_{dep}}{f_{rev}}\right) \frac{m_e}{a} = (61 - f_{dep}/47317 \ Hz) \cdot 440.649 \ MeV \qquad (4.25)$$

with n being the integer part of the spin tune. Figure 4.11 shows a summary of the measurements which have been taken to calibrate the beam energy of HERA. It shows the nominal beam energy as extracted from the currents of the bending dipoles plotted versus the energy as calculated from the depolarisation frequency. The true HERA beam energy in '93 was about 33-36 MeV below the nominal value [100]. The deviation of about one per mil is within the systematic uncertainties of the dipole fields.

4.7   The HERA Beam Polarimeter

There are several methods to measure the polarisation of stored beams. At low energies for example, the spin-dependence of intra-beam scattering in a low-beta
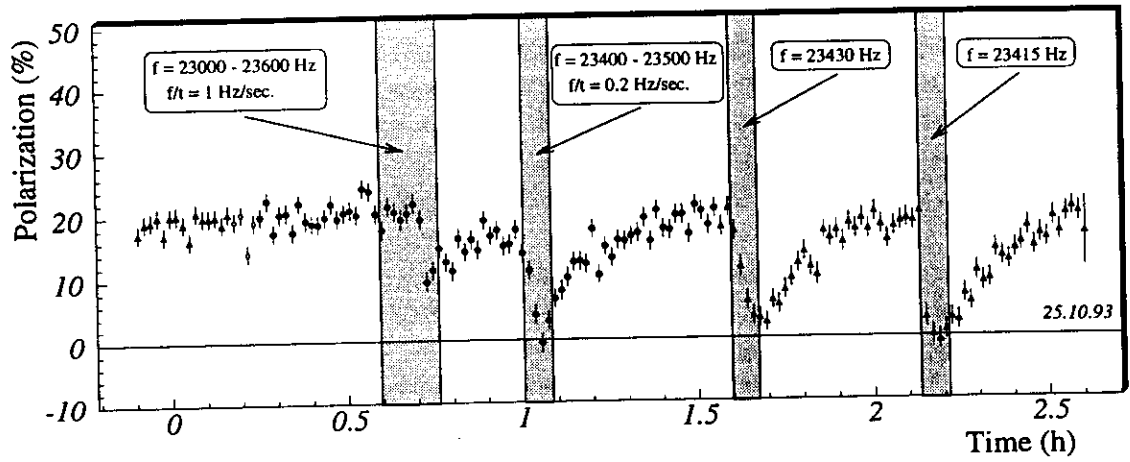
Figure 4.10: Resonant depolarisation of the HERA beam using different frequencies and sweeping speeds. The efficiency of the depolarisation depends on the amplitude of the magnetic field and on the speed of the frequency sweep. The depolarisation frequency is found by tracing back the frequency from the moment at which depolarisation occurred and by iteratively reducing the sweeping ranges. Unlike at LEP, spin-flip could not be observed at HERA.
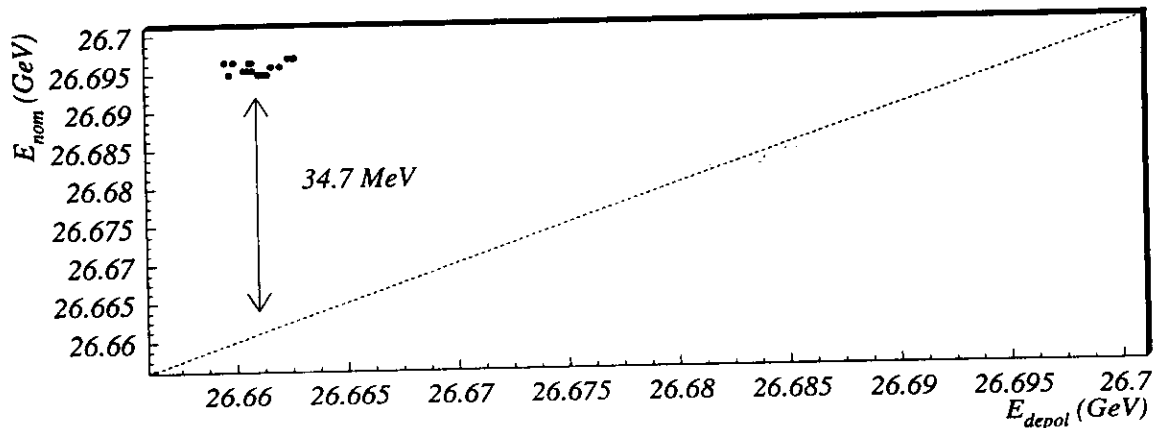
Figure 4.11: The beam energy of HERA was calibrated by rf depolarisation. The 'true' beam energy was found to be 33-36 MeV below the nominal beam energy which is calculated from the dipole currents. The deviation is within the systematic uncertainties of the dipole fields.

section can be used to detect polarisation. The best method at high energy electron beams is Compton scattering of polarised laser light off the electron beam. This method is used at LEP [106], SLAC [107], KEK [108] and also at HERA.

For HERA, a polarimeter was constructed that fulfils two aims: firstly, it provides fast online information about the actual degree of polarisation and thus allows the interactive optimisation of the machine parameters for maximal polarisation. Secondly, the polarimeter can be used as an off-line monitor of the time dependence of polarisation for the experiments HERMES, H1 and ZEUS. It will provide precise information about the vertical spin polarisation of the electron beam with a statistical and systematic precision of a few percent.

The HERA polarimeter is based on the spin dependence of the Compton cross section: left and right circularly polarised laser light is scattered off the HERA electron beam. The up-down asymmetries of the backscattered photons are measured in a position sensitive calorimeter. The 'single-photon method' is used, i.e. the laser intensity is chosen such that the probability of multiple Compton photons per bunch crossing is small and the energy and the position of each single photon is used for the analysis. Thus, in contrast to the 'multi-photon method', photons of a certain energy range can be selected where the analysing power of the cross section is largest. In addition, correlations of position and energy of the Compton photons can be used to study the systematic precision of the polarisation results. In the following the polarimeter is described briefly. A detailed description of the polarimeter and its calibration methods can be found in references [81, 98, 100, 109, 110, 111].

4.7.1   The Compton Cross Section

Laser photons of $E_\lambda = 2.41$ eV are scattered almost head-on with a crossing angle of $\alpha = 3.1$ mrad off the electron beam with $E_e = 27.5$ GeV. Due to the large Lorentz boost of the electrons ($\gamma = 54000$) the laser photons have an energy of 260 keV in the rest frame of the electrons and become high energy photons of $E_\gamma = 0$ to 13.8 GeV after the scattering process. The photons are backscattered in a small cone. For a scattering angle of for example $\theta = 90°$ in the electron rest frame, the Compton photons are backscattered with $E_\gamma = 9.3$ GeV at an angle of $\theta_{lab} = 1/\gamma = 19$ μrad in the lab frame.

The differential cross section for the Compton scattering of a polarised photon and a polarised electron is given in the rest frame of the initial electron as [112]:

$$\frac{d\sigma_c}{d\Omega}(\vec{S}, \vec{P}) = \Sigma_0 + \Sigma_1(S_1) + \Sigma_2(S_3, \vec{P}) \qquad (4.26)$$

with

$$\Sigma_0 = \frac{r_0^2 k_f^2}{2 k_i^2}\left(1 + \cos^2\theta\right) + (k_i - k_f)(1 - \cos\theta) \qquad (4.27)$$

$$\Sigma_1(S_1) = \frac{r_0^2 k_f^2}{2 k_i^2} S_1(\phi)\sin^2\theta \qquad (4.28)$$

$$\Sigma_2(S_3, \vec{P}) = -\frac{r_0^2 k_f^2}{2 k_i^2} S_3(\phi)(1 - \cos\theta)(\vec{k_i}\cos\theta + \vec{k_f})\cdot\vec{P} \qquad (4.29)$$

$$k_i = 2\gamma E_\lambda/m_e \tag{4.30}$$

$$k_f = 1/(1 - \cos\theta + 1/k_i). \tag{4.31}$$

θ is the scattering angle of the backscattered Compton photons in the rest frame of the initial electron and ϕ is the azimuthal angle with respect to the horizontal direction. r_0 denotes the classical electron radius. $\vec{P}$ is the polarisation vector of the electron beam and $\vec{S} = (S_0, S_1, S_2, S_3)$ is the Stokes vector [113] which describes the polarisation of the laser light:

$$S_0 = E_1^2 + E_2^2 \tag{4.32}$$

$$S_1 = E_1^2 - E_2^2 \tag{4.33}$$

$$S_2 = 2E_1 E_2 \cos\delta \tag{4.34}$$

$$S_3 = 2E_1 E_2 \sin\delta \tag{4.35}$$

where E_1 and E_2 are orthogonal components of the electric field with the relative phase δ. Using the normalisation $S_0 = 1$, the linear polarisation of the light is calculated as $S_{lin} = \sqrt{S_1^2 + S_2^2}$ and the circular component is $|S_3|$.

Figure 4.12 illustrates the azimuthal distributions of the backscattered photons when they arrive at the detector at a distance of 64 m. Due to the two-body kinematics, Compton photons of a given energy arrive on a circle of a fixed radius r ($r \approx 1$ mm) at the detector. If the beam and the laser light are unpolarised, the distribution is flat along the circumference. If the laser light is polarised linearly, the intensity of the photons modulates with a $\cos 2\phi$ term. This term is independent of the electron polarisation. If the laser light is circular polarised, the intensity of the photons is modulated with a $\cos\phi$ term which is proportional to the transverse polarisation of the electron beam.

The energy distribution of the backscattered Compton photons can be used to measure the longitudinal polarisation of the electron beam. Figure 4.13 shows the differential cross section $d\sigma/dE$ for an unpolarised and for a right and left circular polarised electron beam which is scattered off a circular polarised laser beam.

4.7.2 The Laser Optics

Figure 4.14 shows an overview of the polarimeter layout. A 10 W argon ion laser provides a continuous, linearly polarised laser beam at the green line of 514 nm. A Pockels cell converts the polarisation state to right (left) circularly polarised light with a switching frequency of about 90 Hz. A chopper which blocks the beam for 20 s once per minute is used for background measurement. A remotely controlled mirror system transports the laser beam down to the interaction point (IP) in the HERA tunnel. A doublet lens system with 14.5 m focal length focusses the beam onto the electron beam with a spot size of $\sigma \approx 600$ μm. Most of the transport line is under vacuum to reduce deflections by air turbulences. For mechanical simplicity, all mirrors are outside the vacuum. Position sensitive photo-diodes behind the mirrors, which detect the small fraction of the transmitted light, are used as position monitors.
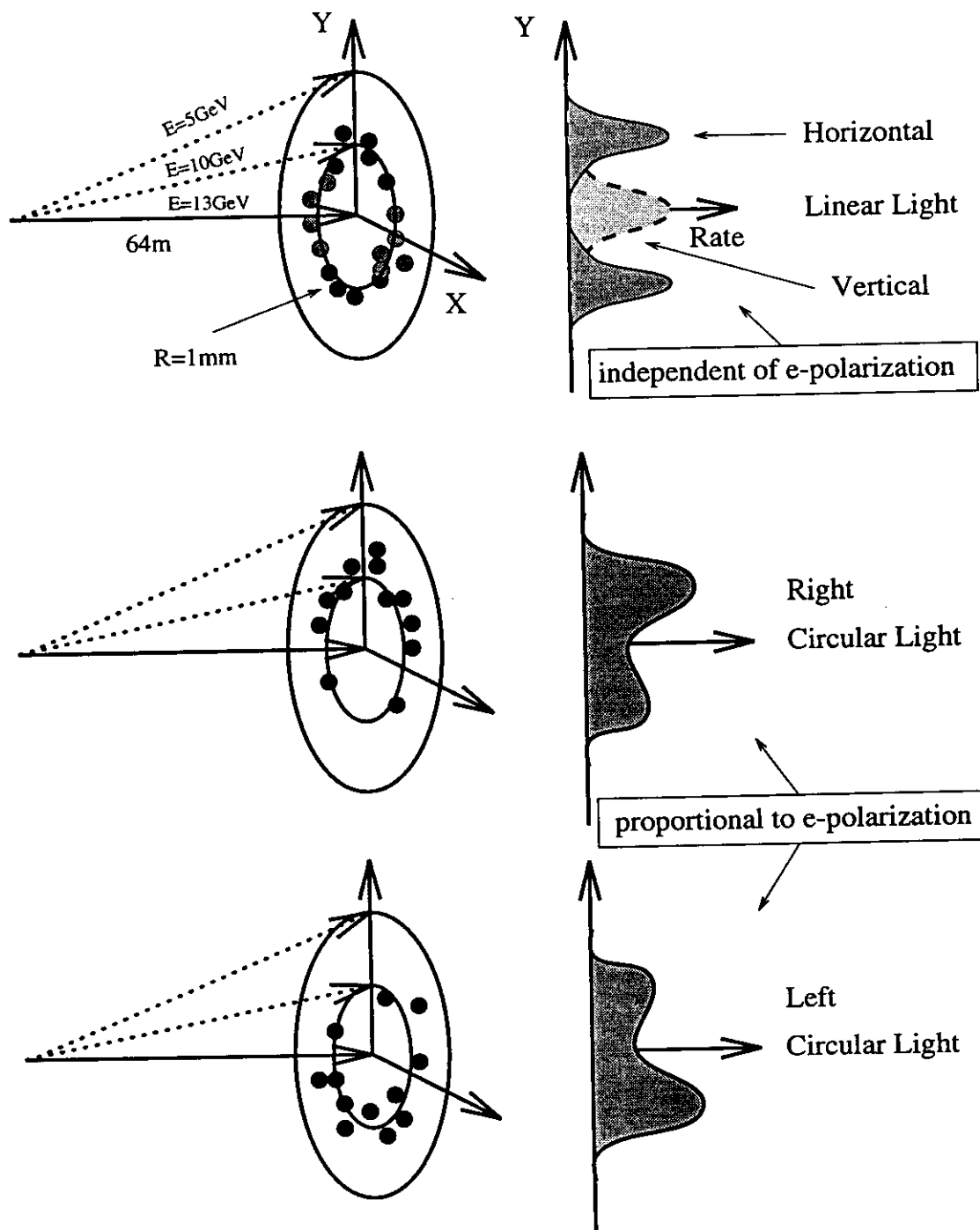
Figure 4.12: Backscattered Compton photons of a fixed energy arrive at the detector in a circle with defined radius. The detector measures the vertical projection of the Compton distribution. For linear light, the distribution is an even function of y and independent of the electron polarisation. For circular light the distribution has an odd component which is proportional to the transverse electron polarisation. This effect is used to measure the transverse polarisation.
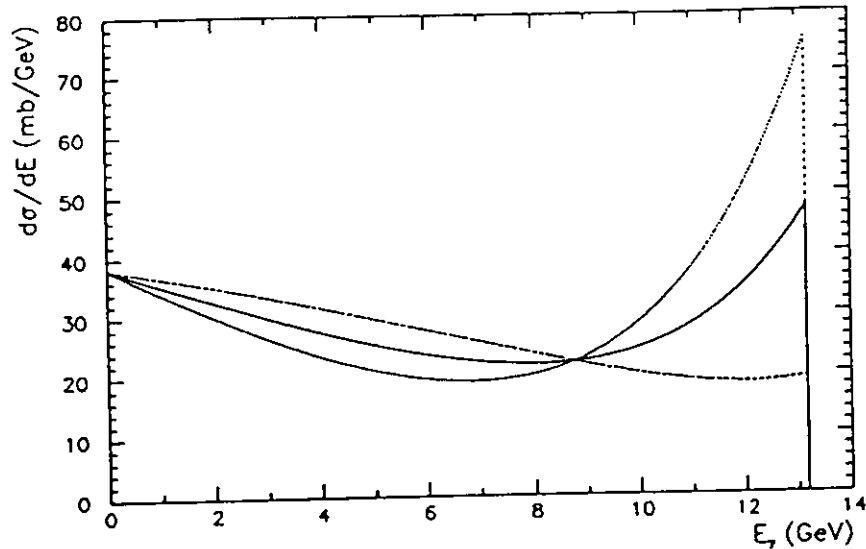
Figure 4.13: The energy spectrum of the backscattered Compton photons is shown for the case that the electrons are unpolarised (solid curve), longitudinally polarised with $S_3 P_z = 1$ (dashed curve) or longitudinally polarised with $S_3 P_z = -1$.

Figure 4.15 shows a scan of the laser beam over the electron beam by a horizontal movement of mirror M3. The backscattered Compton rate shows the combined width of the Gaussian profile of the laser (σ_γ) and the electron beam ($\sigma_{e,x}$). The measured width of $\sqrt{\sigma_{e,x}^2 + \sigma_\gamma^2} = 1$ mm agrees with the expectations. It is important to notice that the transverse position of the laser focus agrees for the two polarisation states with a precision of 2 ± 8 μm. In 1991 large shifts of 320 μm were observed which had the potential to cause false asymmetries. The reason for the shifts could be identified as interference pattern which were generated by the dielectric mirrors. A replacement of the mirrors and a slight change of the reflection angle was the solution to this problem.

Behind the IP, the laser beam hits a mirror attenuator at $0°$ incidence angle. The reflected power is dissipated into the beam line. The transmitted component is measured by a position sensitive diode after passing through a rotating Glan prism. The dependence of the intensity on the rotation angle is used for measuring the linear component of the laser light after the transport through the mirror system. Figure 4.16 shows the intensity as a function of the angle for circular and linear light. As the laser light does not contain an unpolarised component, the circular component of the light is calculated from the relation

$$P_{circ} = \sqrt{1 - P_{lin}^2} \qquad (4.36)$$

Multilayer dielectric mirrors with very high reflectivity have been used for the light transport into the tunnel. It turned out that the multilayer structure introduced large phase shifts on the light. These phase shifts could be compensated by entering elliptical light into the mirror system. The ellipticity and the orientation of the ellipse is adjusted by the voltage of the Pockels cell and by the orientation of a
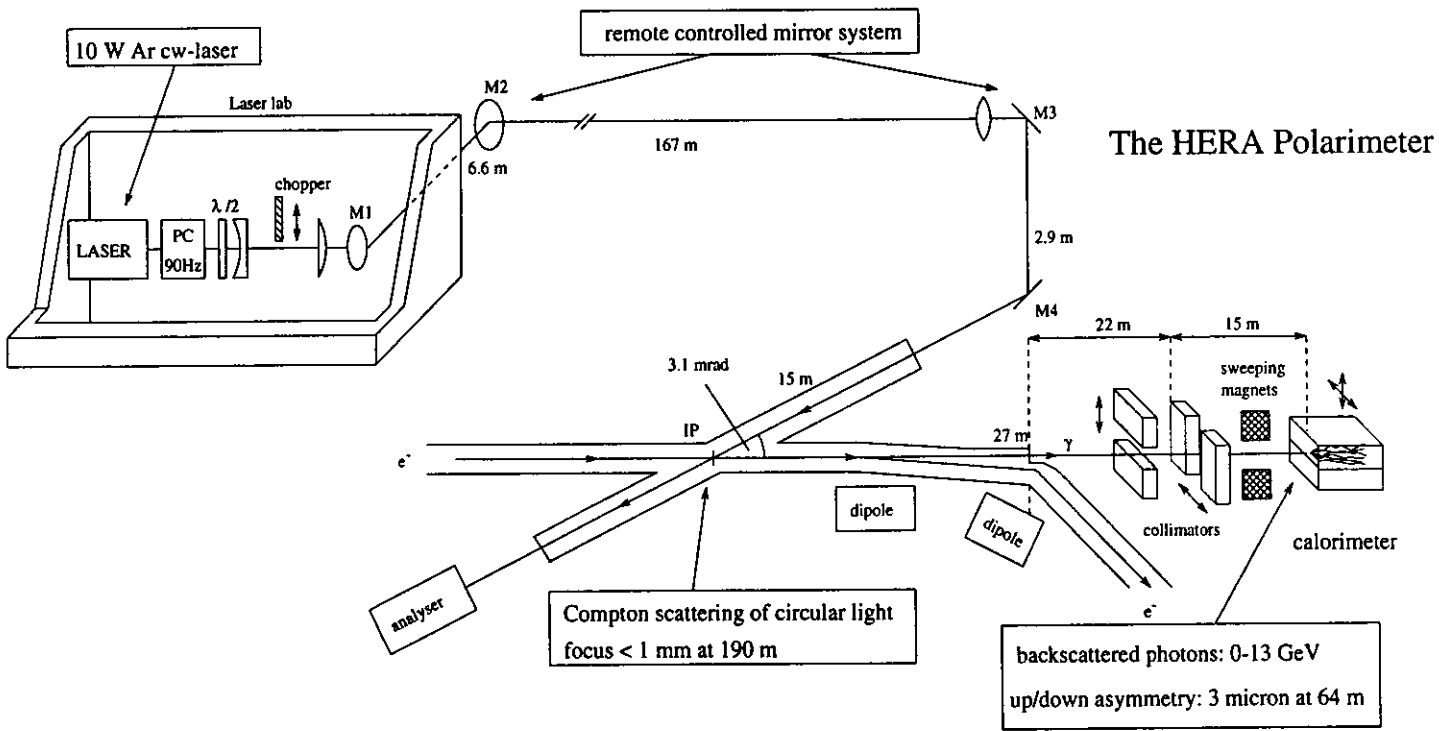
Figure 4.14: Layout of the HERA polarimeter. A laser beam is steered by a remote controlled mirror system into the HERA tunnel where it collides with the electron beam. Backscattered Compton photons are measured in a position sensitive calorimeter.
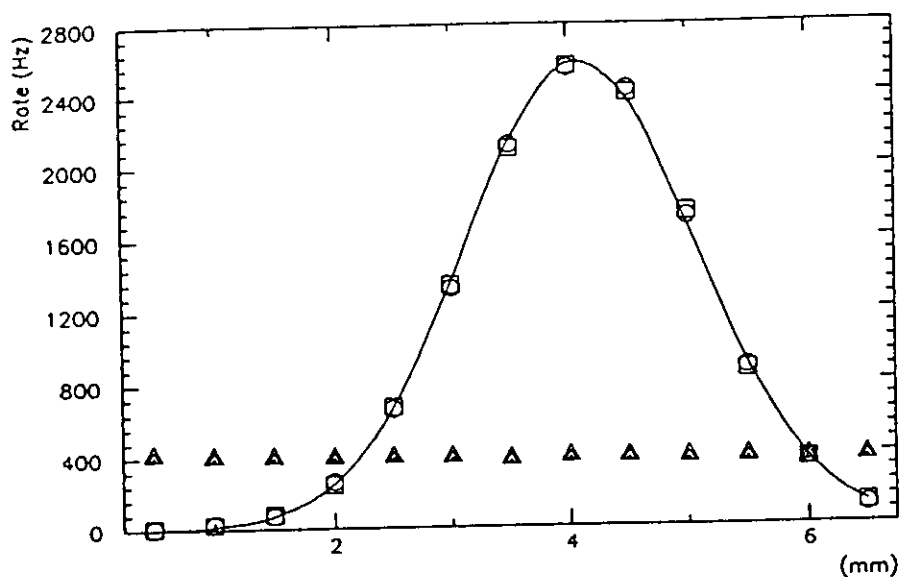
Figure 4.15: The combined width of the laser and electron beam are measured by scanning the laser beam across the electron beam. The circles (squares) show the Compton rate for left (right) polarised circular light. The RMS-width is 1 mm and the shift between the two polarisation states is compatible with zero ($2 \pm 8\mu$m). The triangles show the background rate which decreases slightly due to the decay of the electron current over the time of the scan.
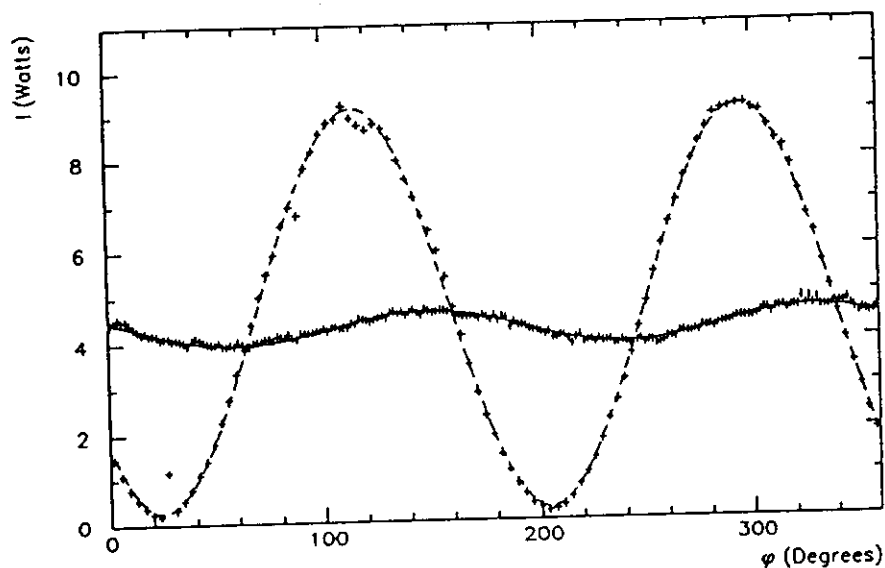
Figure 4.16: The degree of linear and circular polarisation is measured by analysing the intensity of the light versus the orientation of the Glan prism. The fits correspond to a linear polarisation of 94% for the case the Pockels cell is off (broken line) and 8.5% for the Pockels cell on (solid line). The remnant linear component of 8.5% corresponds to a degree of circular polarisation of 99.6%.

$\lambda/2$-plate which is mounted behind the Pockels cell. The light arriving at the IP is circular polarised with a degree of typically better than $P_{circ} = 99.5\%$. In 1995 the mirrors have been replaced by single-layer mirrors with less phase shifts but possibly to the cost of intensity losses.

4.7.3   The Calorimeter

The backscattered Compton photons pass a horizontal and a vertical collimator and two sweeping magnets to reduce the background. The photons are detected in a tungsten scintillator sandwich calorimeter which is split into an optically decoupled upper and lower half as shown in figure 4.17. Wavelength shifters on all four sides collect the light of the scintillators and feed it into four multipliers. The right and left channels are for calibration purposes. The vertical distance of the Compton photons to the centre of the calorimeter is obtained from the quantity η:

$$\eta = \frac{E_U - E_D}{E_U + E_D}.$$ (4.37)

$E_{U(D)}$ is the fraction of the shower energy in the upper (lower) part of the detector. To minimise smearing effects, the electron beam optics have been chosen to provide a virtual focus at the position of the calorimeter. The total energy $E = E_U + E_D$ can be extracted simultaneously with the position η of the Compton photons.

Figure 4.18 (a) shows the 2-dimensional distribution of the Compton photon positions η versus their energy E. The 'bell'-shape is due to the 2-body kinematics of Compton scattering and the non-linear behaviour between η and the vertical position. Figure 4.18 (b) shows the energy projection of the Compton spectrum and of the Bremsstrahlung background. The Bremsstrahlung background is small due to the good vacuum conditions at the IP (10^{-9} mbar). The rate of backscattered Compton photons is about 100 kHz for a 10 W laser beam and a 30 mA electron current.

The Compton edge at 13.8 GeV is used for the absolute calibration of the calorimeter. The upper and lower halves can be calibrated separately by moving each of the two halves separately into the Compton beam. For the polarisation measurement, the relative calibration of the upper and lower channels is critical. The following method is used which allows a very precise monitoring of the relative calibration: The right and left channels are used to obtain an independent measurement of the energy of the photons. The 'horizontal' energy $E_H = E_L + E_R$ can be compared with the 'vertical' energy $E_V = E_U + E_D$. The ratio

$$R = \frac{E_V}{E_H} = \frac{E_U + E_D}{E_L + E_R}$$ (4.38)

should be $R = 1$ in an ideal detector. This ratio can be plotted as function of $\eta = (E_U - E_D)/(E_U + E_D)$, which corresponds to the vertical impact position of the photons. Due to the different sampling and attenuation of the light in the vertical compared to the horizontal channels, the ratio becomes slightly dependent of η. For symmetry reasons, the function has to be symmetric around $\eta = 0$, i.e. $dR/d\eta(0) =$
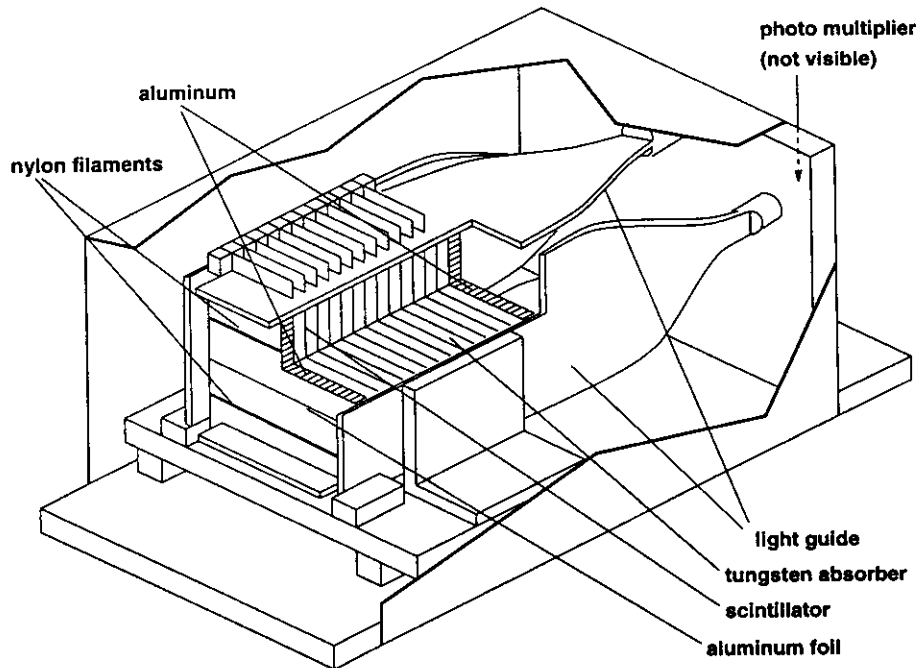
Figure 4.17: A cutaway, perspective view of the tungsten scintillator calorimeter is shown. The calorimeter has an upper and a lower half which are optically decoupled. The scintillating light is collected by wavelength shifters on all four sides. The asymmetry of the shower development in the upper and lower half is used to measure the vertical projection of the impact point of the photon.
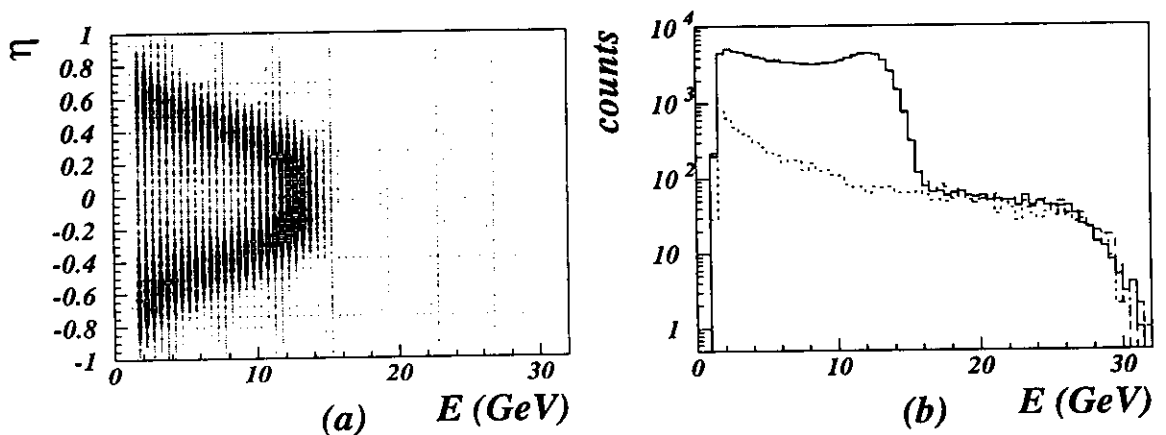
Figure 4.18: The two-dimensional distribution (position η versus energy) of the backscattered Compton photons (a) and its one-dimensional energy projection (b) for the two cases that the laser is on (full line) or off (broken line). The Bremsstrahlung background is suppressed by more then a factor of 10 compared to the Compton rate. The Compton edge at 14 GeV is used for the energy calibration of the calorimeter.

0. The relative calibration of the E_U and E_D is done by fitting a parabola to $R(\eta)$ and then varying the calibration constants until $R(0) = 1$ and $dR/d\eta(0) = 0$. This method is insensitive to the calibration of the horizontal channels and also insensitive to the vertical and horizontal positioning of the calorimeter in respect to the Compton beam. The statistical fluctuations in the ratio are small. A relative calibration with an accuracy of 0.2% can be done within a few minutes. Figure 4.19 shows an example of a calibration fit. A measurement of the calibration constants is repeated every few hours during data taking. The day to day stability is typically better than 0.5%.
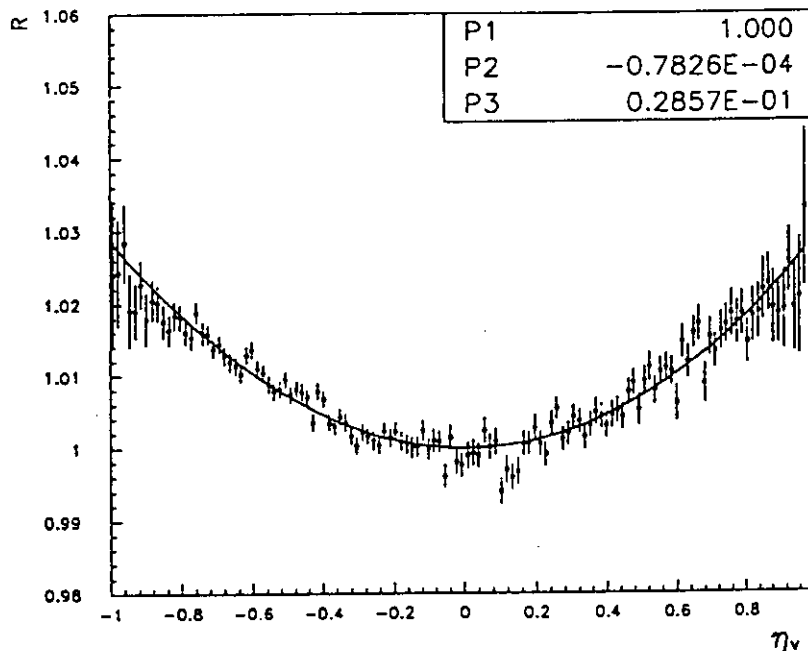
Figure 4.19: The ratio R of the 'vertical energy' divided by the 'horizontal energy' is plotted as function of η. The calorimeter is properly calibrated as the fit $R(\eta) = P_1 + P_2\eta + P_3\eta^2$ gives $P_1 = 1$ and $P_2 = 0$.

4.7.4   Data Acquisition and Experimental Control

The single photon method requires a fast data acquisition system that is shortly described in the following.

Figure 4.20 shows an overview of the DAQ system. The heart of the online system is a VME card with four 1 MHz 12 bit ADC's and a digital signal processor (DSP) [114]. The four PMT signals are integrated, digitised and processed with a speed of up to 100 kHz. 2-dimensional histograms, e.g. η versus E and various calibration histograms are filled in real time. The system is triggered either by the discriminated PMT signals alone or in conjunction with the electron bunch timing. Single electron bunches can be selected.
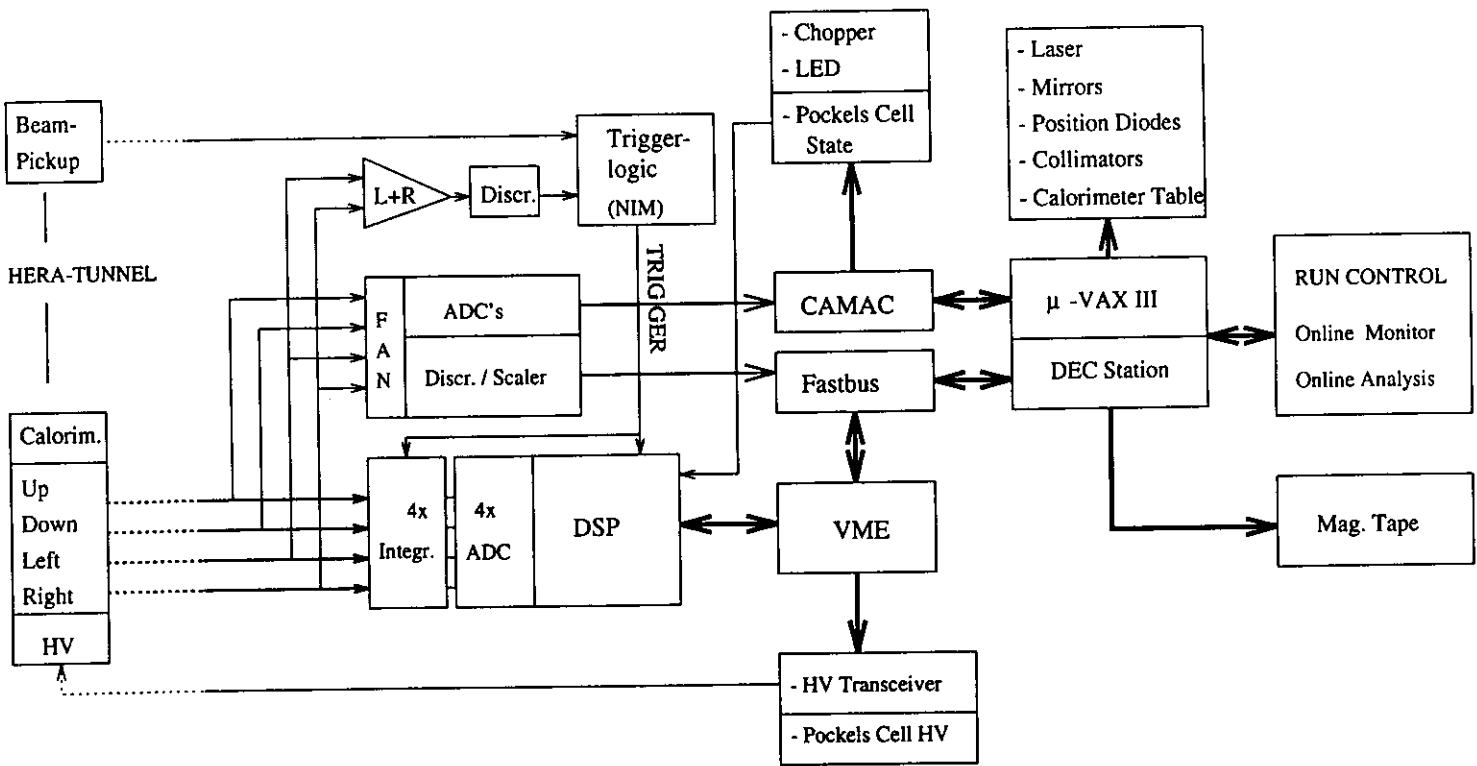
Figure 4.20: An overview of the polarimeter DAQ system.

Various feed-back systems are programmed that allow a fully automatic operation of the polarimeter. In the following the main features of the 'auto-pilot' polarimeter software are outlined:

- The laser beam chopper is opened and closed once per minute for 40:20 seconds. The voltage of the Pockels cell is flipped with about 90 Hz. The 2-dimensional histograms from the DSP processor and the scaler information are analysed in real time once per minute and also stored on tape for off-line analysis. The real-time analysis includes:

  - The dead time corrected Compton rates for right and left polarised light and the Bremsstrahlung background rate.

  - The background corrected energy spectra and η-asymmetries for various energy bins, separately for right and left polarised light and for the Bremsstrahlung background.

  - The specific luminosity is calculated from the Compton rate, the laser intensity and the electron current. The vacuum pressure is calculated from the Bremsstrahlung rate.

  - The position and the size of the Compton spot on the calorimeter is calculated from high energy Compton photons. Photons near the Compton edge arrive in a cone with a very small opening angle. The information is needed to adjust the calorimeter position and to detect problems with the divergence of the electron or Compton beam.

  - Finally, the electron polarisation and the linear component of the laser light are extracted from the η-asymmetries. The method will be described in the next chapter.

- The program optionally starts new runs after certain periods of time (e.g. every 30 min). The polarisation values are stored on disk independently if there is a run going on or not. The data are available on an INTERNET server for distribution to the three HERA experiments. All important values and error messages appear on control monitors. A real-time plot of polarisation versus time is displayed in the HERA main control room for polarisation optimisation. The time between the data-taking and the analysis and display of the polarisation result is less than one minute.

- The 'auto pilot' regularly checks the specific luminosity. If it decreases below a certain threshold, the laser beam is re-centred automatically onto the centre of the e^--beam. The centre of the electron beam is found by a small horizontal scan of mirror M3. The program calculates the Compton rate versus the reflection angle, fits a Gaussian to the beam profile and determines the optimal mirror position from the centre of the Gauss fit.

- Due to temperature drifts in the laser, the position of the laser beam may change after the 180 m transport tube. A program reads out the position sensitive diode behind M3. If the position of the laser spot on mirror M3 is

outside a defined margin, the program adjusts the mirror M2 and centres the laser beam again on M3.

- The relative position of the Compton edge photons on the calorimeter is monitored continuously. It is important that the photons hit the centre of the calorimeter, as the spatial resolution of the calorimeter depends on the vertical position. Due to tiny drifts of the electron orbit, the position usually fluctuates on the order of $10 - 50$ μm over one hour. If the position is outside a margin of about 70 μm, a feed-back loop is started which moves the calorimeter to the centre of the Compton beam.

- When the electron beam is dumped, the collimators automatically close and are opened only after a new beam is injected and ramped to the nominal energy.

- After a beam dump of HERA, the pedestals of the PMT's are measured and passed to the analysis programs.

- The polarisation of the laser light in the tunnel is measured by the analyser. The Pockels cell voltage can be scanned on request to determine semi-automatically the voltage with the best circular polarisation.

- Calibration data which were taken during the last fill are analysed. A program calculates new PMT voltages to equalise the gains of the four multipliers. The new voltages can be loaded on request.

The operation of the 'auto pilot' is usually stable over many fills. It allows for a continuous measurement of polarisation with minimal manpower requirements.

4.7.5 Analysis of the Polarimeter Data

The basic experimental information for the extraction of the electron polarisation is contained in the 2-dimensional η versus E histograms as shown in figure 4.18 (a). A Monte Carlo program [111] has been written that calculates the Compton distributions from the known cross section and from some additional input parametrisations concerning the electron beam divergence and the calorimeter response. Figure 4.21 shows the measured η distributions in comparison with the simulated ones for several energy bins. The model represents the measured distributions with a reasonable precision. As shown in chapter 4.7.1, the vertical polarisation of the electron beam leads to an up-down asymmetry of the backscattered Compton rate. By flipping the helicity of the light, the asymmetry $A(\eta, E)$ of the $\eta - E$-distributions can be measured with small systematic errors:

$$A(\eta, E) = \frac{N_L(\eta, E) - N_R(\eta, E)}{N_L(\eta, E) + N_R(\eta, E)}. \tag{4.39}$$

From equation (4.26) follows that for a fixed energy the asymmetry $A(\eta, E)$ has an even component which is proportional to the linear component of the light and it has
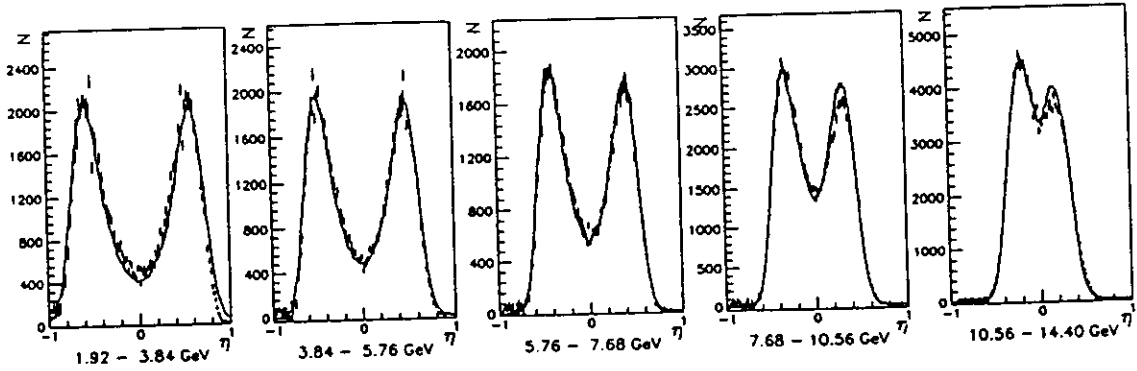
Figure 4.21: The measured, background subtracted distributions $dN/d\eta$ of the backscattered photons are shown in 5 energy intervals. The endpoints of the intervals are indicated below the figures. The width of the distribution decreases with energy as the opening angle of the cone of backscattered Compton photons decreases. The slight asymmetry comes from the fact that the calorimeter is not perfectly centred on the Compton beam. The overlaid curves show the Monte Carlo fits. The calculations are in reasonable agreement with the measurements.

an odd component which is proportional to the product of the circular component of the light and the vertical polarisation of the electron beam. Figure 4.22 shows the measured asymmetry for five different energy bins. These separate histograms are all well described by a single Monte Carlo fit. The result of the fit is that at this time the electron polarisation was $P_e = 54.8 \pm 0.7\%$ and the linear component of the light was $\Delta S_1 = 8.8 \pm 0.4\%$. The systematic error of the Monte Carlo extraction is of the order of $\Delta P/P = 10\%$ and can be improved by a more detailed modelling of the experiment. Figure 4.23 shows the distributions and asymmetries for the case that the Pockels cell sends horizontal and vertical polarised linear light into the tunnel. The asymmetry curve is now an even function and can be used to determine the degree of linear light polarisation. As the degree of linear light in the tunnel can be measured independently by the analyser, this Compton asymmetry can be used as cross-check for the precision of the polarimeter.

As the asymmetry is an odd function of η in the case of circular light, an alternative method to determine the electron polarisation is to measure the shift of the mean values of the η-distributions:

$$\Delta \eta = \frac{\langle \eta \rangle_L - \langle \eta \rangle_R}{2} = \Pi(E)P_e\frac{\Delta P_{circ}}{2} \qquad (4.40)$$

with $\langle \eta \rangle_{L(R)}$ being the mean value of the η distribution for left (right) polarised light and $\Delta P_{circ} \approx 2$ corresponds to the flip of circular polarisation. The analysing power $\Pi(E)$ depends on the energy of the backscattered photons. Figure 4.24 shows that the measured $\Pi(E)$ function is in good agreement with the predicted shape of the distribution with a fitted polarisation of $P_e = 53\%$. For the on-line analysis
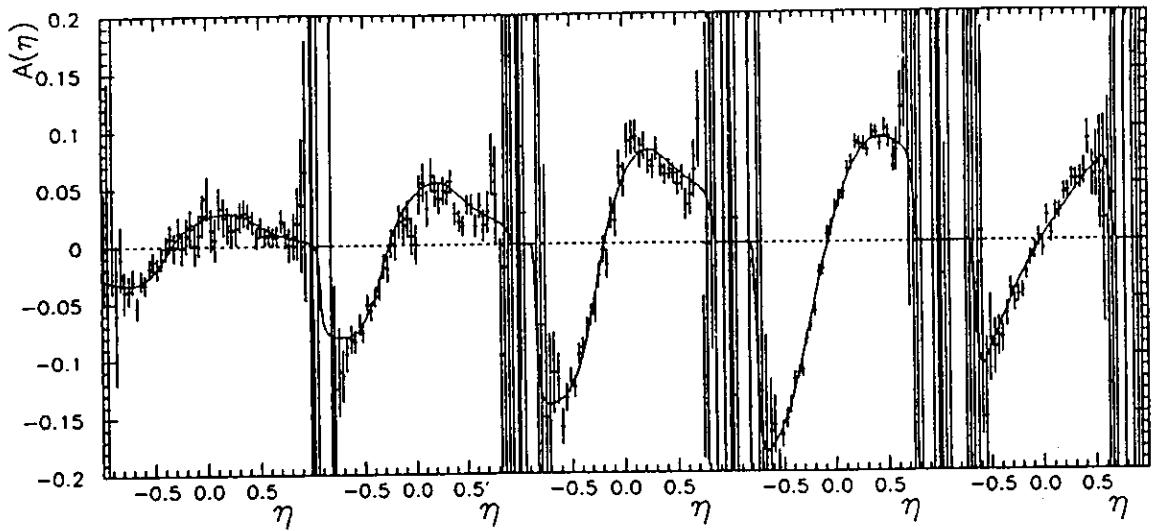
Figure 4.22: The asymmetries $A(\eta)$ are shown for the same energy intervals as in the previous figure. A simultaneous fit gives an electron polarisation of $P_e = 54.8 \pm 0.7\%$ and a linear component of the light of $\Delta S_1 = 8.8 \pm 0.4\%$.

of polarisation, the shift of means is calculated for an energy range of $E = 5.4 - 11.7$ GeV and $\eta = -0.875$ to $+0.875$. The cut in E selects the region of high analysing power and the cut in η reduces the influence of background. The analysing power for this setting is $\Pi = 0.045$. This means: in order to detect a polarisation of $P_e = 1\%$, a shift of the mean values of $\Delta\eta = 0.00045$ has to be observed. Figure 4.25 shows an example for an on-line screen which shows the measured polarisation, the Compton and Bremsstrahlung rates, the position of the Compton beam on the calorimeter and some further information which is useful for a successful operation of the polarimeter. The decay of the rates is due to the lifetime of the beam.

Besides the transverse, also the longitudinal component of the electron polarisation can be measured with the HERA polarimeter. The longitudinal component is derived from the asymmetries of the energy spectrum for right and left circular light. It was always measured to be $P_e^L \leq 1\%$ at HERA which is in agreement with the expectation. Due to spin diffusion and to the precession of the spins around the vertical axis in the bending magnets, a large longitudinal component would be immediately destroyed in a storage ring.

4.7.6 The Rise-Time Calibration of the Polarimeter

The current estimate of the systematic error from Monte Carlo simulations is of the order of $\Delta P_e/P_e \sim 0.1$. This error can be reduced significantly by a more detailed simulation and by a cross check of the Monte Carlo response with the known Compton asymmetries from horizontally versus vertically polarised linear light.

A completely independent and better method to reduce the systematic uncer-
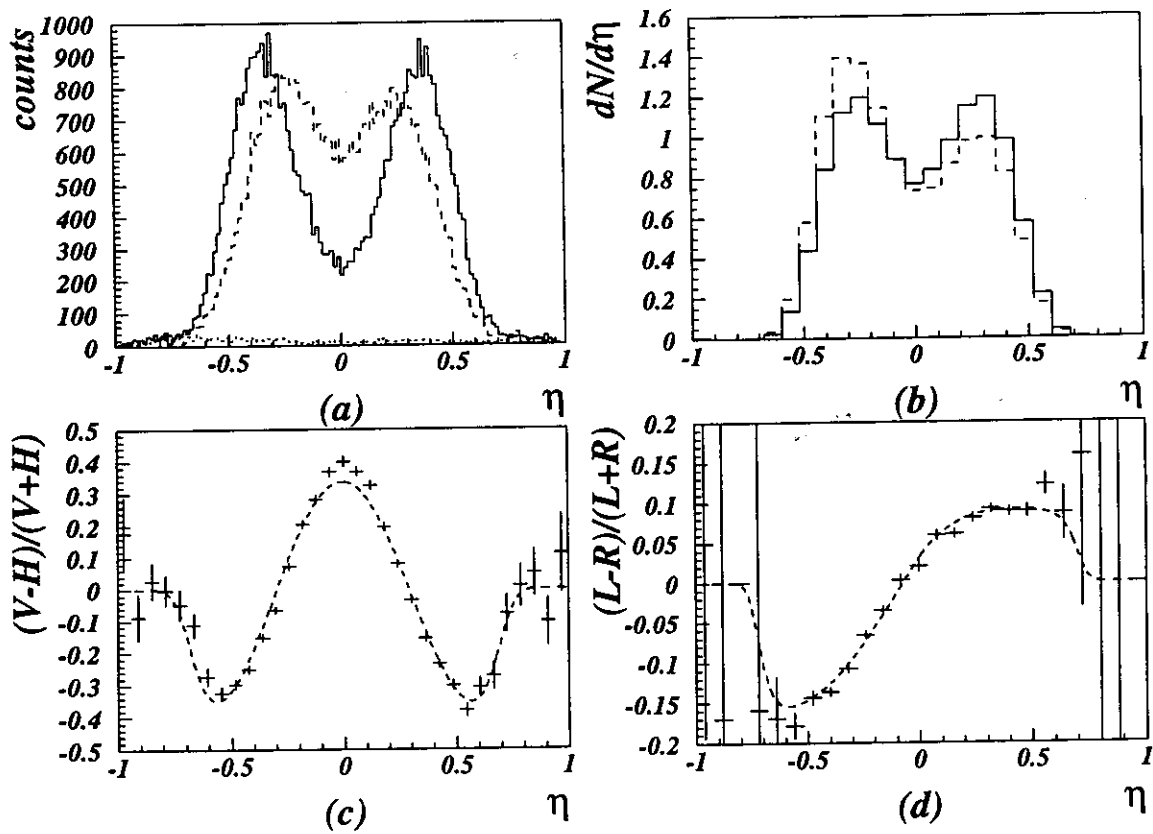
Figure 4.23: The η-distributions for Compton scattering off horizontal and vertical linear (a) polarised light and right and left circular (b) polarised light and its asymmetries (c) and (d). The lower plots are derived from the upper distributions. The even component of the asymmetry curve is proportional to the linear light asymmetry (c) and the odd one is proportional to the product of circular light polarisation and electron polarisation (d).
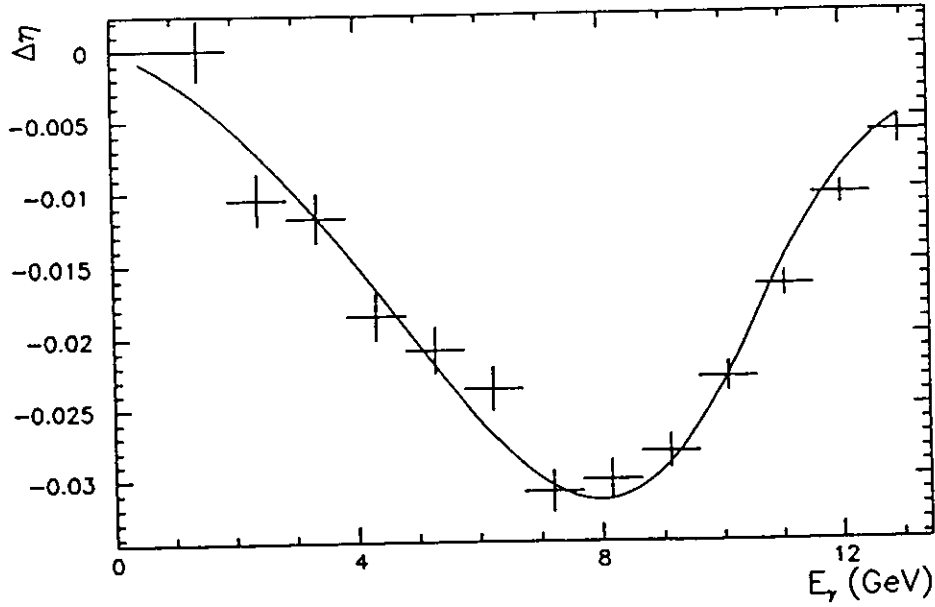
Figure 4.24: The shift of the means $\Delta\eta$ plotted as function of the energy of the backscattered photons. The shape agrees well with the predicted analysing power. From the fit (solid curve) an polarisation value of $P_e = 53\%$ has been extracted.

tainties is the calibration of the polarimeter scale using the rise-time behaviour of the Sokolov-Ternov effect. According to equation (4.15) the slope of the rise time at $P = 0$ is a constant of the storage ring which can be calculated with high precision. The polarimeter can be calibrated by measuring this slope. If $P_m(t)$ is the measured polarisation and k is the calibration constant of the polarimeter, the exact formula for the polarisation rise is

$$P_m(t) = kP(t) = kP_\infty \cdot \left(1 - e^{-(t-t_0)/\tau}\right) \tag{4.41}$$

with the boundary condition that

$$\frac{P_\infty}{\tau} = C. \tag{4.42}$$

C is a constant which can be calculated by integrating certain machine parameters along the closed orbit. The integration is independent of depolarisation effects and can be extracted from the equations (4.21) and (4.22):

$$C = \frac{r_e \hbar c^2}{m_e} \frac{\gamma^5}{L} \oint |\rho|^{-3}(\vec{b}\vec{n}_0)\, ds. \tag{4.43}$$

Equation (4.41) now becomes

$$P_m(t) = kP_\infty \cdot \left(1 - e^{-(t-t_0)\frac{C}{P_\infty}}\right). \tag{4.44}$$

If the polarisation rise is known to start with $P = 0$ at a defined time $t = t_0$, this formula is a two parameter fit for the asymptotic value of polarisation P_∞ and for
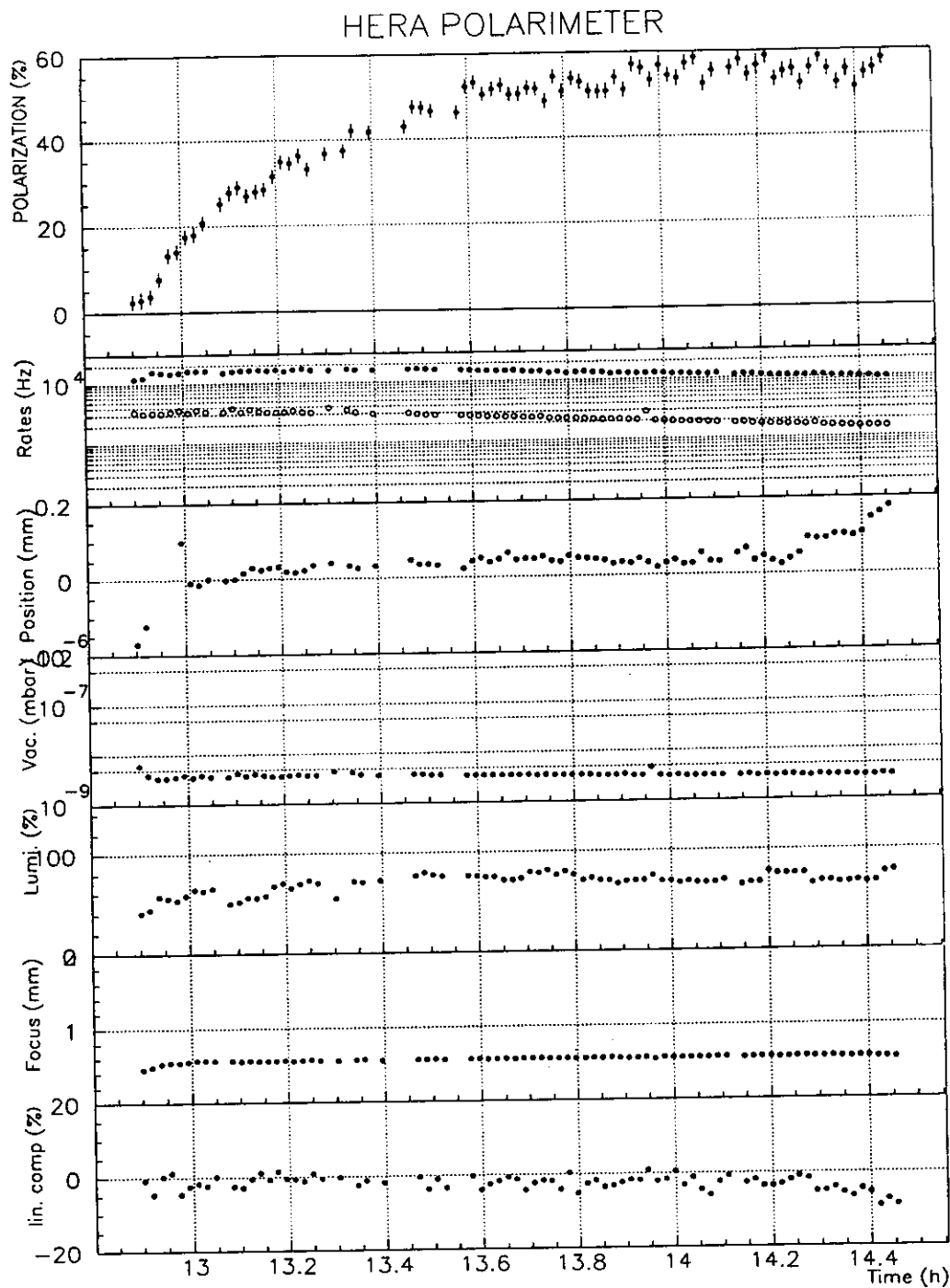
Figure 4.25: The on-line monitor summarises the relevant information of the polarimeter. It shows the electron polarisation, the Compton and background rates, the position of the Compton beam on the calorimeter, the vacuum pressure calculated from the Bremsstrahlung rate, the specific luminosity calculated from the Compton rate, the beam current and the laser power, the spot size of the Compton beam and the linear component of the light calculated from the asymmetries of the η distributions.

the unknown calibration constant k of the polarimeter. If the initial polarisation and/or the starting time of the polarisation rise is unknown the formula becomes a three parameter fit. From the Taylor expansion around $t = t_0$ follows that the initial slope determines the calibration constant k whereas the polarisation value at the end of the rise time curve $P_m(t \to \infty) \approx kP_\infty$ can not be used to obtain information about the calibration constant.

Figure 4.26 shows the first results of the rise time studies which were taken in 1993 [100]. The measured values and the values extracted from the rise time agree within their statistical and systematic errors. The standard deviation of the points from the fit is $\sigma = 2\%$. At the end of the running period of 1994 about 14 rise time curves have
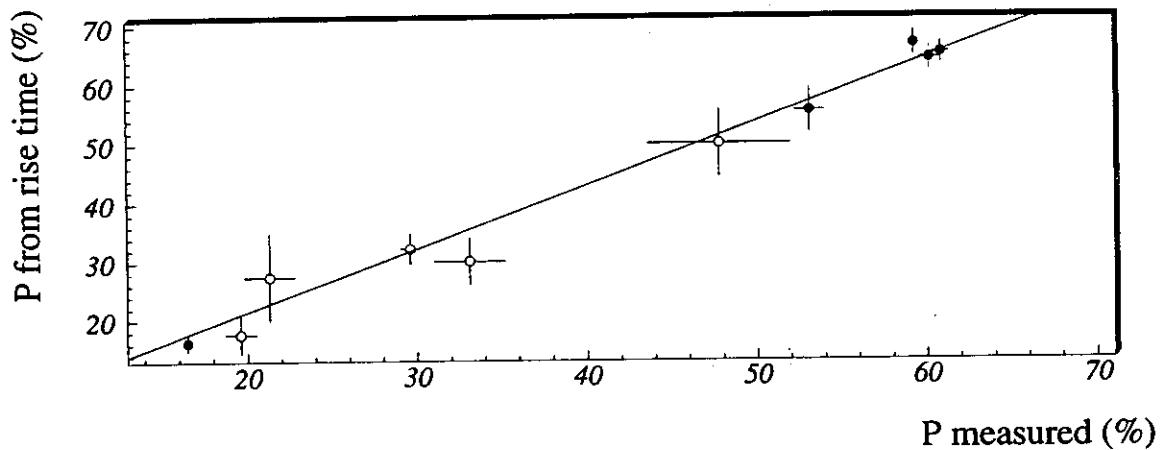
Figure 4.26: Comparison of the polarisation extracted from the rise time constant compared to the measured value in the polarimeter. The two values agree within the statistical and systematic uncertainties.

been measured. Some of these curves show obvious deviations from the exponential behaviour which can be explained by variations of the machine conditions during the time of the polarisation rise. According to a study from Oelwein [109] the calibration constants which are extracted from the rise time curves show fluctuations of 8%. The analysis is still proceeding.

To improve the knowledge of the systematic precision of the polarimeter, rise time studies should to be continued. By sticking to the following rules, a precise determination of the calibration constant should be possible:

- Before the rise starts, the polarisation of HERA should be destroyed completely by rf-depolarisation. That the polarisation is zero has to be verified by successively increasing the rf-power and observing saturation of the depolarisation.

- It has to be checked that the *measured* polarisation P_m is also zero, i.e. that the polarimeter shows no false asymmetries. The measured polarisation during rf-depolarisation is typically well below 1%.

- The rf-depolarisation has to be switched off abruptly at a well defined time t_0. The knowledge of the time with $P = 0$ reduces the number of free parameters in the rise time fit.

- During the polarisation rise, the machine and the polarimeter parameters have to stay absolutely constant. Any change of the depolarising effects in HERA makes the rise time curve useless. The success of the calibration can be studied by a statistical analysis of the (Gaussian) distribution of k factors from many rise time curves.

- The stability of HERA and of the polarimeter can be measured directly in the following way: the depolariser and the polarimeter both allow to select certain bunches. Half of the bunches in HERA should be depolarised and half of them stay at the asymptotic value of polarisation. During the polarisation rise of the depolarised bunches, the stability of the asymptotic polarisation of the other bunches can now be observed. This method is used successfully at LEP [106].

- The spin rotators should be switched off during the calibration of the polarimeter as they introduce an uncertainty of the order of a few percent (according to [115]) in the theoretical rise time constant C.

4.7.7 The Longitudinal Polarimeter

Due to the importance of the polarisation measurements for HERMES, a second polarimeter will be build which directly measures the longitudinal polarisation of the electron beam in the section between the spin rotators [116]. Like the transverse polarimeter, it makes use of asymmetries in the Compton scattering of a circular polarised laser beam off a polarised electron beam. While the transverse electron polarisation produces a small spatial asymmetry in the backscattered photon distributions, the longitudinal electron polarisation produces an asymmetry in the energy spectrum of the Compton photons as shown in figure 4.13. An energy asymmetry of 0.00184 correspond to 1% of longitudinal polarisation.

The set-up of the longitudinal polarimeter will be very similar to the one of the transverse polarimeter. A laser beam, which is switched between the two states of circular polarisation by a Pockels cell, is sent from the HERA EAST hall by means of a computer controlled mirror system down to the HERA beam pipe. It hits the electron beam about 53 m downstream the HERMES gas target with a crossing angle of 6 mrad. The backscattered photons are measured in a calorimeter which consists of an array of four 2.2×2.2 cm^2 NaBi(WO$_4$) crystals. It has an energy resolution of $\Delta E/E = 10\%/\sqrt{E/\text{GeV}}$ and is very radiation hard ($7 \cdot 10^7$ rad).

Unfortunately, the Bremsstrahlung background in this area downstream the HERMES target is expected to be so high that the 'single-photon' method will not work. Instead the 'multi-photon' method will be applied by using a pulsed YAG laser at 532 nm. About $10^3 - 10^4$ Compton photons will be detected per shot. The total energy deposit depends on the polarisation of the electron beam, the intensity

and focussing of the laser beam, the time structure of the laser pulse and on the charge of the bunch which was hit. By averaging over many pulses and over all ($\sim$ 200) bunches, the average polarisation of the HERA beam can be obtained. The estimated systematic error of the measurement is about 2–3%. The precision of the rise time calibration of the longitudinal polarimeter is limited by the theoretical understanding of the rise time constant with spin rotators. Unlike the transverse polarimeter, the longitudinal polarimeter cannot be calibrated with the rotators switched off.

4.8 Polarised Protons at HERA

There is certainly a strong physics motivation at HERA not only to have a polarised electron beam but also a polarised proton beam (e.g. [49]). In this case polarised spin structure functions could be measured at HERA collider energies. Additionally, if the HERMES polarised gas target would be moved into the proton beam, double polarised $\vec{p}\vec{p}$ and $\vec{p}\vec{n}$ scattering could be measured. The detector is constructed in a way that it can be rotated by 180°.

The basic problem with stored polarised proton beams is that no Sokolov-Ternov effect exists to keep the polarisation high. The only feasible way to have a polarised beam is to inject the beam polarised and make sure that it is conserved during ramping and storing. Up to now it is not clear if polarised protons can be realized at HERA and studies are going on. There is a full list of tasks which have to be solved to have polarised protons in HERA:

- a polarised H source,

- acceleration of polarised protons in the LINAC,

- acceleration and storage of protons in DESY III (50 MeV to 7.5 GeV),

- acceleration and storage of protons in PETRA (7.5 GeV to 40 GeV),

- acceleration and storage of protons in HERA (40 GeV to 820 GeV) and

- proton spin rotators in HERA.

As there are depolarising resonances at energy steps of 520 MeV there has to be special care taken in DESY III and PETRA. Possibly (partial) Siberian snakes have to be installed. Siberian snakes are devices similar to spin rotators. They rotate the polarisation by 180° at every turn and cancel certain types of depolarising resonances because the kick that the polarisation gets in the first turn is compensated in the following turn. From the experiences in the AGS (Brookhaven) one would conclude that it should in principle be possible to get polarised protons injected into HERA, however detailed studies would be necessary to find workable technical solutions.

An acceleration of a polarised proton beam to 820 GeV without Siberian snakes is not feasible, as one would have to cross a few thousand resonances and then store the beam at the immense high spin tune of about 1580. Also with Siberian snakes

it seems to be very difficult to keep resonances under control. One could however use lower proton energies to reduce the problem of depolarisation. Actually lower energies at HERA have experimentally advantages over high energies due to the higher cross section and higher analysing power of the asymmetry [117]. As, however, the lifetime of the proton beam decreases with decreasing energy, the beam energy must not be too low.

A completely different approach is to polarise the proton beam after the beam is ramped by applying longitudinal Stern-Gerlach kicks [118]. This method is however difficult to realise due to the smallness of the polarisation dependent kicks.

Two other problems to overcome are the spin rotator and the beam-beam induced depolarisation of the proton beam. What certainly would help is to polarise deuterons instead of protons as the spin tune of the deuterons for the same energy is lower by a factor of 25 due to the smaller gyro-magnetic anomaly. The spacing of the depolarising resonances is 13.2 GeV in the case of deuterons. To summarise, there are immense technical and financial efforts needed to have a chance of realizing a polarised proton beam at HERA.

Chapter 5

The Polarised Internal Gas Target

An important factor for a precision experiment is a pure target with a high degree of polarisation. There is no technology known which would allow one to polarise the nucleons of a pure solid material to a high degree and use them as a target in an electron or muon beam. The only working solution uses mixed materials like ammonium or butanol in which the hydrogen atoms are polarised whereas the other nucleons stay unpolarised. There are however methods to polarise *pure gases* of H, D, ^3He or other materials to a high degree without any dilution by other atoms. In addition, the sign of the polarisation can be flipped very rapidly. That allows the measurement of asymmetries with small instrumental uncertainties.

The polarised internal target system consists of a source of polarised atoms, a storage cell, a magnetic holding field and a polarimeter which measures the degree of target polarisation.

5.1 Polarised Gas Sources

Two different types of polarised gas sources will be used at HERMES: an atomic beam source for hydrogen and deuterium and an optically pumped source for ^3He. Additionally there are several R&D programs running with the aim to build a laser driven source for hydrogen and deuterium which could have a much increased intensity compared to the atomic beam source.

Atomic Beam Source

The presently most intense polarised atomic beam source (ABS) has been built at Heidelberg [119]. A sketch of the source is shown in figure 5.1. It is based on the Stern-Gerlach separation of atomic hydrogen or deuterium and functions as follows. Molecular hydrogen (deuterium) is dissociated by rf discharge into H (D) atoms and a beam is formed by a cooled nozzle and skimmers. The atomic beam is fed through a system of sextupole magnets. Depending on the state of the electron spin of the atom, the beam particle is focussed or defocussed. For efficient separation of the spin states, strong permanent magnets with pole tip fields of 1.5 T are used.
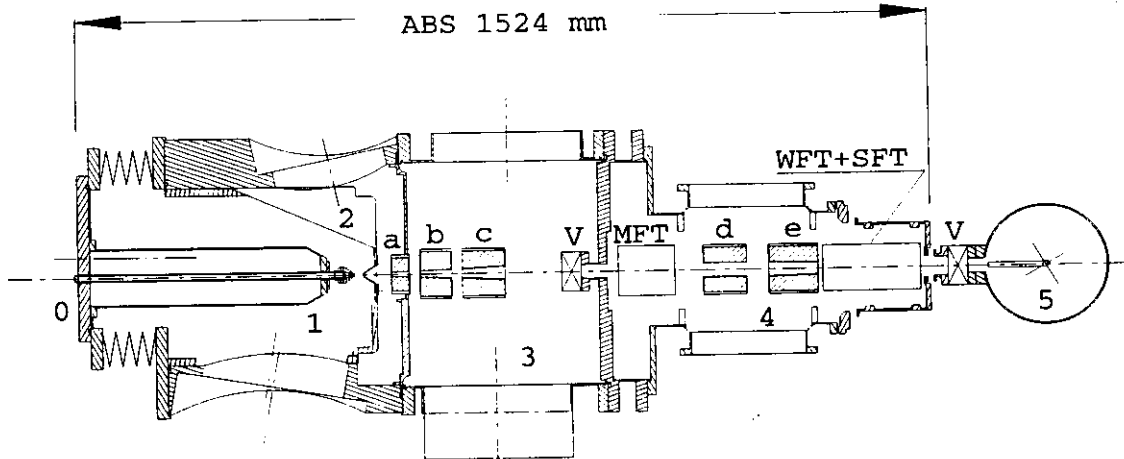
Figure 5.1: Sketch of the polarised atomic beam source for HERMES. The dissociater is in chamber 1. A beam is formed and focussed by the sextupole magnets a-e. MFT, WFT and SFT denote medium, weak and strong field transitions. The atomic beam is injected in the storage cell in chamber 5. The chambers can be separated by valves (V).

To polarise the spin of the atomic nucleus, several hyperfine transitions are induced by rf fields between the two stages of sextupole magnets and at the end of the sextupole system. A strong magnetic field of 0.35 T for the longitudinal and 0.15 T for the transverse polarisation will be applied over the target. The system can select single hyperfine states of hydrogen, however to double the intensity, the HERMES source will select two hyperfine states with opposite electron spin but parallel proton spin. In the case of deuterium the source is able to select all possible states of nuclear vector and tensor polarisation.

The source produces an atomic beam with an intensity of $6 \cdot 10^{16}$ atoms/sec in two hyperfine states and with a polarisation of better than 90% as well for hydrogen as for deuterium. The sign of polarisation can be flipped within milliseconds by a change of the rf frequency.

^3He Source

The ^3He source [120] is based on a completely different physical principle. By electrical discharge a small fraction of helium atoms in a pumping cell is converted into a meta-stable state (2^3S_1). Circularly polarised laser light of high intensity incident on the meta-stable atoms excites transitions in the atoms ($2^3S_1 \to 2^3P_0$) which decay through photon emission and thus transfers angular momentum to the meta-stable atoms. The meta-stable atoms become polarised. Meta-stability exchange collisions that do not alter the nuclear spin transfer the polarisation to the ground state atoms.

The ^3He source is able to deliver high intensities (e.g. $2 \cdot 10^{17}$ atoms/s) however the polarisation is currently only on the order of 50–60%. The sign of the polarisation is flipped by switching the polarisation of the laser light using a Pockels cell. It takes about 20 s until the polarisation in the spin-exchange cell has reached its equilibrium.

A faster way to flip the spins is achieved by turning the orientation of the holding field. By this method, polarisation can be switched within less than 1 s. As the atoms stay a long time in the pumping cell, a very homogeneous magnetic holding field is needed to prevent depolarisation effects by field gradients. The required homogeneity for the HERMES field is better than $|\nabla B_\perp|^2/|B|^2 < 0.01/m^2$. For a field of $B = 10$ G, this means a gradient as small as $|dB/dx| < 10$ mG/cm. The ^3He source has been successfully operated as a storage cell target at the medium energy proton storage ring at IUCF [121].

Laser Driven Source for H and D

A laser driven source (LDS) for H and D [122] is based on the following principle. A glass cell is filled with hydrogen (or deuterium) gas with an admixture of about 0.5% potassium. An Ar^+ pumped Ti-sapphire laser system optically pumps the potassium vapour with polarised light. The alkali atoms become polarised. Via spin-exchange collisions, the polarisation is transferred to the hydrogen or deuterium atoms.

A polarisation of 40 to 60% at an intensity of 10^{18} atoms/s has been achieved in a laser-driven source at Argonne National Lab. A disadvantage of the LDS compared to the atomic beam source is the admixture of high Z atoms which lead to a large dilution factor. Methods to improve the performance are currently being investigated.

5.2 The Storage Cell Technique

One inherent disadvantage of gas targets compared to solid targets is obviously its small density. By using the high current beam in a storage ring compared to an external beam, luminosity can be improved significantly. A free gas jet or a cluster jet that crosses the stored beam gives sufficient luminosity in a strong interacting hadron beam. For an experiment in a lepton beam the achievable densities are however still far too small to obtain high precision polarisation data.

This problem has been overcome with the storage cell technique which has been demonstrated for the first time in 1980 when tested at an external beam [123]. As shown in figure 5.2 polarised gas atoms are injected from the side into a thin-walled, T-shaped tube. The cell acts as an impedance to the polarised gas and increases the target thickness by about two orders of magnitude compared to a free gas jet. The stored beam passes parallel through the centre of the tube without interfering with any walls or windows. The chance of interactions of the beam with the gas is magnified by the high number of wall bounces the gas atoms perform before they leave the cell through one of the three openings.

The HERMES storage cell is a $400 \times 30 \times 10$ mm^3 elliptical tube made of pure aluminium with a wall thickness of < 100 μm. The low wall thickness reduces multiple scattering and energy loss of the particles that are scattered through the cell walls.
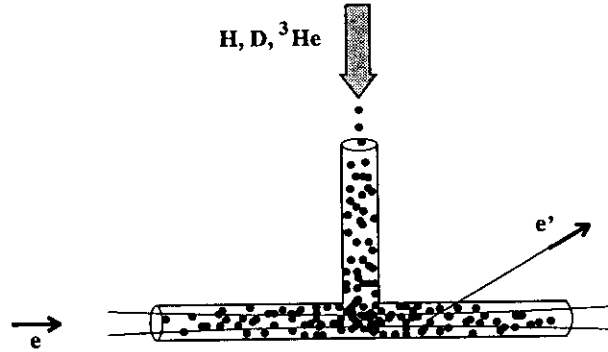
Figure 5.2: Principle of the storage cell target. The atoms are injected into a T-shaped tube and perform several hundred wall bounces before they leave the cell. This way the thickness of a gas target is increased by two orders of magnitude compared to a free gas jet.

5.2.1   Optimisation of Polarisation and Density

The thickness n of a storage cell target depends on the intensity I of the injected atomic beam, the length l of the tube, and its conductance C. In case of a flat elliptical tube one obtains:

$$n \sim \frac{Il}{s_y^2 s_x \sqrt{T}} \tag{5.1}$$

where $s_y \ll s_x$ are the transverse dimensions of the cell and T is the temperature of the cell. To optimise density, the cross section of the tube should be as small as possible. On the other hand the cross section is limited by the size and divergence of the electron beam and of the collimators that protect the cell from synchrotron radiation. The β-functions of the beam optics and the dimensions of the collimator–storage cell system have been optimised to maximise the density of the target [124].

Another way to increase the density of the target is to reduce the velocity of the atoms by cooling the storage cell. The temperature may however not be too low because then the atoms would stay too long on the walls of the storage cell and thus depolarising mechanisms would become prominent. Figure 5.3 shows the polarisation and the density of the gas in the cell as function of the cell temperature as measured in an experiment at the Test Storage Ring in Heidelberg [3, 125]. The density increases with decreasing temperatures as expected. Only at low temperatures below 100 K a significant depolarisation of the hydrogen gas can be observed [126]. For ^3He the polarisation stays constant down to cell temperatures of 20 K. For ^3He target densities of 10^{14} atoms/cm^2 at 100 K for H and D and 3.5 · 10^{14} atoms/cm^2 at 20 K for ^3He are foreseen.

Depolarisation Mechanisms

The atoms experience about 300 wall bounces in the storage cell before they leave the cell. In case of H and D, possible depolarisation of the atoms during the wall bounces is minimised by coating the cell with drifilm. In the case of ^3He a coating of
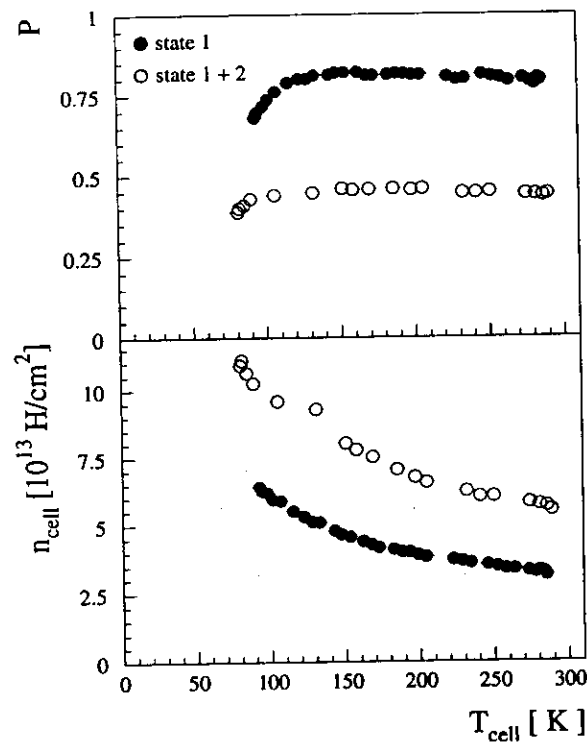
Figure 5.3: Polarisation and thickness of the gas in the storage cell as a function of cell temperature. The polarisation drops only at very low temperatures (upper plot) due to wall depolarisation. The target thickness is higher at low temperatures as the atoms need more time to leave the storage cell (lower plot). In these measurements only a weak magnetic field could be applied to the target resulting in a maximum polarisation of $P_{max} = 0.5$ when using two hyperfine states.

the cell is not needed, as helium shows essentially no depolarisation by wall bounces.

A second possible depolarisation mechanism in H and D is resonant depolarisation by the electron bunch fields. The electrons in HERA are bunched in a length of 1 cm which corresponds to high peak currents of about 80 A with a repetition frequency of about 10 MHz. The high peak currents may depolarise the target nuclei via the coupling of electron and nucleon spins. The effect is the stronger, the higher the current density is, i.e. the more the beam is focussed. This gives another a lower limit for the cross section of the beam and the storage cell. To prevent resonant spin depolarisation effects the storage cell is embedded in a strong magnetic holding field which decouples the electron spin from the nucleon spin. The holding field has to be sufficiently homogeneous and centred between resonances (0.35 T).

5.2.2 Protection from Synchrotron Radiation and Beam Tails

Beam collimators in front of the storage cell are essential at HERA for two reasons: the beam has tails and the beam is accompanied by synchrotron radiation.

The profile of an electron beam is essentially Gaussian, however there are large non-Gaussian tails e.g. due to beam-restgas interactions. As the storage cell has to be small in order to keep the gas density high, the cell walls can easily enter the region of the beam tails. Even if the tails are only very slightly populated, the scattering rate from the wall material could easily dominate the rate from the gas scattering as the wall density is many orders of magnitude larger than the gas density. The collimators have to be thick (e.g. 120 mm tungsten) in order to be able to absorb the shower produced by high energy beam particles.

A second and even more important reason for having a collimator system is synchrotron radiation, which has effects on the operation of the storage cell and the detector:

- The storage cell is heated by synchrotron radiation. The heating leads to a reduction of the target density by temperature rise and in extreme cases to a destruction of the thin cell walls. The HERMES cell with no shielding is heated by about 100 W.

- The wall-coating of the cell may be destroyed by photon irradiation, causing a stronger wall depolarisation of the polarised target gas. The unshielded HERMES cell is irradiated by about 10^{16} photons per second.

- Synchrotron radiation is scattered off the target gas, the walls of the storage cell, the collimator edges and the vacuum pipe. The main scattering processes are Compton scattering, Rayleigh scattering and the photo-electric effect with subsequent fluorescence light emission. The scattered radiation enters the front part of the HERMES detector and prevents the operation of the wire chambers unless counter-measures are taken.

In order to reduce the synchrotron radiation generated in the HERA dipole magnets, the straight section in front of the target was enlarged from 5.8 m to

88.5 m. Secondly the last bending section in front of the straight section is split into a strong bending part and an additional weak magnet. By this means the power density at the target is reduced from $P/\Delta x = 150$ W/mm to $P/\Delta x = 1.5$ W/mm and the characteristic energy is reduced by a factor of 5 to $E_c = 15$ keV. Thus the dipole radiation can be shielded more easily.

A method to reduce quadrupole radiation is to weaken the quadrupoles in the straight section and to place them at a larger distance from the target. The β-functions in the quadrupoles should also be decreased. These requirements are in conflict with the necessary focussing of the beam at the target and with the global HERA beam requirements. Therefore this method is not applicable for the HERMES experiment. Figure 5.4 illustrates the synchrotron emission of an electron that passes the quadrupoles slightly off-centred [127].
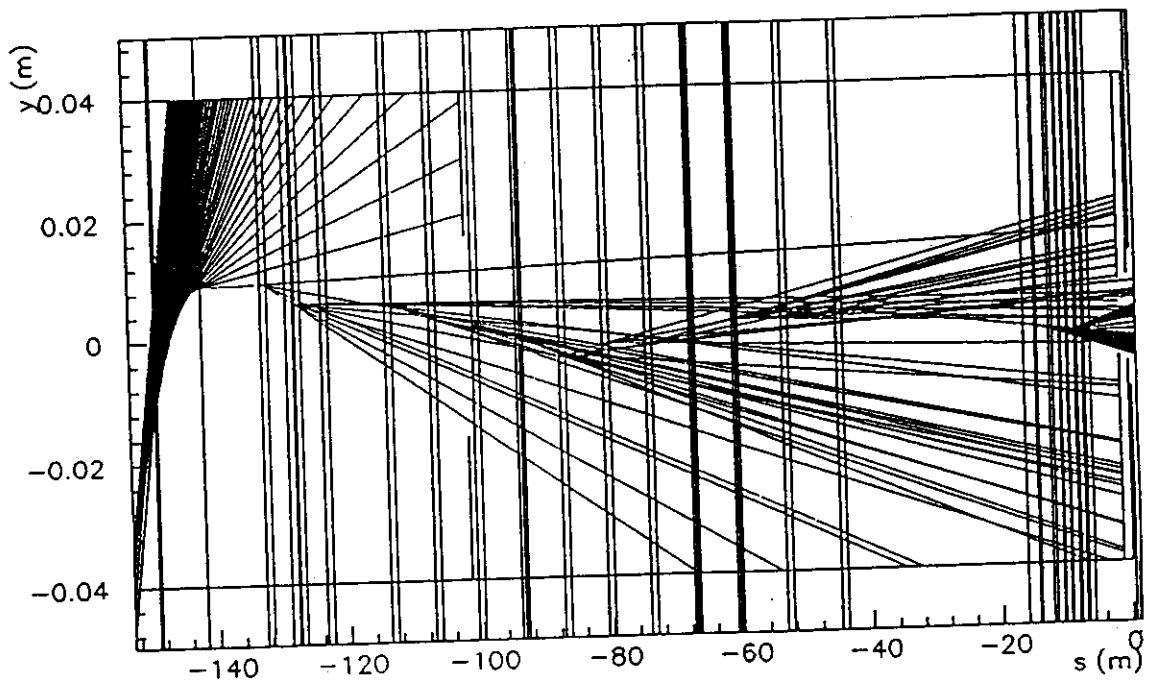
Figure 5.4: Monte Carlo simulation of synchrotron emission: The plot shows a top view of the straight section at HERA in an expanded scale. A single electron enters at the lower left corner and is bended into the horizontal direction and deflected by several focussing quadrupoles. The target is at s=0. The vertical lines mark the positions of dipoles, quadrupoles and collimators. At each tracking step inside a magnet the electron emits a synchrotron photon that is tracked to the next collimator or to the beam pipe. The program repeats the simulation for a large sample of electrons distributed according to the beam emittance.

A very efficient way of reducing the remaining synchrotron radiation is a colli-mator system as sketched in figure 5.5 [127, 128]:

- Movable horizontal and vertical collimators C_{1H} and C_{1V} with an elliptical

opening of $\pm 6.5 \times 2.6$ mm^2 placed about 2 m upstream the target shields the subsequent collimator and the storage cell from direct synchrotron radiation.

- A fixed elliptical collimator C_2 located close to the target with an aperture of $\pm 8.6 \times 3.0$ mm^2 in the shadow of C_{1H} and C_{1V} shields the storage cell from radiation that is edge-scattered at C_1.

With this arrangement only double scattered radiation may hit the detector and the storage cell. An exception is the radiation scattered at the gas which cannot be shielded.
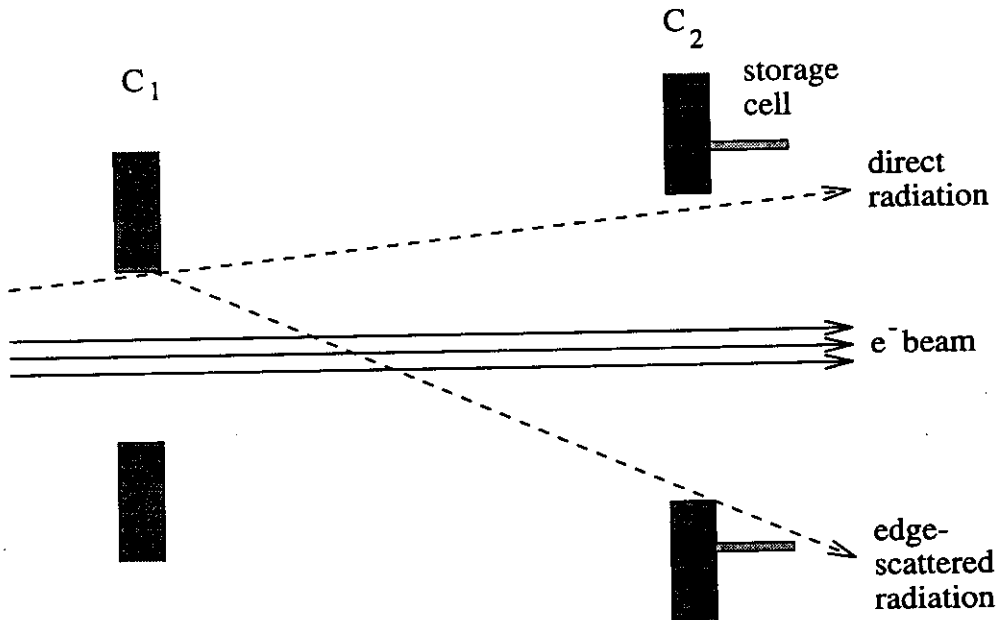
Figure 5.5: Sketch of the collimator system. C_2 is in the shadow of direct synchrotron radiation. The storage cell and the detector are in the shadow of direct radiation and of radiation that is edge scattered at C_1.

A detailed simulation of the synchrotron radiation was performed [127] and gave confidence that the synchrotron radiation can be shielded without causing any problems to the HERMES detector.

5.3 Polarimetry of the Target Gas

The measured spin-asymmetries in the HERMES experiment are proportional to the nuclear polarisation of the target gas. It is essential to know the polarisation of the target with high precision and to monitor its variations permanently.

The H/D Polarimeter

In the case of H or D gas, the gas atoms might suffer from small depolarising effects during the travelling time inside the storage cell. Therefore it is necessary to mea-

sure the polarisation of the gas inside the cell. Monte Carlo simulations have shown that due to the zigzag movements of the gas atoms, there is hardly any gradient of the polarisation with respect to the distance from the atomic beam injection. Depolarisation of the gas shows up globally in the whole cell volume. In order to measure the absolute value of the polarisation, a small fraction of the target gas is analysed in a polarimeter which is connected to the cell by a small tube. The polarimeter is a Breit-Rabi apparatus which allows to determine the relative occupancy of all hyperfine components separately [129, 130]. The anticipated precision of the polarimeter is $\Delta P/P = 3\%$.

The ^3He Polarimetry

For the helium target it is sufficient to know the polarisation of the gas in the pumping cell as there are no depolarising effects of the helium expected in the short time that it travels through the storage cell. The polarisation of the gas in the pumping cell is measured by observing the relative intensity of right and left polarised light which is emitted by the atoms after excitation by discharge.

In order to be able to monitor the polarisation of the gas inside the storage cell, additionally a 'Target Optical Monitor' (TOM) [131] is installed. The TOM consists of a photo-multiplier 30 cm upstream the storage cell which observes (through a mirror) photons that are emitted from the target gas inside the storage cell. The atoms in the target are excited by Coulomb interaction with the electron beam. The intensity of the emitted light is proportional to the luminosity. The signal in the TOM can be used in all three target types to monitor relative changes of the target thickness. In the case of ^3He, the polarisation of the emitted light is analysed in the TOM and is used to extract the nuclear polarisation of the gas.

5.4 Design of the HERMES Target Section

Certainly all apertures in the target region have to be large enough to allow a safe operation of the machine. As the electron beam size is largest during the injection, it was firstly considered to construct a storage cell which can be opened up during injection. It turned out however that in order to shield the storage cell wall from synchrotron radiation, anyhow it had to be made larger than the scaled arc aperture of the machine and that therefore there is no need for opening up the cell during injection.

Abrupt aperture changes close to the beam may introduce kicks on the beam direction. The electron bunch currents induce wake fields and may excite resonant modes in the target chamber. The material and geometry of the target chamber and of the storage cell were carefully chosen and designed in order to minimise the effect on the beam and to prevent destruction of storage cell.

Figure 5.6 shows the design of the HERMES target region [124, 128]. A differential pumping system upstream and downstream of the target chamber assures that the vacuum in the ring is not affected by the injected gas. Rf meshes between the storage cell and the beam pipe and at other positions with rapid changes in

the cross section of the beam pipe prevent the electron bunches from inducing wake fields and resonant rf losses in the target chamber which could heat up and destroy the storage cell and other components.
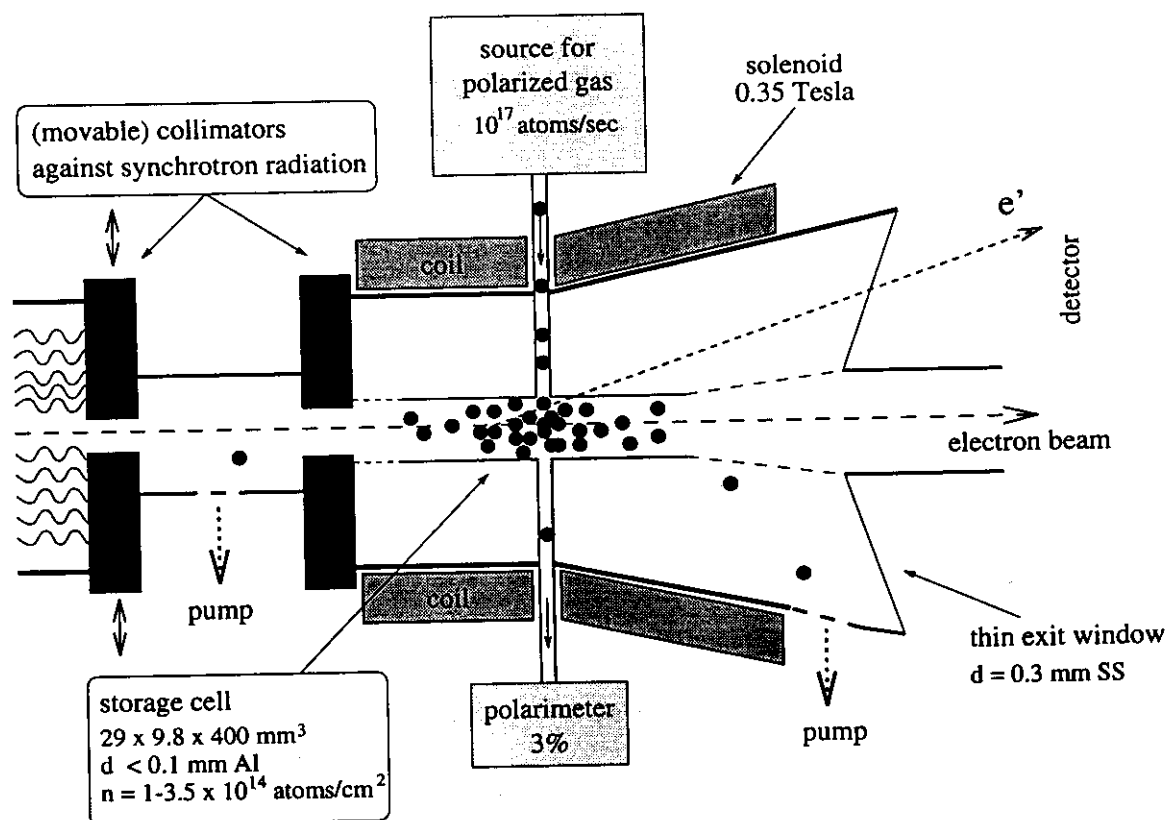

Figure 5.6: Simplified sketch of the HERMES target region. The storage cell is protected against synchrotron radiation and beam tails by a collimator system. Rf-meshes protect from electromagnetic fields. Large pumps keep the vacuum conditions good despite of the target gas leaking out of the storage cell.

For each of the target spin configurations, different magnetic holding fields are required. The helium target needs low fields (0.003 T) with high homogeneity requirements. They are fulfilled by two sets of normal conduction Helmholtz coils in vertical and longitudinal direction. The limiting factor in the homogeneity of the field is the stray field of the HERMES spectrometer magnet which is compensated by an additional coil.

The holding fields for the H/D targets have to be stronger and require a superconducting solenoid (0.35 T) for the case of longitudinal spin and a normal conducting dipole (0.15 T) for the transverse target spin.

The influence of the target fields on the electron beam are negligible except for the case of the transverse field for H/D. In order to prevent depolarisation of the electron beam, the influence of the target dipole is locally compensated by a correction dipole 1.5 m upstream the target and by the correction coil inside the septum plate of the spectrometer magnet 2 m downstream of the target.

Chapter 6

The Spectrometer

6.1 Overview of the Spectrometer

The general design criteria of the spectrometer have been described in chapter 3. Here an overview of the functionality of the spectrometer is given. Figure 6.1 shows a schematic view of the detector.

Vertex Position and Scattering Angles

The deep inelastic scattering takes place in the gas which is stored in the storage cell. The scattered electron and the other particles cross the storage cell wall (< 100 μm Al) and leave the vacuum pipe through a thin walled exit window (0.3 mm stainless steel). The position and direction of the tracks are measured in a series of tracking chambers between the exit window and the spectrometer magnet. First comes a pair of micro-strip gas counters (Vertex Chambers VC1, VC2) followed by two modules of drift chambers (Forward Chambers FC1, FC2). The beam position and direction is known from pick-up monitors up- and downstream the experimental area. The vertex position and the scattering angle can be calculated from the beam and track parameters. The resolution of the chambers is better than the uncertainties which come from the multiple scattering of the particles in the material between the vertex and the chambers. Inside the spectrometer magnet there are three planes of proportional chambers (Magnet Chambers MC1-3). Due to their low resolution (1 mm) they do not contribute to the precision of the track measurement. Their main purpose is to have redundancy in the case of problems with track reconstruction in the drift chambers for high multiplicity events.

Particle Momenta

The momentum of each track and the sign of the charge of the particle are determined from the deflection angle of the track in the magnetic field of the dipole spectrometer magnet. The track parameters behind the magnet are measured by two pairs of drift chambers (Backward Chambers BC1/2 and BC3/4).
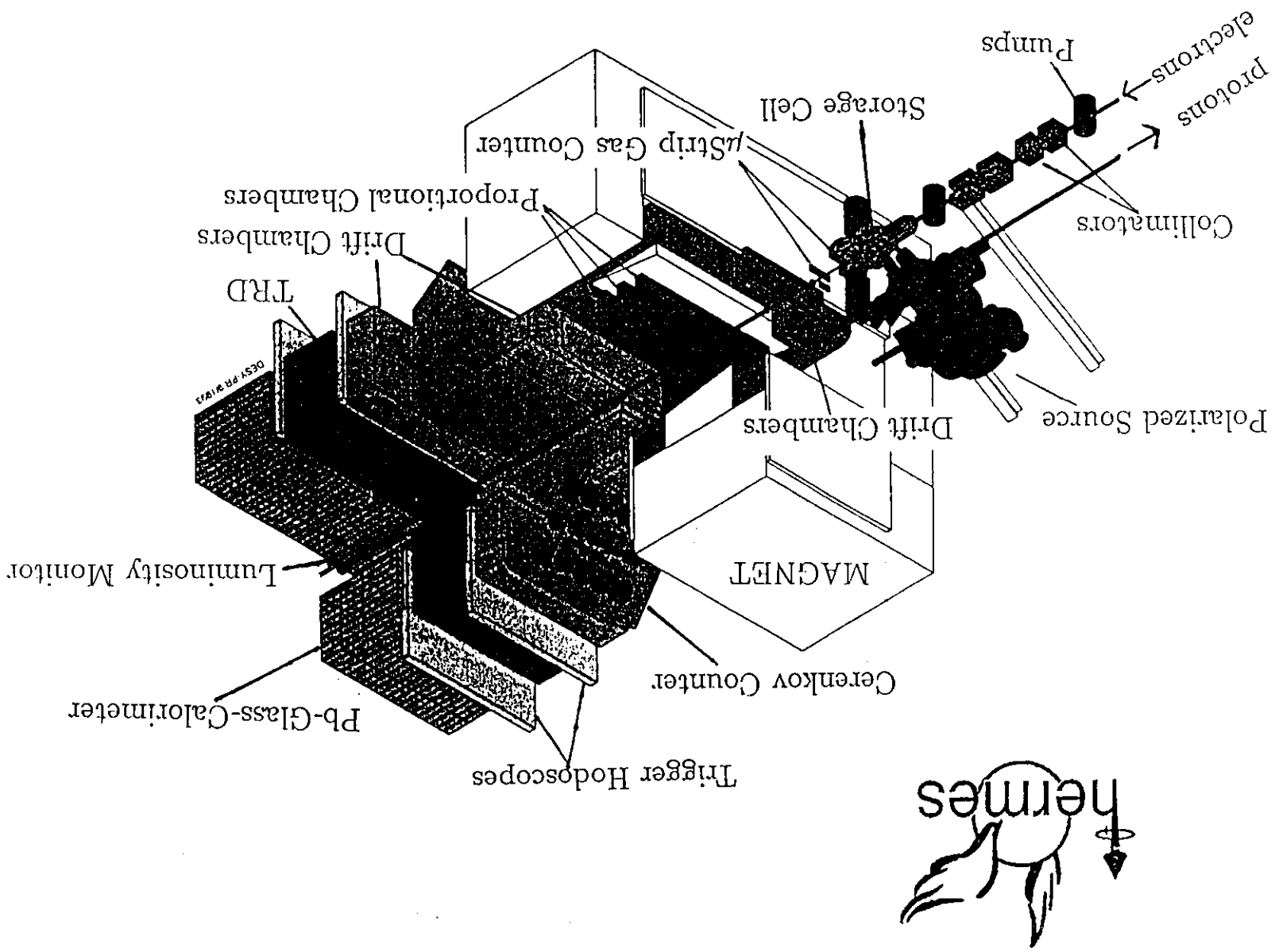
Figure 6.1: A schematic view of the HERMES detector.

electrons

protons

Pumps

Collimators

Storage Cell

μStrip Gas Counter

Proportional Chambers

Drift Chambers

TRD

Drift Chambers

Polarized Source

MAGNET

DESY PR 91/93

Luminosity Monitor

Čerenkov Counter

Pb-Glass-Calorimeter

Trigger Hodoscopes

hermes

Particle Identification and Calorimetry

The most downstream detector of the spectrometer is an electro-magnetic calorimeter. It consists of two pieces: a preshower counter which is a combination of a 11 mm lead sheet and a scintillator (H2) followed by a wall of lead glass blocks (CAL). The calorimeter is used as trigger device and for measuring the energy of electrons and photons. The lead glass calorimeter is also used for pion-electron separation. The preshower improves the electron pion separation to 4000:1 compared to 200:1 for the lead glass alone. A transition radiation detector (TRD) between the last drift chamber and the preshower counter improves the electron identification by another factor of 100. A threshold Čerenkov counter (CER) between the two pairs of backward drift chambers allows for pion-kaon separation in the momentum range below 15.8 GeV.

Trigger

A trigger hodoscope (H1) is placed just behind the last drift chamber (BC4). The physics trigger consists of a coincidence of this hodoscope (H1) with the preshower counter (H2) and the calorimeter (CAL). A minimum energy deposit of 3.5 GeV in the calorimeter is required in order to suppress low energy electrons and false triggers by pions. The coincidence with the hodoscope H1 suppresses triggering by photons. The preshower has been added to the design of HERMES at later stage in order to improve the pion-electron suppression factor. In the original design of the detector, there was a simple hodoscope H2 without radiator foreseen. In this case the coincidence of H1 and H2 was an efficient protection against triggering by photons, as normally photons had no signal in H1 nor in H2. In the new scheme with preshower, lead is added in front of H2 and photons do make signals in H2 and any random hit from any charged background particle in H1 will cause a trigger. A second disadvantage of the preshower is the reduced energy resolution of the calorimeter.

Luminosity

The luminosity is monitored by observing symmetric Møller (Bhabha) events as coincidence signal in two small calorimeters that are placed close to the beam pipe at a distance of 7.2 m behind the target. The Møller (Bhabha) events origin in the scattering of the electron (positron) beam off the shell electrons of the target atoms.

6.2 The Detector Components

6.2.1 The Arrangement in the HERA East Hall

Originally the HERA East Hall was provided for a possible third collider experiment and contained an interaction region with colliding ep-beams similar to the H1 and ZEUS experiments. For HERMES the beam pipes were separated. To optimise background from synchrotron radiation, the electron beam pipe was straightened

out within ±88.5 m. The proton beam runs in the same horizontal plane parallel to the electron beam at a distance of 72 cm. The optics of the electron machine is kept symmetric around the original interaction point in order to ease spin matching. As the collimator and storage cell have to be at the position of the beam waist, the spectrometer has to be build downstream of that point. Unfortunately, the East Hall was build asymmetrically with more space in the proton direction than in the electron direction (which makes sense for collider experiments). The length of the HERMES detector is limited to about 8 m by the size of the hall. In order not to loose acceptance, some focussing quadrupoles around the interaction region were moved towards the tunnel entrance (at ± 8.5 m).

The whole experiment is build on a platform which is movable on rails. In order to allow access to the readout electronics during data taking and to minimise cable lengths at the same time, an electronics trailer is attached to the experimental platform, which is also movable and separated from the radiation area by a concrete shielding around the beam lines and the detector. The machine quadrupoles are mounted on fixed bridges which are connected to the ground floor and do not move together with the detector. That guarantees on the one hand that the beam optics is not effected by small movements of the HERMES platform, on the other hand it requires that the relative alignment of the machine and of the platform are within the small tolerances defined by the HERMES collimator system. A hydraulic system allows to align the platform which carries about 400 tons to a precision of a few ten's of millimetre. The detector-trailer system can be moved to the following three positions:

1. The position for data taking in the HERA beam.

2. In the data taking position, the experiment blocks access to the tunnel for the HERA tram. In case there is a major problem with equipment in the HERA tunnel, e.g. a super-conducting dipole has to be replaced, HERMES can move to a position close to the shielding wall which allows the HERA tram to move into the tunnel. This movement of the detector and the electronics trailer does not require any movement of the shielding wall and can be done within ∼24 hours. Certainly the vacuum pipes of the electron and proton beam have to be disconnected. Valves at both ends allow for the moving out of the detector without that the beam pipes of the ring have to be vented.

3. For repairs of the detector, the experiment can be moved out completely to a parking position in the East Hall. That action requires however to disassemble the wall of concrete shielding blocks. To allow for machine operation when HERMES is moved out, the *ep* beam pipes will be closed by two substitute beam pipes.

6.2.2 The Spectrometer Magnet

The HERMES magnet is a H-frame type dipole magnet with a field integral of $\int B\,dl = 1.3$ Tm. In order to shield the proton and the electron pipe from the

strong dipole field, a septum plate is introduced in the beam plane as shown in figure 6.2. The magnet gap above and below the steel plate allows for an acceptance of 40 mrad $< |\theta_{vert}| <$140 mrad and $|\theta_{horiz}| <$170 mrad with respect to the interaction point plus an additional 100 mrad starting in the middle of the magnet to allow for additional deflection in the magnetic field.
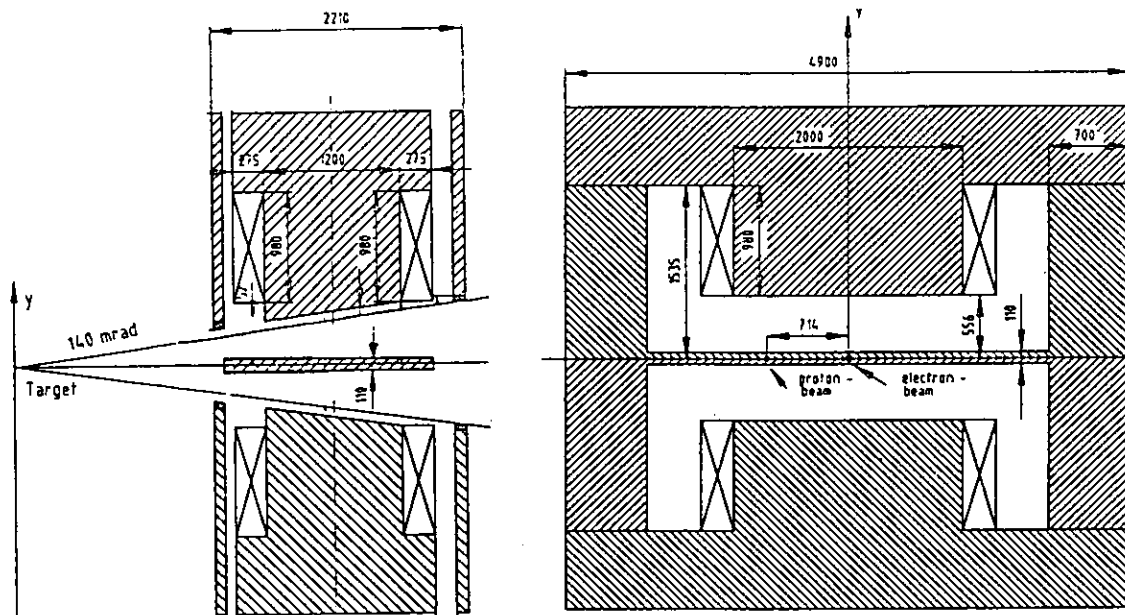

Figure 6.2: Layout of the HERMES spectrometer magnet with septum plate (side and front view).

Extensive field calculations using the MAFIA and TOSCA codes were performed in the design phase with the aim to optimise the homogeneity and strength of the magnet and at the same time minimise the size and the power consumption [132]. The design allows for a later replacement of the normal conducting coils by superconducting coils, however the tight time schedule of the experiment did not allow for the superconducting solution from the beginning on. Additional field clamps were introduced to minimise the stray field of the magnet. The stray field of the magnet at the position of the target holding field is below $B = 20$ G with a maximal gradient of $dB_y/dz = 220$ mG/mm. As this number is still critical for the polarised helium target, additional compensation coils have been introduced in the target region.

Using a precision measuring machine, the magnetic field of the spectrometer magnet has been measured with a precision of $\Delta B_y/B < 0.3$ % and with a grid size of 1 cm longitudinally, 9.8 cm transversely and 4.9 cm vertically. Figure 6.3 shows some of the results [133].

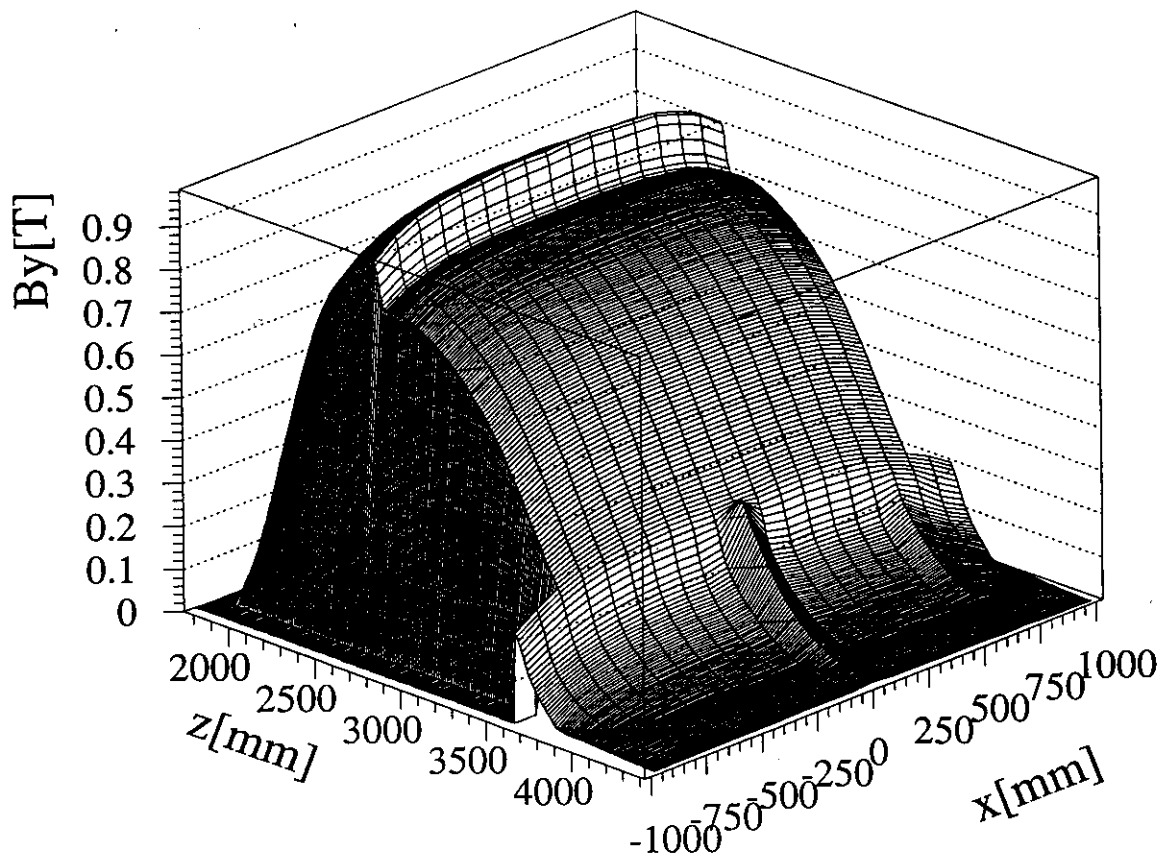It turned out that a passive shielding of the electron beam pipe was not sufficient

Figure 6.3: Measured field map of the HERMES spectrometer magnet for I = 950 A at y = 96 mm.

taking into account the limited thickness of the septum plate. The problem was solved by introducing an additional small coil into the hole of the septum plate which compensates remaining dipole components.

6.2.3 The Tracking Detectors

Figure 6.4 gives an overview of the geometry of the tracking detectors, which all have X, U and V planes. The X-planes have horizontal resolution (i.e. they have vertical wires) whereas the U and V coordinates are tilted by $\pm 30°$. Technical consideration would prefer other angles in certain detectors, however HERMES chose to have the same angles everywhere in order to allow for reconstruction of tracks in 3 projections independently in all detectors and only after the tracks are found in projections they are matched in space. This method of track reconstruction is more robust against single plane inefficiencies compared to methods which reconstruct tracks in space for each module independently. From the track reconstruction point of view Y-planes would be advantageous, however occupancy considerations and technical considerations discarded Y-planes.

In table 6.1 the chamber properties are summarised. Details of the detectors can be found in the Technical Design Report [4]. In the following only a short overview will be given.

The Micro-Strip Gas Counters

The purpose of the front detectors (VC's and FC's) is to provide high precision measurements of the angle of the tracks in front of the magnet. A pair of micro-strip Gas Counters (VC) has been chosen as the appropriate detector behind the target exit window where there is a potentially high background from synchrotron radiation and from shower particles. Each module consists of three planes with the orientations U, X and V. The combination of two modules in one solid box allows a precise inner alignment of the planes. The high channel number of the micro-strip gas counters with a spacing of 200 μm allows for very high occupancies in the chambers. The spatial resolution of each module is 45 μm and the angular resolution of the combination of the two modules is as small as 200 μrad and matches the uncertainties due to multiple scattering in the exit window. The micro-strip Gas Counters have two drawbacks compared to e.g. drift chambers:

- The radiation length of 1.2% per module is relatively high. It is dominated by the glass substrate which has 300 μm thickness. A foil as substrate for the micro-strips would solve the problem, however this technology is not well enough advanced yet.

- The efficiency and resolution of the module strongly depends on the angle of the incident track. Inclined tracks fire several channels at a time. The number of channels depends on the size of the gas gap between the cathode plane and the substrate. In order to improve the resolution for tracks with large horizontal angle, the outer substrates were tilted by 6.93° to make the

Pb Glas Calorimeter

Trigger Hodoscope

TRD

Trigger Hodoscope
BC4
BC3

Cerenkov

BC2
BC1

MC3
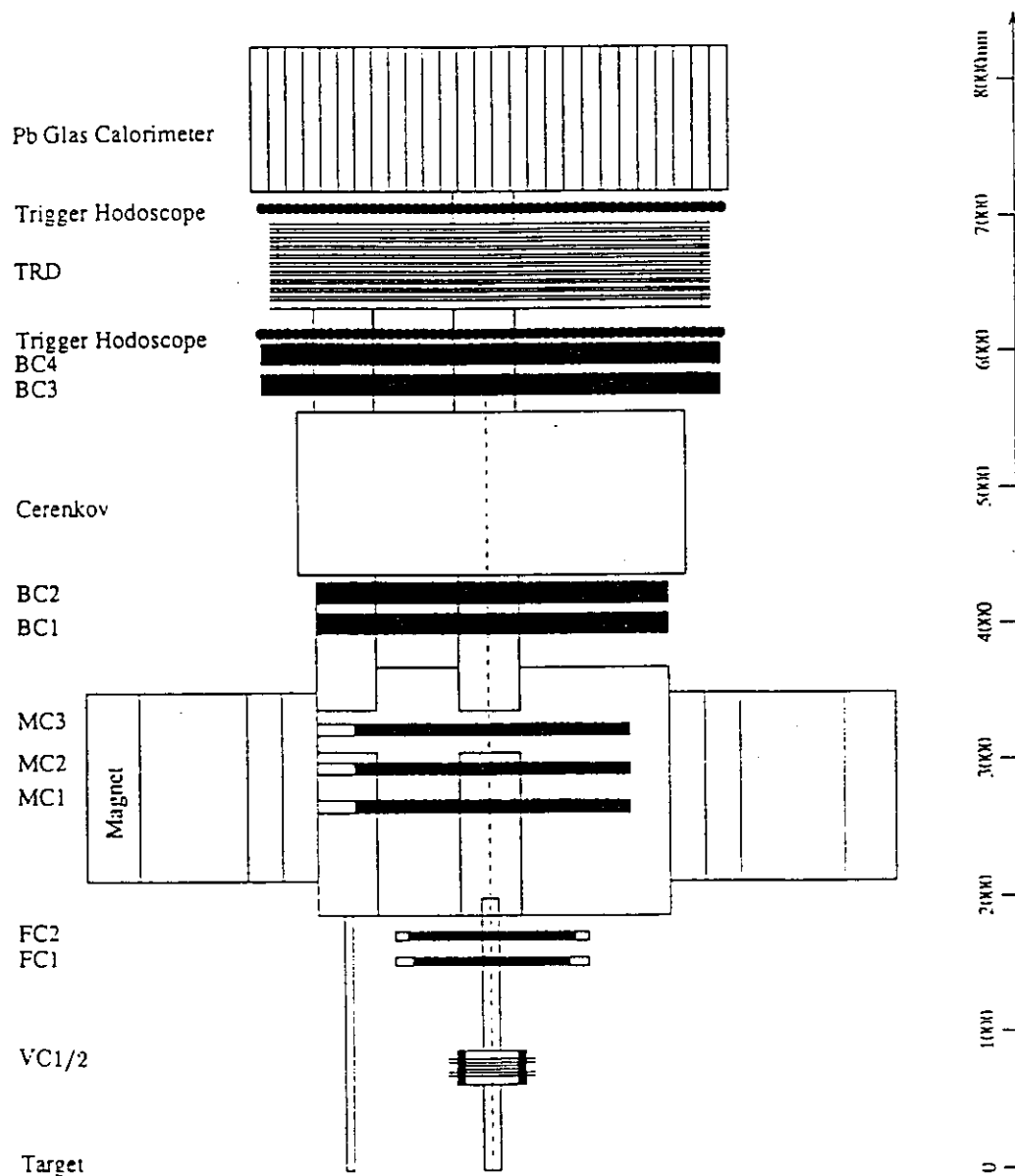
MC2

MC1

Magnet

FC2
FC1

VC1/2

Target

Figure 6.4: Schematic view of the arrangement of the different detector components.

Table 6.1: Properties of the tracking chambers.

WIRE CHAMBER	Vertex		Front		Magnet			Rear	
Detector name	VC1	VC2	FC1	FC2	MC1	MC2	MC3	BC1/2	BC3/4
mm from target	750	1000	1530	1650	2725	3047	3369	3950	5700
Active hor. (mm)	270	343	660	660	1080	1096	1244	1428	2880
Active vert. (mm)	80	100	180	180	290	324	355	520	710
Cell design	microstrip gas		horizontal-drift		MWPC			horizontal-drift	
Cell size (mm)	0.200		7		2			15	
A-C plane gap (mm)	3		4		4			8	
Anode material	$300\,\mu$m glass(Al)		W(Au)		W(Au)			W(Au)	
Anode wire dia.	$7\,\mu$m		$20\,\mu$m		$25\,\mu$m			$25\,\mu$m	
Potential wire mat'l	Al strip		Be-Cu(Au)					Be-Cu(Au)	
Potential wire dia.	$90\,\mu$m		$50\,\mu$m					$125\,\mu$m	
Cathode material	Al on glass		Al+C on Mylar		Be-Cu wires			Al+C on Mylar	
Cathode thickness	$200\,\mu$m		$25\,\mu$m		$50\,\mu$m @ 0.5 mm pitch			$25\,\mu$m	
Gas mixture	DME/CO_2		$Ar/CO_2/CF_4$		$Ar/CO_2/CF_4$			$Ar/CO_2/CF_4$	
Gas percent	60/40		90/5/5		65/35/5			90/5/5	
U,V stereo angle	$\pm 30°$		$\pm 30°$		$\pm 30°$			$\pm 30°$	
Resolution/plane (σ)	$45\,\mu$m		$150\,\mu$m		1 mm			$150\,\mu$m	
Wires in X plane	1350	1900	96	96	540	622	714	128	192
Wires in U,V plane	1350,1350	1900,1900	96	96	540	619	707	128	192
Module config.	UXV		UU'XX'VV'		UXV			UU'XX'VV'	
Rad. length/module	1.2%		0.20%		0.29%			0.26%	
Number of modules (upper or lower)	1	1	1	1	1	1	1	2	2
Channels/module	4050	5700	576	576	1620	1860	2128	768	1152
Total channels	19500		2304		11216			7680	

incident angle closer to being perpendicular as shown in figure 6.5 [134]. This
tilt of the planes causes some problem for the reconstruction algorithms as the
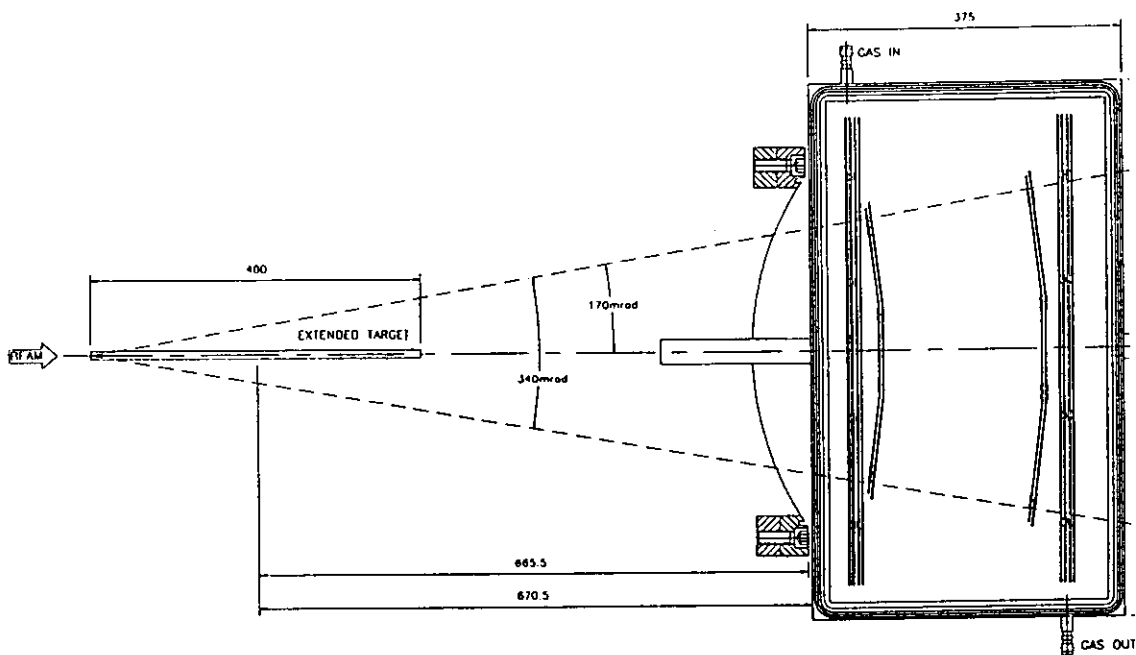tree-search algorithm requires perpendicular planes (see chapter 8.4).

Figure 6.5: Set-up of the HERMES micro-strip gas counters (top view).

The Drift Chambers

There are two modules of conventional drift chambers in front of the magnet (FC1/2)
and four modules behind (BC1-4) [135] with 7 mm (FC) resp. 15 mm (BC) drift
cells. Each drift cell consists of alternating cathode wires and anode sense wires
between a pair of cathode foils. To simplify the readout electronics, the sense wires
are at ground potential. Each module has all three plane orientations with two
staggered planes for each orientation (U, U', X, X', V, V'). The planes are staggered
by half a drift cell size in order to be able to resolve right-left ambiguities. For safety
reasons, a non-flammable gas mixture of Ar (90%), CO_2 (5%) and CF_4 (5%) is used.
The maximal drift time is 150 ns and matches roughly the bunch crossing time of
96 ns of HERA. The radiation length is 0.2% (FC) resp. 0.26% (BC) per module.
The resolution per plane is $\sigma = 150$ μm [136].

The Proportional Chambers

The main purpose of the magnet chambers is to simplify the matching of tracks for
events with high multiplicity found in the forward and rear part of the detector.

Three modules with three planes each (U, X, V) are placed in the rear half of the magnet gap. The rear half was chosen because low energy background particles are mostly reflected by the magnetic field and the occupancy in the rear part is therefore small compared to the number of particles that enter the magnet. Due to the magnetic field, only proportional chambers are an adequate type of detector. The wire distance is 2 mm which results in a total of 11008 electronic channels. The radiation length is 0.29% per module.

The Laser Alignment System

A precise relative alignment of all tracking chambers is essential for a successful track reconstruction. In order to monitor possible movements of the detectors, e.g. caused by thermal expansion of the support structures, an optical alignment system was installed. On the right and left side of the frame of each detector module an optical target is attached. It consists of a Fresnel lens which can be moved into and out of a laser beam which passes the frames of all tracking detectors. In order to measure the position of each detector module, each lens is successively moved into the beam and out again. The Fresnel lenses focus the laser beam onto a CCD camera at the rear end of the spectrometer. Small displacements of the Fresnel lenses produce large displacements of the image interference pattern at the position of the camera and can such be used for monitoring alignment changes of the chambers. The optical targets are also used for manual survey of the chamber positions after installation.

6.2.4   The Calorimeter and the Hodoscopes

The Lead Glass Calorimeter

The function of the calorimeter is to provide a trigger for electrons with energies above a certain threshold ($E > 3.5$ GeV) to separate electrons from pions and to measure the energy of electrons and photons from radiative processes or from π^0 decays. The calorimeter consists of an upper and a lower wall of each 42×10 lead glass blocks. The size of the blocks is 9×9 cm^2 with 50 cm length corresponding to about 18 radiation lengths of radiation-resistant Pb glass F101. The energy resolution of the calorimeter is

$$\frac{\sigma(E)}{E} = 1.47\% + \frac{5.14\%}{\sqrt{E/GeV}} . \tag{6.1}$$

A spatial resolution of the impact point of a cluster of about 0.5 cm can be achieved by analysing the profile of the shower in the neighbouring cells.

During injection of the proton or the electron beam, loss rates of the beams are high and result in high radiation doses near the beam pipes. To prevent radiation damage of the lead glass, both calorimeter walls are vertically moved away from the beam pipe by 50 cm during injection time. The weight of the calorimeter is 2×12.5 tons.

The Preshower Counter

In order to improve pion-electron separation, a preshower counter is installed in front of both lead-glass walls. Each preshower consists of a 11 mm thick lead sheet followed by a hodoscope (H2). The hodoscope consists of 42 plastic scintillator paddles which have a size of $9.3 \times 91 \times 1$ cm^3 and cover each one vertical row of the lead glass blocks. In order to prevent acceptance gaps between the paddles, two adjacent paddles overlap by 1.5 mm. As the longitudinal shower profile for electrons and pions is different, the relative amplitude of the preshower signal compared to the calorimeter signal can be used to improve the electron pion separation to 4000:1 in the first level trigger. After event reconstruction, the momentum of the track is known and can be used to compare with the energy deposit in the preshower and the calorimeter. Electron-pion separation can be further improved this way.

The Hodoscope H1

Another hodoscope (H1) is installed just behind the rear drift chambers and serves as trigger on charged particles. Its structure is identical to the hodoscope H2 of the preshower counter.

6.2.5 The Transition Radiation Detector

A transition radiation detector (TRD) between the hodoscopes H1 and H2 allows to separate electrons and pions. It consists of 6 consequent modules each having a radiator followed by an X-ray detector. The radiator consists of a loosely packed 6.5 cm thick matrix of randomly oriented propylene fibres with $17-20$ μm diameter. The emitted transition radiation consists of photons of typically $2-15$ KeV. The detector is a planar wire chamber with horizontal resolution of 0.5 cm wide cells. The chamber contains a high Z gas (Xenon) for efficient X-ray absorption. X-ray absorption produces clusters of electrons in the gas. Large signals are a signature for transition radiation and thus for relativistic electrons. The combination of 6 modules increases the electron-pion separation factor to 100:1 at 5 GeV. δ-electrons and correlations between different modules limit the separation factor. Special care has been taken to guarantee a constant purity and pressure of the chamber gas as the performance of the detector depends critically on those parameters. The TRD has a total thickness of about 5 % of a radiation length.

6.2.6 The Čerenkov Counter

For hadron identification, a threshold Čerenkov counter has been installed between the two blocks of the rear drift chambers BC1/2 and BC3/4 [137]. It consists of an about 1 m long radiator of tetrafluormethane gas at atmospheric pressure. The radiation is reflected by an array of 2×20 mirrors into photo-multipliers which are mounted on the top (bottom) of the upper (lower) Čerenkov detector. The yield is about 12 photoelectrons for $\beta = 1$ particles. The total thickness of the detector is about 3.5% of a radiation length. Pions can be separated from kaons and protons in

an energy range between 4.4 GeV and 15.8 GeV and kaons and pions from protons in an energy range between 15.8 GeV and 30 GeV.

By changing the gas in the radiator, the energy thresholds can be changed. Heavy gas such as perfluoropentane allows to lower the threshold for pions to 2 GeV. In principle it is feasible to fill the two radiators (upper and lower) with two different gases to measure pion and kaon rates at the same time. For calibration purposes of the TRD-Calorimeter system, the Čerenkov is filled with a light gas (nitrogen) which raises the energy threshold for pions and allows to cross-check the electron-pion separation of the other detectors.

On the long term it is planned to replace the threshold counter by a ring image Čerenkov (RICH). It will allow for a unique identification of pions, kaons and protons. Due to the limited space which is available between the drift chambers, the design is non trivial and feasibility studies are still not conclusive.

6.2.7 The Luminosity Monitor

The luminosity monitor is based on the detection of Møller or Bhabha scattering off the electrons from the shell of the target atoms. Two calorimeters on both sides of the beam pipe measure symmetric scattering with an angular acceptance of 4.5 to 8.2 mrad [138, 139]. The coincidence rates depend on the type of beam: For a the nominal beam current of 56 mA and a nominal H target density of $1 \cdot 10^{14}$ atoms/cm^2 in the case of an electron beam (Møller scattering) the coincidence rates are 116 Hz and in the case of a positron beam (Bhabha scattering and pair production) the coincidence rates are 86 Hz. The energy of the scattered electrons and positrons is in the range of 10 to 20 GeV for particles that are scattered in the acceptance of the detector. Each calorimeter consists of 12 NaBi(WO$_4$)$_2$ crystals which have a size of $22 \times 22 \times 200$ mm^3. They contain in longitudinal direction 19.4 radiation lengths and are very radiation resistant. They act as Čerenkov radiators, are insensitive to low energy background and have a good time resolution. To reduce radiation damage, the counters can be horizontally moved away from the electron beam during injection time of the electron beam.

The luminosity monitor is also of physics interest for detecting electron scattering at very low angles. The idea behind this is to detect the scattered electron from resonance production processes and from J/Ψ production.

6.2.8 The Gain Monitoring System

For gain monitoring purposes, a dye laser at 500 nm has been installed which sends light pulses of different intensity through glass fibres to every multiplier of the hodoscopes, the calorimeter, the luminosity monitor and additionally to a reference photodiode. The different intensities are achieved by a rotating wheel with several attenuation plates. The light is split in several stages and fed into glass fibres. The multiplier signals are compared to the signal of the reference photodiode. As the gain of the photodiode is stable, the ratio of the PMT amplitude and the signal of the photodiode can be used to monitor relative gain changes in the multipliers.

6.2.9 Shielding against Particle Background and Radiation Damage

The two-stage collimator system which shields efficiently against synchrotron radiation and showers which come along the beam pipe was already discussed in chapter 5. In the region outside the aperture of the collimator jaws, the shielding is maintained by a surrounding lead wall which shields radiation which comes along the beam pipe up to a distance of ± 20 cm. Upstream the target a 4 mm thick lead curtain covers the whole cross section of the HERA tunnel and protects the detectors from low energy γ rays which come along the tunnel.

Lead collars around the electron pipe in the region between the FC's and the end of the spectrometer protect from radiation that leaks out of the electron pipe. The beam pipe between the exit window and the FC's is very thin (0.25 mm) in order not to cause secondary showers.

The field clamps of the spectrometer magnet and the edge of the septum plate are excellent sources for secondary particle showers. In order to minimise the amount of particles that leak out of the iron, the space behind the front field clamp and the region close to the edge of the septum plate have been covered by a high Z material (lead and copper respectively). The septum plate is wedge shaped with an angle that is pointing to the target so that particles either pass the acceptance of the gap or they get absorbed without scratching along a surface.

To protect the calorimeter against radiation damage coming from the proton machine, the lower part of the calorimeter is shielded by a 2.4 m thick concrete wall. The upper part is not protected due to technical difficulties. According to simulations, a shielding is not necessary. To confirm the calculations, the amount of radiation that hits the calorimeter is monitored by a few radiation sensitive lead glass blocks which are mounted behind the calorimeter. With the help of the gain monitoring system the transmission of the lead glass is continuously watched. In case some radiation damage is observed in the sensitive counters, measures will be taken to protect the whole calorimeter sufficiently.

6.2.10 The Trigger System

The aim of the trigger system is to select the events of physics interest and to ignore background. A perfect physics trigger for HERMES would trigger only deep inelastic events with scattered electrons (resp. positrons) above an energy threshold of 3.5 GeV. Electrons with energies below this threshold are not of interest as they do not fulfill the y cut demanded by radiative corrections (see sect. 8.7). Three trigger levels are foreseen in the HERMES experiment. The first level trigger fires the conversion of times and amplitudes in the electronic modules (TDC's and ADC's) and also the readout of the fast electronics by the data acquisition system. It has to make its decision within a few hundred nanoseconds. The second level trigger controls the readout of the data acquisition system by the online computers and has processing speeds of about 100 μs. The third level trigger which controls the tape writing has to have processing speeds of an average of about 10 ms.

The first level trigger

The first level trigger is based on fast electronic units which consists of linear adders, discriminators and logical units. A first level trigger appears when the following conditions are fulfilled in either the upper or the lower half of the detector:

(1) The energy of the calorimeter blocks in each column is added and then the signal sums of each two neighbouring columns are formed. One of the two-column sums has to be above a certain threshold which is tuned to the energy deposit of an electromagnetic shower of 3.5 GeV.

(2) There is a signal in the preshower above a certain threshold which will be tuned such that electromagnetic showers will be recognised with a high efficiency whereas hadron showers are suppressed.

(3) There is a signal in hodoscope H1.

(4) The signals (1)–(3) have to arrive within a short time window which is defined by the time when the electron bunch passes the detector. The time window is derived from a signal of the HERA clock.

An electron from deep inelastic scattering with an energy above 3.5 GeV will fulfill all four conditions. Condition (1) ensures that low energy electromagnetic background and to a large extend also all hadronic background does not fire the detector. Condition (2) further suppresses triggers by hadronic showers. Condition (3) suppresses triggers by photons. Condition (4) suppresses triggers by background from the proton machine as the proton bunches pass the rear detectors at a different time than the electron bunches. Remaining background triggers occur in the following cases:

1. A charged pion has an extraordinary energy deposit in the preshower and in the calorimeter (e.g. due to a nuclear reaction).

2. A high energy photon fires the calorimeter while a charged hadron from the same event fires the hodoscope H1.

3. A shower from the proton beam can fire the detector when the proton that produced the shower was in a satellite bunch i.e. it had left its RF-bucket and is off-time compared to the arrival of the main proton bunch. Up to 10 % of the protons can be in satellite bunches. False triggers from the proton beam can in principle be suppressed by a veto signal from scintillators which are installed behind the calorimeter. Currently the rate is sufficiently low to be handled by the data acquisition system (DAQ).

The trigger rate of good events is 65 Hz for a current of 30 mA and a target density of $1.2 \cdot 10^{15}$ nucleons/cm^2 (nominal ^3He density), whereas the typical background trigger rate of the first level trigger is 4.4 Hz under these conditions.

The second level trigger

Currently a second level trigger is not installed, but the possibility is provided. Using a digital signal processors (DSP) in the data acquisition system system, it is possible to pre-process the information of the TRD detector and to trigger on events that have large cluster sums in the TRD. A rough tracking is required which means that the signal from the TRD has to be correlated with the position of the calorimeter row which fired the trigger. This kind of second level trigger would reduce false triggers produced by charged hadrons.

A second possibility of an application of a second level trigger would be to correlate the spatial information of the signal in the calorimeter with the spatial information of H1 and H2, i.e. to perform a rough tracking of the particles. Such a correlation in space would suppress false triggers of the type '2.' in the list above.

The third level trigger

As long as the false trigger rates are small enough that the data acquisition system can handle them, there is no need to program the above conditions in the DSP logic. A safer, easier and a lot more flexible way is to program the above described logic in the on-line workstations. At the beginning of the experiment, no third level trigger is used in order to ensure that there is no bias introduced to the data. At a later stage of data-taking, a third level trigger would reduce the amount of data that are written to tape.

Special triggers

The efficiency of the trigger system has to be known precisely, as inefficiencies reduce the measured event rate and cannot be recovered off-line. Only detectors with efficiencies close to 100% are used in the first level trigger: the hodoscopes and the calorimeter. In order to be able to determine the trigger efficiencies off-line, pre-scaled samples of all various combinations of the trigger conditions are written to tape. They are called 'singles trigger'.

A random trigger is installed which allows to check the background conditions of all detectors. It is also used to check the dead-time logic. A pulser trigger and the trigger from the gain monitoring system is used to determine pedestals and gains of the photo-multipliers.

The luminosity counter has a separate trigger system which reads out the ADC's of the luminosity calorimeter. A pre-scaled sample of this trigger additionally fires the whole HERMES detector and such allows to look for correlated signals in the luminosity detector and the spectrometer.

6.2.11   The Readout and Data Acquisition

The readout and data acquisition system (DAQ) is based on VME and FASTBUS modules. The TRD, the calorimeter and the luminosity monitor use DSP processors for signal preprocessing and for a possible second level trigger. Several detector

related FASTBUS crates are connected via segment interconnects to an event builder FASTBUS crate which transfers the data via SCSI to several on-line workstations (DEC- and ALPHA-stations). The on-line computers distribute the events to several EXABYTE tapes and to staging disks. The events are transferred via FDDI from the disks in the HERA East Hall to staging disks at the DESY computer centre. From there they are written to storage TEC cassettes. The staging disks guarantee continuous operation even if one of the links between the computers is down. The writing to storage TEC silos has the advantage that no manpower is required for mounting of tapes neither for tape writing nor for tape reading during the off-line analysis. The writing to EXABYTE tapes which requires manual mounting, is carried out as safety backup and for exporting tapes to outside labs. The event size is typically 10 kBytes. With a trigger rate of typically 60 Hz a total amount of 2.2 GByte raw data per hour are written to tape.

The Experimental Control System

The experimental control system of HERMES is designed in a way that all information which concerns the control and status of the detector is gathered at one place, namely in the slow control server. It is an application of the 'DAD' system which is a general data base and command passing system. It will be described in the next chapter in more detail. The principle of the experimental control system is sketched in figure 6.6. It contains five levels:

1. the hardware,

2. the software that communicates with the hardware (hardware controller),

3. the general data base and command passing system (slow control server),

4. high level processors (tasks),

5. and the user interfaces (control and display panels).

The hardware consists mainly of CAMAC, RS232 and VME modules. Hardware clients communicate with the hardware. They receive simple commands from the slow-control server and pass the appropriate codes to the hardware. They also receive information from the hardware and pass it to the server. No other software controls the hardware. The hardware specific software is separated this way from the high level software and the user interfaces.

User interfaces allow to monitor the information which is present in the data base and allow to submit high level command to the slow control server. High level processors receive the high level commands, interpret them and convert them to low level commands which are then sent via the slow control server and the hardware client to the hardware itself.

This design of a slow control system separates the programming of the hardware interface from the programming of the process control. This way the detector experts do not have to learn the low level hardware commands and the hardware
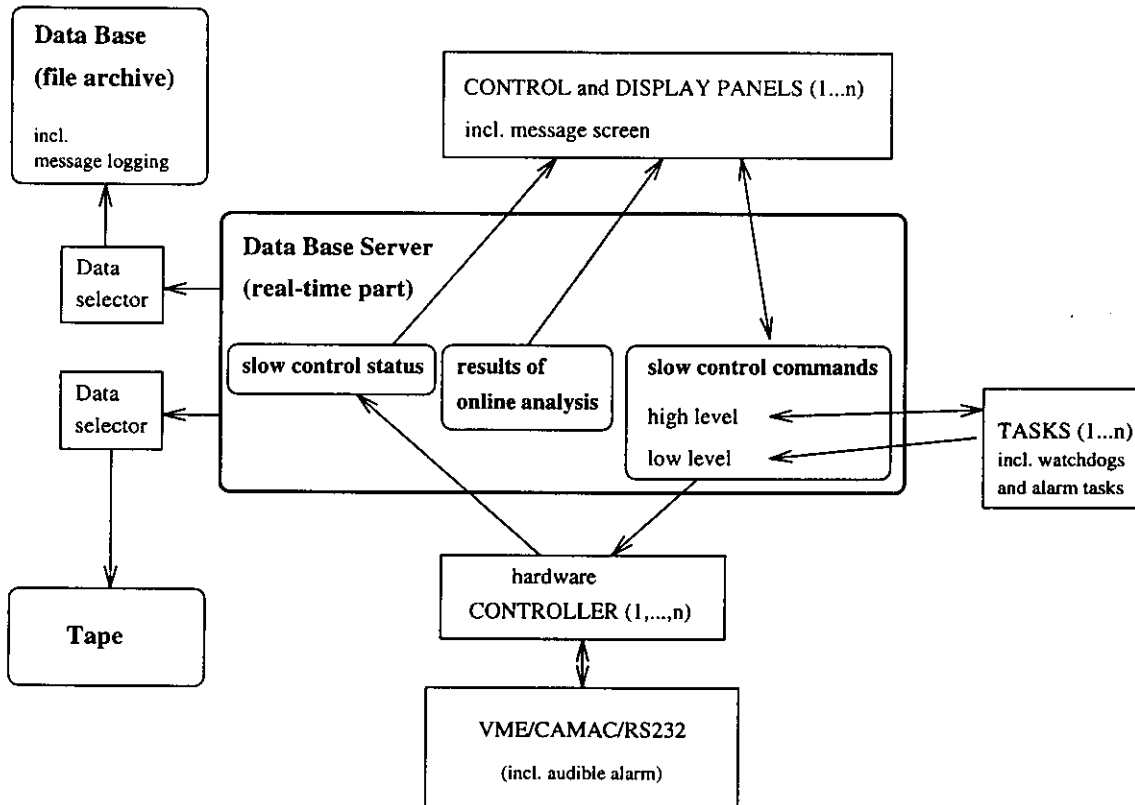
Figure 6.6: Sketch of the general philosophy of the experimental control system of HER-MES. The data base server has two functions: it contains the up to date status of the experiment and it also serves as message passing system for the hardware control. The programming of the user interfaces and hardware controllers can be done by different people as the data base provides a well defined interface. 'TASKS' are running in the background which translate high level commands that the user enters at his control panel into low level commands which are recognised by the hardware controllers.

programmers do not have to know the details of the detector operation. Additionally there are clients installed (data selectors) which write a selection of the slow control data in certain time intervals to a permanent data base and to tape. A protocol of the detector control messages is also included in the data stream.

Watch dogs and alarms can be programmed as high level processors which only communicate with the data base server and need no other input or output stream. This system can at a later stage of the experiment easily be expanded to an expert system which operates the data taking semi-automatically.

Chapter 7

The Anticipated Performance of the HERMES Experiment

The HERMES experiment just started data taking, the calibrations of the detectors are currently being done and the current performance is far from what it will be when all details are understood. Nevertheless, the nominal performance of the experiment can be calculated by a detailed Monte Carlo simulation of the physics, the geometry and the response functions of the various detector components. Figure 7.1 shows a side view of the model of the detector which is used in the Monte Carlo simulation.

7.1 The Acceptance of the Spectrometer

The geometrical acceptance of the detector is limited by the frame of the detectors, the size of the septum plate and the dimensions of the air gap inside the spectrometer magnet. The angular acceptance is roughly

$$40 \text{ mrad} < \quad |\theta_{vert}| \quad < 140 \text{ mrad} \qquad (7.1)$$

$$|\theta_{horiz}| \quad < 170 \text{ mrad} \qquad (7.2)$$

which limits the total accepted scattering angle to

$$40 \text{ mrad} < \theta < 220 \text{ mrad} . \qquad (7.3)$$

In the trigger, a minimum energy of E'=3.5 GeV for the scattered electron is required. This limits the momentum transfer for a beam energy of E_{beam}=27.5 GeV to

$$\nu < 24 \text{ GeV} . \qquad (7.4)$$

For the spin structure function analysis the following kinematic cuts are applied to the data:

$$Q^2 \quad > 1 \text{ GeV}^2 , \qquad (7.5)$$
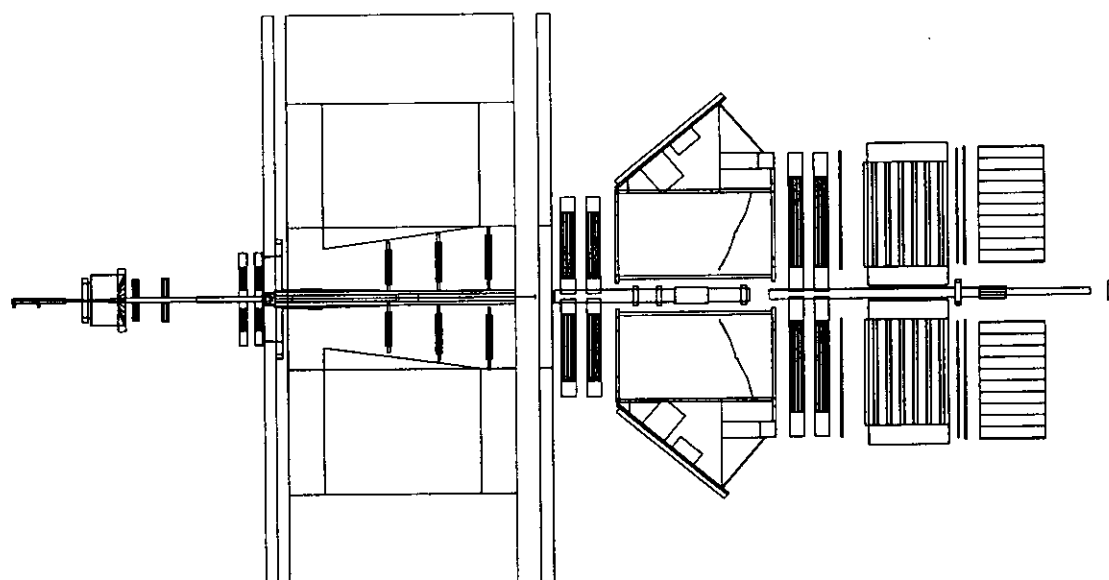
100 cm

|———————|

Figure 7.1: A side view of the HERMES spectrometer as it is modelled in the Monte Carlo program. Material which is relevant for the generation of secondary particles or for the smearing of particle directions and momenta is represented in great detail. The program generates the volumes automatically from the information which is contained in a central geometry data base.

$$W \quad > 2 \text{ GeV} , \tag{7.6}$$

$$0.02 < \quad x \quad < 0.8 \quad \text{and} \tag{7.7}$$

$$y \quad < 0.85 . \tag{7.8}$$

Figure 7.2 shows the Monte Carlo generated distribution of deep inelastic events neglecting radiative corrections. Due to the steep fall of the cross section with increasing scattering angle, most of the events populate the low-Q^2 region. The lines indicate the cuts which are applied to the data analysis. The data in the resonance region ($W < 2$ GeV, $x \sim 1$) will be used for a special analysis. The region of $y > 0.85$, where the radiative corrections are difficult, coincides with the region where the pion background in the trigger is large. The physically interesting region of very small x ($x < 0.02$) is unaccessible due to the limited beam energy and the cut in Q^2.

Figure 7.3 shows the angular acceptances in the scattering angle θ and in the kinematic variables Q^2, x and y. The shape of the distributions is mainly determined by the aperture of the spectrometer magnet and the size of the calorimeter. The rise of acceptance towards low x is due to the effect that with the condition $Q^2 > 1$ the scattering angle of small x events is above the 40 mrad limit.

7.2   The Resolution of the Spectrometer

The resolution of the detector system is limited by the following effects:

- As the scattered electron travels from the vertex through the materials of the storage cell, the exit window and the detector planes its direction and momentum is modified due to Bremsstrahlung processes and knock-on electrons. Additionally its direction is smeared out due to multiple Coulomb scattering.

- Each detector module has a finite position resolution which is of the order of 45 μm for the VC chambers, about 150 μm for the FC and BC drift chambers and about 1 mm for the MC proportional chambers.

- Additional effects that degrade the resolution of the system are uncertainties in the magnetic field map, cluster building in chambers, ambiguities in the reconstruction of multiple tracks and limitations of the reconstruction software.

The smearing effects of the material are minimised by reducing the wall thicknesses and by using low-Z materials. Figure 7.4 (a) shows the integrated radiation length which a particle has to pass on its way through the experiment. The 50 μm thin aluminium storage cell has already a significant effect for particles which pass it with a small angle. The 0.3 mm thick steel exit window cannot further be reduced as it has to stand the atmospheric pressure. A beryllium window would be another possible choice with less radiation length, which has however been discarded because of safety aspects. The next significant amount of material are the glass substrates of the micro-strip gas counters. The figures 7.4 (b) and (c) show the integrated radiation length up to the magnet chambers as a function of the scattering angle.
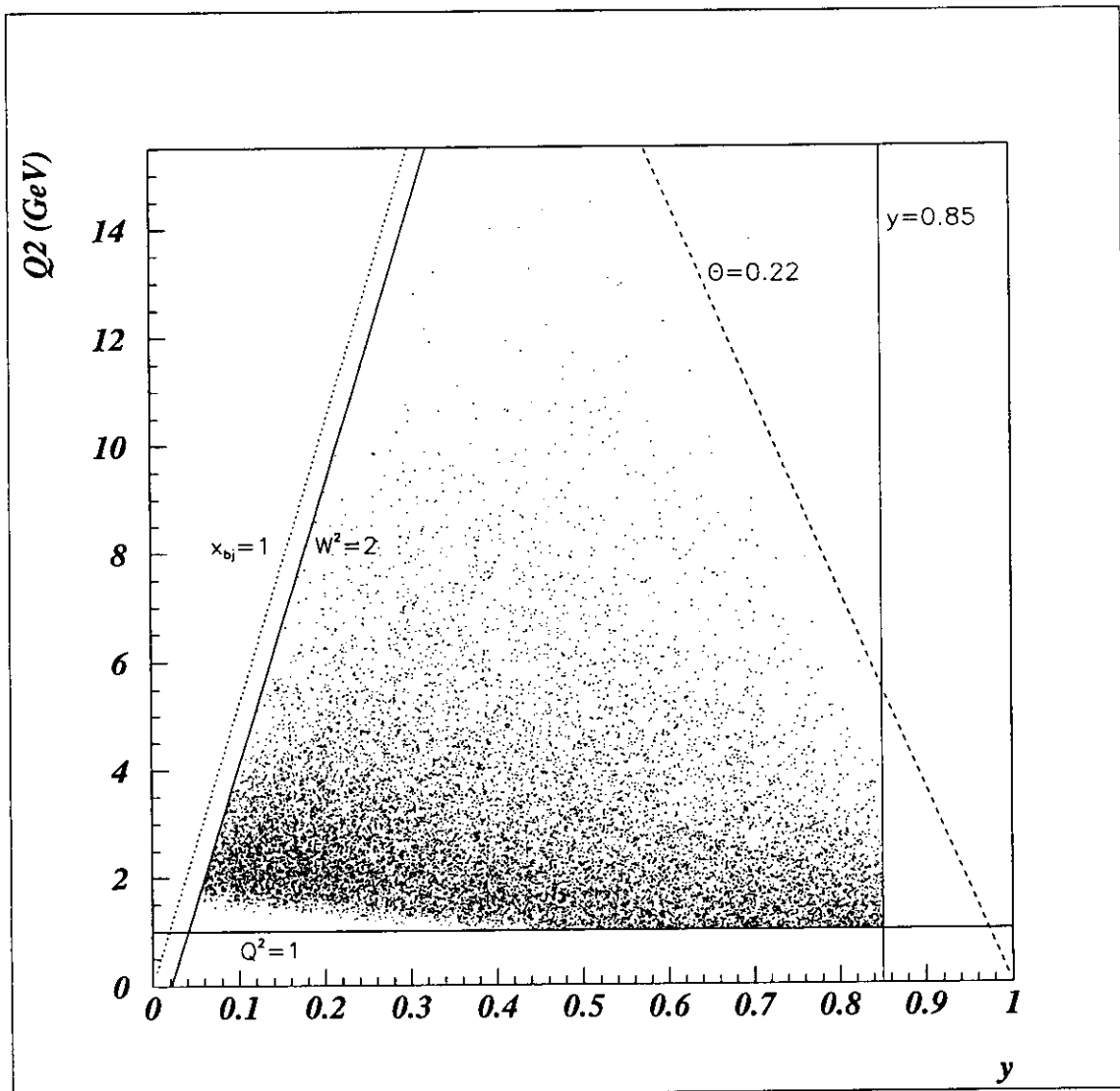
Figure 7.2: Distribution of Monte-Carlo generated deep inelastic events in the kinematic plane. The lines indicate the cuts in x, y, θ, and W which are applied in the physics analysis.
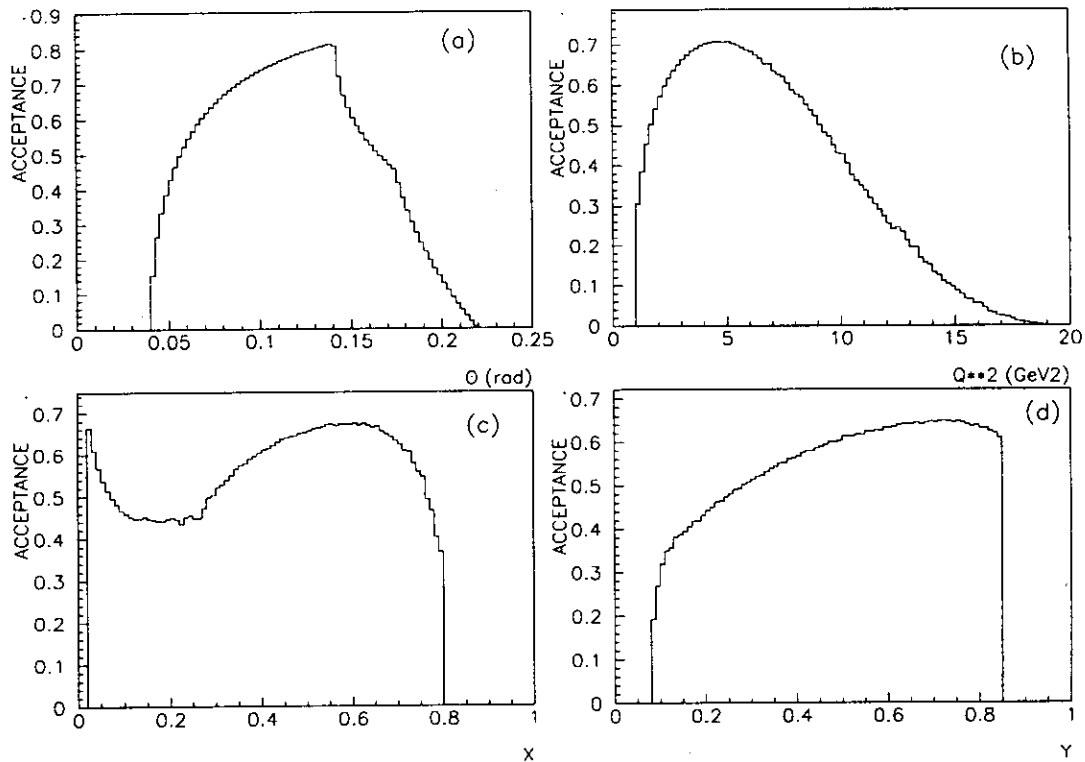
95/06/22 00.57

Figure 7.3: The acceptance of the spectrometer plotted versus θ (a), Q^2 (b), x (c) and y (d). The acceptance is extracted according to the deep inelastic cross section for events which are inside the cuts $Q^2 > 1$ and $0.1 < y < 0.85$. The angular acceptance (a) of the spectrometer is determined by the septum plate and the size of the calorimeter. The shape of the other distributions(b)-(d) is mainly determined by the angular acceptance.

The angular dependence has its origin in the varying travelling path length inside the storage cell wall. The situation is worse in reality as the real storage cell is not completely flat and small deformations of the surface will result in large variations of the integrated path of material.

Figure 7.5 shows the distribution of deep inelastic events as function of the scattering angle θ, the scattered energy E', in the kinematic variables Q^2 and x and in the longitudinal and radial vertex coordinate z and r. The plots were generated from reconstructed Monte Carlo events, i.e. the resolution of the detector is included. The triangular shape of the vertex distribution is due to the gas density profile in the storage cell. For each of those quantities, the experimental resolution has been calculated as shown in figures 7.6 to 7.8. The upper plot in each figure show the smearing due to the interaction of the electrons with material, the plots below show the effects due to the limited detector resolution and the lower plots show the total smearing of the whole detector system including all effects that can be simulated in the Monte Carlo program. The large asymmetric tails in the distributions are mainly due to Bremsstrahlung processes. The width of the distributions can be parametrised by truncating the tails and fitting a Gaussian through the peak. The width is indicated in the figures. The resolution of the spectrometer has been matched to the intrinsic resolution of the experiment which is given by the interaction with material. The total average resolutions are:

$$\sigma(\theta) = 0.13 \text{ mrad} \tag{7.9}$$
$$\sigma(E')/E' = 0.59\% \tag{7.10}$$
$$\sigma(Q^2)/Q^2 = 0.78\% \tag{7.11}$$
$$\sigma(x)/x = 1.0\% \tag{7.12}$$
$$\sigma(z) = 1.7 \text{ mm} \tag{7.13}$$
$$\sigma(r) = 0.1 \text{ mm.} \tag{7.14}$$

The angular resolution for photons is defined by the spatial resolution of the calorimeter. The position of a photon or electron in the calorimeter is determined from the centre of gravity of the weighted shower distribution in neighbouring cells. The expected spatial resolution is about 1 to 2 cm for medium photon energies. It is a lot better than the granularity of the calorimeter which is 9×9 cm.

7.3   The Particle Identification Capabilities

The identification of electrons for the whole accessible momentum range is very good as the information from combination of the six TRD modules, the preshower and the calorimeter can be used simultaneously for each track.

For the separation of pions from kaons and protons the threshold Čerenkov (CER) is used with a threshold of 4.4 GeV for pions, 15.8 GeV for kaons and 30 GeV for protons. The spatial resolution is defined by the number of mirrors and photo-tubes which is $2 \cdot 20$ PMT's distributed equally over the whole angular acceptance.
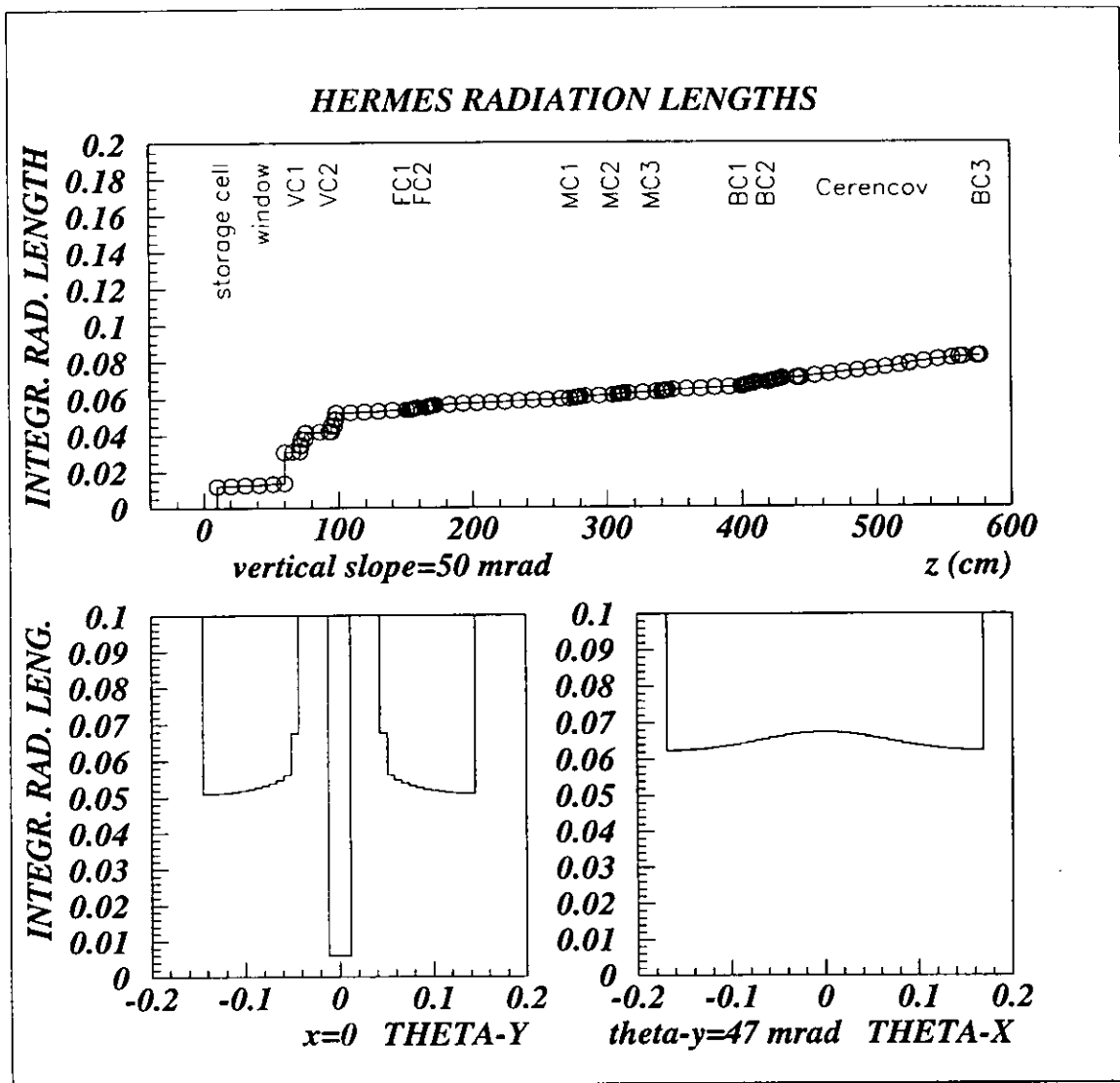
Figure 7.4: The upper plot shows the integrated radiation length which a particle experiences when it travels from the interaction point through the detector. A fixed angle of $\theta_x = 0$ and $\theta_y = 47$ mrad is chosen. The contribution of the cell, the exit window and the detector planes can be seen. The lower left plot shows the integrated radiation length of the material between the target and the magnet plotted versus the angle in the vertical plane. The septum plate and the frames of the chambers are clearly seen. The slow variation in the acceptance region is mainly due to the crossing of the storage cell at small, varying angles. The right plot shows the same quantities in the horizontal plane at a fixed vertical angle of $\theta_y = 47$ mrad. These plots were made for a special study and do not in every detail represent the current status of the detector. They show however all basic features.
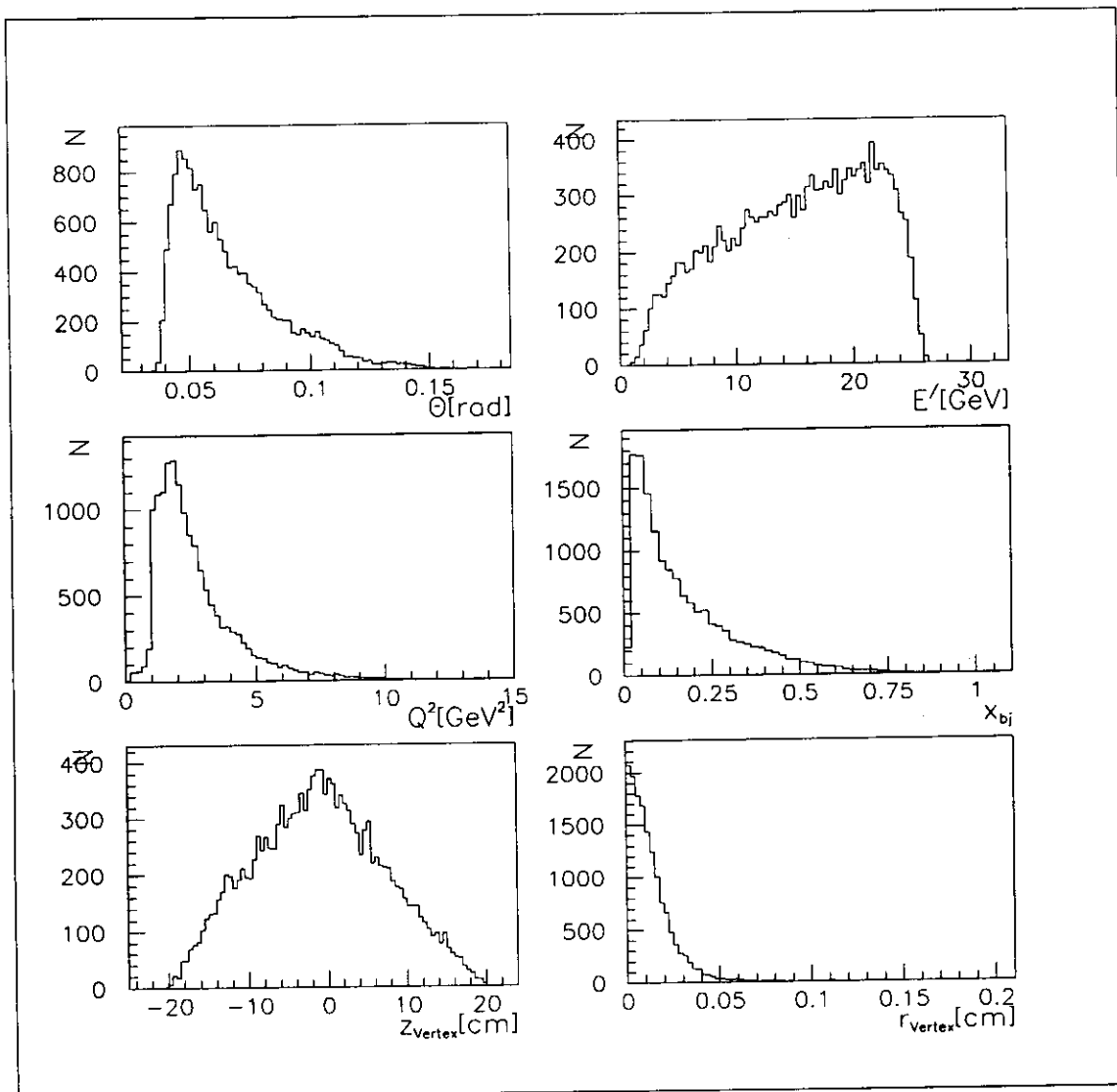
Figure 7.5: The distribution of Monte Carlo generated, reconstructed deep inelastic events is shown in the scattering angle θ, the scattered energy E', the momentum transfer Q^2, the scaling variable x, the longitudinal vertex distribution z and the radial vertex distribution r.
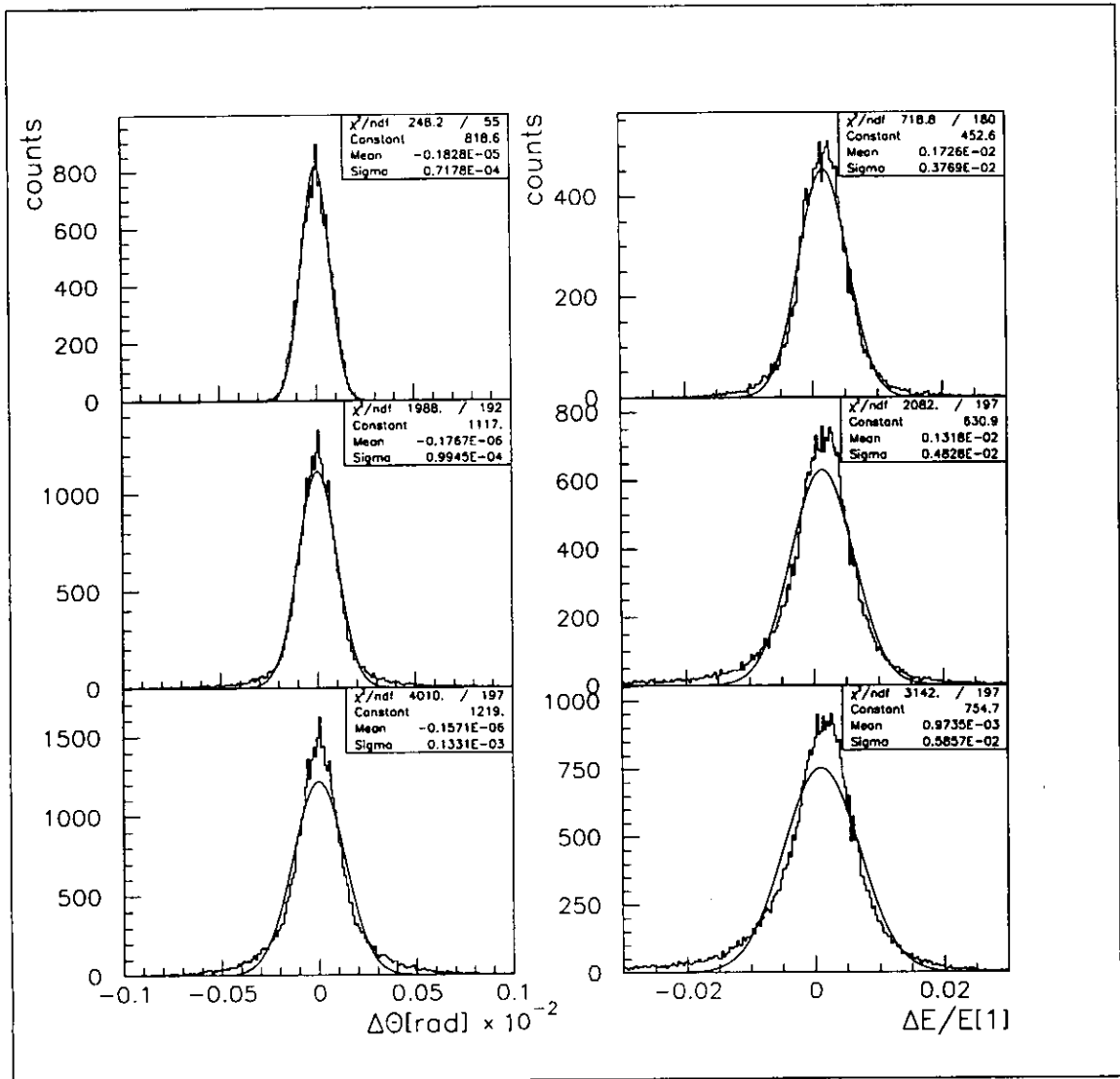
Figure 7.6: The smearing of the scattering angle θ and the scattered energy E' is plotted. The upper plot shows the smearing due to the interaction of the electrons with matter. The middle plot shows the smearing due to the finite resolution of the detectors. The lower plot shows the total resolution as combination of the two plots above. The detectors have been designed such that their resolution is less than the intrinsic resolution which is defined by the material.
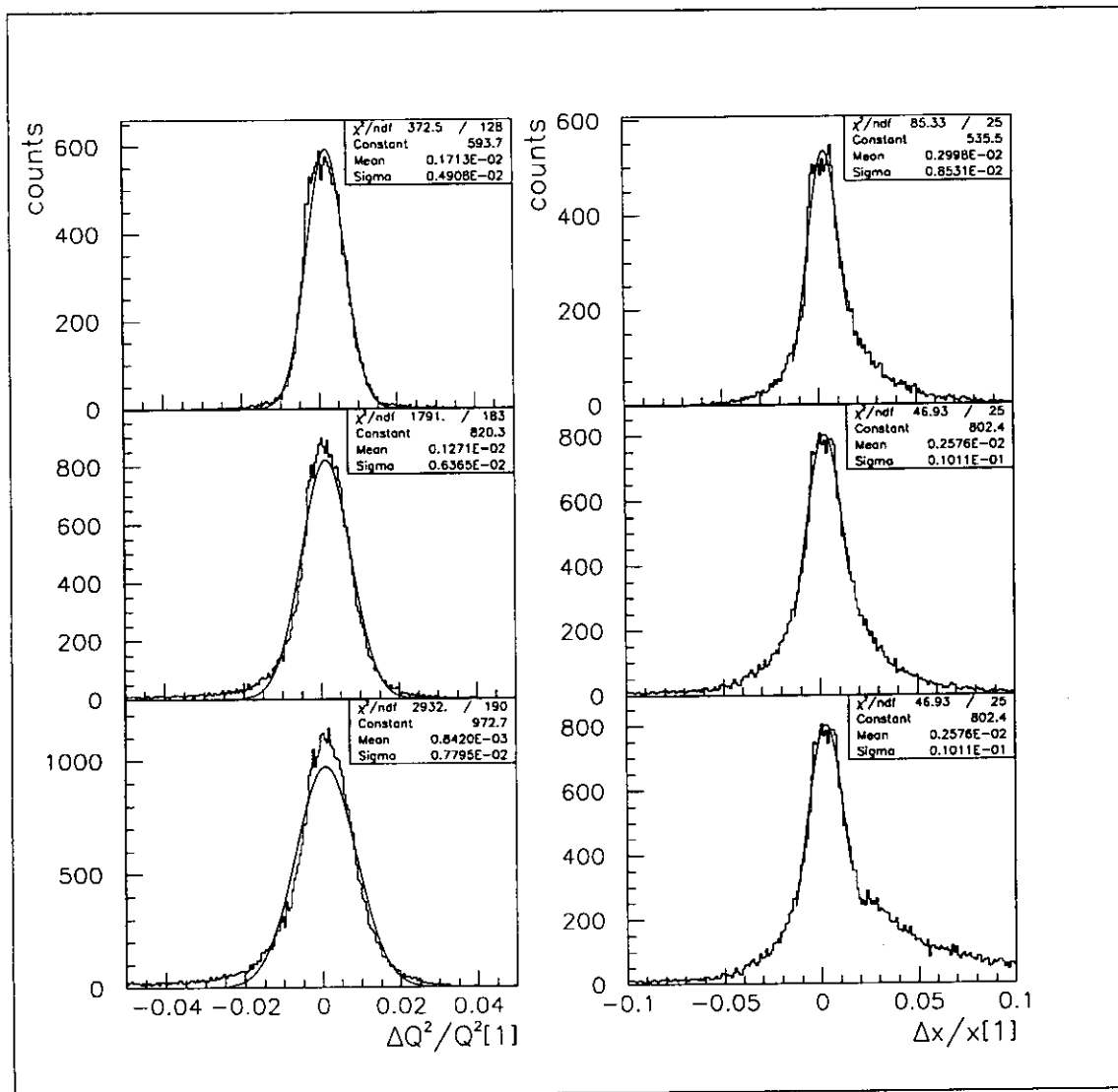
Figure 7.7: The smearing of the kinematic variables Q^2 and x is plotted. As in the previous figure, the contribution by the detector material (upper), by the detector resolution (middle) and the total resolution (lower plot) is given.
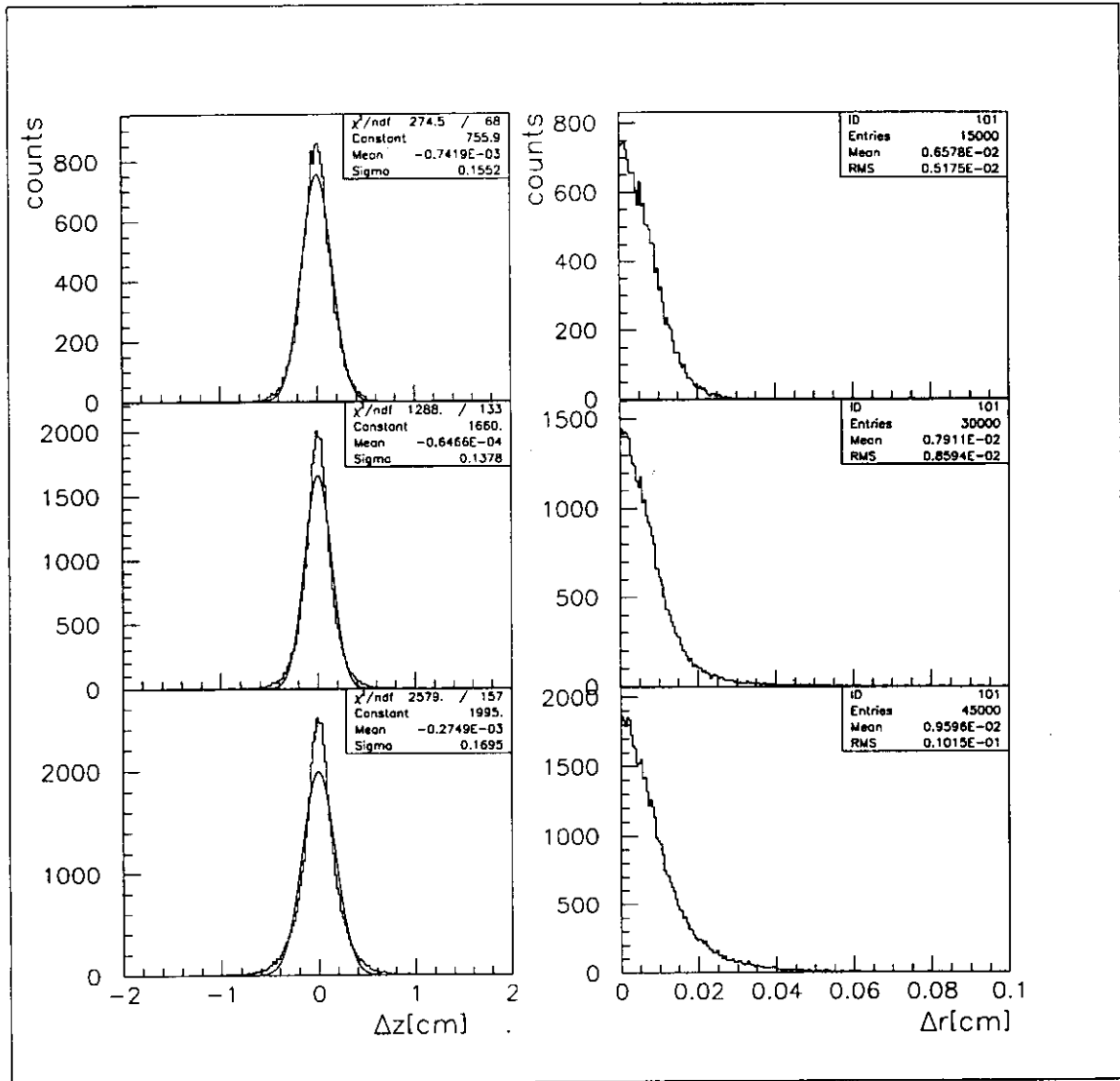
Figure 7.8: The smearing of the longitudinal and radial vertex coordinates z and r is plotted. As in the previous figures, the contribution by the detector material (upper), by the detector resolution (middle) and the total resolution (lower plot) is given.

Detailed studies of the identification methods and efficiencies are currently on-going and will be available soon. The particle identification capabilities can be upgraded by the installation of a RICH counter.

7.4   The Background Conditions

At the time of the proposal, the background conditions of an experiment which uses a storage cell in an electron beam were regarded as serious. The rates have been estimated and measures have been taken to reduce the background. The first data in the HERA environment have shown that the background is under control. The different sources of background will be outlined briefly:

Synchrotron Radiation

Synchrotron radiation is reduced by a special design of the machine lattice and is shielded by a collimator system as described in section 5.2.2. The remaining radiation is dominantly coming from the scattering off the target atoms. The estimated rate is of the order of a few hundred kHz in the acceptance of the chambers. The TRD is the detector which is most sensitive to synchrotron radiation as it is opti-mised to detect low energy photons.

Electron Beam Losses

The finite lifetime of the electron beam corresponds to a certain loss rate. For example a beam of 35 mA with a lifetime of 8 h has an average electron loss rate of 25 kHz/m around the circumference of the ring. As the HERMES collimators are the smallest relative and absolute apertures in the ring, it is expected that the losses happen over-proportionally in the HERMES region. The double collimator system is designed to absorb the showers which are generated [80]. When HERA runs electrons (and not positrons) positively ionised dust particles are trapped by the beam. While dust particles are crossing the orbit, spikes of Bremsstrahlung are generated and produce peak rates in the detectors. Currently HERA runs positrons so that this problem is not relevant.

Proton Beam Losses

Due to the very good lifetime, the beam losses of the proton machine are small. As in the HERMES region there are no small apertures in the proton beam pipe (relative to the beam size) and as the vacuum conditions are optimal ($< 10^{-10}$ mbar) the losses in this region are suppressed further. As proton bunches pass the detectors at different times than the electron bunches, the proton background is outside the trigger gates and can be largely suppressed.

Møller and Bhabha Scattering

Møller and Bhabha scattering off the target electron shell produces large rates, however the energy of the scattered electrons decreases with energy and is below 0.5 GeV in the acceptance of the detector [140]. The electrons which pass the acceptance will be swept away in the field of the spectrometer magnet and thus only affect the front detectors.

Photoproduction

Photoproduction processes are the dominant high energy background in the experiment. There is photoproduction off the target gas and off the restgas upstream the experiment. The expected rate of charged particles above the trigger threshold is in the kHz region for the ^3He standard luminosity. It has been calculated that the pion electron suppression is sufficient to handle the rates on the trigger level. As the total photoproduction rates are small compared to the bunch crossing time and to the drift times of the chambers, there should not be any relevant background which coincides with deep inelastic events.

7.5 The Estimated Statistical Accuracy

The Longitudinal Asymmetries

The measured longitudinal asymmetries are extracted from the number of events which are taken with the target spin parallel ($N^{\uparrow\uparrow}$) and anti-parallel ($N^{\uparrow\downarrow}$) to the electron spin in the following way:

$$A_{measured} = \frac{N^{\uparrow\downarrow} - N^{\uparrow\uparrow}}{N^{\uparrow\downarrow} + N^{\uparrow\uparrow}} .$$ (7.15)

The equation assumes equal luminosity and polarisation for both spin states. If that is not the case, the number of events has to be renormalised accordingly. With the assumption that $\sqrt{Q^2} \ll \nu$ follows from equation (2.33) that the virtual photon asymmetry A_1 is:

$$A_1 = \frac{1}{DfP_BP_T}A_{measured}$$ (7.16)

where D is the depolarisation factor of the virtual photon (see eq. (2.35)), f the dilution factor, P_B is the beam and P_T is the target polarisation. With the assumption that the measured asymmetries are small it follows that the statistical error δA_1 of the asymmetry is calculated from the total number of events $N = N^{\uparrow\uparrow} + N^{\uparrow\downarrow}$ as

$$\delta A_1 = \sqrt{\left\langle \frac{1}{(DfP_BP_T)^2} \right\rangle} \frac{1}{\sqrt{N}} .$$ (7.17)

The brackets $\langle \ \rangle$ denote the averaging over all events. While P_T should be basically stable, P_B changes with time due to the Sokolov-Ternov effect (see chapter 4.1) and

D and f depend on the kinematic variables x and y. From the above equation follows that the relevant figure of merit F averaged over the kinematic plane is:

$$F = \int (fP_BP_T)^2 L\, dt = (f\hat{P}_B P_T)^2 \frac{\eta\epsilon\hat{I}_B\rho_T}{e} t_{tot} \qquad (7.18)$$

with the following definitions:

$$
\begin{aligned}
L &= \text{luminosity,} \\
\hat{P}_B &= \text{equilibrium beam polarisation,} \\
\hat{I}_B &= \text{beam current at injection time,} \\
\rho_T &= \text{target thickness,} \\
\epsilon &= \text{combined running efficiency of HERA and HERMES,} \qquad (7.19) \\
t_{tot} &= \text{total running time,} \\
t_F &= \text{time of one HERA fill,} \\
e &= \text{electron charge and} \\
\eta &= \text{loss factor.}
\end{aligned}
$$

The loss factor η takes into account the polarisation rise time τ_P due to the Sokolov Ternov effect and the finite beam life time τ_B and is given by:

$$\eta = \frac{1}{t_F} \int_0^{t_F} (1 - e^{-t/\tau_P})^2 e^{-t/\tau_B}\, dt. \qquad (7.20)$$

Table 7.1 shows a summary of all parameters which were used for the calculation of the statistical precision of HERMES. The numbers are reasonable guesses for a running in 1995, they can however differ in detail due to changes in the performance of HERMES or HERA. Especially an increase of the beam polarisation seems to be possible. An improvement from 50% to 70% combined with an increase of the injected current from 35 mA to 53 mA would increase the figure of merit by a factor of about 3.

The asymmetry of the neutron A_1^n can be extracted from the asymmetries of deuterium (σ^D) and hydrogen (σ^H) cross sections by the formula

$$A_1^n = \frac{A_1^D}{1 - 1.5w_D} \frac{\sigma^D}{\sigma^D - \sigma^H} - A_1^H \frac{\sigma^H}{\sigma^D - \sigma^H}\,, \qquad (7.21)$$

where $w_D \approx 0.05$ denotes the D-state probability of the deuteron. The error of the asymmetry is obtained as

$$\delta A_1^n = \sqrt{\left(\frac{\delta A_1^D}{1 - 1.5w_D}\frac{\sigma^D}{\sigma^D - \sigma^H}\right)^2 + \left(\delta A_1^H \frac{\sigma^H}{\sigma^D - \sigma^H}\right)^2} \qquad (7.22)$$

where δA_1^D and δA_1^H are calculated according to equation (7.17). It has been shown that the error on the neutron structure function is minimised when the beam time is shared approximately equally between the targets (H:D=43:57) [140] assuming that the deuteron target has twice the nucleon density compared to the hydrogen target.

Table 7.1: A standard run at HERMES is defined as a running time of the experiment over 9 weeks under conditions of the HERA beam and the HERMES target which are realistic in 1995 but may be improved at a later stage of the experiment. It is planned to run the experiment in the following years in parallel with ZEUS and H1 for approximately 7 months per year.

Target	H	D	^3He	[Unit]
ρ_T	10^{14}	$2 \cdot 10^{14}$	10^{15}	nucleons/cm^2
$\hat{I}_B$	35	35	35	mA
L	$2.1 \cdot 10^{31}$	$4.2 \cdot 10^{31}$	$2.1 \cdot 10^{32}$	nucleons/cm^2/s
$\hat{P}_B$	0.5	0.5	0.5	
P_T	0.8	0.8	0.5	
f	1	1	$\sim$0.33	
t_F	8	8	8	h
τ_B	8	8	8	h
τ_P	20	20	20	min
η	0.57	0.57	0.57	
t_{tot}	9	9	9	weeks
ϵ	0.33	0.33	0.33	
F	3.6	7.2	1.6	pb^{-1}

The asymmetry of the neutron can also be extracted from the asymmetry of ^3He. As the spins of the two protons in ^3He are anti-parallel the scattering off those protons appears as a dilution factor f in the asymmetry formula. The neutron asymmetry and its error is extracted by the following formulas:

$$A_1^n = \frac{A^{He}}{DP_BP_Tf} \tag{7.23}$$

$$\delta A_1^n = \sqrt{\left\langle \frac{1}{(DP_BP_Tf)^2} \right\rangle} \frac{1}{\sqrt{N^{He}}} \tag{7.24}$$

with

$$f(x) = \frac{1}{1 + 2F_2^p(x)/F_2^n(x)}. \tag{7.25}$$

$F_2^p(x)/F_2^n(x)$ is the known ratio of the unpolarised structure functions.

The Transverse Asymmetries

The transverse asymmetry is measured by scattering the longitudinally polarised beam off the transverse polarised target and observing asymmetries when the target spin is flipped. As the cross section formula (see equation (2.31)) involves a $\cos \phi$ term, only those events contribute to the asymmetry, for which the scattering plane is approximately parallel to the target polarisation direction. Experimentally the conditions

$$|\phi| < 45° \quad \text{or} \quad |\phi + 180°| < 45° \tag{7.26}$$

$$\text{i.e.} \qquad |\cos \phi| > 0.7 \tag{7.27}$$

are introduced which select events with large contribution to the asymmetry. These conditions match well the acceptance of the spectrometer which has zero acceptance in the horizontal plane. The target polarisation direction has to be vertical.

One way to extract the transverse asymmetry is to calculate the following weighted sum:

$$A_\perp = \frac{1}{N} \sum_{i=1}^{N} \frac{1}{\cos \phi_i}. \tag{7.28}$$

ϕ_i is the azimuthal angle of the scattered electron compared to the polarisation direction of the target in the plane perpendicular to the beam axis. The statistical error of the $A_\perp$ determination is calculated by the formula

$$\delta A_\perp = \sqrt{\left\langle \frac{1}{(D f P_B P_T \cos \phi)^2} \right\rangle / \frac{1}{\sqrt{N}}}. \tag{7.29}$$

The Spin Structure Functions

The statistical accuracy of the spin structure functions can be directly derived from the accuracy of the asymmetries. From the relations

$$A_1 \approx \frac{g_1}{F_1} = \frac{2x(1+R)}{F_2} g_1 \tag{7.30}$$

$$\text{and} \quad A_2 \approx \frac{\sqrt{Q^2}}{\nu} \frac{2x(1+R)}{F_2} (g_1 + g_2) \tag{7.31}$$

one obtains

$$\delta g_1 \approx \sqrt{\left\langle \left(\frac{F_2}{2x(1+R)} \right)^2 \right\rangle} \delta A_1. \tag{7.32}$$

Using the relation

$$a_\perp \approx A_2 - \xi A_1 \tag{7.33}$$

with

$$\xi \approx \eta = \frac{2(1-y)\sqrt{Q^2}}{Ey(2-y)} \tag{7.34}$$

one obtains

$$\delta g_2 \approx \sqrt{\left\langle \left(\frac{\nu}{\sqrt{Q^2}} F_1 \right)^2 \right\rangle (\delta a_\perp)^2 + \left\langle \left(\frac{y}{2-y} F_1 \right)^2 \right\rangle (\delta A_1)^2}. \tag{7.35}$$

Numerical Results

For the calculation of the expected rates and the statistical accuracies the cuts and parameters from equation (7.1) to (7.8) and from table 7.1 have been used. Table 7.2 shows the calculated acceptances and the total number of events for a standard run

Table 7.2: The mean Q^2 value, the acceptance of the spectrometer and the number of events for a standard run of the hydrogen target are given.

x-range	$\langle Q^2 \rangle$ (GeV^2)	accept. (%)	acc.ev.
0.02 - 0.03	1.1	66.5	17,600
0.03 - 0.04	1.2	61.0	52,700
0.04 - 0.06	1.5	55.2	124,100
0.06 - 0.10	1.9	49.1	218,200
0.10 - 0.15	2.3	44.9	206,900
0.15 - 0.20	2.6	44.8	156,100
0.20 - 0.30	2.9	45.4	213,200
0.30 - 0.40	3.6	55.5	105,900
0.40 - 0.50	4.7	62.8	42,800
0.50 - 0.60	6.1	66.7	14,600
0.60 - 0.70	8.1	66.5	3,700
0.70 - 0.80	10.8	57.5	500
0.02 - 0.80	2.5	49.2	1,156,500

of the hydrogen target for various bins in x. The radiative corrections are neglected in this and the following tables. The mean Q^2 value of the data increases with x by almost one order of magnitude. A standard run corresponds to about 1.2 billion accepted hydrogen events, 2.1 billion deuteron and 12.6 billion ^3He events.

Table 7.3 shows the rate of accepted events for the hydrogen, deuteron and ^3He target and for the events used for the analysis of the transverse target polarisation which includes a cut in the azimuthal angle. The rate corresponds to the maximal rate after beam injection of $\hat{I}_B = 35$ mA.

Table 7.4 shows the accepted number of events for one standard hydrogen run split into different x and Q^2 bins. It can be seen that with the proposed binning about 2–3 Q^2-bins are filled with reasonable statistics for every x-bin.

The total number of accepted events in a standard run is used to calculate the accuracies of the asymmetries as shown in table 7.5 and of the spin structure functions as shown in table 7.6. The corresponding figures were shown already in section 2.2. Two runs (H-D) or (H-^3He) are needed to extract both, the proton and the neutron structure functions. The statistical accuracy for the neutron structure function is similar for the ^3He target and for the (H-D) subtraction. The number of events to analyse is however a factor 5 larger in the case of the ^3He target. From the figure of merit F as shown in table 7.1 one could naively expect that the $H - D$ measurements have a much smaller error than the ^3He measurements. This is not the case as the error propagation in formula 7.22 acts approximately like an effective dilution factor of $f = 1/3$.

Table 7.3: The peak event rate with a current of $I_B = 35$ mA is shown for the hydrogen, deuterium and ^3He target. $H_\perp$ denotes the fraction of the event rate used in the transverse spin analysis.

x-range	$\langle Q^2 \rangle$ (GeV^2)	H (Hz)	D (Hz)	^3He (Hz)	$H_\perp$ (Hz)
0.02 - 0.03	1.1	0.018	0.035	0.205	0.014
0.03 - 0.04	1.2	0.053	0.101	0.596	0.043
0.04 - 0.06	1.5	0.125	0.235	1.394	0.107
0.06 - 0.10	1.9	0.223	0.414	2.468	0.192
0.10 - 0.15	2.3	0.208	0.377	2.265	0.178
0.15 - 0.20	2.6	0.156	0.276	1.673	0.135
0.20 - 0.30	2.9	0.214	0.366	2.248	0.184
0.30 - 0.40	3.6	0.106	0.172	1.076	0.088
0.40 - 0.50	4.7	0.043	0.066	0.421	0.032
0.50 - 0.60	6.2	0.014	0.021	0.134	0.009
0.60 - 0.70	8.1	0.004	0.005	0.035	0.002
0.70 - 0.80	10.8	0.001	0.001	0.005	0.000
0.02 - 0.80	2.5	1.165	2.067	12.518	0.984

Table 7.4: Number of accepted events for different Q^2-bins for a standard run of the hydrogen target.

$x \backslash Q^2 (GeV^2)$	1 - 2	2 - 4	4 - 8	8 - 20
0.02 - 0.03	17.6	0.0	0.0	0.0
0.03 - 0.04	52.7	0.0	0.0	0.0
0.04 - 0.06	112.0	12.1	0.0	0.0
0.06 - 0.10	140.5	77.3	0.4	0.0
0.10 - 0.15	105.8	85.7	15.4	0.0
0.15 - 0.20	69.2	63.4	23.6	0.0
0.20 - 0.30	82.9	87.2	41.3	1.8
0.30 - 0.40	19.6	54.0	28.0	4.4
0.40 - 0.50	0.0	21.8	17.0	4.0
0.50 - 0.60	0.0	2.1	9.7	2.8
0.60 - 0.70	0.0	0.0	2.1	1.6
0.70 - 0.80	0.0	0.0	0.0	0.5

Table 7.5: Statistical accuracies for $\delta A(x)$ for a standard run are given. The asymmetry of the neutron can be extracted from the ^3He target and from the difference of the H and D targets with similar statistics. $a_\perp \approx A_2 - \xi A_1$ denotes the transverse asymmetry.

x-bin	δA_1^p (H)	δA_1^d (D)	δA_1^n (D-H)	δA_1^n (^{3}He)	$\delta a_\perp^p$ (H)
0.02 - 0.03	0.021	0.015	0.040	0.035	0.027
0.03 - 0.04	0.014	0.010	0.026	0.023	0.017
0.04 - 0.06	0.011	0.008	0.022	0.019	0.014
0.06 - 0.10	0.012	0.009	0.024	0.021	0.015
0.10 - 0.15	0.018	0.013	0.036	0.032	0.022
0.15 - 0.20	0.027	0.020	0.058	0.051	0.033
0.20 - 0.30	0.031	0.024	0.073	0.064	0.038
0.30 - 0.40	0.048	0.038	0.124	0.109	0.062
0.40 - 0.50	0.069	0.056	0.203	0.178	0.094
0.50 - 0.60	0.102	0.084	0.349	0.306	0.145
0.60 - 0.70	0.166	0.142	0.689	0.604	0.248
0.70 - 0.80	0.351	0.309	1.819	1.592	0.579

Table 7.6: Statistical accuracies for the spin structure functions $g(x)$ are shown. The errors correspond to a standard run of 9 weeks.

x-bin	δg_1^p (H)	δg_1^d (D)	δg_1^n (D-H)	δg_1^n (^{3}He)	δg_2^p (H)
0.02 - 0.03	0.089	0.062	0.153	0.134	2.383
0.03 - 0.04	0.048	0.033	0.083	0.073	1.014
0.04 - 0.06	0.030	0.020	0.052	0.045	0.459
0.06 - 0.10	0.022	0.015	0.039	0.034	0.225
0.10 - 0.15	0.022	0.015	0.038	0.034	0.150
0.15 - 0.20	0.025	0.016	0.042	0.037	0.122
0.20 - 0.30	0.020	0.013	0.033	0.029	0.072
0.30 - 0.40	0.019	0.012	0.030	0.027	0.060
0.40 - 0.50	0.017	0.010	0.025	0.022	0.050
0.50 - 0.60	0.013	0.008	0.020	0.018	0.042
0.60 - 0.70	0.011	0.006	0.016	0.014	0.035
0.70 - 0.80	0.009	0.005	0.014	0.012	0.035

Accuracies of the Sum Rules

The statistical error for the Ellis-Jaffe, Bjørken and Burkhardt-Cottingham sum rules can be directly extracted from the integration of the spin structure functions over the x-range which is accessible for HERMES:

$$\delta I = \delta \int_{0.02}^{0.8} g(x)\, dx \; . \tag{7.36}$$

The absolute errors can be directly calculated from the information in table 7.6. The calculation of the relative errors requires the knowledge of the absolute values of the integrals. The values of SLAC, SMC and EMC were used for this purpose. The results are summarised in table 7.7. The smallest relative errors of the Ellis-Jaffe sum rule are achieved with the hydrogen target (3%). The error in the neutron sum rule is large (15 − 20%) due to the small absolute value of the integral. The statistical precision of the Bjørken sum is of the order of 5-7%. The precision is better using the ^3He target instead of the H/D targets. The precision can not be significantly improved by sharing the beam time between H and D asymmetrically.

The statistical error on the Burkhardt-Cottingham sum rule is dominated by contributions at low x. From table 7.6 can be seen that the error of δg_2 for the first two x-bins is larger than one. By raising the lower integration limit the statistical error can be improved significantly to the cost of the theoretical uncertainty in the extrapolation to zero.

Certainly, the statistical errors of all sum rules can be decreased by having longer running periods compared to the standard run of 9 weeks.

Table 7.7: The absolute and relative statistical accuracies for the sum rules for one standard run of each target. The assumed value I of the sum rule is taken from recent data.

Sum Rule	Target	I	δI	$\delta I/I$
Ellis-Jaffe:				
p	H	0.13	0.0043	3%
(p+n)/2	D	0.04	0.0028	7%
n	$D - H$	-0.04	0.0070	18%
n	^3He	-0.04	0.0062	16%
Bjørken:				
p-n	$2H - D$	0.16	0.0103	6.4%
p-n	$H-^3He$	0.16	0.0075	4.7%
Burkhardt-Cottingham:				
p	H	0	0.0327	∞

7.6   The Estimated Systematic Precision

The systematic error of the beam and target polarisation enters linearly into all asymmetry measurements. The predicted precision for the HERA transverse and

for the longitudinal polarimeter is $\Delta P_B/P_B = 2.5\%$. The target polarisation is measured in all targets with an estimated precision of $\Delta P_T/P_T \leq 3\%$.

The radiative corrections are under control as well for the inclusive as for the semi-inclusive measurements. Uncertainties come from the radiative tails in the resonance region and other parts of the kinematic area which HERMES cannot access directly. The cut of $y < 0.85$ excludes areas where the radiative corrections dominate. The radiative corrections are typically smaller than 5%. The error on the correction is assumed to be less than 15% of the spin-dependent correction factor. The nuclear corrections in the case of ^3He have an uncertainty of about 5%.

The extraction of the spin-structure functions requires the knowledge of the unpolarised structure functions. The estimated errors are $\Delta F_2(x)/F_2(x) = 3\%$ and $\Delta R(x) = 0.03$. The uncertainty of R cancels mostly in the extraction of $g_1(x)$.

The instrumental asymmetries are expected to be small. As soon as the data are available, many cross check will be done to verify that statement.

The total uncertainty of the spin structure functions are obtained by adding up all contributions in quadrature. The errors in the sum rules are obtained calculating the total errors for each x-bin separately and than adding them all up. As the values of the integrand can be negative, the relative error of the sum rule is typically larger than the relative error in the structure function determination. Table 7.8 gives a summary of the systematic errors in the sum rules. This list does not include theoretical uncertainties which come from the extrapolation of the integral in the non-measured region, especially at $x < 0.02$.

Table 7.8: Systematic uncertainties in the sum rules.

Sum Rule	R	P_B, P_T, F_2	rad.corr.	nucl.corr.	tot.syst.
Ellis-Jaffe:					
H	0.2%	4.9%	1.2%	-	5.2%
D-H	0.2%	10.1%	4.0%	-	11.0%
^3He	0.2%	4.9%	3.3%	5%	7.8%
Bjørken:					
2H–D	0.2%	6.0%	1.6%	-	7.1%
$H-^3He$	0.2%	3.6%	1.4%	1.7%	4.3%

The errors for the semi-inclusive measurements are similar to the inclusive ones. An additional uncertainty comes from particle identification of pions and kaons. For the charge asymmetries $\pi^+ - \pi^-$ the instrumental uncertainties are expected to be less than 5%. The total uncertainties in the extraction of the valence quark spin content can be calculated only when the certain model for the spin contributions is assumed. Using the Schäfer model [141] as input, the predicted accuracy is:

$$\delta \int_0^1 \Delta u^v(x)\, dx = 0.09 \tag{7.37}$$

$$\delta \int_0^1 \Delta d^v(x)\, dx = 0.05 . \tag{7.38}$$

Chapter 8

Preparation of the Physics Analysis and First Results

HERMES has very ambitions plans concerning the time scale of the physics analysis. The detector is new and its construction has finished just before data taking in spring '95. The plan is to have the first physics results ready a few months after the end of the data taking period in '95. In order to achieve this goal, a strict organisation of the analysis is needed. Expertise about the systematic uncertainties of the experiment requires more than the understanding of each part of the detector separately.

From the beginning of data taking, the following task forces have been established which concentrate on specific jobs, most of which cover comprehensive aspects of the analysis:

- the calibration of all detector types;

- the efficiency calculation of the tracking detector system and of the trigger system;

- the precise alignment of all tracking detectors;

- the track and vertex reconstruction;

- the particle identification methods;

- the extraction of luminosity and polarisation;

- a comprehensive real-time analysis;

- a well organised off-line data production;

- a detailed Monte Carlo simulation and

- the preparation of radiative correction methods.

An additional organisational structure are the 'physics subgroups' which concentrate on specific corrections and systematic errors of a certain physics process. Table 8.1 gives an overview of the current physics topics of HERMES. They correspond

to the topics described in chapter 2. The most important topics (like the extraction of $g_1(x)$) will be covered by two independent groups in parallel to allow for a cross check of the results.

Table 8.1: Specific Physics Analysis Subgroups

Spin Structure Functions
$g_1^{p,d,He}(x,Q^2)$, Ellis-Jaffe and Bjørken sum rules, α_s from Bjørken sum rule, QCD corrections
$g_2^{p,d,He}(x,Q^2)$ (twist-3, Burkhardt-Cottingham sum rule)
$b_1(x)$ and $\Delta(x)$ of deuteron
resonance production
Polarised Semi-Inclusive Physics
π asymmetries and valence quark flavour decomposition
K asymmetries and strange sea polarisation
azimuthal asymmetries: quark angular momentum
J/ψ production and anomalous gluon contribution
Λ production
gluon contribution acc. to ref. [78] (λ parameter)
production of ϕ-mesons
g_1 with a tagged neutron (suppression of nuclear effects)
chiral-odd structure function $h_1(x)$
Unpolarised Physics
$F_2^{p,n,He}(x,Q^2)$: absolute structure functions
π asymm. of D and H: flavour distribution of valence quarks
$r(x,z)$: flavour asymmetry of the sea
$(e,e'\pi)$: A-dependence of hadronisation
π content of the nucleon
ρ production

8.1   Concepts of the HERMES Software

HERMES is a high statistics experiment with a complex detector, large data through-put (~ 50 billion events/year) and with the need of detailed large-scale Monte Carlo simulations. It is obvious that a high quality of reconstruction, simulation and analysis software is essential for an efficient and precise understanding of the data. HERMES is compared to other high energy experiments relatively small and there-fore in principle cannot afford to do its own software developments on a large scale. Nevertheless quite a few software developments have been done and it turned out that the persistent persecution of a few basic principles paid off afterwards.

HERMES uses as programming languages C, FORTRAN77 and TCl/Tk [142] and makes extensive use of the CERN software libraries [143]. The software is written

machine independent to a large extend, although HERMES currently almost only uses UNIX systems. All program packages are as modular as possible and have a 'keeper' who is responsible for upgrades, debugging and documentation. The source code and the documentation is kept in World Wide Web (WWW) so that all collaborators have access to the latest releases.

'Data Driven' Programming

One basic principle of the software is that all programming is 'data driven' as much as possible. This means that the program should only contain the (generalised) algorithms whereas all specific information (i.e. information which can be expressed in numbers or character strings) is stored in a data base in an easily understandable way, so that they can be modified and checked by anybody, not only by the programmer. A good example is the geometry definition in the HERMES Monte Carlo program (HMC): instead of defining the geometry of the detectors in the source code of HMC, a data base has been defined that contains all details of the geometry and the materials of the spectrometer. The data base knows for example that there is a drift chamber at a certain position with a certain number of planes. It contains the number of wires in each plane, the distances, the materials of the wires and many more informations. A general interface to this data base has been written that builds up internally a list of volumes that are needed to describe the drift chamber including frames, materials etc. The list of volumes is passed to the GEANT [144] tracking routines whereas the number of wires is passed to the digitisation routine in HMC which automatically produces the TDC signals and writes them to an output stream. The reconstruction program and the event display use the same database which ensures that they use identical geometry descriptions.

The concept of 'data driven' programming allows that this software is applicable to other experiments without major changes. We had benefited from this concept already in the HERMES test experiment in 1994, which had a significantly different set-up compared to the real experiment. Nevertheless the simulation and reconstruction software could be used easily for this experiment as soon as the data base has been set up appropriately.

A Uniform and Safe Data System

A second basic principle is that all program packages use a unique data system. We have chosen ADAMO [145] as it is the only one which fulfils our requirements and at the same time is compatible with programming in FORTRAN and C. In ADAMO all data are stored in tables. Before writing a program, the tables are defined using a specific 'data definition language' (DDL). Unique table and column names are given to each entity, together with a type declaration, the allowed range and a comment that describes the meaning of the entity. An example is the table 'mcHits' (Monte Carlo Hits) and the column with the name 'X', which contains the x-coordinate of the Monte Carlo hits. The user and the programmer always refer to the variable by the name mcHits_X. Common sources of errors that come from mixing up array indices or pointers, overwriting arrays, or misinterpreting variables are excluded in

ADAMO to a large extend. ADAMO can check the existence and the allowed range of the variables internally.

Additionally, ADAMO can be used to define relationships between the rows of tables which allows to create hierarchical data structures without having to handle pointers. Each relationship is defined in DDL and a unique name is assigned to it. The DDL allows to generate automatically the documentation of all data structures.

One big advantage of ADAMO is its unique I/O format which contains the definition of the variables in the header of each data file in addition to the general definition in the DDL of the program. This makes it is possible to read certain variables (referred by table & column name) without knowing before the specific data format on the file which is read. This is especially useful when data formats are changing during the development phase of the experiment and of the program.

An example which demonstrates the advantage of both, the modular programming and the unique data system is the event display (EVE) [146]: the GEANT based drawing package of the Monte Carlo program was originally designed to display the digitised information of Monte Carlo events. Without any (major) modifications the same program could be adapted to the 'real' data coming from the on-line data stream. Although the data format in detail is different, the real data are interpreted by the program in the right way as all entities are referenced by unique table and column names.

Our system allows for a trivial way of writing what is usually called a MINI-DST or MAXI-DST: The I/O in ADAMO is controlled by a construct called 'dataflow'. A dataflow is a list of tables (or sub-dataflows) which is defined in DDL. Only the tables defined in the dataflow are written to tape. 'Selectors' can be specified which select a subsample of rows. A MINI-DST is produced by simply reducing the number of tables, rows and columns in the dataflow according to the needs of the application. As each data value is defined by a unique table name, column name and row identifier, the application program is able to read any type of MINI-DST without having to change source code.

The Interactive Data Access

The data format of ADAMO allows for an interactive access of the data to an extend which is superior to most other systems. A program called HEP (HERMES Event Processor) [147] based on the CERN packages PAW (Physics Analysis Workstation) [148] and TIP [145] allows to read any (ADAMO) data file, access the values, manipulate them using the FORTRAN interpreter COMIS [149] and histograming them using the PAW functionality. This way, most of the physics analysis can be done in principle interactively.

The ADAMO system has been extended by us with an object oriented interface called PINK [150] which is based on the TCl/Tk language and allows for an easy high level programming of graphic user interfaces. PINK is used extensively in the HERMES experimental control system.

The Distributed Client–Server Systems

The data analysis requires a large amount of various time-dependent information. Examples are alignment and calibration constants, polarisation values, geometry modifications etc. Storing the information in many different files always contains the danger to mix them up. In addition, as HERMES is an intercontinental collaboration, a system is needed which allows to keep outside collaborators always up to date without large administrative overhead. Therefore it has been decided to extend the ADAMO data system by a package called DAD (distributed ADAMO database) [151], which automatically distributes updates of values using either local networks or the world wide INTERNET system. DAD can be used as follows: if a program needs e.g. the calibration value of a detector for a certain event, it sends a request to a calibration DAD-server which is installed somewhere on the INTERNET. This DAD-server sends back an ADAMO table that contains the requested information in combination with a validity range of the data that are stored in the table. The DAD software is able to serve many clients at the same time. DAD-servers have the capability to wake up clients in case a modification of the data-base has occurred. The DAD system is also used for passing slow control commands to so-called hardware clients which directly control the spectrometer hardware. As well HEP as PINK have interfaces to the DAD system to allow for a user friendly interactive access to all HERMES data bases.

8.2 Overview of the Analysis Chain

Figure 8.1 shows a flow-chart of the on- and off-line data processing at HERMES. The whole reconstruction and analysis chain is set up in a way that it can be used on-line as well as off-line. The raw data, as they come from the data acquisition system are written to tape robots and at the same time a sub-sample is used for real-time analysis. A high level of on-line analysis during data taking is an essential presupposition for an efficient utilisation of beam-time, especially in the running in phase of a new detector. The aim of the on-line analysis is to recognise problems in the detector early and thus be able to fix them immediately during the data taking period. A number of high level check tasks control the quality of the data in real time and alarm the data taking crew if anomalies are found in the data. One example is that the efficiencies of all wire chambers are periodically calculated and compared with default conditions.

The Decoding

The first stage of data processing is done with a general decoder program (HDC) [152] which reads the raw data format and uses mapping tables to assign the signals from the hardware channels to the corresponding detectors. In the next step calibration tables are applied to convert the ADC or TDC channel numbers into energies or relative positions respectively. Dead wires are marked for the further analysis and noisy wires are suppressed to reduce the event size. Clusters of wires are recognised.

HERMES On- and Off-Line Processing

HERA/polarimeter

TARGET DETECTOR

ELECTRONICS READOUT REMOTE CONTROL

RAW DATA

EVENT staging and distribution

local TAPES

TAPE ROBOTS

experimental control

On-Line Pre-Analysis

Off-Line Analysis

data base server

HERMES Analysis Chain (HAC)

run summaries:
bookkeeping
histograms
message logging

event environment:
beam polarization
target polarization
luminosity
slow control status

detector parameters:
efficiencies
calibrations
alignment
mapping tables

detector constants:
geometry
materials
detectors

HERA beam parameter
HERA polarimeter program
target programs
luminosity program

alignment program
calibration programs
efficiency program
(ACE)

monte carlo (HMC)
physics generators
detector geometry
digitizations

RADCOR

Decoder (HDC)

reconstruction (HRC)
detector processors
pattern recognition
track fitting
vertex fitting
particle identification

event processor (HEP)
event filter
data/MC ratios
cuts/corrections
histogramming

reconstructed events

event display (EVE)

histogram display (PAW/HEP)

Figure 8.1: Overview of the on- and off-line data processing. The raw data are written to tape robots and a subsample is used for real-time analysis. The analysis chain consists of a general decoder, the reconstruction program and event processors that analyse and histogram the events. Single events can be studied with the event display. The measured distributions are compared with predictions that are generated by a detailed Monte Carlo program. Calibration programs extract alignment, efficiency and calibration data and send the results to a general data base. Analysis programs extract the polarisation and luminosity related quantities and also send them to a data base. The same data base contains also the running conditions of the experiment and the status of the hardware components.

Relative positions are converted to absolute positions by making use of the geometry and alignment tables.

All mapping, calibration, alignment and geometry tables are supplied by data base servers from outside the program in accordance with our philosophy of data driven programming. This allows a rearranging of detectors or electronics without having to modify the program. Most of the data tables are time dependent. The program checks for each event the validity range of the conversion tables and requests new tables if the range is expired, making use of the 'update feature' of the DAD system.

The output of the decoder program is a series of ADAMO tables for each event which contain the decoded quantities as well as the original channel numbers in a self-explaining format. As in ADAMO a unique table and column name is assigned to every quantity and relation, it is very easy to use the decoded quantities in the reconstruction and analysis programs.

The Reconstruction and Particle Identification

The HERMES reconstruction program (HRC) [153] is the central software package in the data analysis. It converts the decoded informations from the various detector modules into physics quantities like tracks, energies, angles, particle types and vertices. Like the decoder it makes use of various data base servers which supply information about geometries, calibrations, efficiencies and alignment parameters.

The reconstruction of all data is done centrally on a computer cluster at DESY. It is planned to reconstruct the data quasi immediately after data taking by distributing the events to different processors and collecting the reconstructed events in a single file. A reprocessing of the data is done as soon as all calibrations are finalised.

The Event Processor and Event Display

The HERMES event processor (HEP) is a general tool which allows to filter events, apply cuts and histogram the results. It is used on- and off-line. For the quality check of the data a set of standard histograms is filled at real time and is available for manual check by the data taking crew and for automatic check by programs which compare it to default histograms with given tolerances.

A single event display (EVE) gives a fast and intuitive insight into the performance of the detector and the background conditions. Single events can be reconstructed on-line and the result can be compared with eye-fits in the various detector views. Figure 8.2 shows an example of an on-line reconstructed event.

The Calibration Programs

Before a final reconstruction of the events is possible the precise determination of the calibration, alignment and efficiency parameters of all detector components is needed. A sub-sample of the events is used to extract those numbers using the ACE (alignment, calibration, efficiency) [154] programs which are based on HEP.
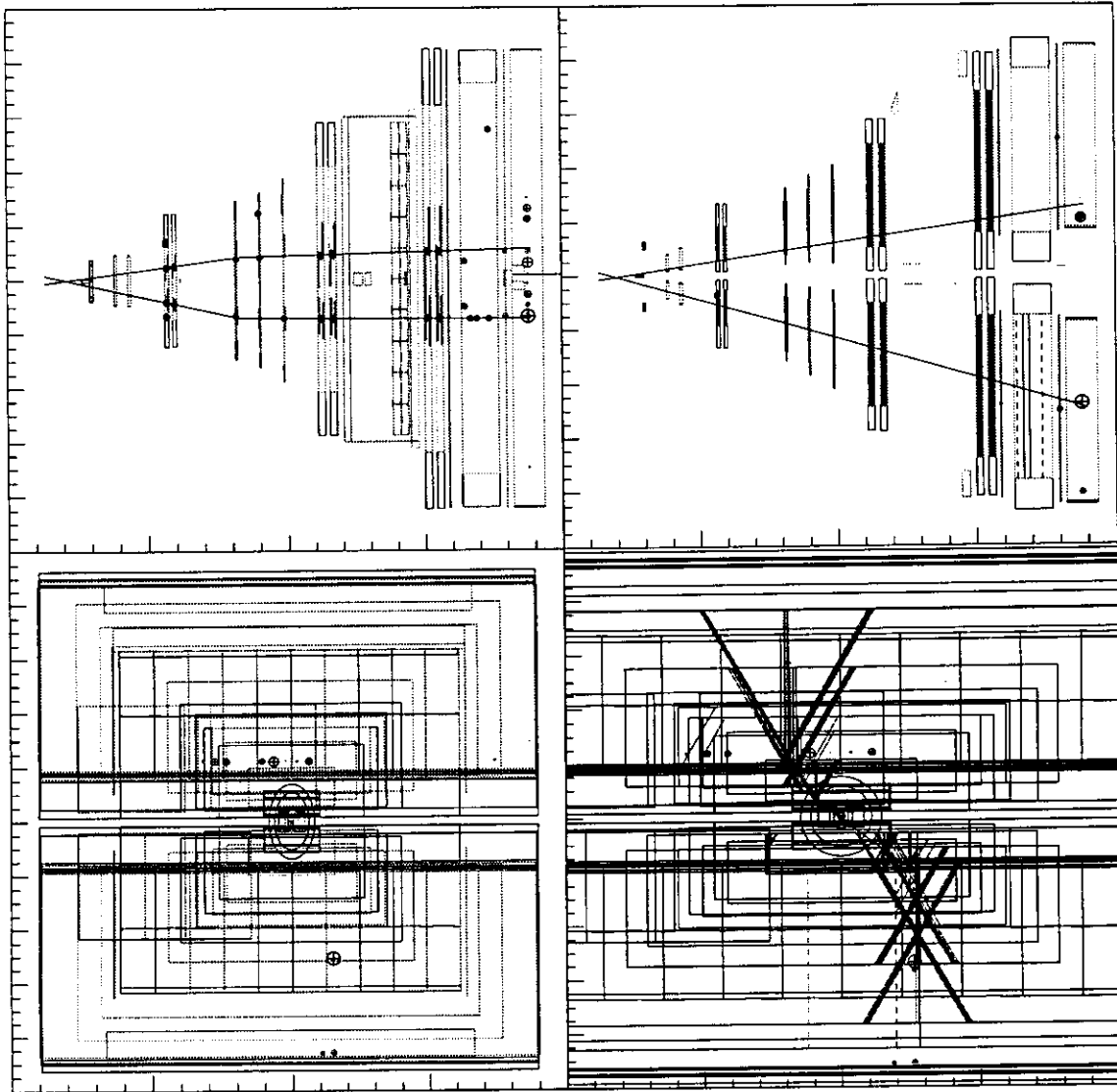
Figure 8.2: Display of an on-line reconstructed event. The upper left (right) figure shows a top (side) view of the detector. The lower figures show the projection in beam direction. The left plot indicates the calorimeter signals and the right one the hits in the wire chambers. The hits in wire chambers are indicated as projections of the wires. For projections where the wires are perpendicular to the view, the hits are indicated as circles. In case of drift chambers two hits are plotted which correspond to the two ambiguous positions of both sides of the sense wire. For detectors which measure amplitudes, the radius of the circle is proportional to the pulse height. Reconstructed tracks are plotted as straight lines in the region in front and after the magnet. The curvature of the track is neglected in the display. The coloured, interactive version of the event display is a lot clearer than the picture shown here. It allows to zoom into details and to choose many different projections.

The results of the calibrations are stored in a time-dependent fashion in several data base servers.

Event Environment Programs

Every event which is recorded was generated under certain beam, target and detector conditions. Special programs were written which provide the relevant information and store the results in a (time-dependent) data base. The most important quantities are the beam current and polarisation, the target density and polarisation and the luminosity as measured with the luminosity monitor.

The Monte Carlo Program and Radiative Corrections

A detailed Monte Carlo (HMC) is available to generate physics processes, track the generated particles through the detector and simulate the detector response using as input the alignment, efficiency and calibration constants as they were determined from the real events.

Several radiative correction programs are available to calculate polarised and unpolarised correction factors and also to generate real Bremsstrahlung photons in the Monte Carlo. Physics analysis is mainly done by using the HEP and PAW software packages to generate and manipulate histograms from data and Monte Carlo events.

Large scale Monte Carlo productions are needed to study details of the physics cross sections and of the detector response. The Monte Carlo program is also used to correct for instrumental effects like acceptances, efficiencies and smearing. Due to the immense CPU requirements Monte Carlo productions can not be done at DESY centrally. Instead, a large number of workstations at the home institutes of the HERMES collaborators is used to run Monte Carlo productions in batch mode. A semi-automatic system (FUNNEL) [155] has been adapted that distributes the Monte Carlo jobs through the INTERNET and re-collects the output files centrally.

8.3 Basic Calibrations

Before physics events can be reconstructed from the data as they come from the data acquisition system, a series of calibrations has to be performed for each type of detector.

The calibration of the drift chambers consists mainly of two items: the determination of the T_0, which is the time offset of the TDC channel and the determination of the space-drift time relation (SDTR) which is the mapping between the drift time and relative position of a track in respect to the sense wire position. The T_0's are different for each wire and can change in time as they depend on details of the trigger timing. The SDTR's depend on the chamber gas conditions, on high voltages and magnetic fields. The T_0's and SDTR's can be extracted from the data by histograming residuals between reconstructed tracks versus the position extracted from the TDC values. Figure 8.3 shows first results of the calibration of the backward drift chambers. Plotted is the measured drift time versus the distance of the track
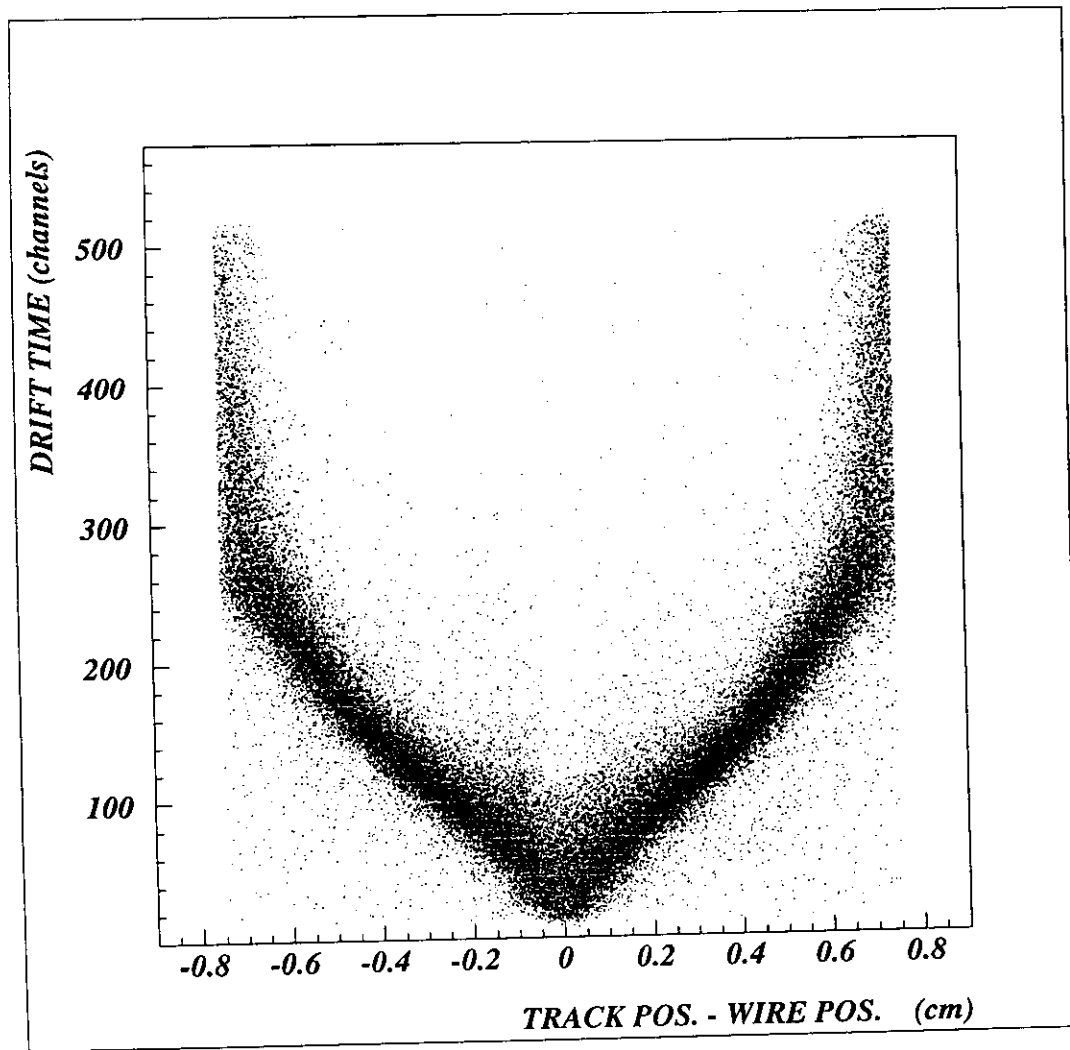
Figure 8.3: Shown is the drift time versus the distance of the reconstructed track to the nearest sense wire for the backward drift chambers. One channel in the TDC corresponds to 0.5 ns. The 'V' plot is a multi-purpose plot. It can be used to extract alignment constants, T_0's, SDTR's and the resolution of the detector.

from the position of the sense wire. The position of the track is calculated by the reconstruction program. Due to its shape the plot is called V-plot. It can be used to for several purposes: a possible horizontal shift of such a plot indicates a misalignment of the plane relative to the other detectors. A vertical shift corresponds to a shift of the T_0 determination. The non-linear shape of the two arms of the 'V' corresponds to the SDTR function. The width of the bands of the 'V' indicate the resolution of the chamber. In this plot all drift cells of several backward chambers are plotted on top of each other. The apparent width of the band is partially defined by the resolution of the chamber, partially defined by small relative shifts of the 'V' between different planes and drift cells due to the non-perfect T_0 and alignment determination at the current state of the experiment.

Figure 8.4 shows the resolution of the backward drift chambers. Plotted is the residual between the track position as given by the reconstruction program versus the hit position in the drift chamber. The hit position is the position of the sense wire plus or minus the SDTR-corrected drift distance. The width of the curve corresponds to the width of the band in the 'V'-plot. The resolution is $\sigma = 470$ μm currently and will be improved by a more precise alignment and T_0 and SDTR determination.
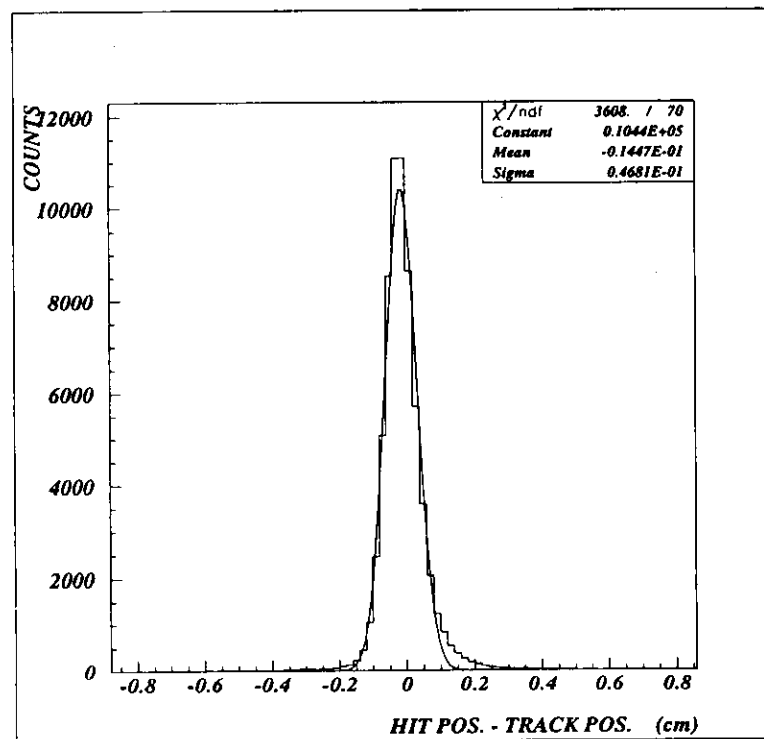
Figure 8.4: Plotted is the residual of the tracks compared to the position measured in the backward drift chambers. The current value of $\sigma = 0.47$ mm will be further optimised by a more precise alignment and calibration.

A precise determination of the T_0's has to take into account that the T_0 depends on the position of the hit along the wire. An iterative procedure of the calibration is

needed as the position of the track is known with high quality only after all detectors have been properly aligned and calibrated.

The calibration of detectors with multipliers consists first of all in the determination of the pedestals (i.e. the base line of the ADC's or pre-amplifier) and of the (relative) gain. The pedestals are calculated from a special pulser trigger which fires the readout when there is no particle. A 'gain monitoring system' has been set up which sends at certain intervals laser light pulses of well defined intensity into each multiplier and allows to calculate changes of the gains. ADC values of the pulser and gain monitoring triggers are histogrammed in order to extract the pedestals as well as relative gains.

The absolute calibration of gains is more complicated and differs for the various detector types. The hodoscopes are calibrated by investigating signals from minimum ionising particles which produce a peak in the energy spectrum. The lead glass calibration constants are known from test beam data and are recalibrated by studying the invariant mass of the photons from π^0 decays. Figure 8.5 shows first results of the π^0 mass reconstruction. The abscissa of this preliminary plot shows an uncalibrated energy scale. The π^0 peak at 0.157 is clearly shown. Additionally a small bump at 0.640 indicates the η^0. Figure 8.6 shows a blown up scale of the π^0 peak after background subtraction. From the known mass of $m_{\pi^0} = 135$ MeV (and $m_{\eta^0} = 640$ MeV) a correction of 18% compared to the given scale can be extracted [156]. This calibration agrees roughly with the results form the test beam data when all corrections are taken into account. A detailed study is in progress. Additionally the calibration of the calorimeter is checked by comparing the cluster energy of electrons with the momentum of the electrons as measured in the spectrometer.

The luminosity monitor crystals were calibrated in test beams. The absolute calibration of the luminosity counters can be monitored continuously as the total energy of the two final state particles (e^-e^- or e^+e^-) in Møller or Bhabha scattering is the known beam energy.

The Čerenkov detector is self-calibrating as the PMT spectrum resolves peaks of 1, 2, 3, etc. photoelectrons.

The TRD signal is calibrated using the peak of minimum ionising particles and by studying spectra of electrons and pions that are recognised in the calorimeter or in the Čerenkov. For this purpose the Čerenkov counter runs with nitrogen currently which allows for an electron–pion separation. The calibration depends critically on the composition of the chamber gas and on the value of the high voltage.

The proportional chambers and the micro-strip gas counters do not need a calibration as they only record wire or strip numbers. However the dead and hot wires have to be extracted before the chambers can be used for tracking.

8.3.1   The Alignment Procedures

The alignment procedures have three steps: the survey of the detectors, a laser alignment system and the relative alignment of the detector components calculated from the residuals of tracks.
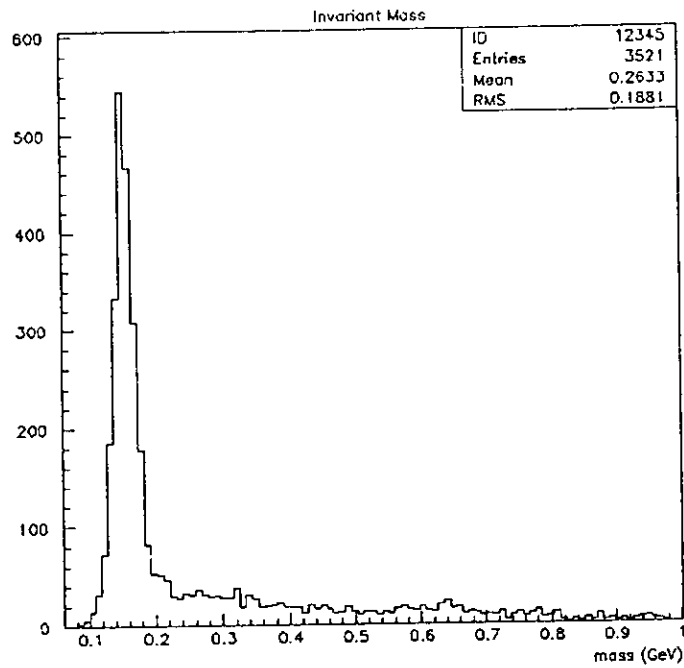
Figure 8.5: Plotted is the invariant mass of two photon clusters in the calorimeter. The abscissa is not calibrated. At 0.157 a clear π^0 peak is seen. At 0.640 there is a small peak of the η^0.
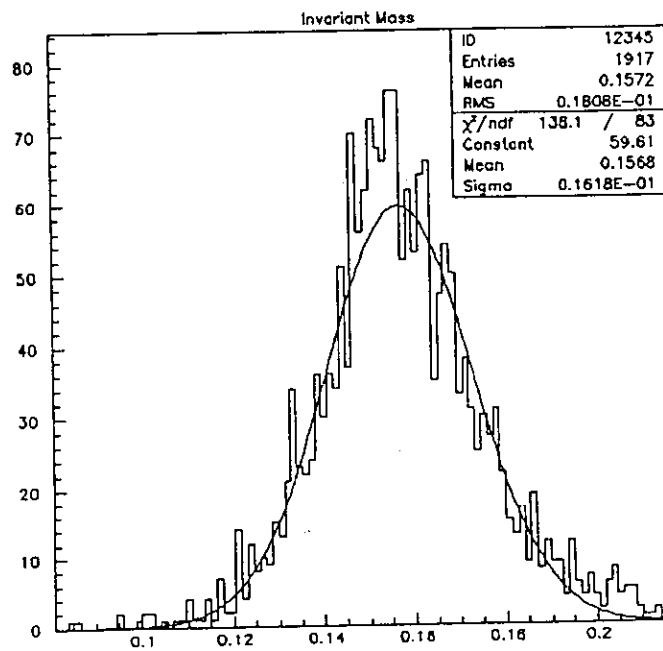
Figure 8.6: A blown-up scale of the π^0 peak shows that the scale of the abscissa is off by 16%. The true value of the π^0 mass is 135 MeV.

Detector Survey

After installation and reinstallations, each detector component is surveyed by optical telescopes. The survey takes place relative to the movable detector platform. The platform itself is surveyed relative to the HERA machine system, which is mainly determined by the position of the last quadrupoles of the machine. Each detector has alignment marks which are visible from outside. The relative positioning of the inner components of the detectors was determined during construction and during test measurements. Using a special laser based measuring system, the position of each single wire of the backward drift chambers relative to the detector frame has been determined with a precision of 0.03 mm. The precision of the optical survey is about 0.3 mm in the transverse and 1 mm in the longitudinal direction. The data from the survey are stored in the geometry data base and are used by the reconstruction program as well as by the Monte Carlo program.

Laser Alignment System

In order to monitor possible time dependent changes of the relative alignment of the chambers, a laser alignment system is used. The data from the cameras that record the laser position are analysed by an image processing systems and the relative position of each detector module is extracted.

Alignment from Track Residuals

The most sophisticated method of alignment uses the residuals of the reconstructed tracks to determine the relative positions of the chambers. To simplify the method, data with magnetic fields switched off are used for this analysis. In an iterative procedure, tracks are reconstructed using the given geometry input data. Residuals of the track position compared to the hit position in a given chamber are plotted and used to extract corrections for the chamber position. The newly calculated alignment constants are used in the next iteration of the procedure. By comparing residuals in different regions of the chambers, not only transverse displacements but also tilts of the chamber can be identified. Using tracks with large slope, also a longitudinal alignment of the chambers is possible.

Figure 8.4 showed the residual of the backward chamber hits summed over all planes. The same information can be plotted separately for each plane as shown in figure 8.7. The width of the band indicates the resolution of each plane separately. Shifts of the maximum indicate alignment offsets. Alignment offsets of typically 300 μm are seen in this figure. The alignment offsets will be entered into the data base and used for a re-run of the reconstruction program.

The relative alignment of the detector and the beam is not possible using this method as the beam particles are not seen in the detectors. It is however possible to align the beam with respect to the luminosity monitor, using symmetric Bhabha scattering. As an improvement of the set-up, one could provide in future a small counter in front of the luminosity monitor, which has a rigid connection to the calorimeter frame and such allows an absolute alignment of the detector system
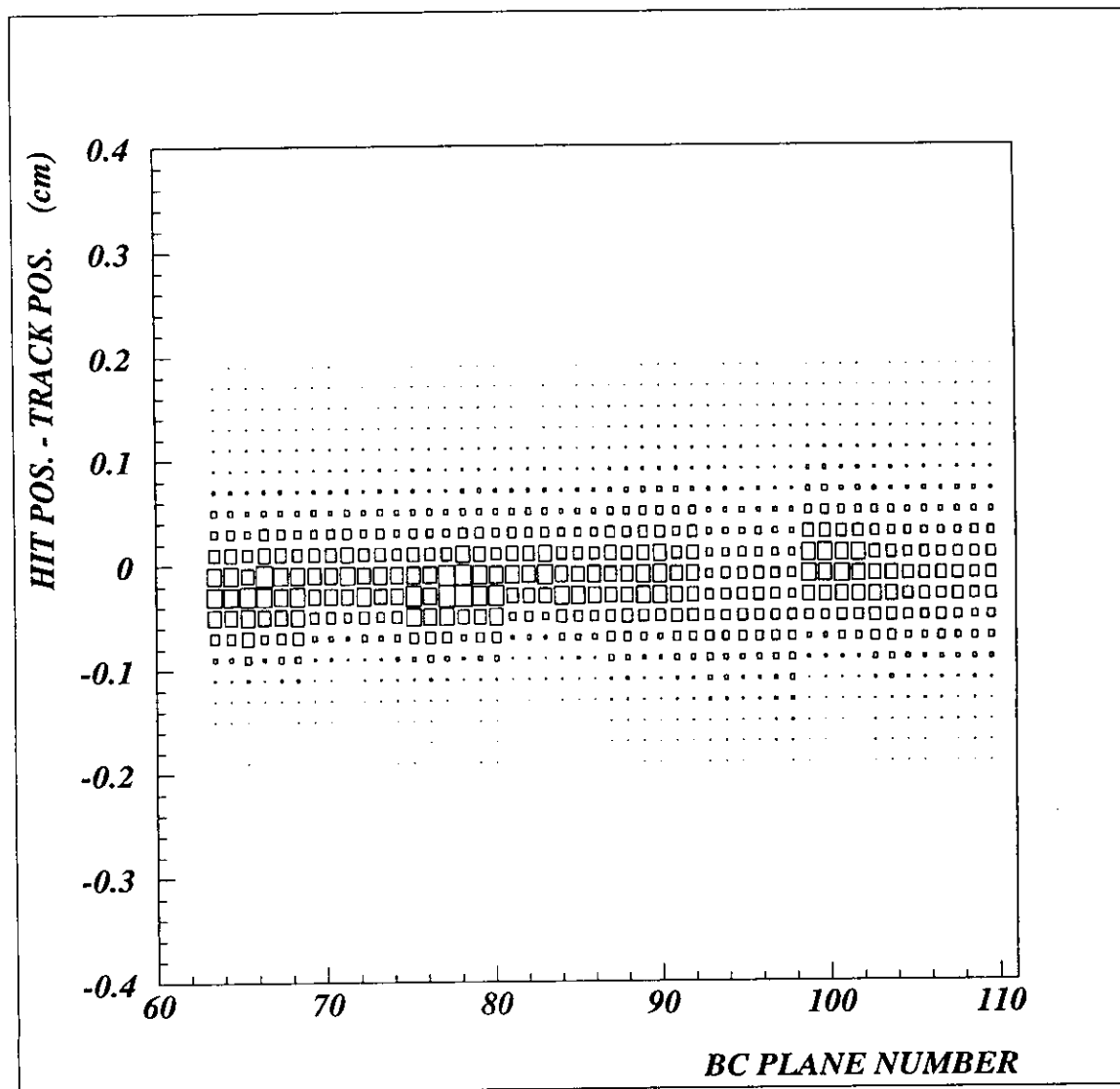
Figure 8.7: Shown is the residual of the hits for each drift chamber plane separately. The size of the boxes indicate the number of tracks in each bin. The width in the vertical projection indicates the resolution of the plane and the offset indicates the relative alignment of the plane. The planes are numbered successively in beam direction and alternating between blocks of 6 planes of the upper and the lower half of the detector. As there are less tracks reconstructed in the lower part of the detector the sizes of the boxes alternate every 6 columns.

in respect to the beam direction. Currently the alignment of the detector system compared to the HERA machine system relies on the absolute measurements of the surveyors. The position of the beam in respect to the machine system is measured by beam position monitors which are installed at the quadrupoles on both sides of the experiment. The monitors measure the position with an uncertainty of about 0.1 mm. The position of the monitors with respect to the HERA system is know better than 1 mm. The bending of the beam by the target holding fields and the correction dipoles in the HERMES region have to be taken into account in the determination of the beam position at the interaction point.

8.3.2   The Efficiency Calculations

In order to be able to measure physics cross sections, the efficiency of the detector- and reconstruction system has to be known in detail. The measurement of asymmetries, i.e. cross section *ratios*, is less critical, as most of the inefficiencies cancel in the ratio. However, there can be second order effects which do not cancel and which become important in a precision experiment. A typical second order effect for our experiment is the following: as the distribution of hadrons and radiative photons and the absolute trigger rate are spin-dependent, also the reconstruction efficiency and the signal to background ratio can be spin-dependent. Of course, the uncertainty is expected to be small, however those effects have to be studied in detail using Monte Carlo methods.

Chamber Efficiencies

Due to the importance of efficiencies for the analysis and the final precision of the results, the procedure of the efficiency determination will be described in some more detail. The efficiency of a single detector plane is the probability to find a signal in this chamber when a track is going through. The efficiency determination starts with extracting the dead and noisy wires by looking for holes and peaks in wire maps. The efficiency ϵ of the remaining area of the detector plane is defined as the ratio:

$$\epsilon = \frac{\# \text{ of tracks which have a hit in the detector plane}}{\# \text{ of all tracks}} . \qquad (8.1)$$

Obviously, the total number of all tracks is not known experimentally, as the efficiency of the detector system is finite and not all tracks are found. Therefore this formula has to be modified. A subsample of tracks has to be used to determine the efficiency of a plane. It is important that the selection of the subsample does not introduce a statistical bias. If simply all tracks were used which are found in the experiment, the efficiency determination is certainly biased as the probability of finding the track is correlated with the efficiency of the plane:

$$\epsilon < \frac{\# \text{ of tracks which have a hit in the detector plane}}{\# \text{ of all tracks that are found}} . \qquad (8.2)$$

A much better way to define the subsample is to select tracks which are found by the reconstruction program without using the information if there is a hit in the

given chamber or not. The efficiency ϵ_s for the subsample is then

$$\epsilon_s = \frac{\#\ \text{of selected tracks which have a hit in the detector plane}}{\#\ \text{of all tracks which are found after ignoring the plane}} . \tag{8.3}$$

Unfortunately, the above definition, which is also used in other experiments, is not completely free of bias. Mathematically it can be understood by introducing different classes i of tracks (T^i). In general, the efficiency of the detector plane becomes class dependent and the total efficiency is the weighted average of all classes $\epsilon = \langle e^i \rangle$. The selection of tracks as described above will then also be class dependent as the planes which are used for the reconstruction may also have class dependent efficiencies. Therefore, the true efficiency ϵ from eq. (8.1) is in general different from ϵ_s as calculated in eq. (8.3) as the relative weights of the classes i may be different in the two samples.

How can this be interpreted in terms of physics? There are classes of tracks which are accompanied by e.g. δ-electrons or hadron showers and there are classes of tracks which are simply minimum ionising particles. It can be that both classes of tracks have different efficiencies and introduce a bias in the efficiency determination. For example in the EMC experiment, the above described problem lead to serious systematic problems in the determination of absolute structure functions, as hadron showers produced serious correlations between the efficiencies of adjacent chamber planes. The only way to get hold of the problem is to study all possible correlations using Monte Carlo events, where the 'true' efficiencies and the total number of tracks are known. Therefore the Monte Carlo program needs a realistic model of the detector, including a parametrisation of the efficiencies.

Chamber efficiencies are typically time dependent as the high voltage, the temperature, pressure or composition of the chamber gas might change and they are a function of the distance from the sense and potential wire and might also depend on the distance from the proton and electron beam due to background or radiation damage. Figure 8.8 shows first examples of efficiency determination for the forward and backward drift chambers. Whereas the average efficiency of the BC's is already at a high level ($\langle \epsilon_{BC} \rangle = 96\%$), the optimisation of the FC's is still at its beginning ($\langle \epsilon_{BC} \rangle = 85\%$). The lower plot in 8.8 shows the hit position plotted versus the distance of the corresponding track from the sense wire. The shape of the distribution shows that the efficiency drops as expected close to the sense wire. The plateau of the distribution corresponds to an efficiency of close to 100%.

It should be mentioned that a week after this chapter was written, also the FC chambers reached high efficiencies. In other words, all figures in this paper should only show principles but do not represent the final performance of the detector.

Trigger Efficiencies

The determination of the trigger efficiencies is even more complicated. The main physics trigger is the trigger on electrons above a certain energy threshold which enter the acceptance of the detector. It is a combination of the hodoscope H1, the preshower detector and the calorimeter as described in chapter 6.2.10. There is no
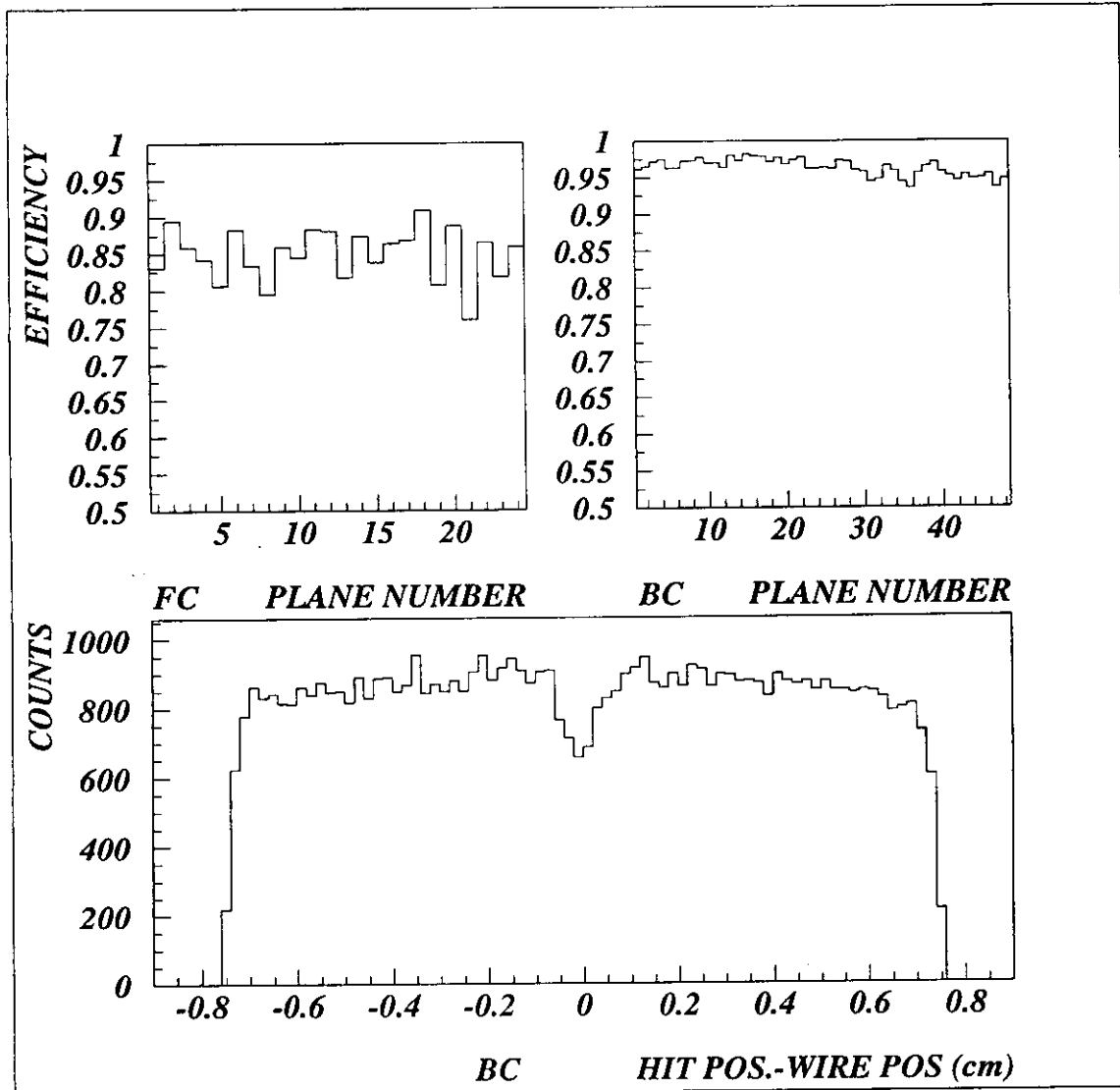
Figure 8.8: The left (right) upper figure shows the average efficiency of the forward (backward) drift chambers plotted versus the plane number. The calibration of the backward chambers has already reached a high level. The efficiency is high for all planes and has a mean value of 96%. The forward chambers have currently an efficiency of 85% which will be improved in future. The lower plot shows the distribution of hits in the backward chambers plotted versus the distance of the corresponding track from the sense wire. The efficiency drop close to the sense and potential wires is the main reason why the average efficiency is below 100%.

way to calculate the trigger efficiency by studying only events which have fulfilled the physics trigger, as one wants to know the number of events which have not fired the trigger.

Therefore additional ('single') trigger types have to be written to tape which also allow to identify electrons, but don't need the part of the detector for which the efficiency is to be calculated. From the redundancy of information, the efficiencies can be roughly calculated. As long as the efficiencies of hodoscopes and of the calorimeter are close to 100%, the trigger efficiency is not critical for the systematic error. The overall performance of the trigger is studied by modelling the trigger system in the Monte Carlo, including a precise model of the geometry of all components and of the logic of the trigger electronics.

Reconstruction Efficiencies

The most complex part of efficiency determination concerns the reconstruction efficiency, i.e. the probability that the reconstruction program finds a track when a certain number of chambers have seen a signal. The reconstruction efficiency very much depends on the algorithms and on the cuts and parameters which are used in the program. The reconstruction efficiencies can always be increased by loosening the conditions that a track candidate has to fulfill before it is called a good reconstructed track. If the cuts are too lose, two many 'ghost tracks' are found, i.e. tracks which are artificially generated by the program by using combinations of background hits.

Detailed Monte Carlo studies are needed to calculate and optimise the reconstruction efficiencies and at the same time minimise the number of ghost tracks. The reconstruction efficiency of a track in a given event is correlated with the distance to neighbouring tracks and depends on the total multiplicity in the chambers. The Monte Carlo needs realistic chamber multiplicities and realistic hadron correlations for a precise determination of the reconstruction efficiency.

There are several ways to cross-check the extracted efficiencies. As the absolute spin averaged structure functions are known to a sufficiently high precision, they can be used as physics input for the Monte Carlo. The reconstructed Monte Carlo events should give the same particle distributions in all (instrumental) distributions as the real experiment, provided that the efficiencies are correctly represented in the digitisation part of the Monte Carlo. A second way of checking the efficiency calculations is to plot Monte Carlo corrected physics results versus purely instrumental variables, e.g versus the azimuthal angle or the distance from the sense wire or versus time. In no cases a corrected physics result should depend on such instrumental variables.

8.4 The Reconstruction Program

The reconstruction program converts the decoded detector informations into physics quantities like tracks, energies, angles, particle types and vertices. In many experiments, the reconstruction program is the most time consuming program. The

HERMES reconstruction program (HRC) [153] is very fast because it makes use of two unusual methods: the tree-search algorithm allows for fast track finding and a look-up table is used for fast momentum determination of the tracks. The full reconstruction of 30 Monte Carlo events on an SGI processor R4400 takes only one second.

8.4.1 The Fast Pattern Recognition Algorithm

The main task of the reconstruction program is to find particle tracks using the hits in the tracking chambers. Each detector plane gives spatial information in one coordinate and only by combining the information of many detectors it is possible to reconstruct the tracks uniquely in space. There are several track finding algorithms commonly used. HRC uses the tree-search algorithm which turned out to be very fast even at high chamber multiplicities. The tree-search algorithm is used in the following way:

As a first step, tracks have to be found in projections, separately in the region in front and behind the spectrometer magnet. The track projections are more or less straight lines in those regions, except for small curvatures by the magnetic fringe fields and for kinks coming from secondary interactions and straggling.

The basic idea of pattern recognition using the tree-search algorithm is to look at the whole hit pattern of the detectors with variable (increasing) resolution as illustrated in figure 8.9. Like in a hologram where each part of it contains the whole information with reduced resolution, at each step of the iteration the full track is seen, however only at the end the full detector resolution is reached. At HERMES the detector resolution is roughly 100 μm and the size of a chamber is of the order of 4 m. Therefore after about 16 steps in the binary tree, the resolution of the detector of $\sim 1 : 2^{16}$ would be reached. For the purpose of track finding (not fitting) a resolution of $1 : 2^{11}$ is sufficient, which reduces the maximum number of iterations in the tree-search at HRC to about 11.

In each step of the iteration, the algorithm checks if the pattern (at the given resolution) contains a sub-pattern which matches with the pattern of an allowed track. Figure 8.10 shows an example for allowed and forbidden pattern. All allowed patterns are generated and stored in a data base at the initialisation phase of the program. The comparison is very fast as only look-up tables are used; no calculations have to be done during event processing.

The number of allowed track patterns at the full resolution is of the order of 100,000,000. Without tricks, this large number would make the algorithm useless for two reasons: memory space problems to store all the patterns and CPU time problems to compare with each of them for every event would prevent any application. The following methods elude the problems:

- If one compares the allowed patterns from one iteration to those from the following one (called father and son in the following) it becomes obvious that only a very limited number of sons exist for each father. At initialisation time all links between the allowed pattern of each generation are calculated, i.e. all sons for each father are stored in the data base. The number of comparisons
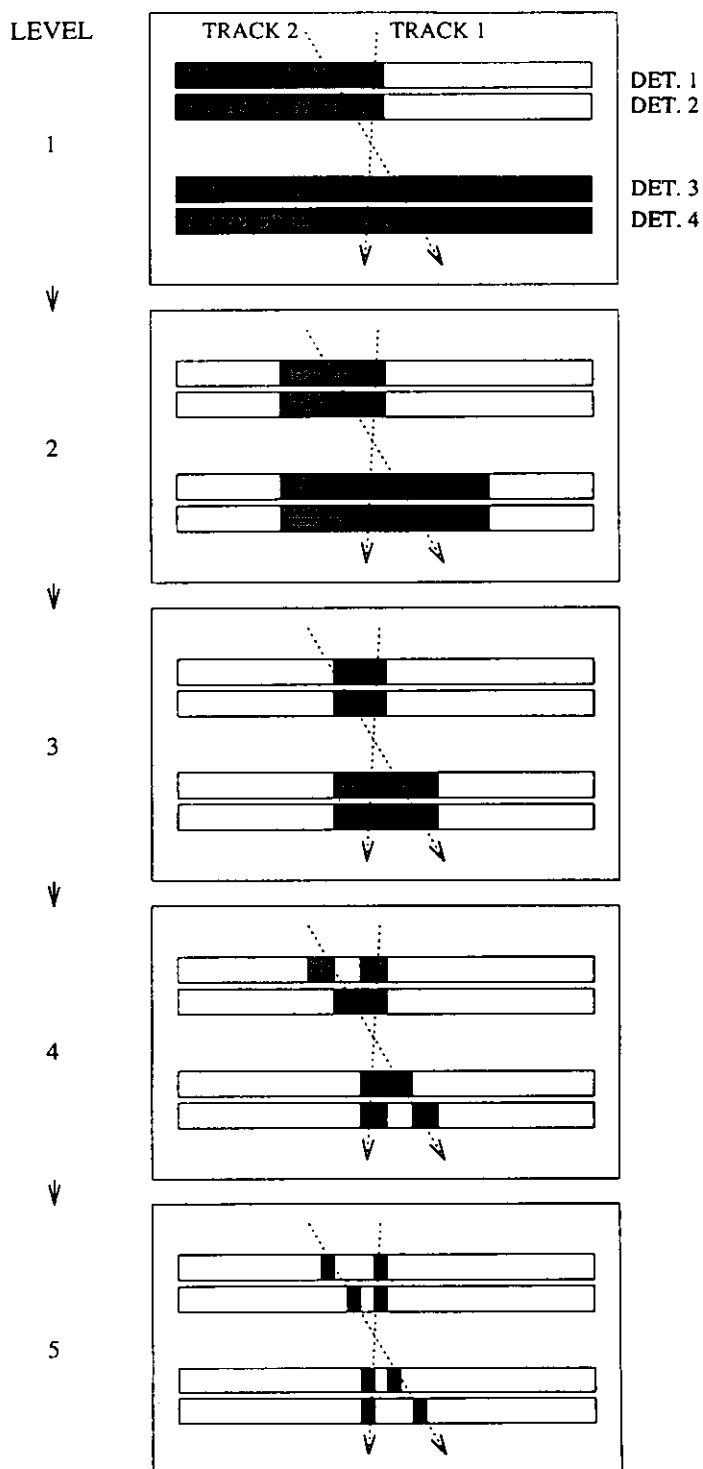
Figure 8.9: The tree search algorithm looks at the hits of the tracking detectors with artificially reduced resolution. In every tree search level the resolution is doubled until a resolution is reached which is optimal for track finding. The optimal resolution is determined by the resolution of the chamber plus some alignment uncertainties.

ALLOWED

DET. 1
DET. 2

DET. 3
DET. 4
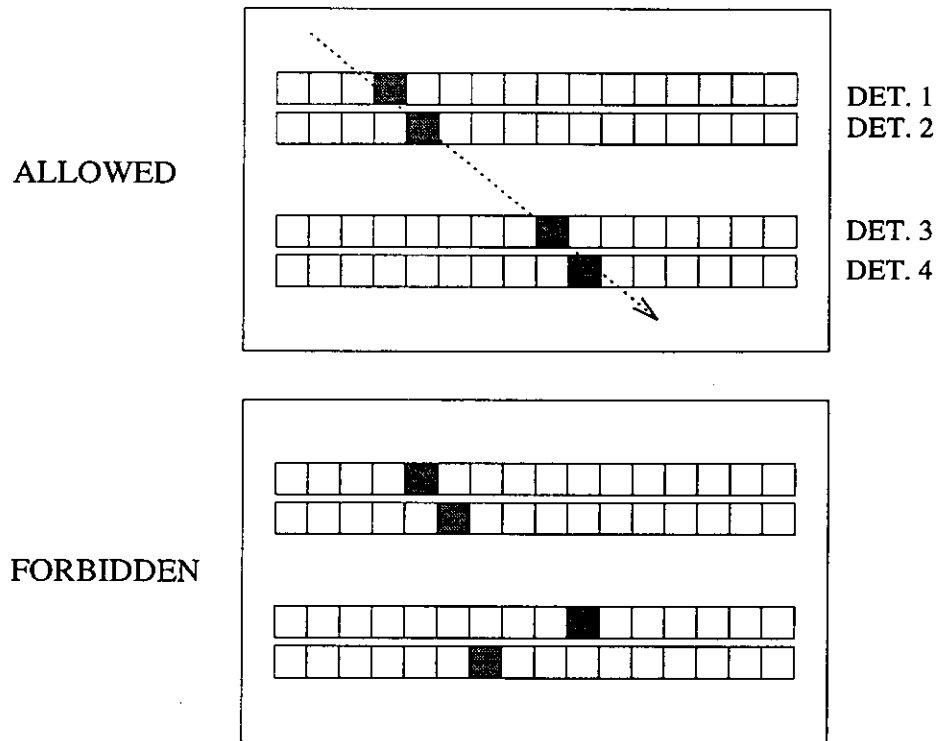
FORBIDDEN

Figure 8.10: At each tree search level, the allowed and forbidden pattern are well defined. The program compares the measured pattern with the data base and finds out if the measured pattern contains a pattern of an allowed track. Symmetry considerations allow to reduce the number of different allowed pattern in each level to a number which can be handled by the computer.

becomes now very small: if a pattern is recognised at one generation, only its sons have to be compared in the next generation. The number of sons for each father it typically 4 to 8. This way the CPU problem is solved.

- Symmetry considerations can be used to reduce the number of patterns which have to be stored. If two pattern are mirror symmetric, or if they are identical except for a transverse shift, they are stored as one pattern. Most important is that if a son is identical to a father, then the son is linked to the father and all grand children become identical to the children. This 'fractal-like' self-symmetry is based on the fact that we are looking for (more or less) straight tracks only. This 'self-symmetry' reduces the number of different branches in the tree-search significantly. The number of different patterns in the data base is of the order of 50,000 which is small compared to the original number of 100,000,000.

After applying the tree search algorithm to the U and V planes, the tracks in these projections are defined. They are called tree-lines. By testing all combinations of tree-lines and merging them with hits in the x coordinate, the tracks in space are found. The tree-search algorithm is not applied to the x-coordinate directly as the X-planes of the VC chambers are tilted and thus do not fulfil the self-symmetry conditions. In the backward region also the x projections are used for track finding.

8.4.2 The Fast Momentum Look-Up

As a second specific feature in HRC a very fast method has been developed to determine the momentum of a track which is given by the deflection of the track in the inhomogeneous field of the spectrometer magnet. The tracking through a magnetic field is very CPU time consuming. The new method makes the tracking through the magnetic field on the track by track basis obsolete. Instead a large look-up table is generated only once which contains the momentum of a given track as function of the track parameters in front and behind the magnet. The relevant track parameters are the position and the slope of the track in front of the magnet and the horizontal slope behind the magnet. The resolution of the table has been chosen such that, using interpolation methods, the precision of the track momentum determination is better than $\Delta P/P = 0.5\%$. The look-up table contains 520,000 numbers. This method of momentum determination is extremely fast.

The vertical slope and the position of the track behind the magnet are no additional degrees of freedom and are only used to determine the track quality and to reduce the number of ghost tracks. They are not used in the determination of the track parameters as the resolution and alignment of the VC-FC system is superior to the resolution of the backward chambers. During the running in phase of the detector, the VC's were not operational for some time and for this case the program has an option to determined the momentum from the position and slope of the track in the backward chambers combined with the position in the FC's.

8.4.3   Overview of the Program

Figure 8.11 shows the basic program flow of HRC. For each event the following steps are processed:

After decoding and calibration, the positions of the particles in the tracking detector are available. The gas micro-strip counters (VC) and the drift chambers (FC) and (BC) are used for pattern recognition using the tree-search algorithm as described above. The reconstructed tree-lines are combined to tracks in space, separately for the region in front and behind the magnet. Now, as the track positions in space are known, additional corrections can be applied to the drift times, which take into account time of flight and corrections due to the inhomogeneous magnetic stray field. The newly corrected drift times are used to recalculate the precise track parameters. The track segments in front and behind the magnet are 'bridged' and for each valid combination the track momentum is determined using the momentum look-up table. Finally, the vertex position is fitted by either finding the point of closest approach of the track and the beam or by finding the point which has the minimal distance to the beam and all additional hadron tracks.

As a next step the calorimeter is searched for clusters. Several cluster algorithms are available. One of them looks for maxima in the energy deposit of the calorimeter and adds the energy of all adjacent lead glass blocks to the energy in the central block. From the relative pulse heights in the neighbouring blocks the impact point of the cluster can be calculated with a precision of typically 2 cm.

A trigger processor uses the calibrated signals from the hodoscope, the preshower and the calorimeter and applies trigger conditions which are a bit narrower than the hardware thresholds. The reason for this procedure is to have well defined trigger conditions which are independent of drifts and edge effects in the hardware.

As a next step the clusters which are found in the calorimeter and in the preshower are correlated with the tracks which are found in the tracking chambers. The energy deposit in the preshower and in the calorimeter is compared with the momentum of the tracks. The information from the TRD and the Čerenkov is assigned to the tracks. Special particle identification algorithms extract the probabilities of tracks and clusters of being photons, electrons, pions or heavier hadrons.

The magnet chambers are currently not used for track finding or momentum determination, as the drift chambers have superior information. It is planned to use them in future for finding low energy tracks which miss the drift chambers, for the reconstruction of tracks from secondary vertices behind the VC chambers and for studying reconstruction efficiencies.

8.5   The Particle Identification Methods

Particle identification at HERMES consists of the following steps:

First electrons are identified. They are defined as tracks that are seen in the tracking detectors and have a signal above a certain threshold in the preshower counter and in the calorimeter. Photons are clusters in the calorimeter which cannot be assigned to tracks in the tracking detectors. Hadrons are tracks that have a signal

The HERMES Reconstruction Program
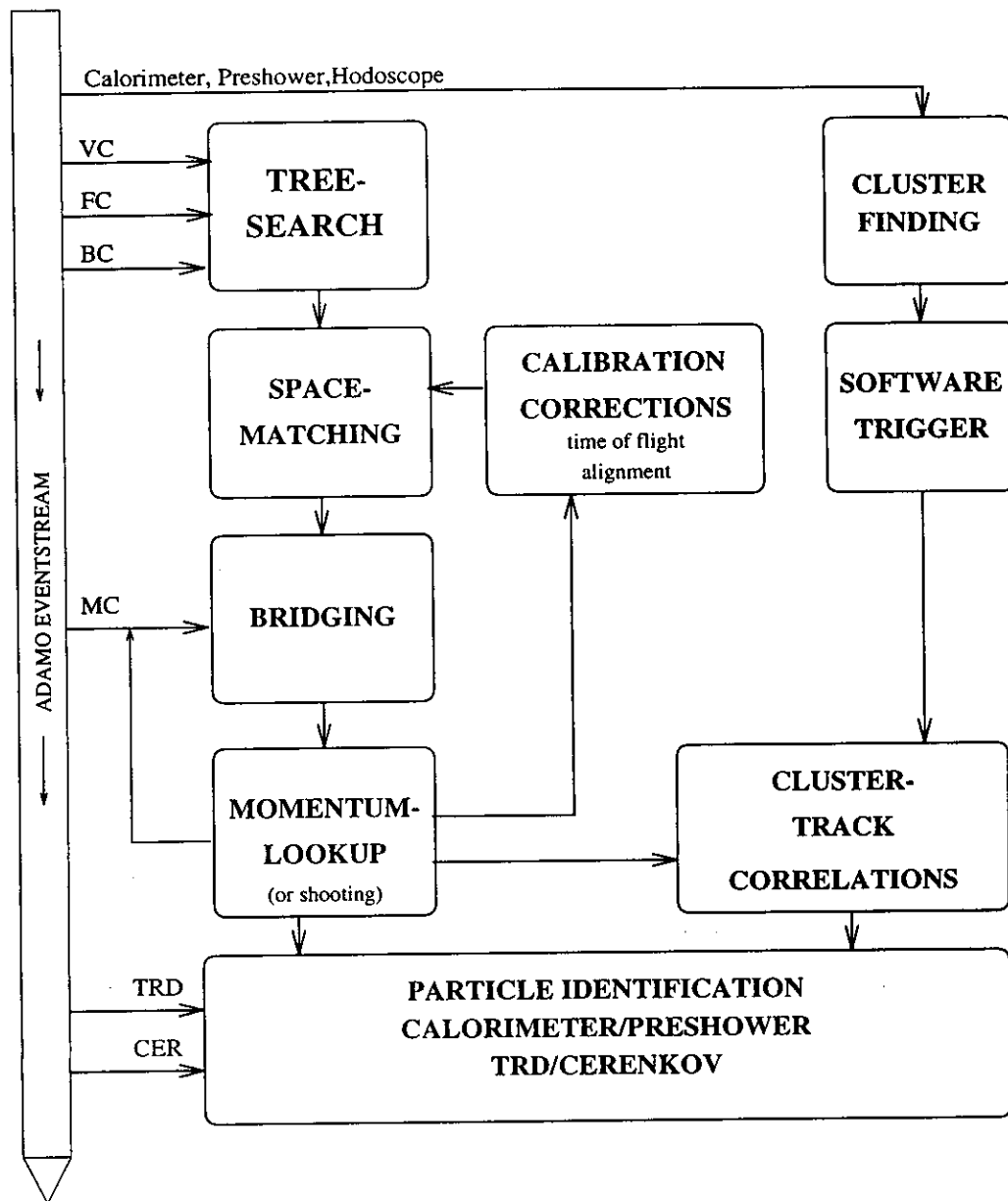
Figure 8.11: A simplified flow chart of the reconstruction program is shown. The tree search algorithm is used for finding tracks in the front and rear part of the detector in the x, u and v projections. The projections are matched in space and the front and rear part of the track is bridged in the magnet. A momentum look-up table is used to determine the momentum. Cluster finding algorithms are used to identify electrons and photons in the calorimeter. The trigger conditions are reapplied to the clusters. The clusters are correlated to tracks. The information of the TRD and the Čerenkov counter are used in combination with the calorimeter and preshower information to assign particle types to the tracks and clusters.

in the calorimeter and in the preshower which is small compared to what is expected for an electron. Pions are hadrons that have a signal in the Čerenkov counter. The various thresholds are determined after studying the spectra and comparing them with expectations from Monte Carlo and from test-experiment data. The Čerenkov counter is filled with nitrogen at the beginning of the experiment which allows a clear identification of electrons and thus can be used to cross check the performance of the pion-electron suppression by the calorimeters and the TRD.

A more sophisticated identification method [157] assigns conditional probabilities $P(R_d|p_i)$ to each track and each detector. $P(R_d|p_i)$ denotes the probability that a particle of type p_i causes a response R_d in a certain detector d. The conditional probabilities have to be extracted from test measurements or from Monte Carlo simulations. When the a priori probabilities $P(p_i)$ of all particle types are known, which means that the total rate of electrons, hadrons, etc. is known over the whole phase space of the experiment, then the Bayes' Theorem allows to calculate the probability that a certain track belongs to a certain particle type:

$$P(p_i,|R_d) = \frac{P(R_d|p_i)P(p_i)}{\sum_{j=1}^{n} P(R_d|p_j)P(p_j)} \qquad (8.4)$$

with $P(p_i,|R_d)$ being the probability that for a given response R_d the particle is of type p_i. The sum j is over all particle types. The response of the total detector system corresponds to the product over all detectors:

$$P(p_i,|R_1 \cdot R_2 \cdot R_3 \cdot ...) = \prod_d P(p_i,|R_d) . \qquad (8.5)$$

In the experiment, the total rates of the particle distributions, i.e. the a priori probabilities, are subject to the measurement and in general not known beforehand. Therefore the formula (8.4) has to be applied iteratively: starting with equal probabilities for each particle type, the Bayes' Theorem is applied to obtain the the next iteration and so on. The method finally should converge to the real particle probabilities. Correlations between different detectors might complicate the situation.

8.6   The Monte Carlo Program

The HERMES Monte Carlo program (HMC) [164] has been written in the design phase of the experiment and has been revised several times since then. It has many applications:

- to study the background conditions in the HERA ring,

- to study the performance of various detector systems in the design phase of the experiment,

- to calculate the acceptances, resolutions and the statistical errors of the experiment,

- to develop and test a fast and efficient reconstruction program,

- to test the analysis software by comparing the analysed reconstructed Monte Carlo events with the physics input of the program,

- to compare the trigger rates and particle distributions in the detectors with the predictions from Monte Carlo in order to understand the performance of the detector during data taking,

- to study and to correct for systematic errors in the physics results which origin in acceptance, efficiency and resolution effects of the detector.

As a side application, the graphics package in the HMC program is used as an event display during data taking and analysis.

8.6.1 General Structure of the Program

The HMC program is based on the GEANT program which is part of the CERN program library. A simplified flow chart is shown in figure 8.12. Before the event generation is started, the program reads the specifications of all detectors and additional equipment which is part of the spectrometer from a data base. This includes positions, sizes, materials, 'sensitive volumes', frames, number and position of wires, etc. The program itself contains general conversion routines which use these input specifications and build up hundreds of volumes with materials assigned to it. The material definitions are needed to calculate secondary interactions. The 'sensitive volumes' describe the sensitive area of the detectors. Detector types like drift chambers, proportional chambers, calorimeter, etc. are assigned to each sensitive volume which allows the program to calculate the appropriate response function.

As a first step in the event generation, a primary physics process is generated. This can be a deep inelastic scattering process, a Møller or Bhabha event, a photoproduction process or simply randomly generated background tracks. Also externally generated physics events in ADAMO format can be fed into the program. Synchrotron radiation is currently calculated in a separate program, will however be included into HMC in future. In case a deep inelastic event is generated, first the cross section has to be calculated. In order to take polarisation effects into account, some model of the spin structure functions is required as input. Then the kinematics of the scattered electron is generated according to this cross section. As a next step, the electromagnetic radiative corrections are calculated and if necessary, a Bremsstrahlung photon is generated. The radiative correction factor is assigned as a weight factor to the event.

In a following step the deep inelastic hadronic final state is produced using either the LEPTO [158] program in the unpolarised case or the PEPSI [159] program in the polarised case. LEPTO (PEPSI) requires the unpolarised (polarised) quark flavour distribution functions of the proton and neutron as input. The programs generate the quark final states including the first order QCD corrections like gluon Bremsstrahlung and gluon fusion. The JETSET program simulates the fragmentation of the quarks into hadrons.

The tracking of the particles through the detector and the simulation of secondary interactions in matter like Bremsstrahlung, conversions, multiple scattering,

The HERMES Monte Carlo

```
┌─────────────────────────────────────────────┐
│              Initialisation                  │
│  conversion of geometry and calibration data tables  │
└─────────────────────────────────────────────┘
```

```
┌──────────────────────────────────────────────────────────┐
│                  Physics Generation                        │
│  ┌────────────────────────────────┐    OTHERS:            │
│  │ DEEP INELASTIC SCATTERING:     │                       │
│  │ F2(x,Q2), R(x,Q2), g1(x)       │    photo production   │
│  │ cross section calculation      │    Moller/Bhabha      │
│  │ scattered electron             │    background tracks  │
│  │                                │    background hits    │
│  │ radiative corrections          │                       │
│  │ Bremsstrahlungs photon         │                       │
│  │ quark final state (LEPTO/PEPSI)│                       │
│  │ hadronisation (JETSET)         │                       │
│  └────────────────────────────────┘                       │
└──────────────────────────────────────────────────────────┘
```

```
┌─────────────────┐
│ primary particles │
└─────────────────┘
```

```
┌──────────────────────────────────────────────┐
│              Tracking (GEANT)                  │
│           secondary interactions               │
│                 energy loss                    │
│              multiple scattering               │
│                particle decays                 │
│           bending in magnetic field            │
│  generation of HITS in 'sensitive volumes'     │
└──────────────────────────────────────────────┘
```

```
┌─────────────────────────────────┐
│           Digitisation           │
│  simulation of detector response │
└─────────────────────────────────┘
```

```
┌─────────┐
│ 'raw' data │
└─────────┘
```

```
┌──────────────────────────────┐        ┌──────────────────┐
│     ADAMO output stream       │        │   Event Display   │
│       tape/disk writing       │        │                   │
│ piping to reconstruction program │     └──────────────────┘
└──────────────────────────────┘
```

Event Loop

Figure 8.12: Simplified flow chart of the Monte Carlo program. The program has five main parts: the initialisation, the generation of the physics primary process, the tracking of the generated particles through the detector, the simulation of the detector response and the output of the information in ADAMO format. Single events may be visualised using the event display.

nuclear reactions etc. is done using the GEANT code. In the case of the Čerenkov counter the radiated light is generated in the gas volume and the generated photons are tracked to the mirrors and multipliers. As a special feature of HMC a new artificial particle has been defined which makes no interactions with matter, is however bent in the magnetic field. In special studies this particle is tracked in parallel with the scattered electron. The difference of the electron track and the track of the special particle was used to understand the effect of the materials in the detector during the design optimisation of the experiment.

The intersection of the tracks with the detector modules or planes is called a 'hit' and is stored in ADAMO tables. The response of the detector is calculated in detail using the detector specifications and calibration constants from test measurements and from real data. The output of the Monte Carlo program contains the equivalent information as the real data after the decoding stage. The 'hit' tables are added to the output stream and they are comprehensive enough to allow for a recalculation of the detector response. This opens the possibility to study various models of detector response without having to redo the tracking each time, which is the most time consuming part of the Monte Carlo.

Details of the program are described in the HMC manual [164]. Figure 8.13 shows an example of a deep inelastic event generated by HMC.
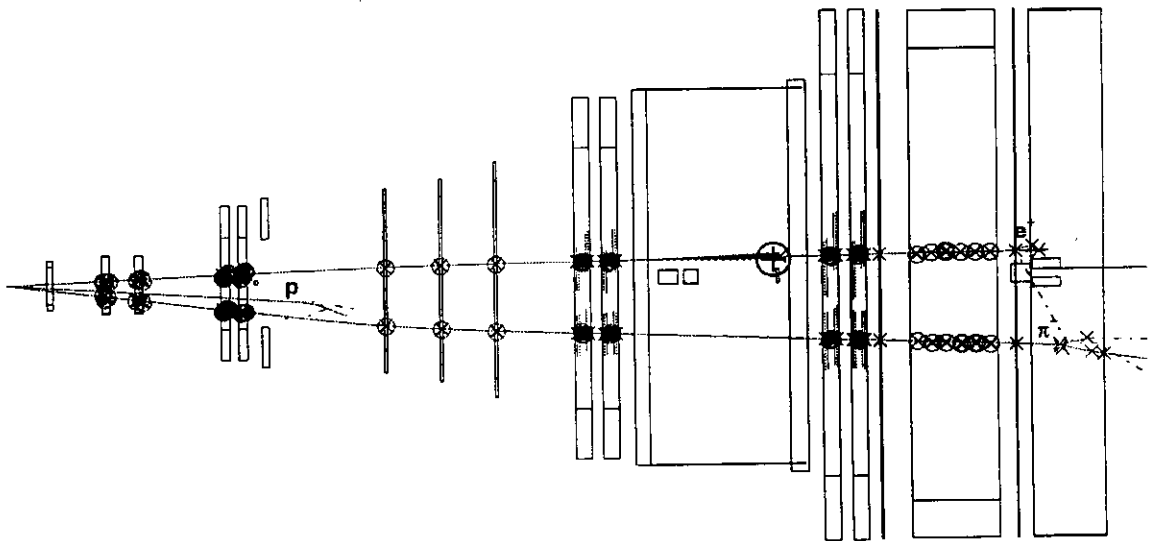
Figure 8.13: Top view of a Monte Carlo generated deep inelastic event.

8.6.2 Polarised Leptoproduction with PEPSI

In order to be able to study polarised semi-inclusive deep-inelastic scattering, the Monte Carlo generator PEPSI (Polarised Electron Proton Scattering Interactions) [159] has been developed which is a modification of the LEPTO program. It generates the hadronic final state of deep inelastic scattering off a polarised target.

PEPSI calculates the first order QCD corrections in the scattering process of the virtual photon and the quark. According to the calculated probabilities, the

final state will contain either a simple current quark as shown in figure 8.14 (a), a double structure which consists of a quark and a Bremsstrahlung gluon (b) or a quark anti-quark pair in the case of a gluon fusion event (c). The calculations take the spin of the partons into account and make use of polarised and unpolarised quark $(q_f(x) \pm \delta q_f(x))$ and gluon $(G(x) \pm \delta G(x))$ distributions which are input to the program. The same input functions are used to determine the flavour of the quark which is struck.
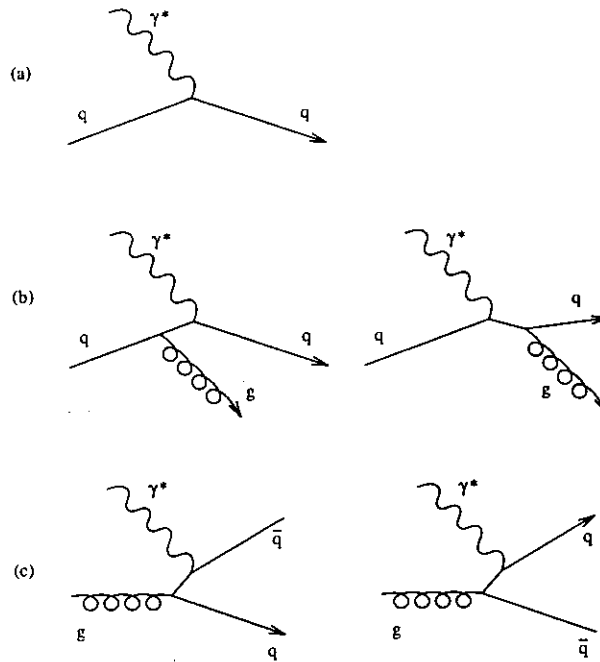
Figure 8.14: The PEPSI program calculates the polarised quark scattering in lowest order QCD (a), the gluon bremsstrahlung (b) and the gluon fusion graph (c).

The fragmentation of the quarks into jets is done using the standard JETSET program. It is assumed that the fragmentation of pseudoscalar mesons is spin independent. This assumption is certainly one of the limitations of the program.

8.7   Radiative Corrections

The measured deep inelastic cross section in electron-proton scattering contains all higher order electro-weak contributions. The extraction of structure functions requires correction procedures which reduce the measured cross section to the Born term. It turns out that the contributions from QED corrections to the absolute cross sections are large (up to $\sim 100\%$), that however most of the contributions are spin independent and that therefore the corrections to the measured asymmetries remain small ($\ll 10\%$).

8.7.1 Correction of the Absolute Cross Sections

The absolute structure functions can be extracted from the total unpolarised or spin-averaged cross section by applying the radiative correction formulas as calculated by Mo and Tsai [160, 161] or Akhundov et al. [162]. The main Feynman graphs of the lowest orders of electro-weak corrections are shown in figure 8.15:

(a) the basic one-photon-graph,

(b) vertex loop correction at the lepton vertex,

(c,d) vacuum polarisation by leptons and quarks,

(e) two photon exchange,

(f) vertex correction at the hadronic vertex,

(g,h) pair production,

(i) weak interaction.

(k,l) the emission of a Bremsstrahlung photon by the incoming and scattered electron and

(m) Bremsstrahlung emission at the hadronic vertex.

The lowest order corrections to the Born cross section are the interference terms of (a) with (b) to (f) and the squared sum of the amplitudes of (k) to (m).

Weak corrections and corrections by multi-photon exchange are small compared to the other corrections at the HERMES beam energy of $E = 27.5$ GeV. The vertex loop correction (b) is infrared divergent and is compensated by the Bremsstrahlung emission (k,l) of low energy photons, which is also divergent. In the Mo-Tsai approach, the divergence is avoided by introducing an artificial infrared cut which is set to approximately 30 MeV in the numerical integration. In the Akhundov et al. approach the divergence is avoided by analytical integration.

Emission of Bremsstrahlung Photons

The treatment of radiative processes with a real photon in the final state will be discussed in more detail as it is the most critical part of the radiative correction procedure. Without Bremsstrahlung emission, the kinematics of the virtual photon and of the hadronic final state are completely defined by a measurement of the kinematics of the incoming and scattered lepton:

$$\nu = E - E' , \tag{8.6}$$

$$Q^2 = 4EE' \sin^2 \frac{\theta}{2} \tag{8.7}$$

$$\text{and} \quad W^2 = M^2 + 2M\nu - Q^2 . \tag{8.8}$$
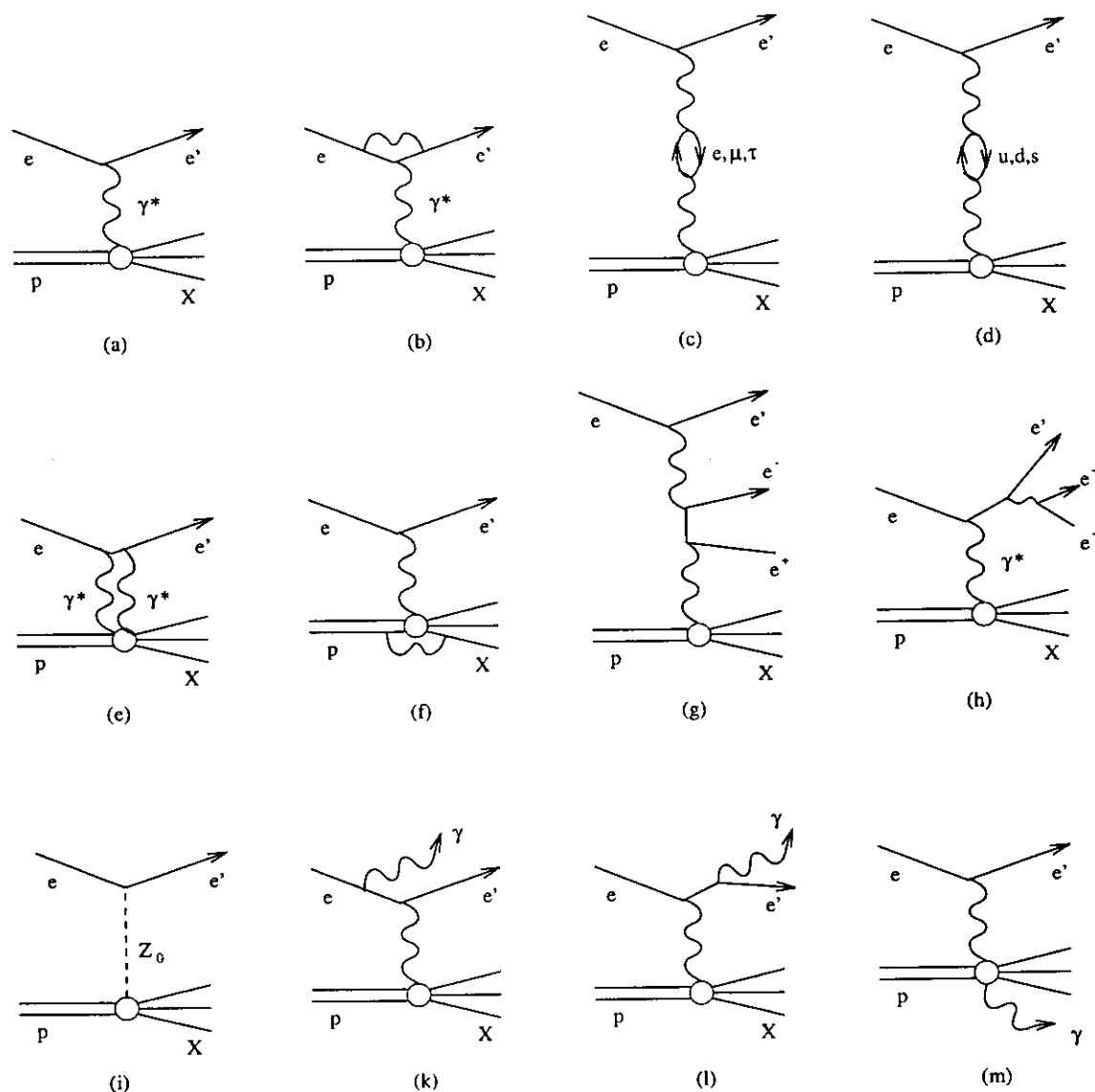
Figure 8.15: The Feynman graph of the Born term is indicated as (a). Among the lowest orders of electro-weak corrections are the following components: the vertex loop correction at the lepton vertex (b), vacuum polarisation by leptons (c) and quarks (d), two photon exchange (e), vertex correction at the hadronic vertex (f), pair production in the propagator (g) and at the lepton arm (h), exchange of a Z_0 (i), the emission of real Bremsstrahlung photons at the incoming (k) or scattered (l) lepton or at the hadronic vertex (m).

The emission of a real photon on the lepton arm implies that for a given kinematics of the incoming and outgoing lepton, the true kinematics of the exchanged virtual photon is modified:

$$\nu_{true} = E - E' - E_{Brems} < \nu \, , \tag{8.9}$$

$$Q^2_{true} \neq Q^2 \tag{8.10}$$

$$\text{and} \quad W^2_{true} < W^2 \, . \tag{8.11}$$

The change of kinematics has two consequences:

1. The hadronic final state of Bremsstrahlung events is different from the one which corresponds to the kinematics of the scattered electron. Especially it has the effect that the total energy and the invariant mass of the final state becomes smaller. In case high energy Bremsstrahlung photons are emitted, the virtual photon may probe the resonance region or elastic regions instead of probing the substructure of the nucleon. High energy Bremsstrahlung events can in principle be tagged by measuring either the radiative photon itself in the calorimeter or by registering missing hadronic energy. As the detection of photons and hadrons is incomplete in the detector, both methods can only be used as a cross check, but they cannot replace the calculation of the radiative correction factors.

2. The calculation of the correction factors i.e. of the total radiative cross section requires the integration over all kinematically allowed contributions. The kinematically allowed region is indicated in figure 8.16: point (A) indicates the kinematics of a given event as calculated from the measured lepton arm. The true physics process has a kinematics which can either lie in the inelastic region (B), the resonance and quasi-elastic region (C) or in the coherent region (D). The quasi-elastic region (C) denotes the scattering off a bound nucleon, the coherent region (D) describes the coherent scattering off a nucleus. The region close to point (A) is the region where the radiative cross section is infrared divergent.

   Due to the low mass of the electron, most of the Bremsstrahlung is emitted collinear with the incoming (s) or the outgoing (p) electron. The two lines in figure 8.16 indicate the position of the s- and p-peak of the correction factor.

The largest systematic uncertainty of the radiative correction factors comes from the limited knowledge of the cross section in the triangle as indicated in figure 8.16. A large part of the area can be measured by HERMES itself, the rest of the area has to be taken from other experiments, especially the resonance region and the quasi-elastic region.

Figure 8.17 shows the size of the radiative correction factor for the ^3He target as function of y for various x values. The ratio of the radiative cross section and the Born term is large at low x and high y.
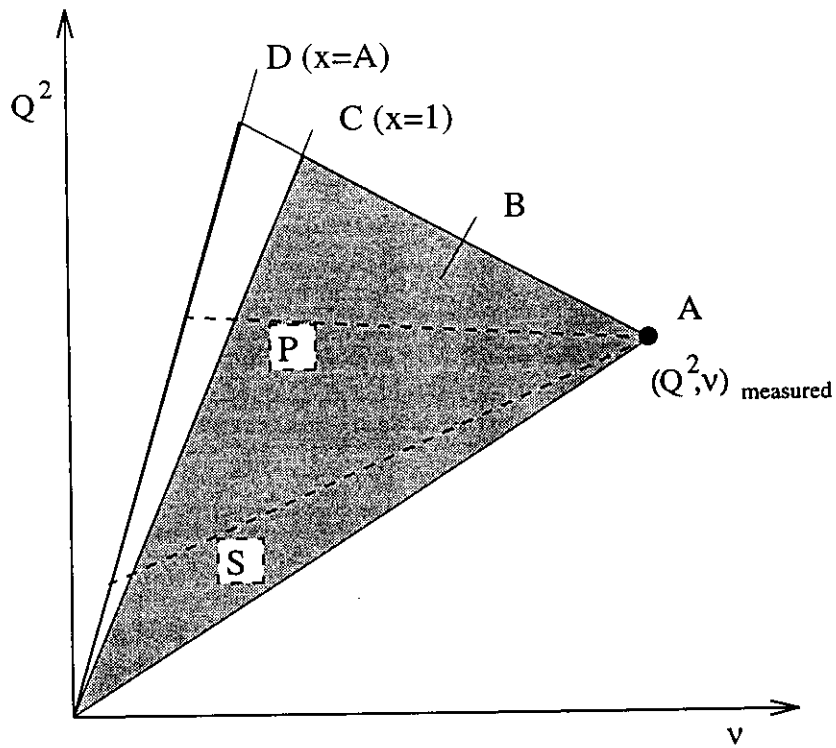
Figure 8.16: The area of integration for radiative corrections. A measured lepton arm at point (A) obtains contributions of the inelastic regions (B), the resonance and quasi-elastic region (C) or in the coherent region (D). The region close to (A) is infrared divergent. Most of the radiative tails origin in the s- and p-peak.
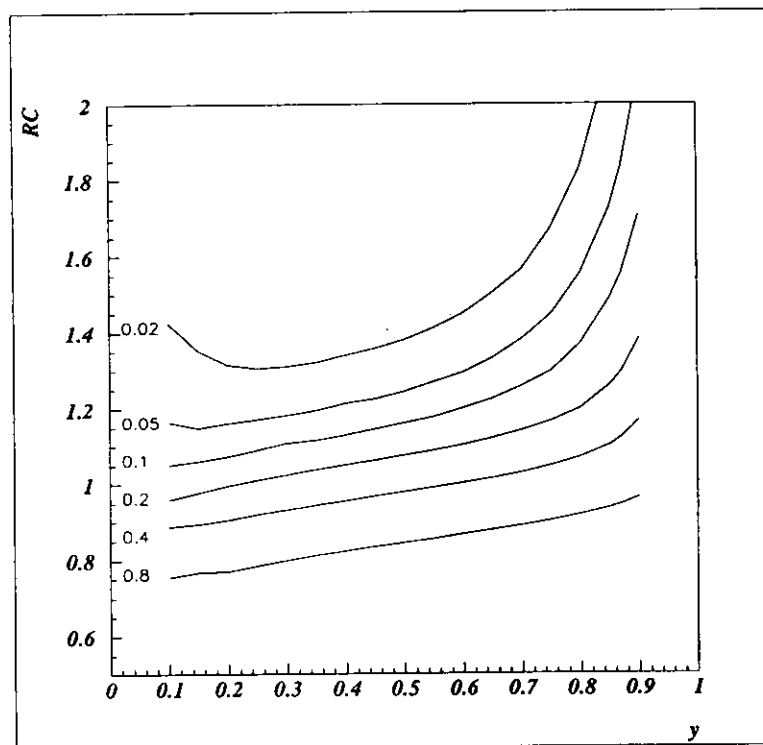
Figure 8.17: The ratio of the observed and the Born cross section is plotted versus y for various x values as indicated in the figure. The corrections are large at high y and at low x.

External Bremsstrahlung

Additionally to the above described Bremsstrahlung processes, which are called internal Bremsstrahlung, the process of external Bremsstrahlung exists. This occurs when the Bremsstrahlung process happens in a different atom than the primary (deep inelastic) process. External Bremsstrahlung is negligible in the HERMES experiment as the target density is so small ($\sim 10^{14}$ atoms/cm^2) that the probability of having a second interaction is close to zero. The target has approximately $3 \cdot 10^{-9}\%$ of a radiation length.

The scattered electron has to cross the wall of the storage cell, the exit window and chamber windows. It penetrates about 5 to 8% of a radiation length before its angle and momentum is measured. This material also produces Bremsstrahlung, however this process differs from external Bremsstrahlung as the emission is not coherent with the primary process. There are no interference graphs and therefore the correction for this kind of Bremsstrahlung can be treated as a simple instrumental correction which is independent of the radiative correction procedure. The photons from internal Bremsstrahlung and those from the Bremsstrahlung processes in the detector material can in general not be distinguished in our apparatus.

8.7.2 Iteration of Radiative Correction Procedures

The radiative correction factor δ_R

$$\delta_R(x, Q^2) = \frac{\sigma_{total}(x, Q^2)}{\sigma_{Born}(x, Q^2)} - 1 \tag{8.12}$$

can be calculated from the structure functions and form factors in the triangular area as described in figure 8.16 by double integration. For simplicity, we assume in the following that there is only one structure $f(x, Q^2)$ covering the whole area and that there is a linear relation between this structure function $f(x, Q^2)$ and the Born cross section σ_{Born}. The iterative scheme which will be described now can easily be generalised to the real situation where there are two structure functions and an electric and magnetic form factor in the elastic region.

If the structure function $f(x, Q^2)$ is known from other experiments in the whole triangular area, the radiative correction factors can be directly calculated using QED formulas as derived by Mo and Tsai or Akhundov et al.:

$$\delta_R = \delta_R(f(x_{true}, Q^2_{true}), x, Q^2). \tag{8.13}$$

However, if the structure function or form factors have to be derived from the experiment itself, only an iterative procedure allows to calculate the correction factors. Starting with an (almost) arbitrary structure function $f^0(x_{true}, Q^2_{true})$, the first iteration is done by correcting the measured cross section $\sigma_{measured}(x, Q^2)$ with a correction factor calculated from f^0.

$$\delta_R^0 = \delta_R(f^0(x_{true}, Q^2_{true}), x, Q^2). \tag{8.14}$$

With σ_{Born}^i being the Born cross section as calculated from i^{th} iteration of the structure function f^i, the following formulas can be derived for the $(i+1)^{th}$ iteration of the procedure:

$$f^{i+1}(x, Q^2) = f^i(x, Q^2) \frac{\sigma_{measured}(x, Q^2)}{\sigma_{Born}^i(1 + \delta_R^i)} \tag{8.15}$$

$$\delta_R^{i+1} = \delta_R(f^{i+1}(x_{true}, Q_{true}^2), x, Q^2). \tag{8.16}$$

If the initial structure function $f^0(x, Q^2)$ is taken from physically reasonable extrapolations of structure functions from other experiments, the procedure usually converges after a few iterations.

8.7.3 Correction of the Spin Asymmetries

The formulas for the radiative corrections of the spin asymmetries have been calculated by Shumeiko et al. [163]. Also a program for numerical calculations of the correction factors is provided by the group. In analogy to the unpolarised case, the calculations require the knowledge of the spin dependent form factors and spin structure functions in the whole area of integration. The size of the correction factors is much smaller compared to the unpolarised case as the major part of the corrections is spin independent and cancels in the spin asymmetry.

As the spin structure functions are unknown to a large extend, and will be measured by HERMES, an iterative procedure similar to the one described in the previous section has to be applied. One advantage compared to other spin experiments is that HERMES covers a large fraction of the integration area which is required for the double integration.

Figure 8.18 shows the size of the radiative correction of the asymmetries as function of y [165]. Plotted is the Born asymmetry and the observed asymmetry for a longitudinally and a transversely polarised proton target. Most of the large correction factors from figure 8.17 cancel in the asymmetry ratio. Figure 8.19 shows the same quantities for the ^3He target as calculated by [166]. The upper (lower) plot shows the asymmetries plotted versus x for a y value of 0.15 (0.85). The solid line is the measured asymmetry, the dashed line is the Born asymmetry. The calculations are based on an input parametrisation which is similar to the existing data. The real correction will use the measured asymmetry as input for the first iteration of the radiative correction factors.

8.8 Nuclear Corrections

HERMES uses ^3He as a neutron target. As the nucleons in the ^3He nucleus have momentum and binding energy, certainly nuclear effects play a role in ^3He. Besides trivial effects like the Fermi motion of the nucleon there are more sophisticated influences of the nuclear surrounding on the quark distributions which are called the nuclear EMC-effect. There are no measurements of the nuclear EMC-effect on
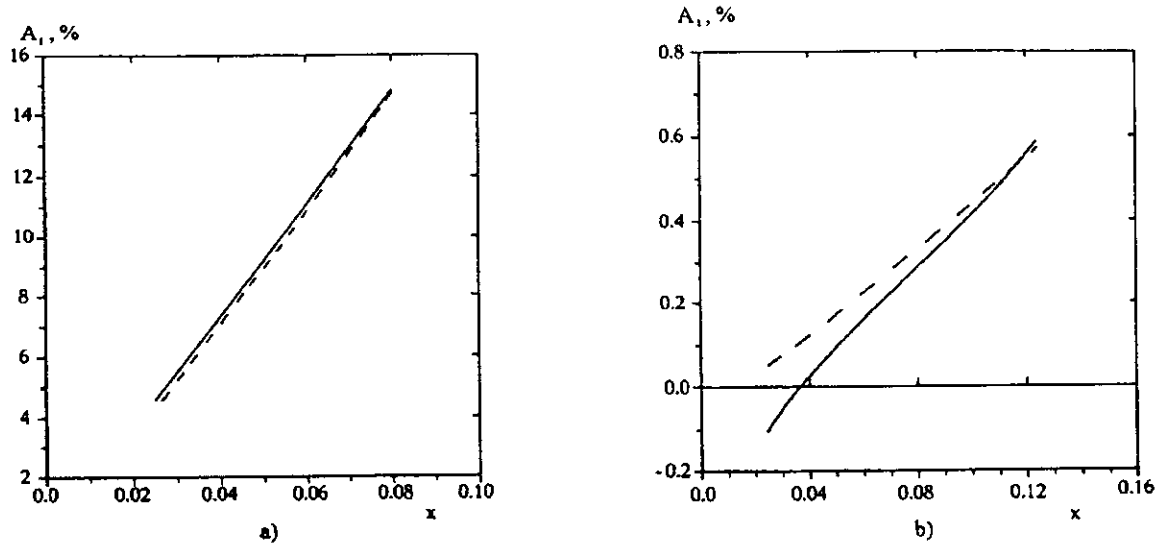
Figure 8.18: The x dependence of the Born asymmetry (dashed line) and of the observed asymmetry (solid line) are plotted for a longitudinal (a) and transverse (b) polarised hydrogen target.
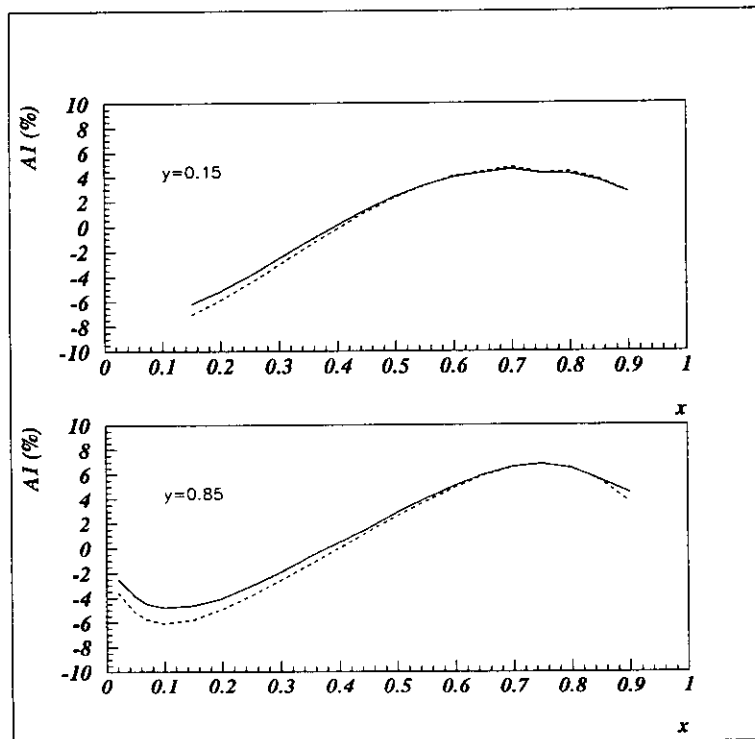
Figure 8.19: The x dependence of the Born asymmetry (dashed line) and of the observed asymmetry (solid line) are plotted for the ^3He target at a y value of 0.15 (0.85) in the upper (lower) plot.

^3He yet, but there are measurements for ^4He by EMC where the structure function is modified on the 5% level by the EMC-effect [167].

The above effects are relevant for the spin-averaged cross section of ^3He. The dominant nuclear effect on the polarisation asymmetry in ^3He is expected to be the admixture of different wave functions which describe the ^3He nucleus.

In the naive picture 90.3% of the ^3He wave function is in the S-state where the proton spins compensate each other and the total spin is generated by the neutron as shown figure 8.20. The S' contribution is 1.4% and the D-state has a probability of 8.3% . In the D-state the proton and neutron spins are all anti-parallel to the ^3He nucleus. Therefore the D-state asymmetry is an admixture of the (negative) proton and neutron asymmetries. The S' state contains an admixture of different states, some of which have the neutron spin anti-parallel to the ^3He spin and the proton spins aligned with the ^3He spin.
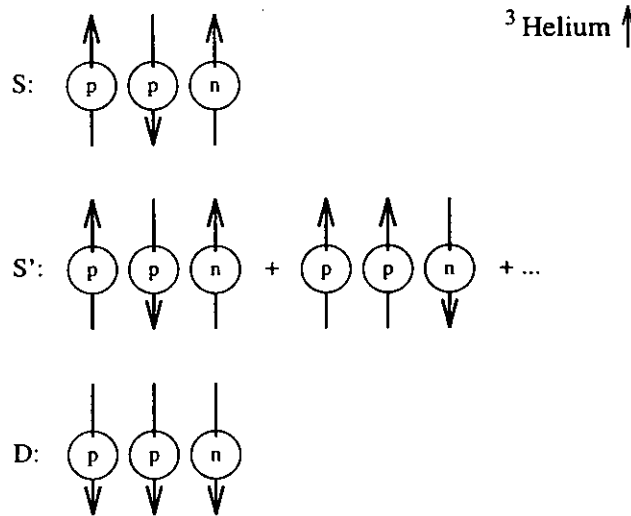
Figure 8.20: Spin structure of the ^3He wave function.

Using convolution models, the effect of the wave functions on the spin asymmetries in deep inelastic scattering can be directly calculated and used for the correction of the ^3He data. As a cross check similar calculations in the quasi-elastic region have been performed. The results show a good agreement with data from recent experiments .

The nuclear corrections in deuterium are expected to be small. The D-state probability for the deuteron amounts to about 5%.

In principle a 'spin-nuclear' EMC effect, i.e. the modification of the spin distributions of quarks in nuclear matter, can not be excluded. This is one reason why HERMES extracts the neutron spin structure function independently from $D - H$ and from ^3He. A comparison of the two results will clarify this point.

8.9   Luminosity and Polarisation

Beam Current and Polarisation

The beam polarisation is determined as described in chapter 4.7. The on-line polarisation values are corrected using the rise time calibration of the polarimeter. As data are taken during the rise of polarisation, a precise synchronisation of the polarimeter data and the HERMES data is needed. Low polarisation values will not be used for the spin structure function measurements. Runs with $P_B = 0$ are used to verify that there are no false asymmetries in the experiment introduced by the switching of the target polarisation.

The beam current is measured by the HERA machine group using beam pickups. HERA is filled with typically 180 bunches. As not all bunches have the same intensity, it is important to be able to measure bunch currents separately. The information which bunch produced a given event is included in the event data stream.

Target Thickness and Polarisation

The target polarisation is measured as described in chapter 5.3. The polarisation values for the two spin states are stored and applied in a similar way as the values for of the beam polarisation. The sign of the polarisation and the on-line polarisation values are written to the data stream with each event. The transition period between the two spin states is not used for the analysis. The actual sign of the polarisation is stored in the event stream for each event separately in order to guarantee a synchronisation with the spin flip.

The calculation of the target thickness requires the knowledge of the gas flow entering the storage cell, the cell geometry and the cell temperature. All those quantities are known and can be used to calculate the target thickness, however the precision of the calculation is only at the level of 10%. A way to calibrate the target thickness measurement is to increase the target thickness such that the beam lifetime is reduced significantly. The target density can then be extracted from the lifetime measurement. The information from the target optical monitor is used to monitor relative luminosity changes.

The Luminosity

For measuring absolute cross sections and structure functions, the absolute luminosity has to be known precisely. For measuring asymmetries, the absolute luminosity cancels to first order when polarisation is switched frequently and when the relative integrated luminosity is known for the two spin states. In a precision experiment however one has to care about second order effects: background processes have the potential to dilute the measured asymmetries. A subtraction of background processes requires the knowledge of the absolute luminosity [139].

The integrated luminosity is the product of target density, beam current and measured time (corrected for dead time effects). Each of the components can be

measured separately, however the product can be measured with higher precision using the luminosity counter.

In the case of an electron beam, the luminosity monitor measures Møller scattering off the electrons of the target atoms, in the case of positrons it measures a combination of Bhabha scattering and pair production. The cross section are precisely known, including radiative corrections. e^-e^- or e^+e^- pairs are measured in coincidence in the right and left part of the luminosity detector. They are counted as soon as they exceed an energy threshold of 5 GeV. Figure 8.21 shows the energy deposit in the left luminosity counter plotted versus the energy in the right one. The two bands show background from Bremsstrahlung showers or from elastic scattering which hit only one of the counters. The energy spectrum of those events reaches the beam energy. The patch in the middle shows clearly the coincidence signal from Bhabha scattering. The sum of the two energies is roughly the beam energy. As the aperture of the counters is limited by the beam pipe, a fraction of the shower leaks out of the crystals and reduces the total energy deposit.
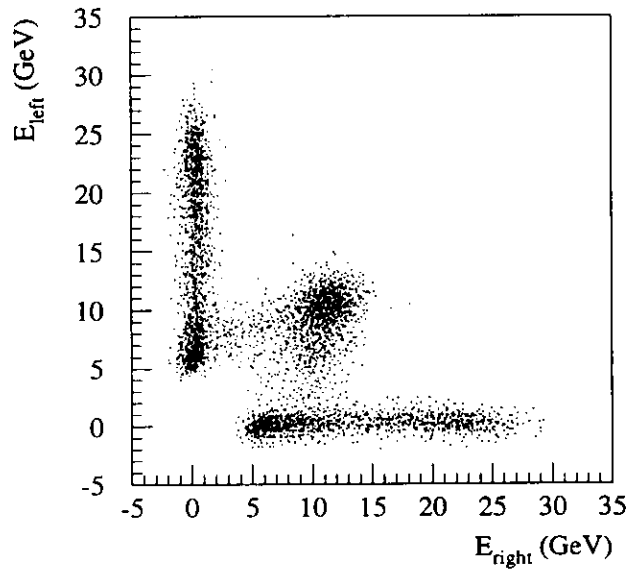
Figure 8.21: Plotted is the energy deposit in the left versus the right luminosity counter. The bands are mainly due to Bremsstrahlung background in one of the counters. The patch in the middle shows a clear signal of Bhabha scattering. The sum of the energies in the counters is approximately the beam energy of 27.5 GeV. Part of the showers is lost due to the limited apertures of the crystals. The trigger threshold is 5 GeV.

The absolute determination of luminosity requires a good knowledge of the shower distribution, the energy response of the detector crystals and the absolute position of the counters. The calibration can only be done using Monte Carlo tech-

niques. The relative monitoring of the luminosity between the two spin states is straight forward, as the electrons of the ^3He atoms are unpolarised and therefore the count rate, reduced by the background, is directly proportional to the luminosity. The background is determined by measuring with an empty storage cell.

The Product of Luminosity and Polarisation

The important quantity which enters into the physics cross sections is the product of luminosity L, target polarisation P_T and beam polarisation P_B. In the list of possible systematic uncertainties of the HERMES experiment, this product has a significant contribution. Currently possibilities are investigated to measure the known asymmetries in the resonance region and use the measurement to extract or cross-check the product of luminosity and polarisation.

8.10 First Experiences with a Storage Cell Target in HERA

The HERMES storage cell was installed in a test experiment in the HERA ring in spring '94 together with the collimator system and a set of detectors that allowed to measure the background conditions. A gas feed system was used to inject H_2, ^3He and N_2 with arbitrary density, however unpolarised only.

The test of the storage cell target was a complete success:

- The lifetime of the electron beam was reduced by the target gas as expected.

- High energy particles scattered off the target gas could be observed.

- The synchrotron radiation was reduced efficiently by closing the movable collimators as shown in figure 8.22.

- The closure of the collimators did not reduce the lifetime of the beam nor did it produce high additional shower background.

- There was no heating of the storage cell, neither by synchrotron radiation nor by rf heating.

In the real experiment which was installed in spring 1995, a storage cell is mounted which has a liquid helium cooling and is fed by a polarised ^3He source. The storage cell is kept on temperatures down to 20 K during full beam operation without any significant heating by synchrotron radiation or bunch currents. The polarisation of the optically pumped ^3He is of the order of $P_T = 50\%$.

Due to thermal or mechanical stress, the glass pumping cell of the ^3He target broke in May '95. During this accident the storage cell was mechanically deformed, probably due to the icing up of the cooled cell. By studying the lifetime reduction of the positron beam it was found that the thickness of the gas target decreased by a factor of 4.5, which will make a replacement of the storage cell necessary in the next possible access.
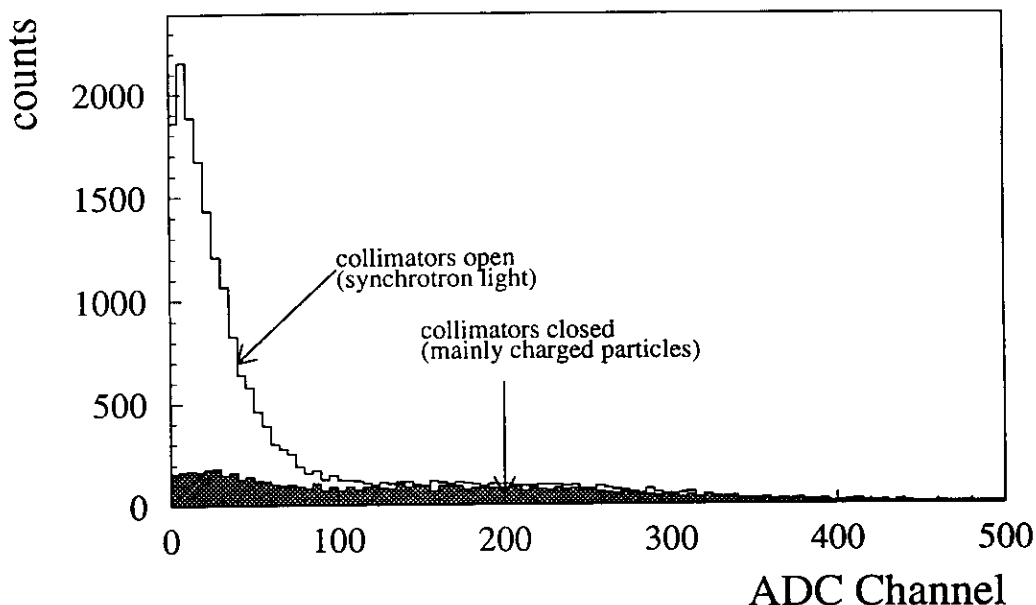
Figure 8.22: Shown is the ADC spectrum of a silicon counter behind the target window which is sensitive to synchrotron light. When the movable collimators are open and only one elliptical fixed collimator protects the cell, a peak at low energy deposit is observed which is caused by synchrotron light. The peak completely disappears when the movable collimators were closed.

8.11 First Deep Inelastic Events

As important parts of the detector are still in the commissioning phase and as the storage cell has an undefined shape currently, no physics results can be expected yet. Nevertheless, the first data have been taken and analysed.

The physics trigger is the coincidence of the hodoscope, the preshower and the calorimeter. The threshold of the preshower is currently set low so that it accepts all minimum ionising particles. The threshold of the calorimeter is at 3.5 GeV. During the running in phase, the Čerenkov counter is filled with nitrogen at a threshold which allows to separate electrons and pions. The Čerenkov signal can be included in the trigger to select electrons and positrons.

First measurements have shown that the background trigger rate is usually low. As the rate depends on the tuning of the HERA beams, on-line rate monitors have been installed in the HERA control room which allow the machine operators to optimise the beam steering in the HERMES region for minimum background in the trigger and in the chambers. For an empty storage cell the trigger rate at a beam current of 14 mA is less than 2 Hz. When the Čerenkov signal is included, the rate goes down to 0.35 Hz which shows that the background is, as expected, mainly pion background. The background from the proton beam is included in these numbers. It depends on the emittance and on the steering of the beam.

The storage cell can be filled with unpolarised hydrogen, deuterium and with po-

larised or unpolarised ^3He. With a target thickness of $\rho_T = 0.41 \cdot 10^{15}$ nucleons/cm^2 of ^3He, the trigger rate at 14 mA was measured to be 9 Hz, with the Čerenkov signal included the rate goes down to 3 Hz. This number agrees approximately with the expectations from deep inelastic scattering within the currently large uncertainties of the target density and the threshold of the calorimeter. The ratio of signal to background in the trigger is currently already very good and will be improved when the target runs at the nominal density and when more experience is gained with the optimal tuning of the machine.

Most of the events show low multiplicities in the chambers. The average multiplicity in the forward (backward) drift chambers is only one (two) for the upper and lower half of the detector! First data were processed by the reconstruction and analysis programs with the aim to understand the performance of the software and the detector. As the alignment and calibration of the detector is still very preliminary, no precision results can be expected. Only the drift chambers are used for track reconstruction as the efficiency of the vertex chamber was low at the time when the data were taken.

It turned out that the reconstruction program worked well from its beginning. Using the tree search algorithm, tracks are found in the backward region with an efficiency of better than 90%. A fine-tuning of the tracking parameters and an improved calibration of the chambers will increase the efficiency in future. The situation in the forward region is currently not optimal yet as the SDTR determination in the FC's is not finished. As the vertex chambers are not used in this analysis, only the FC's are left over to determine the track parameters in front of the magnet. The matching of the two track parts in front and behind the magnet is done using the the look-up method as described in chapter 8.4. It turned out that due to the low chamber multiplicity, the FC's alone allow for a sufficient track finding. However the resolution of the track parameters was not sufficient. The resolution has been be improved by the following method: the backward track is extrapolated into the magnet and is used as an additional space point for the forward track. A Monte Carlo simulation showed that once the drift chambers have reached the nominal resolution, this method should allow for a momentum resolution of 1 to 1.5% and an angular resolution of typically 0.35 to 1 mrad.

A vertex is assigned to every track as the point of closest approach of this track to the positron beam. Using the current resolution and alignment of the drift chambers, the mean distance of closest approach is 2 mm. Figure 8.23 shows a first vertex distribution. Plotted is the number of counts versus the horizontal (x) and vertical (y) position of the track at the point of closest approach. The most striking result of this analysis is that there is essentially no background, neither from scattering off the wall of the storage cell or from the collimators. It has been shown that with an empty target cell there are hardly any tracks reconstructed which origins in the target area. This proves that a storage cell target in combination with a well designed collimator system provides an excellent experimental technique.

Figure 8.24 shows the longitudinal vertex distribution. The points are real data from the experiment, the line is the result of the Monte Carlo simulation. The storage cell extends from -20 cm to $+20$ cm. The deviation of the two sets can be
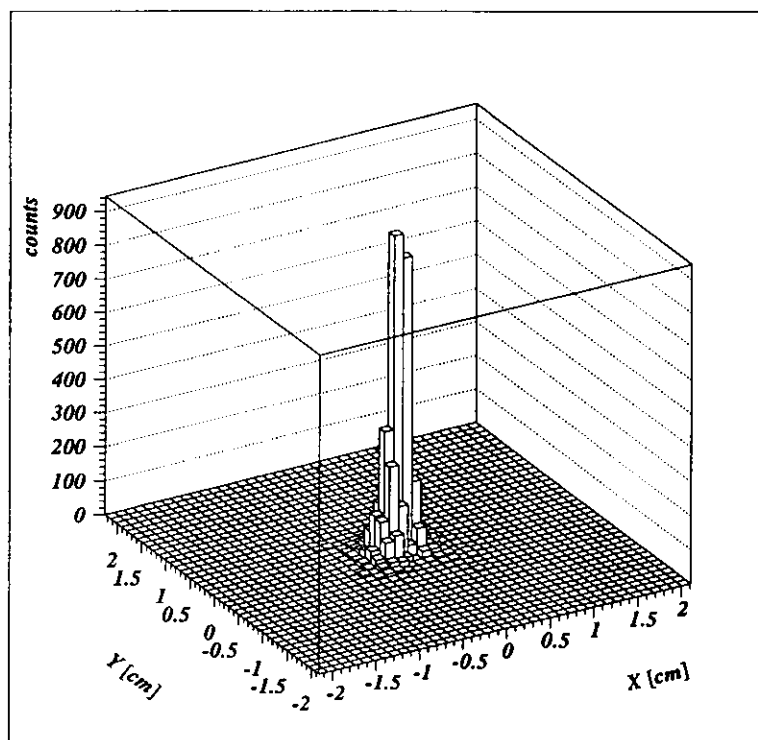
Figure 8.23: Plotted is the transverse vertex distribution. The mean distance of closest approach of tracks to the beam is only 2 mm. There is almost no background coming from scattering off the storage cell or the collimators.

explained: the cell is presently mechanically deformed and has a larger cross section in the central region now whereas the end of the tube has still its nominal cross section. This leads to the effect that the density distribution of the gas in the cell is not triangular any more but comes closer to a rectangular shape. The shift of the central position can be explained by a small vertical misalignment of the chambers or the beam which is magnified in longitudinal direction by the small angle of the tracks. The tails are partially explained by the smearing of the position measurement as the drift chambers have not yet reached their nominal resolution. A second contribution comes from the rf shielding tubes which have a finite conductance and make a smooth transition between the gas density in the storage cell and in the surrounding vacuum chamber. This contribution is not yet included in the Monte Carlo program.
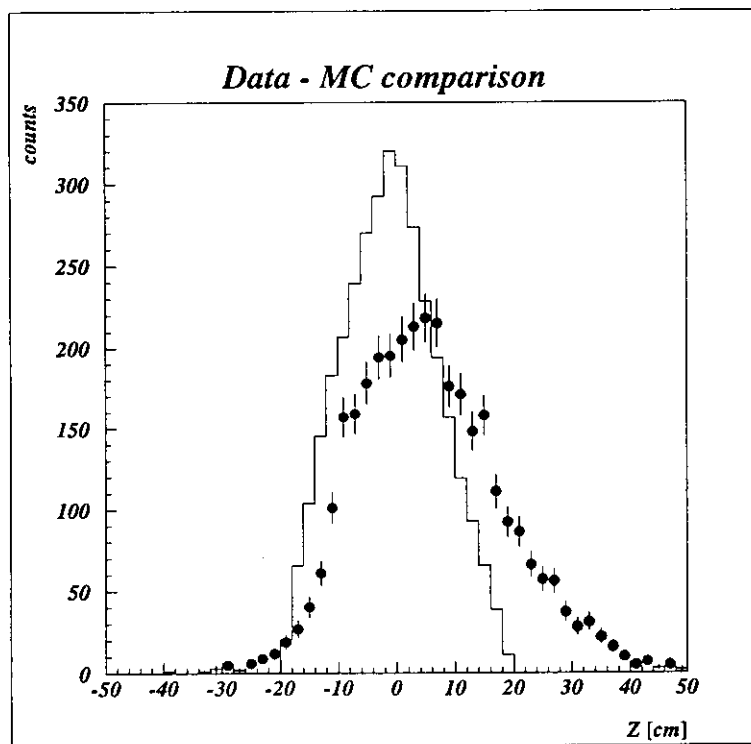
Figure 8.24: Plotted is the longitudinal vertex distribution. Due to the present mechanical deformation of the cell the vertex distribution is no longer triangular. The shift and the smearing of the distribution is mainly due to the fact that the alignment and calibration of the chambers is not finished yet.

The tracks which are found in the drift chambers can be correlated with clusters that are found in the calorimeter. Figure 8.25 shows the horizontal projection of the difference of the track position and the position of the cluster. A Gaussian fit shows that the resolution of the cluster position is 1.6 cm. This is much less than the granularity of 9 cm of the calorimeter. The cluster position is calculated from the relative pulse heights of neighbouring calorimeter blocks.

The momentum of a track can be compared to the energy which is measured in the calorimeter. Figure 8.26 shows the energy of the cluster which a track points
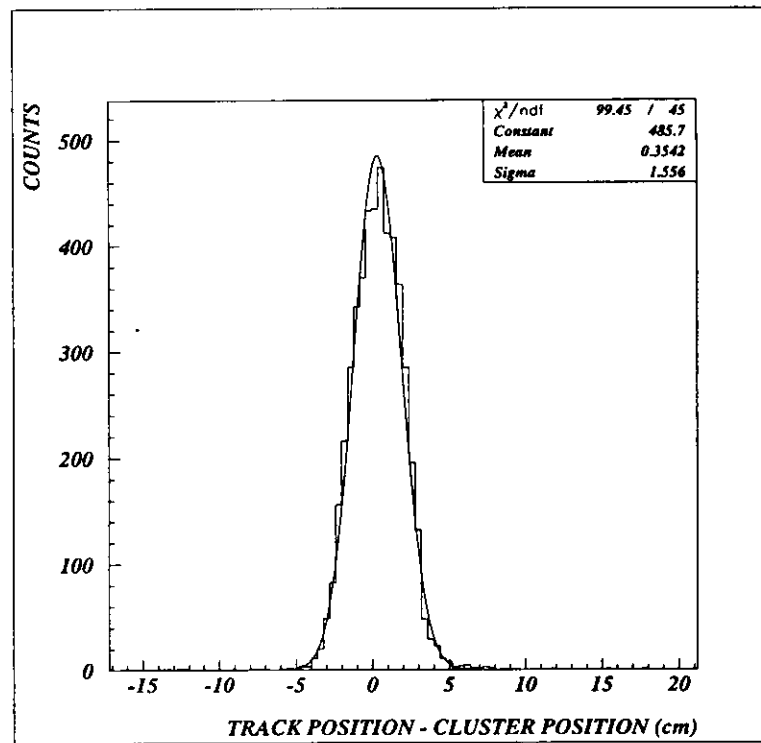
Figure 8.25: Clusters in the calorimeter are correlated with tracks. The granularity of the calorimeter is 9 cm. The position of the centre of a cluster is reconstructed from the relative energy sharing between neighbouring cells. The figure shows that the centre of the clusters agrees with the position of the extrapolated track within a resolution of $\sigma = 1.6\ cm$.

at plotted versus the momentum of the track. The signal in the preshower counter
is used to distinguish electrons and hadrons. A track which deposits more than
10 MeV in the preshower is identified as electron or positron, the rest of the tracks
are assumed to be hadrons. Certainly this kind of particle identification is very crude
and is used only preliminary. The upper plot in figure 8.26 shows the response of
electrons. A clear linear behaviour between the energy deposit and the momentum
can be seen. The slope of the band can be used to calibrate the calorimeter scale and
the width of the band corresponds to the combined resolution of the calorimeter and
the tracking. The improvement of the calibration and the resolution are currently in
progress. The lower plot in figure 8.26 shows the signal of the particles which have
a low preshower signal. Most of these tracks have, as expected, low momentum and
an energy deposit which is small compared to the response of electrons. The plot
shows a remnant band at $E_{CALO} \approx P$ which is caused by misidentified positrons.

The identification of electrons can be improved by the condition that the energy
response in the calorimeter agrees within 20% with the momentum. Figure 8.27
(a) shows the momentum distribution of positive and negative particles that fulfill
this condition. The spectrum of positive particles agrees roughly with the expected
positron spectrum from deep inelastic scattering. It extends to the full beam energy
at 27.5 GeV. At low x it is cut by the trigger threshold. The spectrum of negative
particles is completely different. It has only a low momentum component and orig-
inates from pair production and from misidentified hadrons. The spectrometer has
been build symmetrically so that electrons have the same acceptance as positrons
and can be used to correct the positron spectrum.

Figure 8.27 (b) shows the corresponding spectrum of positive and negative parti-
cles which have a low signal in the preshower. The low rate at high energy indicates
that the positron contamination in this sample is small and that the spectra mainly
corresponds to hadrons. The results agree with the expectation that the rate of
positive pions in the forward jet is higher than the rate of negative pions. Studies
to improve the particle identification using the Čerenkov counter and the TRD are
currently in progress.

Figure 8.28 shows a first comparison between the measured kinematic variables
and the expectations from Monte Carlo simulation. As in the previous figure, elec-
trons are identified by a cut in the preshower energy of 10 MeV and by requiring that
the energy in the calorimeter agrees within 20% with the momentum. Only events
with a Q^2 larger than 1 GeV^2 are used for this analysis. As a few amplifiers cards
in the upper chambers were not functional during data taking, for simplicity only
the lower part of the detector was used in this comparison. The Monte Carlo data
are normalised to the same number of events as the real data. The statistics shown
here corresponds to 50 minutes of data taking. The figures show the distributions of
the scattering angle θ, the azimuthal angle ϕ, the energy E, the squared invariant
mass W^2, the Bjørken x and y. The agreement between the experiment and the
Monte Carlo is already rather good, taking into account that the simulation does
not include any details about the efficiencies of the detector. Also internal radiative
corrections to the cross section are neglected in the calculation. The high quality of
the first results gives confidence that there is no major problem in the detector or
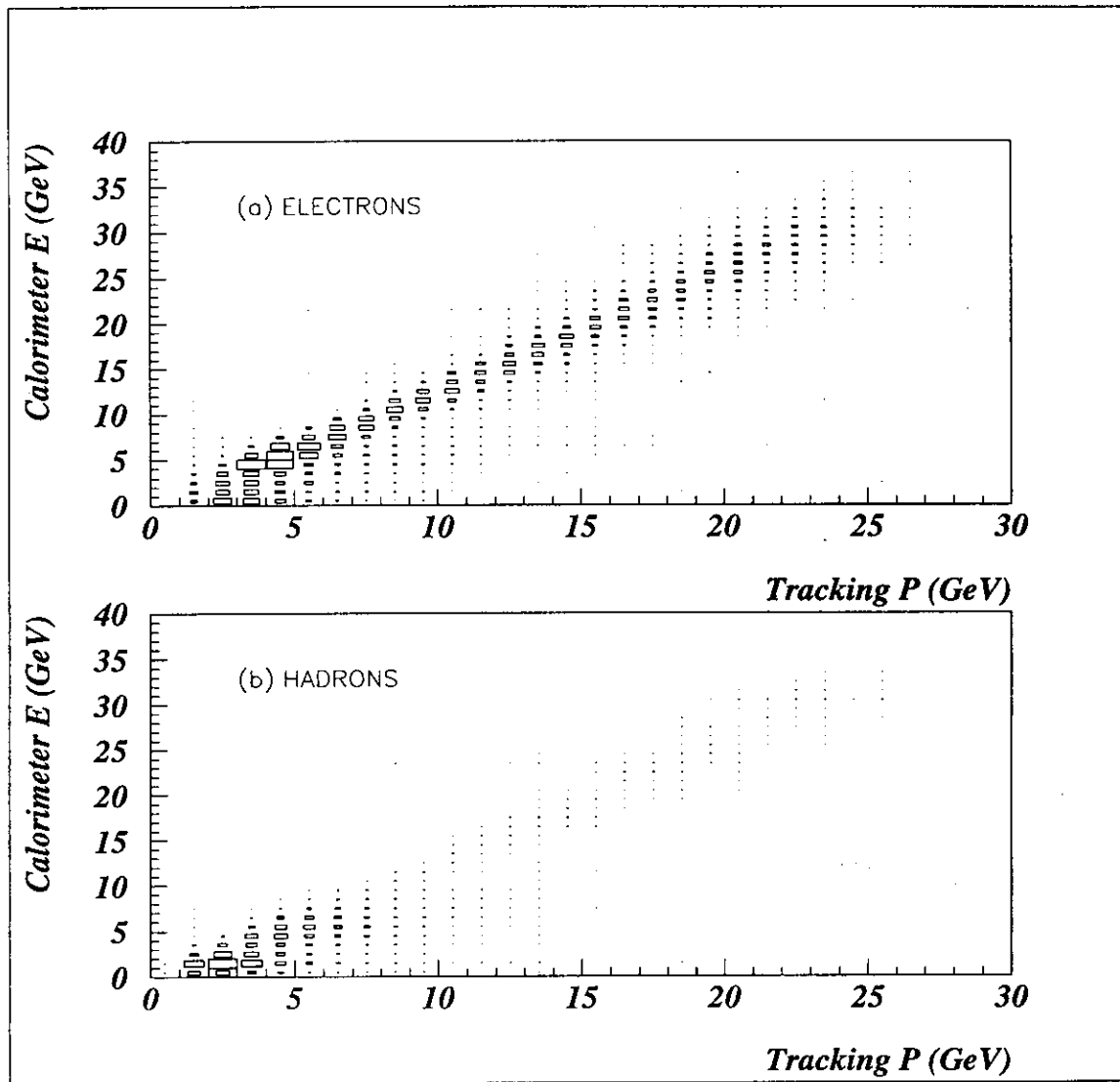
Figure 8.26: The energy of the cluster in the calorimeter is plotted versus the momentum of the corresponding track. Figure (a) contains all tracks which have a signal larger than 10 MeV in the preshower and figure (b) contains the rest of the tracks. This way electrons and hadrons can be separated to some extend. The band in figure (a) can be used to calibrate the calorimeter scale. The band in figure (b) comes from misidentified positrons.
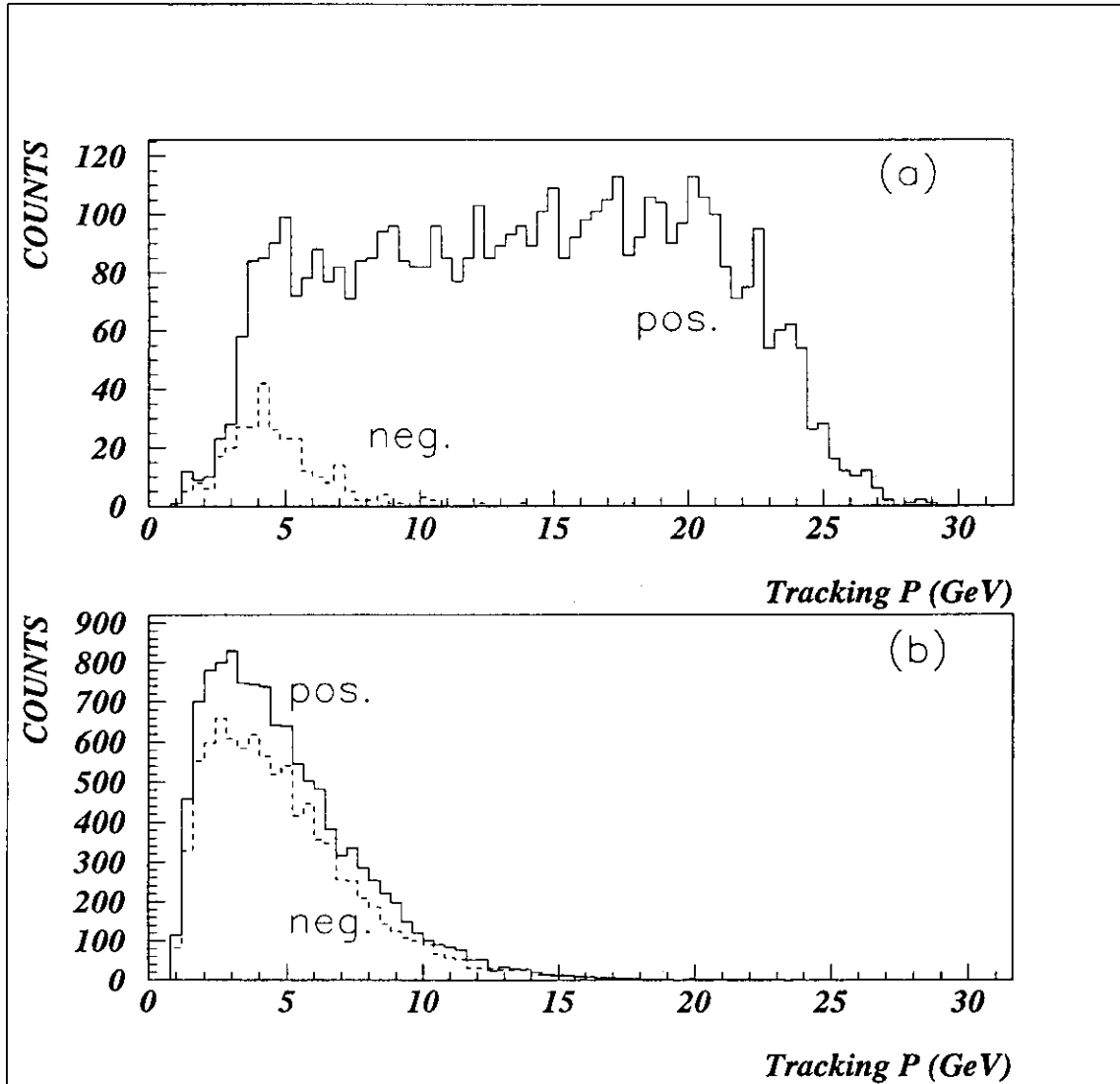
Figure 8.27: Figure (a) shows the momentum spectrum of positive and negative tracks which have a high preshower signal and where the energy deposit in the calorimeter agrees within 20% with the expectation. The spectra are dominated by positrons from deep inelastic scattering and by electrons from pair production. At low momenta there might be a contribution from misidentified hadrons. The positron spectrum goes as expected up to the full beam energy of 27.5 GeV. Figure (b) shows the spectrum of the rest of the tracks. They are expected to be mainly pions. As expected there are more positive than negative pions in this energy range.
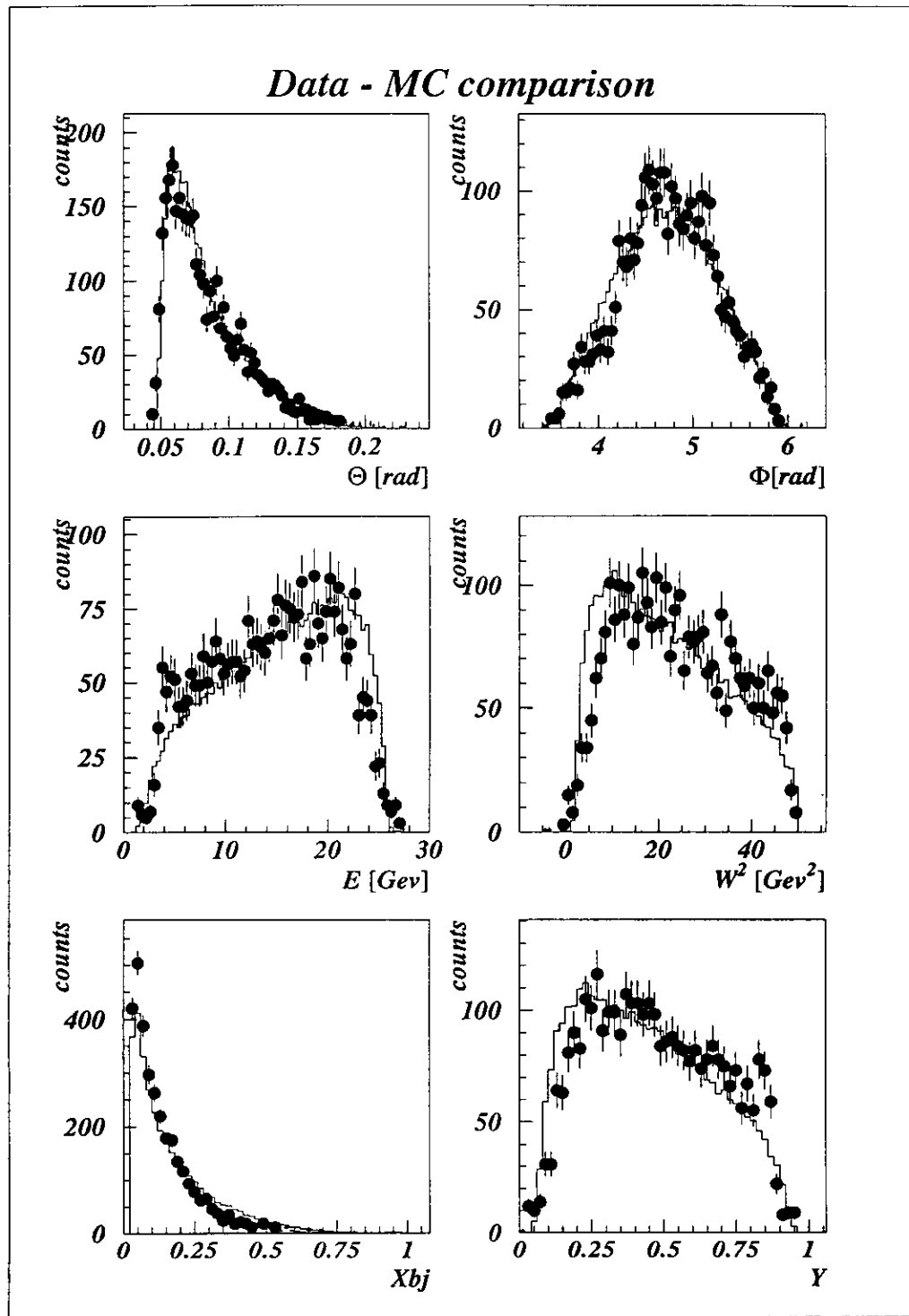
Figure 8.28: Kinematic distributions of real data (points) are compared to Monte Carlo expectations (full lines). Plotted are the scattering angle θ, the azimuthal angle ϕ, the energy E, the squared invariant mass W^2, the Bjørken scaling variables x and y. The approximate agreement of the two data sets shows that there are no obvious problems in the detector and in the reconstruction software. The Monte Carlo comparison will be continued in more detail once the detectors are calibrated and aligned.

in the analysis software.

Figure 8.29 shows the distribution of the events in the kinematic plane. There are many events at $Q^2 < 1$ GeV^2 which are not used for the analysis. There are no events at $\theta < 45$ mrad due to a wrong fiducial cut in one of the chambers which will be fixed. Only very few events are found at $x > 1$ indicating that the track reconstruction is mostly reliable.
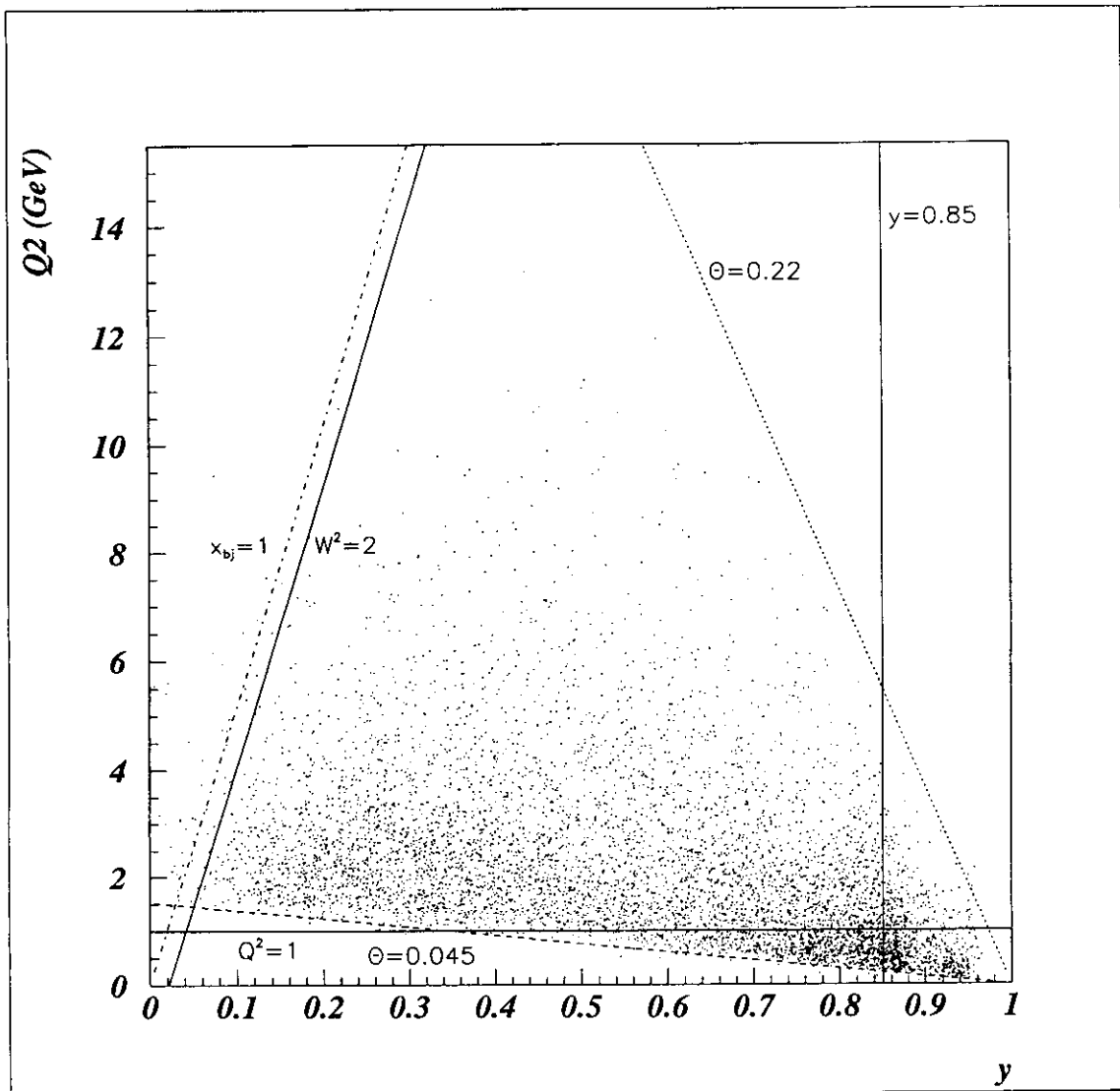
Figure 8.29: The distribution of real data events in the kinematic plane is shown. According to the deep inelastic cross section the highest population is at low Q^2.

Figure 8.30 demonstrates the statistical precision of the HERMES experiment. Shown is a false asymmetry obtained by splitting a 50 minutes run at 12 mA into two parts and plotting the difference of the events from the first and the second half of the run over the sum of the events. The result is, as expected, compatible with zero. Just as a reminder: the statistical precision which we collected in the EMC in

1 month will be achieved at HERMES within 1 day of running.
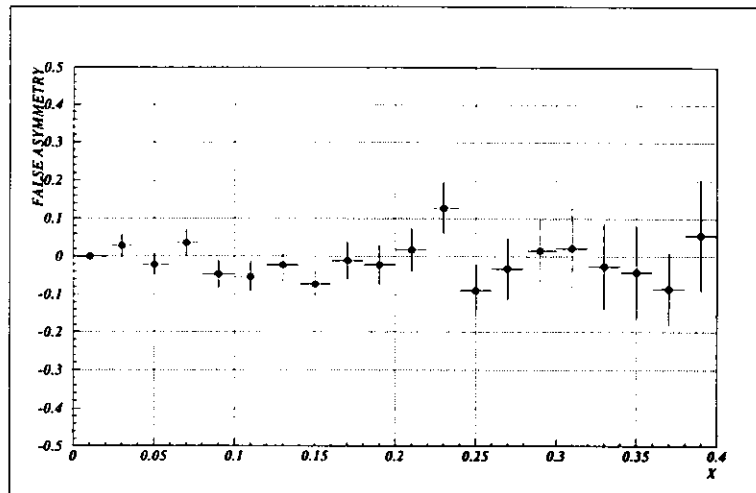
Figure 8.30: The data from a 50 minute run have been split into two parts (A and B). A false asymmetry $(A - B)/(A + B)$ which is formed from the two subsets is compatible with zero. It illustrates the size of the statistical errors which can be expected for the polarisation measurements.

Figure 8.31 shows an event which has three tracks, all coming from the same vertex. These kind of events will be used for the semi-inclusive analysis of polarised deep inelastic scattering and hopefully soon bring light into the question what the origin of the spin of the proton and neutron is.
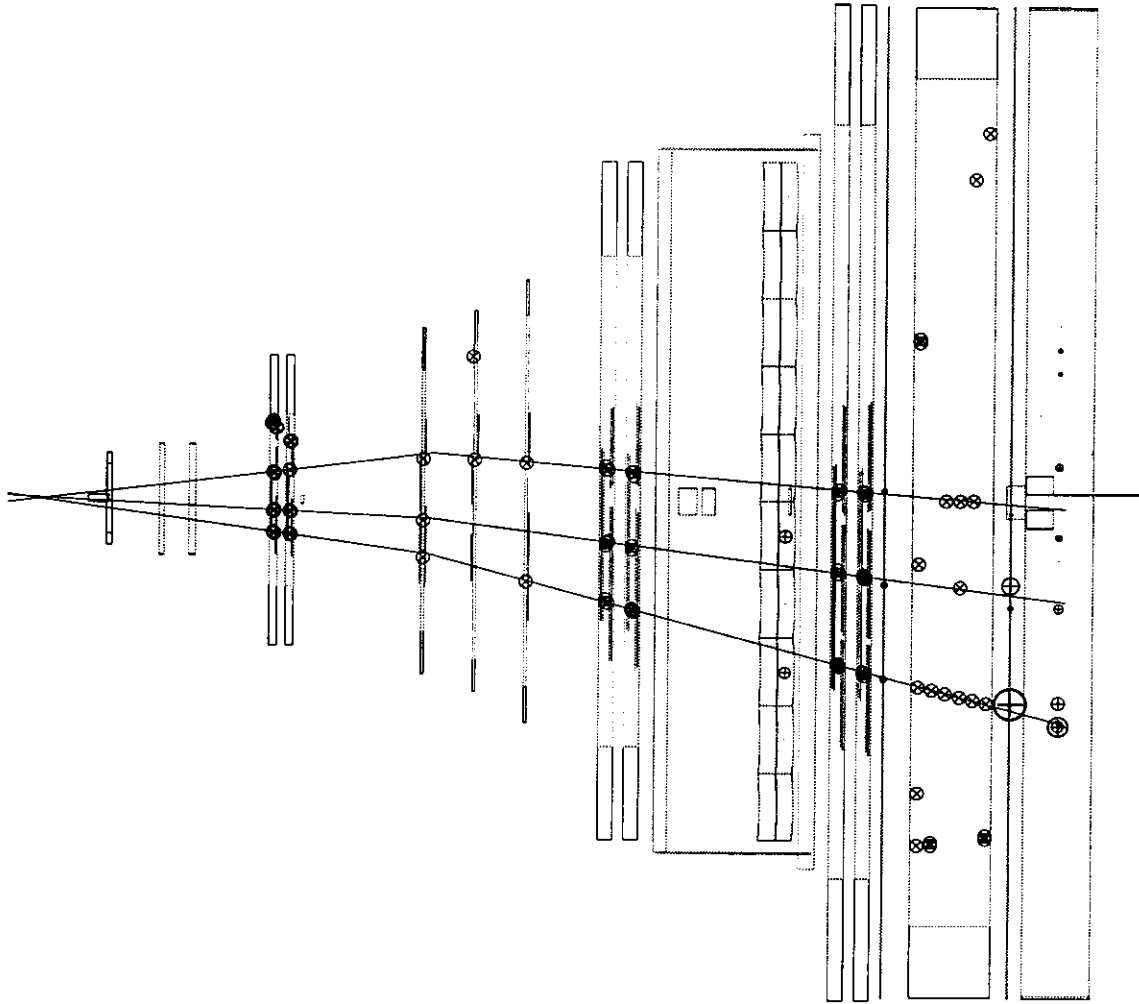
Figure 8.31: The plot shows a top view of an event with three tracks and a common vertex.

Chapter 9

Conclusions

Spin physics is a rich field that has gained a boost of interest during the *spin crisis* which was induced by the surprising results from EMC in 1987. Since then large progress has been made theoretically, and also experimentally with the recent results from SMC and SLAC. The violation of the Ellis-Jaffe sum rule has been established on the 3-σ level and is explained by the assumption that strange quarks carry a significant part of the spin of the nucleon. First measurements on the Bjørken sum rule indicate its validity on the 10% level. Higher order QCD corrections have been calculated which allow the extraction of the strong coupling constant α_s from the Bjørken integral.

The existing data are not nearly sufficient to understand the spin structure of the nucleon. Many new theoretical models have been developed over the last years and more complete and precise experimental data are needed to distinguish between them. The HERMES experiment has been designed to cope with these requirements in two ways: it will measure with high systematic and statistical precision the spin structure functions of proton and neutron by studying double-polarised, inclusive deep-inelastic scattering. Secondly, by measuring the semi-inclusive channel, HERMES will be able to disentangle the spin contributions from up, down and strange quarks and to some extend also the contributions from gluons and from the angular momentum of the quarks.

The aims of HERMES became feasible by the development of two new experimental technologies: the longitudinally polarised electron storage ring and the polarised storage cell gas target. Prototype storage cells were successfully operated in smaller storage rings. High target thickness was obtained simultaneously with high nuclear polarisation. Collimator schemes have been developed which allow a safe and almost background free operation of the cell in a high energy storage ring. A test experiment at HERA proved that the collimator scheme works and that the storage cell produces the predicted density.

The demonstration and optimisation of electron polarisation at HERA was the last hurdle which had to be taken before the experiment could be approved. For this purpose a fast Compton polarimeter has been built: a circular polarised laser beam is guided by a remote controlled mirror system 190 m down into the HERA tunnel where it collides head-on with the circulating electron beam. The electron polari-

sation is extracted from small spatial asymmetries of the back-scattered Compton photons which are detected in a calorimeter at a distance of 64 m. The measured asymmetries are of the order of 3 μm for each percent of polarisation. The polarimeter works reliable and is used for the online optimisation of the electron polarisation.

Empirical optimisation is necessary as strong depolarising resonances dominate the spin dynamics in high energy electron storage rings. The sensitivity of polarisation on various machine parameters has been studied in great detail and is basically understood now. In May 1994 spin rotators have been brought into operation and longitudinal electron polarisation has been demonstrated the first time in a high energy electron storage ring. Today, HERA is in the situation that high longitudinal polarisation is reproduced routinely. As a side-application of the polarisation studies, the electron beam energy of HERA was calibrated with a precision of better than one per mil by resonant spin depolarisation.

The HERMES detector is a conventional spectrometer. The design has been optimised according to detailed Monte Carlo simulations. It has been built and assembled in less than 2 years and is currently being commissioned in the HERA beam.

Since the design phase of the experiment, emphasis has been laid on a modern software environment and on a fast reconstruction and analysis system. A tree-search algorithm is used for track finding and a momentum look-up table replaces the fitting of tracks in magnetic fields. Both methods are highly efficient, precise and significantly faster than conventional programs. A unique data system has been adapted which allows for a transparent interactive access to all HERMES data. A data base system that operates on the internet has been developed which distributes time-dependent calibration data between different computers on site and to outside laboratories. The same system is used for the control and monitoring of the experiment. An on-line analysis chain has been set-up which reconstructs the events in real-time and allows for a high-level quality check of the detector performance during data taking.

The first data which are taken during the running in phase of the experiment prove that the experiment works: the storage cell target runs at the required temperatures and is able to produces the predicted luminosity. The background, especially the one coming from the collimators is small compared to the signal. The multiplicities in the chambers are tolerable. A few days after the chambers were operational, the reconstruction program was able to reconstruct tracks which pointed to the target. The precise alignment and calibration of the detector is currently in progress.

As soon as HERMES is commissioned, large amounts of interesting polarisation data will be taken. HERMES will run in 1995 on ^3He. From the beginning, semi-inclusive events will be analysed in parallel to the spin structure functions. In 1996 it is planned to interchange between hydrogen and deuterium gas and to disentangle spin distributions of different quark flavours. Additionally to the spin physics program, HERMES may be used as a general purpose detector for deep inelastic electron scattering off nuclei of almost any kind. An exciting future has started for the HERMES experiment with good chances to solve a large fraction of the spin puzzle.

Bibliography

[1] M. Düren, *Longitudinal Electron Polarization at HERA and the Status of HERMES*, Proc. of the 27th Int. Conf. on High Energy Physics, Glasgow, 1994, eds. P.J. Bussey and I.G. Knowles (Inst. of Physics Publishing, Bristol, 1995) Vol.2, p. 675.

[2] D.P. Barber *et al.*, Phys. Lett. **B343** (1995) 436.

[3] K. Zapfe *et al.*, Rev. Sci. Instrum. **66** (1995) 28;
M. Düren *et al.*, Nucl. Instr. Meth. **A322** (1992) 13.

[4] HERMES Collaboration, K. Coulter *et al.*, *Proposal* DESY-PRC 90/01 (1990);
HERMES Collaboration, *Technical Design Report*, DESY-PRC 93/06 (1993);
also:
M. Düren and K. Rith, *Polarized Electron Nucleon Scattering at HERA: The HERMES Experiment.*, Proc. of Physics at HERA, Vol. 1, eds. W. Buchmüller and G. Ingelman, Hamburg, DESY, Oct. 1991, p. 427.

[5] E. Rutherford, Phil. Mag. **21** (1911), 669.

[6] J.D. Bjørken, Phys. Rev. **179** (1969) 1547.

[7] M. Gell-Mann, Phys. Lett. **8** (1964) 214.

[8] G. Zweig, internal CERN report, CERN-TH-412 (1984).

[9] D.H. Perkins, Proc. of the 16th Int. Conf. on High Energy Physics, Batavia, Vol. 4 (1972).

[10] EMC, J.J. Aubert *et al.*, Nucl. Phys. **B272** (1986) 158.

[11] G. Altarelli and G. Parisi, Nucl. Phys. **B216** (1977) 298.

[12] EMC, J.J. Aubert *et al.*, Phys. Lett. **B105** (1981) 315;
EMC, J.J. Aubert *et al.*, Phys. Lett. **B105** (1981) 322.

[13] B.H. Wiik, Proc. of the Int. Conf. on Neutrinos, Weak Interactions and Cosmology, Bergen, Norway, June 1979, p.113.

[14] NMC, M. Arneodo *et al.*, Phys. Rev. **D50** (1994) 1.

[15] EMC, J.J. Aubert *et al.*, Phys. Lett. **B123** (1983) 275.

[16] P.A.M. Dirac, Proc. Roy. Soc. (London) **A117**, (1928) 610.

[17] K. Heller, Proc. of the 7th Lake Louise Winter Institute, Chateau Lake Louise, 1992, eds. B.A. Cambell *et al.*(World Scientific, Singapore, 1992) p. 47.

[18] J.D. Bjorken, Phys. Rev. **148** (1966) 1467;
J.D. Bjorken, Phys. Rev. **D1** (1970) 1376.

[19] J. Ellis and R.L. Jaffe, Phys. Rev. **D9** (1974) 1444;Phys. Rev. **D10** (1974) 1669.

[20] EMC, J. Ashman *et al.*, Phys. Lett. **B206** (1988) 364,Nucl. Phys. **B328** (1989) 1.

[21] review articles and references therein e.g.:
A.V. Manohar, *The g_1 Problem: Much Ado About Nothing*, Proc. of Polarized Collider Workshop, Univ. Park, USA (1990) AIP Conf. Proc. **223** (1991) 90;
F. Close, *The Nucleon Spin Crisis Bible*, Proc. of the $6^t h$ ICTP Workshop, Trieste, 1993; RAL-93-034 (1993);
V.W. Hughes and J. Kuti, Ann. Rev. Nucl. Part. Sci. **33** (1983) 611;
R. Windmolders, Int. Jour. Mod. Phys. **A7** (1992) 639;
H. Rollnik, *Ideas and Modells for the Proton Spin*, Proc. of the 9th Int. Symp. of High Energy Spin Physics, Bonn, 1990, Vol I: Conf. Proc., eds. K.-H. Althoff and W. Meyer, Springer, Heidelberg, 1991) p. 183;
S. Brodsky, J. Ellis and M. Karliner, Phys. Lett. **B206** (1988) 309;
D.B. Kaplan and A.V. Manohar, Nucl. Phys. **B310** (1988) 507;
B.L. Ioffe and M. Karliner, Phys. Lett. **B247** (1990) 387;
R.D. Carlitz, J.C. Collins and A.H. Mueller, Phys. Lett. **B214** (1988) 229;
G. Altarelli and G.G. Ross, Phys. Lett. **B212** (1988) 391;
R.L. Jaffe and A.V. Manohar, Nucl. Phys. **B37** (1990) 509.

[22] R. Feynman, *Photon Hadron Interactions* (Benjamin, Reading, Massachusets, 1972) p. 159.

[23] e.g. R.G. Roberts, *The Structure of the Proton* (Cambridge University Press, 1990).

[24] A. Manohar, p. 1 in ref. [17].

[25] W. Greiner, A. Schäfer, *Theoretische Physik Bd. 10 Quantenchromodynamik* (Verlag Harri Deutsch, 1989).

[26] R.L. Jaffe, Colloque de Physique **C6** (1990) 149.

[27] C.G. Callan and D.G. Gross, Phys. Rev. Lett. **21** (1968) 311;
Phys. Rev. Lett. **22** (1969) 156.

[28] CCFR, P.Z. Quintas *et al.*, Phys. Rev. Lett. **71** (1983) 1307.

[29] M. Virchaux and A. Milsztajn, Phys. Lett. **B274** (1992) 221.

[30] For a review of Operator Product Techniques applied in QCD see: ref. [24]; M.E. Peskin and D.V. Schroeder, *An Introduction to Quantum Field Theory* (Addison-Wesley, Menlo Park, 1993).

[31] SLAC-Yale E-80 Collaboration, M.J. Alguard *et al.*, Phys. Rev. Lett. **37** (1976) 1261; **41** (1978) 70.

[32] SLAC-Yale E-130 Collaboration, G. Baum *et al.*, Phys. Rev. Lett. **51** (1983) 115.

[33] E-142, P.L. Anthony *et al.*, Phys. Rev. Lett. **71** (1993) 959.

[34] E-143, K. Abe *et al.*, Phys. Rev. Lett. **74** (1995) 346.

[35] SMC, B. Adeva *et al.*, Phys. Lett. **B302** (1993) 533.

[36] P. Amaudruz *et al.*, Phys. Lett. **B295** (1992) 159.

[37] L.W. Whitlow *et al.*, Phys. Lett. **B250** (1990) 193.

[38] J. McCarthy, *Spin Structure Measurements at SLAC*, p. 663 in ref. [1].

[39] F.E. Close and R.G. Roberts, Phys. Lett. **B316** (1993) 165.

[40] L. Montanet et al., Particle Data Group, Phys. Rev. **D50** (1994) 1173.

[41] E-143, K. Abe *et al.*, SLAC preprint, SLAC-PUB-6734 (1995), subm. to Phys. Rev. Lett.

[42] SMC, D. Adams *et al.*, Phys. Lett. **B329** (1994) 399.

[43] S.A. Larin, Phys. Lett. **B334** (1994) 192.

[44] J. Ellis and M. Karliner, Phys. Lett. **B341** (1995) 397.

[45] S.L. Adler, Phys. Rev. **177** (1969) 2426.

[46] J.S. Bell and R. Jackiw, Nuovo Cim. **60A** (1969) 47.

[47] J.D. Bjorken, Phys. Rev. **148** (1966) 1457;Phys. Rev. **D1** (1970) 1367.

[48] S.D. Bass and P.V. Landshoff, Phys. Lett. **B336** (1995) 233.

[49] F.E. Close, *Spin Dependence of Diffractive Processes and Polarisation at Small x*, p. 669 in ref. [1].

[50] G. Altarelli, P. Nason and G. Ridolfi, Phys. Lett. **B320** (1994) 152.

[51] L. Klostermann, PHD thesis, NIKHEF, Amsterdam (1995), unpublished; SMC, B. Adeva *et al.*, Phys. Lett. **B320** (1994) 400.

[52] W. Wandzura and F. Wilczek, Phys. Lett. **B172** (1977) 195.

[53] A. Schäfer and L. Mankiewicz, *The Polarized Structure Function* $g_2(x)$., Proc. of Physics at HERA, Vol. 1, eds. W. Buchmüller and G. Ingelman, Hamburg, DESY, Oct. 1991, p. 411.

[54] L. Mankiewicz and A. Schäfer, *The physical interpretation of g2(x)*, Preprint Univ. Heidelberg (1991) HD-THEP-91-17.

[55] A.P. Bukhostov, E.A. Kuryaev and L.N. Lipatov, JETP Lett. **37** (1983) 482; Sov. Phys. JEPT **60** (1984) 22.

[56] X. Ji and C. Chou, Phys. Rev. **D42** (1991) 3637.

[57] R.L. Jaffe and X. Ji, Phys. Rev. **D43** (1991) 733.

[58] SMC, D. Adams *et al.*, Phys. Lett. **B336** (1994) 119.

[59] G.H. Burkhardt *et al.*, Ann. Phys. (NY) **56** (1970) 453.

[60] A. Schäfer, *Semi-inclusive Reactions and* g_2, Workshop on The Spin of the Nucleon, Jan. 19-20, 1995, Saclay, unpublished.

[61] T. Sloan *et al.*, Phys. Rep. **162** (1988) 45.

[62] L. Mankiewicz *et al.*, *PEPSI 1.1*, Proc. of Physics at HERA, Vol. 3, eds. W. Buchmüller and G. Ingelman, Hamburg, DESY, (Oct. 1991) p. 1395.

[63] T. Sjöstrand, Computer Phys. Comm. **39** (1986) 347.

[64] E. Nappi *et al.*, *Semi-Inclusive Muon Scattering from a Polarised Target*, CERN/SPSLC 95-27 (1995).

[65] W. Wislicki, Proc. of the 29th Renc. de Moriond, 'QCD and High Energy Hadronic Interactions', Meribel, France, March 1994.

[66] R.D. Field and R.P. Feynman, Phys. Rev. **D15** (1977) 2590.

[67] R.D. Field and R.P. Feynman, Phys. Rev. **B136** (1978) 1.

[68] TASSO, M. Althoff *et al.*, Zeit. Phys. **C22** (1984) 307.

[69] EMC, M. Arneodo *et al.*, Zeit. Phys. **C36** (1987) 527.

[70] EMC, J.J. Aubert *et al.*, Phys. Lett. **B160** (1985) 417.

[71] M. Veltri *et al.*, *Polarized Quark Distributions from Semi-Inclusive Leptoproduction*, Proc. of Physics at HERA, Vol. 1, eds. W. Buchmüller and G. Ingelman, Hamburg, DESY, (Oct. 1991) p. 447.

[72] H.E. Jackson, *HERMES Proposal for a RICH Conversion*, HERMES internal note, in preparation.

[73] S. Manayenkov and S. Belostotski, Workshop 'Physics at HERMES', unpublished, DESY Jan. 1995.

[74] R.L. Jaffe and X. Ji, Phys. Rev. Lett. **67** (1991) 552; and private communication.

[75] T.C. Meng *et al.*, Phys. Rev. **D40** (1989) 769.

[76] J.-Ph. Guillet, Zeit. Phys. **C39** (1988) 157
A.D. Martin, C.-K. Ng and W.J. Stirling, Phys. Lett. **B191** (1987) 200.
A. Borissov and W.-D. Nowak, *Can HERMES probe the Gluon Spin through J/Ψ Leptoproduction?*, HERMES-Zeuthen-Internal Note 01/95 (1995).

[77] G. Altarelli and G.G. Ross, Phys. Lett. **B212** (1988) 391.

[78] S. Güllenstern *et al.*, Phys. Lett. **B312** (1993) 166.

[79] J. Levelt, P.J. Mulders and A.W. Schreiber, Phys. Lett. **B263** (1991) 498.

[80] M. Düren, *Effect of the Electron Beam Tails at the HERMES Collimators*, DESY-HERMES 1/90 (1990).

[81] D.P. Barber *et al.*, Nucl. Instr. Meth. **A329** (1993) 79.

[82] M. Düren, *The HERA Polarimeter*, Proc. of the 10th Int. Symp. of High Energy Spin Physics, Nagoya, 1992, eds. T. Hasegawa *et al.* (Univ. Acad. Press, Tokyo, 1993) p. 911.

[83] M. Böge, *Analysis of Spin Depolarizing Effects in Electron Storage Rings*, Ph.D. Thesis, Univ. of Hamburg, 1994, DESY 94-087 (1994).

[84] A.A. Sokolov and I.M. Ternov, Sov. Phys. Doklady **8** (1964) 1203.

[85] J. Buon and J.-P. Koutchouk, *Polarization of Electron and Proton Beams*, Advanced Accelerator Physics Course, Cern Accelerator School, Rhodes, Greece, 1993, CERN SL/94-80 (1994).

[86] J.D. Jackson, Rev. Mod. Phys. **48** (1976) 417.

[87] D.P. Barber *et al.*, DESY Report 85-044 (1985).

[88] H. Mais and G. Ripken, DESY Report 83-062 (1983).

[89] E. Gianfelice-Wendt, in F. Willeke (editor), DESY-HERA 92-07 (1992) p. 202.

[90] E. Gianfelice-Wendt and M. Böge, *Polarization Studies for HERA-e in Presence of Spin Rotators*, p. 915 in ref. [82].

[91] L. Thomas, Philos. Mag. **3** (1927) 1.

[92] V. Bargman, L. Michel and V. Telegdi, Phys. Rev. Lett. **2** (1959) 435.

[93] V.N. Baier, V.M. Katkov and V.M. Strakhovenko, Sov. Phys. JEPT **31** (1970) 908.

[94] D.P. Barber, *Theory and Observation of Electron Polarization in High Energy Storage Rings*, in ref. [82].

[95] Y.S. Derbenev and A.M. Kondratenko, Sov. Phys. JEPT **37** (1973) 968.

[96] S.R. Mane, Phys. Rev. **A36** (1987) 105.

[97] J. Kewisch *et al.*, Phys. Rev. Lett. **62** (1989) 419.

[98] D.P. Barber *et al.*, Nucl. Instr. Meth. **A338** (1994) 166.

[99] M. Böge, *Optimization of Spin Polarization in the HERA Electron Ring using Beam-Based Alignment Procedures*, Proc. of the 11th Int. Symp. of High Energy Spin Physics, Sep. 15-22, 1994, Bloomington, in preparation.

[100] C. Grosshauser, Diploma thesis, Univ. Erlangen-Nürnberg (1994); DESY-HERMES 94-01 (1994).

[101] J. Buon and K. Steffen, Nucl. Instr. Meth. **A245** (1986) 248.

[102] D.P. Barber *et al.*, Part. Accel. 17 (1985) 243.

[103] M. Böge and T. Limberg, Proc. of 16th IEEE Part. Acc. Conf., Dallas, 1995, in preparation.

[104] D.P. Barber, *Spin Depolarization in Storage Rings*, in ref. [99].

[105] L. Arnaudon *et al.*, CERN - SL /92-16 (1992).

[106] R. Assmann *et al.*, CERN preprint, CERN SL/94-08 (1994).

[107] J.R. Johnson *et al.*, Nucl. Instr. Meth. **204** (1983) 261.

[108] K. Nakajima, *Polarisation Study and Polarimeter Development at TRISTAN*, p. 919 in ref. [82].

[109] Ph. Oelwein, Diploma thesis, Univ. Heidelberg (1995); to be published as DESY-HERMES report.

[110] R. Kaiser, Diploma thesis, Univ. Münster (1992); DESY F35D-92-02 (1992); Ch. Büscher, Diploma thesis, Univ. Heidelberg (1992); A. Mücklich, Diploma thesis, Univ. Heidelberg (1992); D. Westphal, Diploma thesis, Univ. Hamburg, DESY F35D-93-04 (1993); G. Schmidt, Diploma thesis, Univ. Hamburg (1994).

[111] M. Lomperski, Ph.D Thesis. Univ. of Wisconsin-Madison; DESY 93-045 (1993).

[112] U. Fano, J. Op. Soc. Am. **39** (1949) 859.

[113] M. Born and E. Wolf, *Principles of Optics*, Pergamon Press (1959).

[114] A. Caldwell *et al.*, ZEUS Note 92-022 (1992).

[115] D.P. Barber, DESY, private communication.

[116] HERMES Collaboration, *Proposal for a Longitudinal Electron Polarimeter at the HERA-East Section*, HERMES report (May 1994)

[117] T. Sloan, Lancaster Univ., private communication (1994).

[118] M. Conte et al, Nuovo Cim. **108A** (1995) 127.

[119] F. Stock *et al.*, Nucl. Instr. Meth. **A343** (1994) 334.

[120] K. Lee *et al.*, Nucl. Instr. Meth. **A333** (1993) 294.

[121] K. Lee *et al.*, Phys. Rev. Lett. **70** (1993) 738.

[122] K.P. Coulter *et al.*, Phys. Rev. Lett. **68** (1992) 174.

[123] M.D. Barker *et al.*, *Polarization Phenomena in Nuclear Physics*, eds. G.G. Ohlsen *et al.*, AIP, New York, (1981) p. 931.

[124] K. Zapfe, *The HERMES Target*, Proc. of the Workshop on Polarized Beams and Targets, Sensitive Tools for the Study of Solids, Nuclei and Particles, Les Houches, 1994, eds. M. Leduc and E. Steffens.

[125] K. Zapfe *et al.*, *Detailed Studies of a High-Density Polarized Hydrogen Gas Target for Storage Rings*; accept. for public. Nucl. Instr. Meth. **A** (1995) .

[126] W. Korsch *et al.*, *Temperature Dependence of ^3He Polarization in the HERMES Internal Target*, Proc. of Int. Workshop on Polarized Beams and Polarized Gas Targets, June 6-9, 1995, Köln, in preparation.

[127] M. Düren, *Protecting the HERMES Experiment from Synchrotron Radiation*, Proc. of the 9th Int. Symp. of High Energy Spin Physics, Bonn, 1990, Vol. II: Workshops, eds. W. Meyer, E. Steffens and W. Thiel (Springer, Heidelberg, 1991) p. 217.

[128] K. Zapfe-Düren, *The Internal Storage Cell Target for HERMES* in ref. [126].

[129] H.-G. Gaul, Ph. D Thesis, Univ. Heidelberg (1991);
Max-Planck-Institut für Kernphysik. Heidelberg, MPIH-V12-1991 (1991);
H.G. Gaul and E. Steffens, Nucl. Instr. Meth. **A316** (1992) 297.

[130] B. Braun, Ph. D Thesis, Univ. München, (1995).

[131] M. Pitt *et al.*, *A Target Optical Monitor of Polarization and Luminosity for Polarized ^3He Internal Targets*, in ref. [126].

[132] MAFIA computer code, ©Prof. Dr.-Ing. T. Weiland, Ohlystraße 69, D-65285 Darmstadt, Germany.

[133] G. Roeper, Diploma Thesis, Univ. Hamburg (1995), to be published as DESY-HERMES report.

[134] J. van den Brand *et al.*, *The Construction of a Microstrip Gas Tracker for HERMES*, Proc. of Intern. Workshop on Microstrip Gas Chambers, Oct. 13-14, 1994, Legnaro, in preparation.

[135] F. Neunreither, Diploma Thesis, Univ. Heidelberg (1993), unpublished;
A. Gute, Diploma Thesis, Univ. Erlangen-Nürnberg (1995), unpublished;
S. Bernreuther, Diploma Thesis, Univ. Erlangen-Nürnberg (1995), unpublished;
H. Russo, Diploma Thesis, Univ. Erlangen-Nürnberg, in preparation;
F. Schmidt, Diploma Thesis, Univ. Erlangen-Nürnberg, in preparation;
F. Meissner, Diploma Thesis, Univ. Berlin, in preparation;
D. Hasch , Diploma Thesis, Univ. Berlin, in preparation.

[136] S. Bernreuther *et al.*, *Design and Performance of the Large HERMES Drift Chambers*, Proc. of Wire Chamber Conference, 1995, Wien, in preparation.

[137] H.E. Jackson, V. Papavassiliou, M. Poelker and Dale Woodin, *Hadron Identification in HERMES*, Argonne Nat. Lab., PHY-6980-ME-92 (1992).

[138] M. Düren, *A Luminosity Monitor for the HERMES Experiment*, DESY-HERMES 5/90 (1990)

[139] Th. Benisch, Diploma Thesis, Univ. Erlangen-Nürnberg (1994), unpublished;

[140] M. Düren, *Elastic and Inelastic Event Rates and Statistical Accuracies of the HERMES Experiment*, DESY-HERMES 2/89 (1989).

[141] A. Schäfer, Phys. Lett. **B208** (1988) 175.

[142] J.K. Ousterhout, *Tcl and the Tk Toolkit*, Addison-Wesley Pub. Co., Massachusetts 1994.

[143] Application Software Group – Computing and Networks Division, *CERNLIB Edition May 1994*, CERN, Genf, 1994

[144] *GEANT, Detector Description and Simulation Tool*, CERN Program Library, CERN Geneva, Switzerland.

[145] *ADAMO – Entity-Relationship Programming System, Version 3.3*, Programming Techniques Group, ECP Division, CERN Geneva, 1994.

[146] M. Düren *et al.*, *The HERMES Event Display*, HERMES Collaboration, 1995.

[147] M. Ferstl, *HERMES Event Processor Manual*, Version 2.1, HERMES Collaboration, 1995.

[148] *PAW – Physics Analysis Workstation, Edition July 1994, CERN Program Library entry Q121*, CERN, Genf, 1994

[149] *COMIS – Compilation and Interpretation System* Application Software Group – Computing and Networks Division. CERN, Genf, 1994.

[150] K. Ackerstaff, M.-A. Funk *PinK (PinK is not KUIP) – an interface between Tcl/Tk, ADAMO and DAD*, Proc. of CHEP95, Rio de Janeiro, 18.-22. Sept. 95, to be published.

[151] W. Wander, *DAD – Distributed Adamo Database system at HERMES*, Proc. of CHEP95, Rio de Janeiro, 18.-22. Sept. 95, to be published.

[152] A. Kisselev *et al.*, *The HERMES Decoder*, HERMES Collaboration, 1995.

[153] W. Wander, Diploma thesis, Univ. Heidelberg (1992)

[154] M. Kolstein *et al.*, *The Alignment, Calibration and Efficiency Program*, HERMES Collaboration, 1995.

[155] B. Burow, *Monte Carlo Production Using Hundreds of Computers around the World: Towards Comfortable Large Scale Computing* , Proc. of CHEP95, Rio de Janeiro, 18.-22. Sept. 95, to be published.

[156] P. Carter, CALTECH, private commmunication (1995).

[157] G. D'Agostini, DESY internal report, DESY 94-099 (1994).

[158] G. Ingelmann, *LEPTO Program* Cern programming pool W5045 (1986)
B. Andersson, G. Gustafson and T. Sjoestrand, Zeit. Phys. **C9** (1981) 233.

[159] M. Veltri *et al.*, *PEPSI*, HERMES Collaboration (1995).

[160] L.W. Mo and Y.T. Tsai, Rev. Mod. Phys. **41** (1969) 205.

[161] Y.T. Tsai, SLAC-PUB-848 (1971).

[162] A.A. Akhundov, D.Y. Bardin and N.M. Shumeiko, Sov. J. Nucl. Phys. **29** (1979) 499.

[163] T.V. Kuchto and N.M. Shumeiko, Nucl. Phys. **B219** (1983) 412.

[164] M. Düren *et al.*, *The HERMES Monte Carlo Program*, HERMES Collaboration (1995).

[165] I.V. Akushevich and N.M. Shumeiko, J. Phys. G: Nucl. Part. Phys. **20** (1994) 513.

[166] D. Ryckbosch, I. Akouchevitch, private communication (1995).

[167] P. Amaudruz *et al.*, Zeit. Phys. **C51** (1991) 387

List of Figures

List of Tables

Acknowledgements

I would like to thank all my colleagues and friends in the HERMES collaboration and in the HERA polarisation group. This work would not have been possible without their remarkable support and cooperation.

Klaus Rith is certainly the person who deserves the most credit as he made this work possible. Especially in the design phase of the experiment he initiated a creative atmosphere at the MPI für Kernphysik in Heidelberg in the department of B. Povh.

V. Soergel and G.A. Voss gave me the opportunity to work on beam polarisation at HERA, a challenging and interesting field which was new to me at that time. R. Klanner introduced me into the calorimetry of Compton beams and D. Barber and R. Brinkmann into accelerator physics and spin dynamics. People that I worked with on the daily basis were also W. Brückner, H.-D. Bremer, Ch. Büscher, E. Gianfelice-Wendt, J. Klute, M. Lomperski, N. Meyners, A. Mücklich, R. Kaiser, Ph. Oelwein, D. Westphal, F. Zetsche and many others. They and especially C. Großhauser and M. Böge contributed a lot during all the exciting polarisation studies. Also the members of the LEP polarisation group should be mentioned as they contributed to the common aim by mutual exchange of experience.

Since HERMES is approved, B. Wiik and A. Wagner have supported the experiment in all aspects. The monthly 'Wagner meetings' turned out to be a fruitful deadline for all problems which nobody likes to solve. M. Vetterli, E. Steffens and Y. Holler represent the people which made sure that the spectrometer was assembled in a very short time.

Despite the infinite amount of work, the preparation of the software and of the physics analysis of HERMES was a pleasure because it was another opportunity for me to combine scientific work with a personal team spirit. Special thanks belong to W. Wander who is one of the key persons of the HERMES software development together with K. Ackerstaff, M. Ferstl, M.A. Funk, P. Green, A. Kisselev, M. Kolstein, N. Makins, P. Welch and some others. The people in the DESY computer centre and the group of P. Palazzi at CERN have to be mentioned in the same context.

All other members of the HERMES collaboration have to be mentioned as the whole work depends on everybody's contribution. I want to thank especially N. Akopov, A. Borissov, H. Böttcher, A. Brüll, G.R. Court, B. Filippone, P. Galumian, H. Ihssen, H.E. Jackson, A. Miller, R. Milner, W.D. Nowak, T. O'Neill, D. Ryckbosch, J. Sowinski, M. Spengos and M. Veltri for their (daily) support. Not to forget Sabine Krohn who always found a room for my numerous meetings.

Respect is given to our Armenian, Belorussian and Russian colleagues who man-

232

age to do scientific work of high quality in a surrounding which is not alway easy.

Forward-Chamber (FC)   Magnet-Chamber   Back-Chamber BC1, BC2   Back-Chamber BC3, BC4   Transition Radiation Det.

Magnet   Čerenkov   Hodoscope 1

Electron Beam Pipe   Hodoscope 2

Vertex-Chamber (VC)   Calorimeter

^{3}He-Target